博士論文

First measurement of the strangeness axial coupling constant using neutral current quasi-elastic interactions of atmospheric neutinos at KamLAND

(KamLAND における大気ニュートリノの中性カレント準弾性反応を用いたストレンジネス軸性電荷の初めての測定)

安部　清尚

令和４年

Doctoral Dissertation

First measurement of the strangeness axial coupling constant using neutral current quasi-elastic interactions of atmospheric neutinos at KamLAND

by Seisho Abe

Tohoku University

A dissertation submitted for the degree of Doctor of Science

2022

Abstract

This dissertation reports a measurement of the strangeness axial coupling constant g_A^s using atmospheric neutrino data at KamLAND. This constant is a component of the axial form factor of the neutral current quasi-elastic (NCQE) interaction and represents the contribution of the strange quarks existing as sea quarks to the nucleon spin. By determining this value, we can answer the question about fundamental nucleon structure: Are the strange quarks in the nucleon polarized?

The value of g_A^s significantly changes the ratio of proton and neutron NCQE cross sections. KamLAND is suitable for measuring NCQE interactions as it can detect nucleon recoils with low energy thresholds and measure neutron multiplicity with high efficiency. KamLAND data, including the information on neutron multiplicity associated with the NCQE interactions, makes it possible to measure g_A^s with a suppressed dependence on the axial mass M_A, which has not yet been determined.

For a comprehensive prediction of the neutron emission associated with neutrino interactions, a simulation of particle emission via nuclear de-excitation of ^{12}C, a process not considered in existing neutrino Monte Carlo event generators, is established. The simulation result shows a good consistency between our prediction and experimental data in neutron emission probability. Energy spectrum fitting for each neutron multiplicity gives $g_A^s = -0.14^{+0.25}_{-0.26}$, which is the most accurate measurement obtained using NCQE interactions without M_A constraints. This analysis will add great knowledge to many next-generation experiments aiming to measure neutrons associated with neutrino interactions.

Acknowledgement

First of all, I would like to express my great appreciation to all people who advised and supported me in conducting this research. I would like to express my sincere gratitude to my supervisor, Associate Professor Itaru Shimizu, who gave me, then an undergraduate student, the opportunity to conduct these exciting research topics about neutrino interactions. I was given many brilliant discussions and corrections on my analyses, slides, and papers. I am deeply grateful to Professor Kunio Inoue, the spokesperson of the KamLAND experiment, who gave me the opportunity to work on the KamLAND experiment as a member of the Research Center for Neutrino Science (RCNS) and fruitful discussions in the weekly meeting. I would also like to acknowledge the crucial role of Professor Yasuhiro Kishimoto, who provided meaningful advice on my presentation for this dissertation. Furthermore, a special gratitude I give to the people at the RCNS, the KamLAND Collaboration, the Graduate Program on Physics for the Universe (GP-PU), and the T2K Collaboration for their help and cooperation. I would also thank Professor Kevin S. McFarland and Associate Professor Yoshinari Hayato for advising us on my neutrino simulation. Finally, I would like to thank my wonderful friends and family for their support throughout my university life.

This work was supported by JSPS KAKENHI Grant Number 21J10185 and by the GP-PU, Tohoku University.

Contents

List of Figures

List of Tables

Part I

Introduction

Chapter 1

Neutrino Physics

Neutrino is a fascinating elementary particle that broke the Standard Model (SM) by discovering neutrino oscillation. In recent days, there have been developments not only in precise measurements of neutrino oscillation but also in experiments to investigate other exciting properties of neutrinos. Furthermore, we also discuss neutrino astronomy searches of neutrinos from astronomical objects and proton decay searches using neutrino detectors. In order to improve the sensitivity of these measurements, the dominant systematic uncertainty, the neutrino interaction with nucleon in the nucleus (simply denoted as neutrino-nucleon interaction in this dissertation), must be understood further. Since the neutrino-nucleon interaction involves a many-body system, we need multifaceted verification through various experiments.

This study focuses on neutral current quasi-elastic interactions and measures the neutron multiplicity associated with them, which has not been measured in other experiments. This study is expected to provide new insight and knowledge into neutrino-nucleon interaction, proton decay, and neutrino astronomy. This chapter briefly introduces neutrino physics and an outline of this dissertation. Sec. 1.1 firstly introduces neutrinos in the SM, and Sec. 1.2 shows neutrino oscillation found as evidence for the violation of the SM. Sec. 1.3 explains experimental hot topics in neutrino physics these days. Sec. 1.4 briefly describes the neutrino-nucleon interaction, which is the dominant systematic uncertainty in these experiments. Sec. 1.5 introduces the strangeness axial coupling constant, the target of this study, then Sec. 1.6 guides through the outline of this dissertation.

1.1 Neutrino in the Standard Model

In the Standard Model (SM) of particle physics, neutrino is an elementary particle that has 1/2 spin, no electric charge, no color, and no mass. It interacts only via weak interaction. Neutrino has three flavors ν_e, ν_μ, and ν_τ, which associated with charged leptons e, μ, and τ, respectively. Various theories and experiments described below established these properties.

Pauli predicted the existence of the neutrino for the first time in 1930 to explain the continuous spectrum of the β decay ($n \rightarrow p+\bar{\nu}_e+e^-$), expecting no electric charge and 1/2 spin. Thirty years later, Reines and Cowan discovered the neutrino in 1953 by observing inverse β decay ($\bar{\nu}_e+p \rightarrow e^+ + n$) from the nuclear reactor. In 1956, Lee and Yang noticed that parity is not always conserved in weak interaction. In 1957, the parity violation was discovered experimentally by Wu. In 1958, an experiment by Goldhaber showed that the helicity of neutrino emitted by the β decay is left-handed. These experiments established massless left-handed neutrino and V−A theory. The electroweak theory, which combines electromagnetic and weak interaction, was built by Grashow, Weinberg, and Salam in 1967. The electroweak theory, together with QCD (Quantum Chromodynamics) for the description of the strong interaction, is called the "Standard Model".

The electroweak interaction has $SU(2) \times U(1)$ symmetry, and there are three gauge bosons ($W^{\pm}$, Z^0), which incorporate the weak interaction. An interaction mediated by the $W^{\pm}$ boson involving an exchange of electric charge is called Charged Current (CC) interaction. On the other hand, an interaction mediated by the Z^0 boson, which maintains electric charge, is called Neutral Current (NC) interaction. The SM successfully explains almost all the experimental results. However, a phenomenon beyond the SM, neutrino oscillation that requires non-zero neutrino mass, was found in 1998 as described in Sec. 1.2.

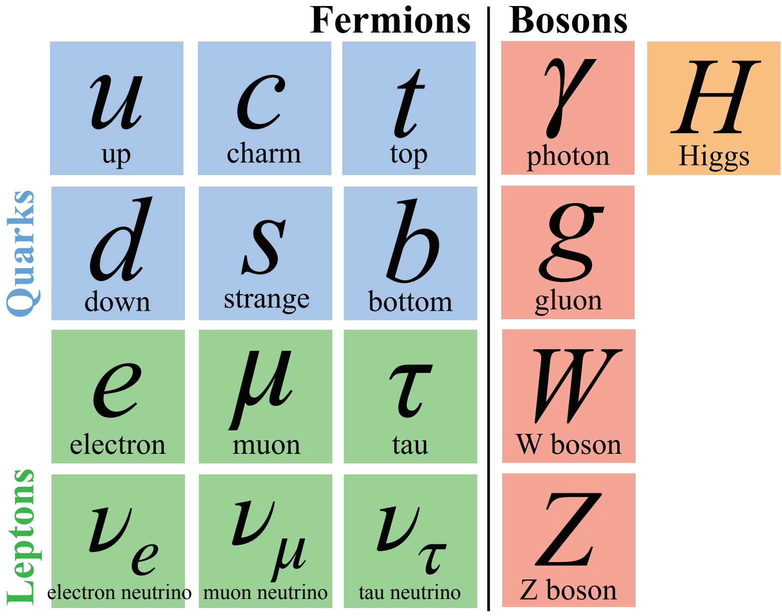

Figure 1.1: Particles in the Standard Model. Neutrinos are electrically neutral leptons.

1.2 Neutrino Oscillation

Neutrino oscillation occurs when the mass eigenstate and the flavor eigenstate are not identical. Thus, this phenomenon is evidence of the non-zero mass of neutrinos. The Super-Kamiokande got the evidence of neutrino oscillation by observing atmospheric neutrino in 1998 [1]. The theory of neutrino oscillation is described in Sec. 1.2.1, and the experimental measurements are introduced in Sec. 1.2.2.

1.2.1 Theory of Neutrino Oscillation

The relation between flavor and mass eigenstates is written with a unitary matrix called Pontecorvo-Maki-Nakagawa-Sakata (PMNS) matrix U [2,3].

$$|\nu_\alpha\rangle = \sum_i U^*_{\alpha i} |\nu_i\rangle , \tag{1.1}$$

where $|\nu_\alpha\rangle$ ($\alpha = e,\, \mu,\, \tau$) represents the flavor eigenstate and $|\nu_i\rangle$ ($i = 1, 2, 3$) represents the flavor eigenstate. The PMNS matrix U contains three mixing angles (θ_{12}, θ_{13}, θ_{23}) and CP-violation phase (δ_{CP}).

$$U = \begin{pmatrix} 1 & 0 & 0 \\ 0 & c_{23} & s_{23} \\ 0 & -s_{23} & c_{23} \end{pmatrix} \begin{pmatrix} c_{13} & 0 & s_{13}e^{-i\delta_{CP}} \\ 0 & 1 & 0 \\ -s_{13}e^{i\delta_{CP}} & 0 & c_{13} \end{pmatrix} \begin{pmatrix} c_{12} & s_{12} & 0 \\ -s_{12} & c_{12} & 0 \\ 0 & 0 & 1 \end{pmatrix}, \tag{1.2}$$

where $s_{ij} = \sin\theta_{ij}$ and $c_{ij} = \cos\theta_{ij}$. When a neutrino travels in vacuum with distance L, neutrino energy E_i, momentum p_i, and time t, the time evolution of the mass eigenstate is given as

$$|\nu_i(t)\rangle = e^{-i(E_i t - p_i L)}\, |\nu_i(0)\rangle\, . \tag{1.3}$$

Since the neutrino has small mass and ultrarelativistic, $m_i \ll E_i$ and $p_i \simeq p_\nu \simeq E_\nu$ can be assumed.

$$E_i = \sqrt{p_i^2 + m_i^2} \simeq p_i + \frac{m_i^2}{2p_i} \simeq p_i + \frac{m_i^2}{2E_\nu}. \tag{1.4}$$

Assuming $L \simeq ct = t$ under the natural unit, Eq. 1.3 can be written as follows.

$$|\nu_i(t)\rangle = \exp\left(-i\frac{m_i^2 L}{2E_\nu}\right) |\nu_i(0)\rangle\, . \tag{1.5}$$

Using Eq. 1.1 and 1.5, the time evolution of the flavor eigenstate $|\nu_\alpha(t)\rangle$ is given as

$$|\nu_\alpha(t)\rangle = \sum_i U^*_{\alpha i} \exp\left(-i\frac{m_i^2 L}{2E_\nu}\right) |\nu_i(0)\rangle\, . \tag{1.6}$$

The neutrino oscillation probability $P(\nu_\alpha \to \nu_\beta)$ is given as

$$\begin{aligned}
P(\nu_\alpha \to \nu_\beta) &= |\langle \nu_\beta(0)\,|\,\nu_\alpha(t)\rangle|^2 && (1.7)\\
&= \left|\sum_i U_{\beta i}U^*_{\alpha i} \exp\left(-i\frac{m_i^2 L}{2E_\nu}\right)\right|^2 && (1.8)\\
&= \sum_{i,j} U_{\beta i}U^*_{\alpha i}U^*_{\beta j}U_{\alpha j} \exp\left(-i\frac{\Delta m_{ij}^2 L}{2E_\nu}\right) && (1.9)\\
&= \sum_{i,j} U_{\beta i}U^*_{\alpha i}U^*_{\beta j}U_{\alpha j} \left[1 - 2\sin^2\left(\frac{\Delta m_{ij}^2 L}{4E_\nu}\right) - i\sin\left(\frac{\Delta m_{ij}^2 L}{2E_\nu}\right)\right] && (1.10)\\
&= \delta_{\alpha\beta} + 2\sum_{i>j} U_{\beta i}U^*_{\alpha i}U^*_{\beta j}U_{\alpha j} \left[-2\sin^2\left(\frac{\Delta m_{ij}^2 L}{4E_\nu}\right) - i\sin\left(\frac{\Delta m_{ij}^2 L}{2E_\nu}\right)\right] && (1.11)\\
&= \delta_{\alpha\beta} - 4\sum_{i>j} \mathrm{Re}(U_{\beta i}U^*_{\alpha i}U^*_{\beta j}U_{\alpha j}) \sin^2\left(\frac{\Delta m_{ij}^2 L}{4E_\nu}\right) \\
&\quad + 2\sum_{i>j} \mathrm{Im}(U_{\beta i}U^*_{\alpha i}U^*_{\beta j}U_{\alpha j}) \sin\left(\frac{\Delta m_{ij}^2 L}{2E_\nu}\right). && (1.12)
\end{aligned}$$

Assuming CPT symmetry, the antineutrino oscillation probability $P(\bar{\nu}_\alpha \to \bar{\nu}_\beta)$ is the same as $P(\nu_\beta \to \nu_\alpha)$. Therefore, the neutrino (antineutrino) oscillation probability can be summarized as

$$\begin{aligned} P(\nu_\alpha(\bar{\nu}_\alpha) \to \nu_\beta(\bar{\nu}_\beta)) = \delta_{\alpha\beta} - 4\sum_{i>j} \mathrm{Re}(U_{\beta i}U^*_{\alpha i}U^*_{\beta j}U_{\alpha j}) \sin^2\left(\frac{\Delta m^2_{ij} L}{4E_\nu}\right) \\ \pm 2\sum_{i>j} \mathrm{Im}(U_{\beta i}U^*_{\alpha i}U^*_{\beta j}U_{\alpha j}) \sin\left(\frac{\Delta m^2_{ij} L}{2E_\nu}\right). \end{aligned} \tag{1.13}$$

The difference in oscillation probability between neutrino and antineutrino ΔP $(\alpha \neq \beta)$ is

$$\Delta P = P(\nu_\alpha \to \nu_\beta) - P(\bar{\nu}_\alpha \to \bar{\nu}_\beta) \tag{1.14}$$

$$= -16 J_{\alpha\beta} \sin\Delta_{21} \sin\Delta_{32} \sin\Delta_{13}, \tag{1.15}$$

where

$$\Delta_{ij} = \frac{\Delta m^2_{ij}}{4E_\nu} L, \tag{1.16}$$

$$J_{\alpha\beta} = \mathrm{Im}(U_{\beta i}U^*_{\alpha i}U^*_{\beta j}U_{\alpha j}) = \pm J_{CP}, \tag{1.17}$$

(positive if it is e, μ, τ cycle and negative if it is a reverse cycle)

$$J_{CP} = \frac{1}{8} \cos\theta_{13} \sin 2\theta_{13} \sin 2\theta_{12} \sin 2\theta_{23} \sin\delta_{CP}. \tag{1.18}$$

A parameter J_{CP}, called the Jarlskog parameter, represents the magnitude of CP violation, and if $J_{CP} \neq 0$, namely $\delta_{CP} \neq 0, \pi$, CP symmetry is violated.

Matter Effects

When neutrinos travel through a medium such as the Earth, they interact with particles in matter. While all neutrino flavors interact via NC interaction, only ν_e additionally interacts via CC interaction. Therefore, electron neutrinos are affected by different potentials from the other flavor neutrinos, changing the oscillation probabilities. This effect, called the MSW effect, is described as an effective potential. Here, two-flavor oscillation is assumed for simplification. Using the potential of CC (NC) interaction V_{CC} (V_{NC}), the time evolution of flavor eigenstate is written as

$$i\frac{\partial}{\partial t}\begin{pmatrix} |\nu_e\rangle \\ |\nu_\mu\rangle \end{pmatrix} = \left[U \begin{pmatrix} E_1 & 0 \\ 0 & E_2 \end{pmatrix} U^\dagger + \begin{pmatrix} V_{\mathrm{CC}} + V_{\mathrm{NC}} & 0 \\ 0 & V_{\mathrm{NC}} \end{pmatrix} \right] \begin{pmatrix} |\nu_e\rangle \\ |\nu_\mu\rangle \end{pmatrix}, \tag{1.19}$$

where

$$U = \begin{pmatrix} \cos\theta_{12} & \sin\theta_{12} \\ -\sin\theta_{12} & \cos\theta_{12} \end{pmatrix}. \tag{1.20}$$

It is converted to the diagonal component and non-diagonal component as

$$\begin{aligned} i\frac{\partial}{\partial t}\begin{pmatrix} |\nu_e\rangle \\ |\nu_\mu\rangle \end{pmatrix} = & \left[\left(E_\nu + \frac{1}{2E_\nu}\frac{m_1^2 + m_2^2}{2} + V_{\mathrm{NC}} + \frac{V_{\mathrm{CC}}}{2} \right) I \right. \\ & \left. + \begin{pmatrix} -\frac{\Delta m^2_{21}}{4E_\nu}\cos 2\theta_{12} + \frac{V_{\mathrm{CC}}}{2} & \frac{\Delta m^2_{21}}{4E_\nu}\sin 2\theta_{12} \\ \frac{\Delta m^2_{21}}{4E_\nu}\sin 2\theta_{12} & \frac{\Delta m^2_{21}}{4E_\nu}\cos 2\theta_{12} + \frac{V_{\mathrm{CC}}}{2} \end{pmatrix} \right] \begin{pmatrix} |\nu_e\rangle \\ |\nu_\mu\rangle \end{pmatrix}, \end{aligned} \tag{1.21}$$

where I is the 2×2 identity matrix. The non-diagonal term can be diagonalized by a unitary matrix U_m.

$$U_m = \begin{pmatrix} \cos\theta_m & \sin\theta_m \\ -\sin\theta_m & \cos\theta_m \end{pmatrix}, \tag{1.22}$$

$$\tan 2\theta_m = \frac{\frac{\Delta m^2_{21}}{2E_\nu}\sin 2\theta_{12}}{\frac{\Delta m^2_{21}}{2E_\nu}\cos 2\theta_{12} - V_{\mathrm{CC}}}. \tag{1.23}$$

Here, the mass eigen value $\tilde{m}$ is

$$\begin{aligned}\tilde{m}^2_\alpha =& \frac{m_1^2 + m_2^2}{2} + 2E_\nu\left(V_{\mathrm{NC}} + \frac{V_{\mathrm{CC}}}{2}\right) \\ &\mp \sqrt{\left(\frac{\Delta m^2_{21}}{2}\cos 2\theta_{12} - V_{\mathrm{CC}}E_\nu\right)^2 + \left(\frac{\Delta m^2_{21}}{2}\sin 2\theta_{12}\right)^2}.\end{aligned} \tag{1.24}$$

The sign is negative (positive) if $\alpha = e$ (μ). The potential of NC V_{NC} affects all flavors identically, leading to no distortion on the oscillation probability. The CC and NC potentials can be written as follows using the Fermi constant G_F, the electron density of the matter N_e, and the neutron density of the matter N_n.

$$V_{\mathrm{CC}} = \sqrt{2}G_F N_e, \tag{1.25}$$

$$V_{\mathrm{NC}} = -\sqrt{2}G_F N_n. \tag{1.26}$$

N_e and proton density N_p do not appear in the V_{NC} because the potentials of proton and electron are offset in usual matter with $N_p = N_e$. The sign of N_e is the opposite if it is antineutrinos. If we assume null mixing hypothesis ($\theta_{12} = 0$), the mass eigenstate is expressed as

$$\tilde{m}^2_e = m_1^2 + 2\sqrt{2}G_F N_e E_\nu, \tag{1.27}$$

$$\tilde{m}^2_\mu = m_2^2. \tag{1.28}$$

The mass of electron neutrino $\tilde{m}^2_e$ increases in proportion to the electron density while that of muon neutrino $\tilde{m}^2_\mu$ is constant. If there is mixing θ_{12}, the MSW effect occurs, which separates these mass eigenstates. Fig. 1.2 shows the relation between effective neutrino mass and electron density in a medium under the three-flavor oscillation.

As shown in Eq. 1.13, neutrino oscillation is sensitive to the difference of squared mass (Δm_{ij}) but not to the sign and absolute mass. However, as shown in Eq. 1.24, the matter effect is sensitive to the sign of the squared mass difference, i.e., mass hierarchy (Sec. 1.2.2).

1.2.2 Measurements of Neutrino Oscillation Parameters

Various experiments measure the neutrino oscillation parameters. The best-fit values and 3σ ranges of the parameters are summarized in Tab. 1.1.

$\theta_{12}, \Delta m^2_{21}$

These parameters are measured by solar neutrino experiments ($\nu_e \to \nu_e$) and long-baseline reactor neutrino experiments ($\bar{\nu}_e \to \bar{\nu}_e$). The long-baseline reactor neutrino experiments, KamLAND [6], gives better constrain on Δm^2_{21} than the solar neutrino experiments (Super-Kamiokande [7] and SNO [8]). The sign of Δm^2_{21} is determined to be positive ($m_2 > m_1$) by measuring the matter effect in the solar.

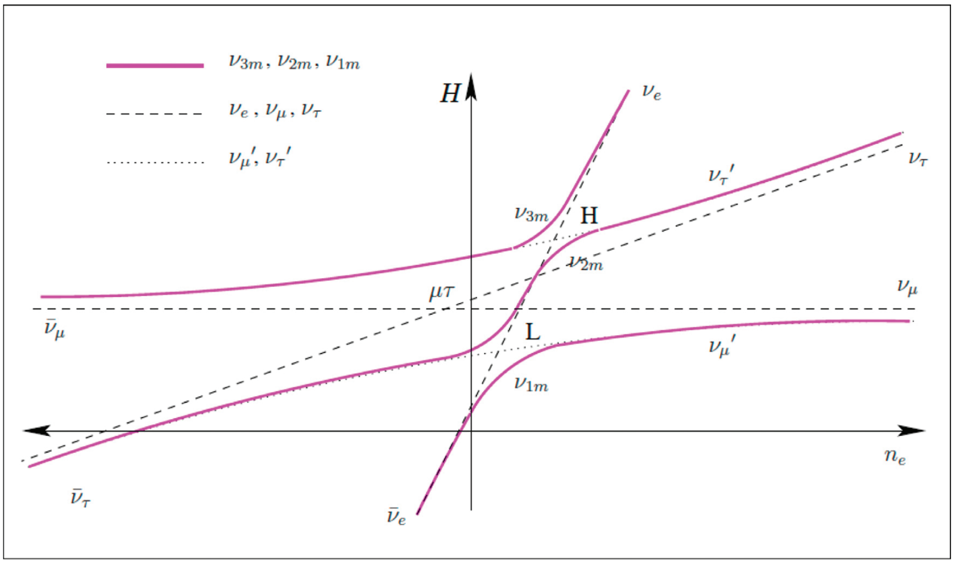

Figure 1.2: Relation between effective neutrino mass and electron density in a medium. Normal hierarchy is assumed. The dashed lines are with the null mixing hypothesis, and the solid magenta lines are with the mixing. The negative electron density means the case of antineutrinos. If there is mixing, mass eigenstates are separated (the solid magenta lines). The figure is from [4].

$\theta_{23}, \Delta m^2_{32}$

These parameters are measured by atmospheric neutrino experiments and accelerator neutrino experiments (Both $\nu_\mu(\bar{\nu}_\mu) \rightarrow \nu_\mu(\bar{\nu}_\mu)$). Super-Kamiokande [9] is representative of atmospheric neutrino experiments. T2K [10], K2K [11], MINOS [12], and NOvA [13] are representative for accelerator neutrino experiments. It is known that the θ_{23} is almost maximally mixed ($\theta_{23} \sim 45°$). The sign of Δm^2_{32} is still unknown.

θ_{13}

This parameter is measured by accelerator neutrino experiments ($\nu_\mu \rightarrow \nu_e$) and short-baseline reactor neutrino experiments ($\bar{\nu}_e \rightarrow \bar{\nu}_e$). The short-baseline reactor neutrino

Table 1.1: The best-fit values and 3σ ranges of neutrino oscillation parameters. NH (IH) represents normal hierarchy (inverted hierarchy). The values are from [5]

Parameter	best-fit	3σ
$\Delta m^2_{21} [10^{-5}\,\mathrm{eV}^2]$	7.37	6.93 - 7.96
$\lvert \Delta m^2_{32} \rvert\, [10^{-3}\,\mathrm{eV}^2]$	2.54	2.42 - 2.66
$\sin^2\theta_{12}$	0.297	0.250 - 0.354
$\sin^2\theta_{23}$ (NH)	0.425	0.381 - 0.615
$\sin^2\theta_{23}$ (IH)	0.589	0.384 - 0.636
$\sin^2\theta_{13}$ (NH)	0.0215	0.0190 - 0.0240
$\sin^2\theta_{13}$ (IH)	0.0216	0.0190 - 0.0242
δ_{CP}/π (NH/IH)	1.38 / 1.31	(2σ) 1.0 - 1.9 / 0.92 - 1.88

experiments (Double Chooz [14], Daya Bay [15], and RENO [16]) which measure $\bar{\nu}_e$ disappearance with a few km baselines, are more sensitive to θ_{13} than the accelerator neutrino experiments. Therefore, the results of the reactor neutrino experiments are often used in the analysis of accelerator neutrino experiments to constrain θ_{13}.

δ_{CP}

The precise value of δ_{CP} is still unknown. In order to measure this parameter, it is necessary to measure the difference in oscillation probability between neutrinos and antineutrinos (Eq. 1.14). In other words, it is necessary to distinguish between neutrinos and antineutrinos. Thus, this parameter can be measured only by accelerator neutrino experiments switching between neutrino-dominated and antineutrino-dominated modes. Fig. 1.3 shows two-dimensional allowed regions for $\sin^2\theta_{23}$ and δ_{CP} reported by T2K [10] and NOvA [13]. The measurements of δ_{CP} highly depend on the mass hierarchy, described later, due to the matter effect. T2K has better sensitivity for δ_{CP} while NOvA has better sensitivity for the mass hierarchy, since the baseline of T2K is $\sim$ 295 km while that of NOvA is $\sim$ 810 km. It is expected that a joint fit with T2K and NOvA gives a better understanding of δ_{CP} and mass hierarchy.

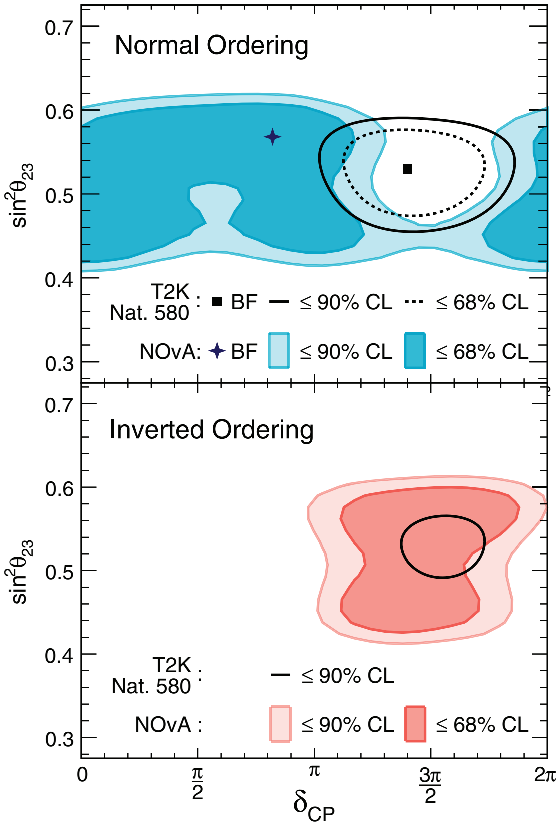

Figure 1.3: Constraints on oscillation parameters $\sin^2\theta_{23}$ and δ_{CP} by T2K and NOvA experiments. The upper (lower) panel shows two-dimensional confidence intervals for $\sin^2\theta_{23}$ and δ_{CP} assuming the normal (inverted) hierarchy. The black lines represent the result of T2K experiment [10]. Although these experiments slightly prefer normal hierarchy, it has been expected that a joint fit might converge on an inverted hierarchy. The figure is from [13].

Mass hierarchy

The sign of Δm^2_{ij} can be determined by measuring the matter effect. The sign of Δm^2_{21} is determined to be positive ($m_2 > m_1$) by the solar neutrino experiments. However, the sign of Δm^2_{32} is not known yet. Therefore, there are two possible cases in mass ordering: $m_3 > m_2 > m_1$ and $m_2 > m_3 > m_1$ as shown in Fig. 1.4. The former is called "normal hierarchy," and the latter is called "inverted hierarchy". As mentioned above, the determination of the mass hierarchy is very important because it affects the Δ_{CP} measurements. The results of neutrino oscillation experiments prefer the normal hierarchy, however, the significance is small.

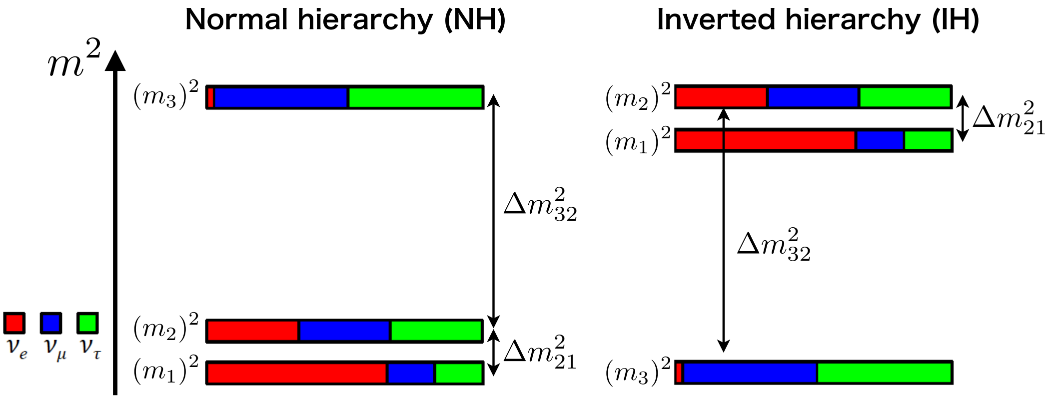

Figure 1.4: Mass hierarchy of neutrino. There are two possibilities: Normal hierarchy (left) and inverted hierarchy (right).

1.3 Recent Hot Topics in Neutrino Physics

This section introduces some of the neutrino (related) physics that has been actively discussed recently. These topics are closely related to neutrino-nucleon interactions, especially the associated neutron emission, and their understanding becomes a significant issue. We briefly introduce recent and next-generation detectors aiming to explore these neutrino physics in Sec. 1.3.4.

1.3.1 Values of δ_{CP} and Matter Dominant Universe

The CP violation in neutrino is expected to have played an essential role in making our matter-dominant universe. Our universe is baryon asymmetry, i.e., the baryon number is not equal to anti-baryons. We do not know how the baryon asymmetry arose in the early universe. Sakharov proposed three conditions, called Sakharov's condition, to create the baryon asymmetry [17]. One of the conditions is CP violation.

The Jarlskog parameter (Eq. 1.18) for quarks J^{Quark}_{CP} is known to be small to explain our universe [5].

$$J^{\mathrm{Quark}}_{CP} \simeq 3 \times 10^{-5}. \tag{1.29}$$

On the other hand, for neutrinos, it can be three orders of magnitude larger than the quarks, although the value of δ_{CP} is unknown:

$$J_{CP}^{\text{Neutrino}} \simeq 0.033 \sin \delta_{CP}. \tag{1.30}$$

While we cannot limit whether this is the origin of the baryon asymmetry or not, Pascoli *et al.* said that if J_{CP}^{Neutrino} is about 0.02, it can create our matter-dominant universe through a scenario called leptogenesis [18].

Neutrino oscillation experiments, including δ_{CP} measurements, use charged-current quasi-elastic (CCQE) interaction as a signal. The CCQE is a quasi-elastic scattering with a single nucleon and has a charged lepton in the final state. Since it is a two-body reaction, the neutrino energy can be easily reconstructed using the scattering angle and momentum of the outgoing charged lepton. In practice, however, neutrinos interact with carbon, oxygen, and argon in detectors. The reconstructed energy, therefore, is smeared due to nuclear effects that have large uncertainty. The nuclear effects lead to the largest systematic uncertainty in the measurement of δ_{CP} in the T2K experiment.

The background contributions of charged-current resonance pion production (CCRES) and charged-current two-body interaction (CC 2p2h) are particularly problematic. The CCRES is a charged current interaction that involves a pion production from the resonance state of a nucleon. The contribution of the CCRES is generally excluded by detecting the pions in analysis. However, if the pions are absorbed in the nucleus, the events are misidentified as the CCQE. The CC 2p2h is an interaction with two nucleons in the nucleus. Almost all detectors cannot distinguish the CC 2p2h from the CCQE because the detectors are not capable of detecting nucleons. These misidentified non-CCQE interactions bias the reconstructed neutrino energy.

1.3.2 Searches for Supernova Relic Neutrino

Mechanisms of supernova explosions contain the key to understanding the history of cosmogenesis and star formation. Neutrinos from supernova explosions (SN) directly provide internal information about the stars due to their high transparency. However, supernova explosions around the Earth are rare, and 1987A is the only time we have been able to observe neutrinos from the SNs [19].

Supernova relic neutrino (SRN) is neutrinos from all the past supernova explosions diffused in our universe. The SRN would also provide valuable information on the supernova rate and physics of the neutrino emission processes. The SRN signal has never been discovered yet despite enormous experimental efforts. Almost all experiments use inverse beta decay (IBD), $\bar{\nu}_e + p \to e^+ + n$, as a signal. The background contribution can be significantly reduced by using spatial and time correlations between positron and gamma-ray emitted via neutron capture in the IBD event selection. Fig. 1.5 shows the predicted SRN $\bar{\nu}_e$ flux and experimental upper limits. We need to improve the experimental sensitivity by one order of magnitude to validate the theoretical predictions.

The dominant systematic uncertainty comes from the serious background, neutral-current quasi-elastic (NCQE) interactions of atmospheric neutrinos. The NCQE is a quasi-elastic scattering with a single nucleon and does not change the charge of lepton between the initial and final states. Since the presence of single neutron capture is required when selecting IBD candidates, the atmospheric NCQE events with a neutron could be the background: For example, $\nu +^{12} \mathrm{C} \to \nu + n +^{11} \mathrm{C}^*$. The emitted neutrons recoil protons, which can be misidentified as e^+. Then the neutrons can be absorbed in the nucleus or emitted by nuclear de-excitation so that many channels can contribute as the backgrounds.

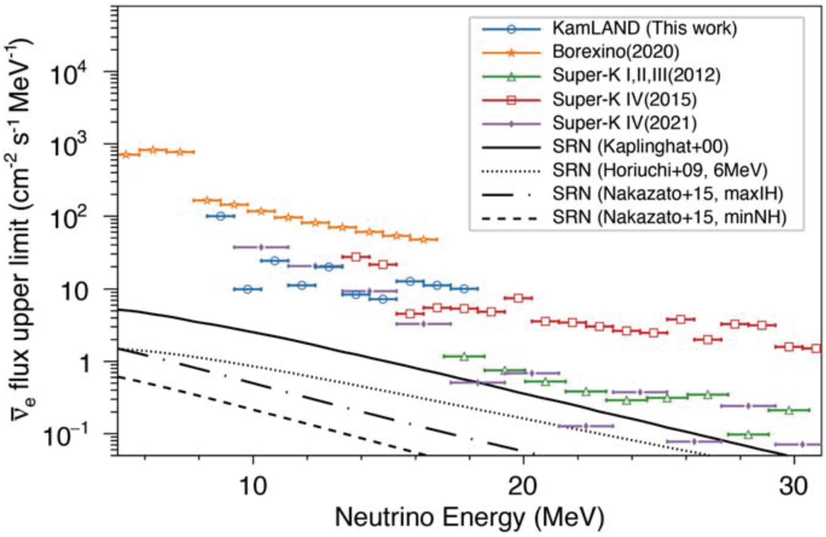

Figure 1.5: Model-independent upper limits on the SRN $\bar{\nu}_e$ flux. The black lines show theoretical predictions. We need to improve the experimental sensitivity by one order of magnitude to validate the theoretical predictions. The figure is from [20].

Furthermore, in the low-energy region below 30 MeV, remarkably accurate nuclear models are needed because of the relatively large contribution of binding energy.

For example, the KamLAND analysis assigns large errors on the atmospheric neutrino NCQE events, becoming a significant obstacle to improving the sensitivity [20]. Fig. 1.6 shows the best-fit energy spectrum of the SRN candidates observed at KamLAND. The atmospheric neutrino NCQE events are the most dominant background: 7.5 events in 18 observed events. In this spectrum fit, the analysis treats the number of NCQE events as a free parameter due to the considerable uncertainty in the prediction. The spectrum fit with constraints on the NCQE events is expected to improve the upper limits on the SRN flux significantly. We may have two critical issues to get reasonable constraints on the NCQE events: The formalism of the NCQE interaction and the nuclear effects. This study aims to measure the strangeness axial coupling constant, which appears in the formalism of the NCQE interactions. Thus, it may contribute to improving the SRN upper limits.

1.3.3 Searches for Proton Deacy

The Grand Unified Theory (GUT), which unifies the electroweak theory and the QCD, predicts the presence of proton decay as a general consequence. This phenomenon allows transitions between quarks and leptons, resulting in a baryon-number violation. Various modes of proton decay are considered, such as $p \to e^+\pi^0$ and $p \to \bar{\nu}K^+$. Although proton decay itself is not neutrino physics, neutrino detectors containing many protons are suitable for the search. While it has not been discovered yet, many experiments have established lower limits for the lifetime of $\mathcal{O}(10^{32} - 10^{34})$ years as shown in Fig. 1.7. Some theories have been rejected, but it is necessary to realize a search up to 10^{37} years to test the remaining theories. It should be noted that most of the decay modes do not involve neutron emissions. In experiments, events that do not involve neutron capture are selected to reduce the background contributions [21, 22].

The accuracy of nuclear models is essential both for the signal and background in the

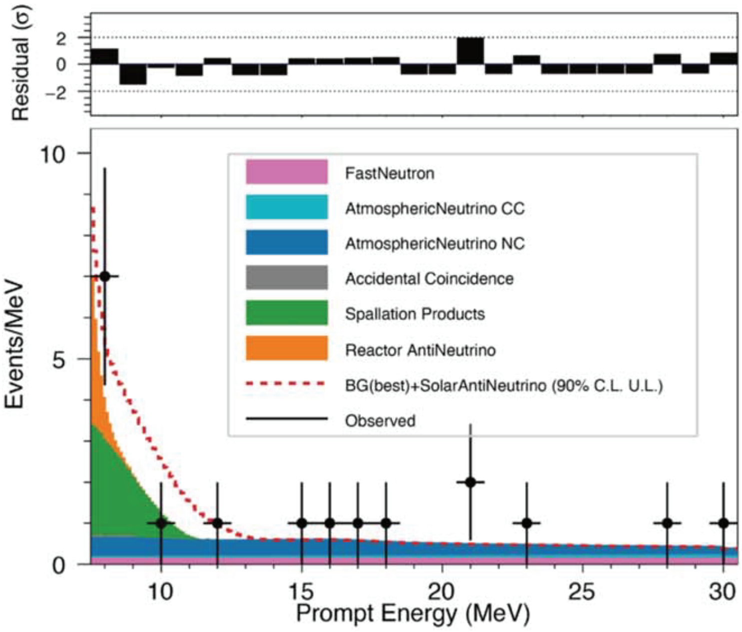

Figure 1.6: Best-fit energy spectrum of the SRN candidates at KamLAND. Atmospheric neutrino events are the dominant background. The figure is from [20].

proton decay search. For the signal, we need to consider the decay of protons in the nucleus in the actual detector. The Fermi motion of nucleons and the effect of re-scattering of produced pions (kaons) in the nucleus are estimated using simulations based on theoretical models [1]. The main background is CCRES interactions of atmospheric neutrinos. Since events without neutron capture can be background, a nuclear model that can accurately predict neutron emission is also needed. It is noted in [21] that the main systematic uncertainties in both the signal and background are related to nuclear models.

1.3.4 Next-Generation Detectors

In this section, recent and next-generation detectors aiming to explore these neutrino physics are briefly introduced.

Super-Kamiokande Gadolinium

Super-Kamiokande Gadolinium is an upgrade project of the Super-Kamiokande by loading gadolinium (Gd) into ultrapure water [24]. In ultrapure water, most neutrons are captured by hydrogen emitting gamma rays of 2.2 MeV. By detecting these gamma rays, neutrons associated with neutrino interactions can be identified. However, the 2.2 MeV gamma rays are too low-energy for water Cherenkov detectors. In the case of Super-Kamiokande, the detection efficiency is about 20%. This project loads gadolinium into ultrapure water, targeting higher efficiency of more than 80%. Since Gd has a thermal neutron capture cross section more than 10^5 times larger than hydrogen, most neutrons are captured by Gd emitting gamma rays with energies as high as 8 MeV. These features of Gd enable high neutron detection efficiency.

---

[1] In most cases, these simulations are the same as those for neutrino-nucleon interactions.

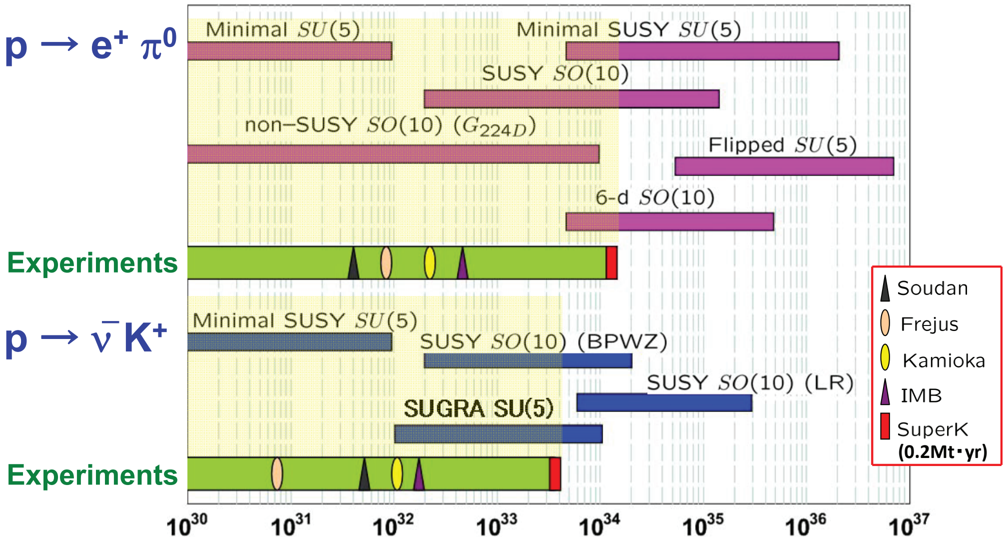

Figure 1.7: Lifetime of major two proton decay modes ($p \to e^+\pi^0$ and $p \to \bar{\nu}K^+$) for theoretical prediction and upper limit by experiments. Some theories have been rejected, but it is necessary to realize a search up to 10^{37} years to test the remaining theories. The figure is from [23].

The second Gd loading was completed in July 2022, with a concentration of 0.03% solution of the Gd. A detection efficiency of about 75% is expected, and they are taking data for several months.

Hyper-Kamiokande

Hyper-Kamiokande is the next-generation detector for the Super-Kamiokande [25]. While the Super-Kamiokande has 22.5 ktons of fiducial volume, the Hyper-Kamiokande will have 190 ktons of fiducial volume, aiming to improve statistics significantly. The rough detector design is similar to the Super-Kamiokande, although there are various upgrades of photo sensors and ultrapure water. It is currently under construction in Kamioka mine, Gifu Prefecture, Japan, intending to start observation in 2027.

JUNO

The Jiangmen Underground Neutrino Observatory (JUNO) is a 20 ktons underground liquid scintillator detector in China [26]. Compared with KamLAND, the world's largest liquid scintillator detector at this time containing 1 kton, JUNO is expected to improve statistics significantly. Liquid scintillator detectors are generally able to achieve low-energy threshold and thus can detect neutron capture gamma rays with high efficiency. Construction is underway to obtain data in 2023.

1.4 Introduction of Neutrino Interactions

Understanding neutrino-nucleon interactions is one of the most critical issues in various neutrino experiments. To predict the response of the interactions in the detector, neutrino Monte Carlo event generators (simulators) that implement theoretical models are used (Chap. 4). Therefore, the generator's prediction accuracy determines the experiments' accuracy. Neutrino-nucleon interactions are generally described in terms of an approximation called impulse approximation. It is divided into two parts: the interaction with a single nucleon and the nuclear effects (See Chap. 2 for details). While interactions with a single nucleon are well understood, the nuclear effects, which are many-body systems, are highly uncertain.

It is challenging to study the neutrino interaction. The difficulties are roughly composed of three factors. First, neutrino cross sections are very small because it interacts only via weak interaction. Large detectors are needed to improve the statistics. This situation is only now being realized due to recent technological advances. Second, most neutrino fluxes have finite widths in their energy. For example, it is relatively easy to generate an electron beam with monochromatic energy by accelerators. On the other hand, neutrino beam generated via μ, π decay in flight has finite width in their energy. Third, the neutrino interaction involves a complex physics process. Although the interaction with free nucleons is easy to describe, neutrinos interact with nucleons in nuclei. Therefore, a formalism that includes information on their structures is necessary. In addition, since there are various modes for neutrino interaction, channels other than the one we are focusing on could be backgrounds. Thus, neutrino interaction measurements are subject to compounding factors. To avoid overlooking systematic factors, verification by various experiments is particularly essential.

So far, most neutrino interaction detectors have specialized in measuring charged leptons with some track length. Because their track resolution was not so good, they were not suitable for measuring charged particles with low momentum or protons with tracks of only a few centimeters. Also, it is difficult to measure neutrons via proton recoils and capture gamma rays. The increasing importance of accuracy in predicting neutron emission has led to various detector development studies. Construction or update of detectors with better track resolution and sensitivity to neutron capture gamma-rays has been planned. Some experiments are already in the phase of starting data acquisition, but it still takes some time to obtain the results of the physics analysis.

This study focuses on the high efficiency of neutron capture gamma-rays of KamLAND, getting inspired by the situation. We measured neutron multiplicity associated with atmospheric neutrinos. This measurement is the first example with high neutron tagging efficiency of about 80% and presents a new observable in the field of neutrino interactions. Since KamLAND achieves a low-energy threshold, the analysis focusing on NCQE interactions, which dominate in the low-energy region, is possible.

1.5 Introduction of Strangeness Axial Coupling Constant

Among many types of neutrino interactions, the NCQE interaction (See Sec. 2.1.2 for detailed formalism) contains fundamental and interesting information about nucleons. The NCQE interaction, $\nu_l + N \rightarrow \nu_l + N$, where N denotes either a proton or neutron, does not change the charge of the lepton between the initial and final states. In contrast, the CCQE interaction (See Sec. 2.1.1 for detal formalism), $\nu_\mu + n \rightarrow \mu^- + p$, does. The CCQE interaction only involves isovector weak currents, while the NCQE interaction is sensitive to isoscalar weak currents. Therefore, searching for strange quarks existing as sea quarks in nucleons through their isoscalar contribution to the NCQE interaction is possible. Fig. 1.8 shows the schematic view of the contribution of the strange quarks to the NCQE interaction. In experiments, one measures the strangeness axial coupling constant g_A^s, the strange axial form factor at four-momentum transfer squared $Q^2 = 0$. Since the Q^2 dependence of the axial form factor is parameterized by an axial mass M_A, the interaction rate depends on both g_A^s and M_A.

One challenge in measuring g_A^s using the NCQE interaction is the strong correlation with M_A. In experiments, protons are used as the target primarily because of the difficulty of measuring NCQE on neutron targets. A measurement exclusively on a proton target (or neutron target) depends highly on M_A and other normalization uncertainties. Conversely, when measuring the ratio, the normalization cancels out, and we can measure g_A^s with only a slight dependence on M_A because the value of g_A^s significantly changes the ratio of proton and neutron NCQE cross sections. In practice, nucleons measured by detectors are also emitted by final-state interactions (FSI), nuclear de-excitation, and secondary interactions (SI). These effects somewhat smear the information about the target nucleon. Nevertheless, information about both the target nucleons and g_A^s can be extracted by measuring the neutron multiplicity with high efficiency. Further is discussed in Chap. 3.

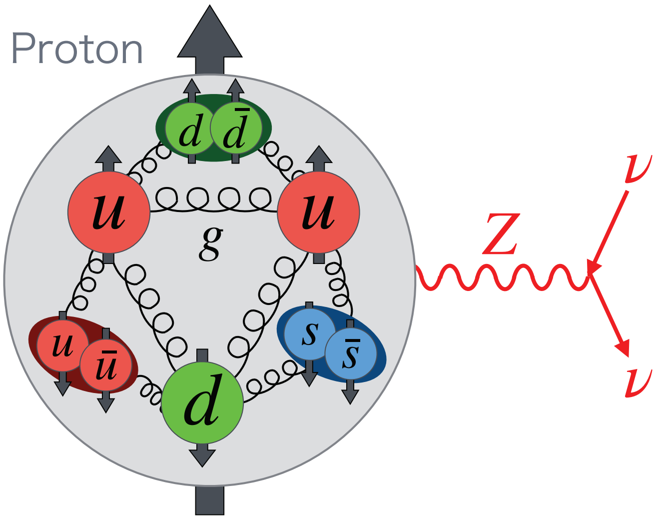

Figure 1.8: Schematic view of the contribution of strange quarks to neutral current quasi-elastic scattering. In addition to u and d quarks, strange quarks existing as sea quarks can contribute to the nucleon's spin.

1.6 Outline of This Dissertation

The purpose of this dissertation is to measure the neutron multiplicity of atmospheric neutrino NCQE interactions at KamLAND, and to obtain g_A^s with a small dependence on M_A. We analyze KamLAND atmospheric neutrino data.

This dissertation is organized as follows. Details about neutrino interaction, such as theories, experimental measurements, and Monte Carlo generators, are explained in Chaps. 2–5. Details about g_A^s, the objective of this study, are in Chap. 3. The overview of the KamLAND detector is shown in Chap. 6, and the event reconstruction and the calibration are described in Chap. 7, The detailed detector Monte Carlo simulation is summarized in Chap. 8. The analysis of atmospheric neutrino interaction at KamLAND is discussed in Chaps. 9–11. The conclusion is given in Chap. 12.

Part II

Neutrino Interactions and Monte Carlo Event Generators

Chapter 2

Neutrino Interactions

Except for the gravitational interaction, neutrinos interact only via the weak interaction mediated by $W^{\pm}$ and Z^0 bosons. The elementary process is the neutrino-electron interaction, which has a small cross section and can be neglected in this study, or neutrino-quark interaction. As for neutrino-quark interaction, the neutrino interacts with nucleons and nuclei in practice. Therefore, formalism must include structure information of nucleons and nuclei. The theories and measurements of neutrino interactions, especially scattering with free or bound nucleons, are described in this chapter.

The description of neutrino-nucleon interaction in most models is based on an approximation called "Impulse Approximation" (IA). This approximation treats the remaining nucleons as mere spectators and allows us to view neutrino-nucleon interaction as two individual parts: Reactions with a single nucleon and nuclear effects. The former, reactions with a single nucleon, is relatively simple to model, while the latter is generally modeled using electron scattering experiments. The IA is valid when the momentum transfer is larger than $\sim 400\,\mathrm{MeV/c}$. Below that momentum, the correlation with other nucleons becomes non-negligible. This issue is solved by applying Random Phase Approximation (RPA), which considers long-range nucleon-nucleon correlation. The detail of the RPA is introduced in Sec. 2.2.2. Under the impulse approximation, the description of neutrino-nucleon interaction consists of four parts as follows (see Fig. 2.1).

- Primary Interaction (Sec. 2.1)

  It describes an initial neutrino interaction with a single free nucleon (or nucleus).

- Nuclear Effects (Sec. 2.2)

  It describes properties of bound nucleons, such as the momentum and potential of the initial state and the Pauli blocking effects in the final state. Based on the initial state information, corrections are made to the description of the primary interaction.

- Final State Interaction (FSI) (Sec. 2.3)

  It describes the re-scattering of particles produced via the primary interaction in the nucleus.

- Nuclear de-excitation (Chap. 5)

  It describes nuclear de-excitation after the FSI. Various particles, such as nucleons, α, and γ, can be emitted.

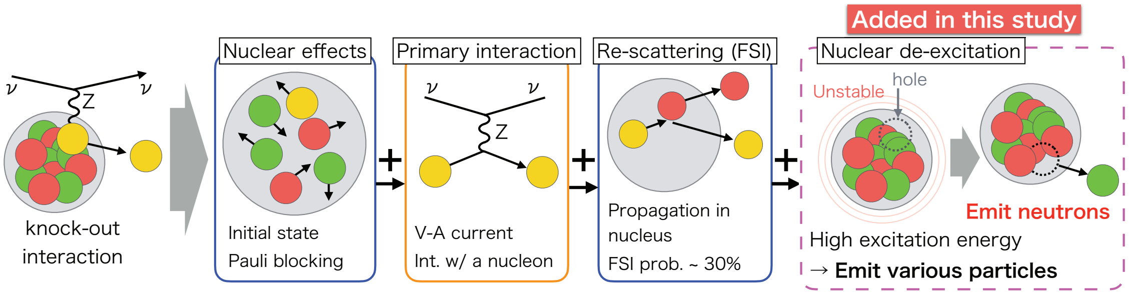

Figure 2.1: Overview of the impulse approximation. Under the impulse approximation, the description of neutrino-nucleon interaction is divided into four parts. The last process, nuclear de-excitation, is not considered in commonly-used generators. We newly added this process in the description in this study (Chap. 5).

If it is an interaction with free nucleon, only the first part, primary interaction, is considered. Taking advantage of the fact that most nuclear effects are common in electroweak interactions and pure weak interactions, we generally use large-statistical electron scattering experimental data to model the nuclear effects.

Neutrino-nucleon interactions involve complex physical processes. Neutrino experiments commonly use neutrino Monte Carlo event generators (simulators) that implement theoretical models to predict the detector response. The prediction accuracy of the generator limits the accuracy of experiments, and its understanding and improvement are one of the most important issues in the field of neutrino physics. Chap. 4 introduces commonly-used generators. While these generators consider the primary interaction, nuclear effects, and FSI, they do not consider the nuclear de-excitation. Thus, to measure neutron multiplicity associated with neutrino interactions, it is necessary to build a simulation of the nuclear de-excitation that can be used with the neutrino event generators. The details of nuclear de-excitation developed in this study are in Chap. 5. In this chapter, the details of three parts, primary interaction, nuclear effects, and FSI, which are considered in the generators, are described.

2.1 Primary Interaction

Primary interaction basically describes an initial neutrino interaction with a free nucleon (or nucleus). Neutrino interactions can be firstly divided into two channels: charged current (CC) and neutral current (NC) interactions. The CC interaction mediated by $W^{\pm}$ has flavor information because a charged lepton appears in the final state. There is a neutrino energy threshold for the CC interaction because it needs to create the charged lepton. On the other hand, the NC interaction mediated by Z^0 transfers the momentum to the other particles without flavor change and contributes equally to all flavors. Therefore, we cannot distinguish flavors via the NC interaction. Neutrino oscillation experiments use the CC interactions containing flavor information as signals.

There are various channels in both CC and NC interactions, as shown in Fig. 2.2. For small neutrino energies $\mathcal{O}(1)$ MeV, interaction with a nucleus called coherent scattering (COH) is dominant. As the energy increases $\mathcal{O}(1)$ GeV, interactions with a nucleon become dominant. There are two major channels in this energy region: Quasi-elastic scattering (QE) and resonance pion production (RES). The RES is slightly more dominant than the QE in the higher energy region above $\gtrsim 3$ GeV. In the higher energy region $\mathcal{O}(10)$ GeV, inelastic scatterings with a quark, called deep inelastic scattering (DIS), take place. Furthermore, in the energy region between QE and RES, known as the dip region, the 2p2h interaction, which is the scattering with two correlated nucleons, is considered to exist.

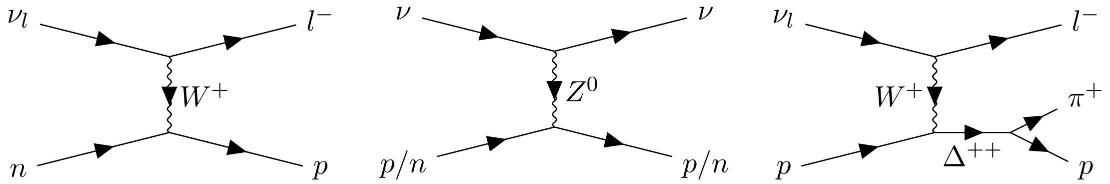

(a) CCQE (b) NCQE (c) CCRES

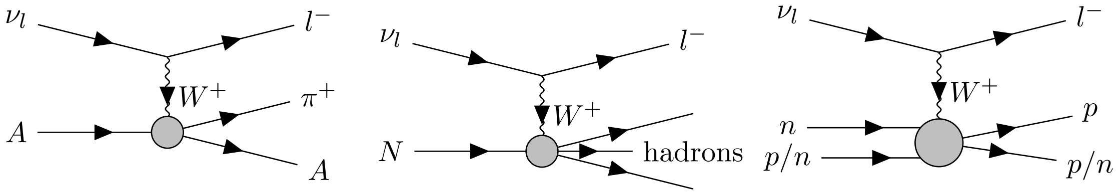

(d) CCCOH (e) CCDIS (f) CC 2p2h

Figure 2.2: Feynman diagrams of major neutrino interactions.

The effective Lagrangian density of neutrino-nucleon interaction is written by

$$\mathcal{L}_{eff} = \frac{G_F}{\sqrt{2}}\left[j^{\dagger}_{\lambda}(k,k')J^{\lambda}(p,p') + h.c.\right], \tag{2.1}$$

where G_F is the Fermi constant, j_λ is leptonic current, J_λ is hadronic current, k (k') represents the four-momentum of the initial (final) state lepton, and p (p') represents the four-momentum of the initial (final) state nucleon. The differential cross section can be written in terms of the leptonic tensor $L_{\mu\nu}$ and hadronic tensor $H_{\mu\nu}$, which are calculated from the leptonic and hadronic current,

$$\frac{d\sigma}{dQ^2} = \frac{1}{32\pi}\frac{1}{M^2E_\nu^2}G_F^2c_{\mathrm{EW}}^2L_{\mu\nu}H^{\mu\nu}, \tag{2.2}$$

where M is the nucleon mass, E_ν is the neutrino energy, and $q^2 = (k-k')^2 \equiv -Q^2$ is squared of four-momentum transfer. c_{EW} is a constant: $\cos\theta_c$ (θ_c : Cabibbo angle) for CC interaction, and 1/4 for NC interaction. The leptonic tensor is written by

$$L_{\mu\nu} = k_\mu k'_\nu + k'_\mu k_\nu - g_{\mu\nu}(k,k') \pm i\epsilon_{\mu\nu\rho\sigma}k'^{\rho}k^{\sigma}, \tag{2.3}$$

where $g_{\mu\nu}$ is Lorentz metric tensor and $\epsilon_{\mu\nu\rho\sigma}$ is Levi-Civita symbol. The hadronic tensor $H^{\mu\nu}$ is usually complicated and depends on the models.

The following sections contain the formalism of the various neutrino interaction channels. Fig. 2.3 shows the neutrino and antineutrino cross section on carbon obtained using NuWro [27]. Below 1 GeV, where the dominant region of atmospheric neutrino flux, the QE and RES of CC and NC dominate.

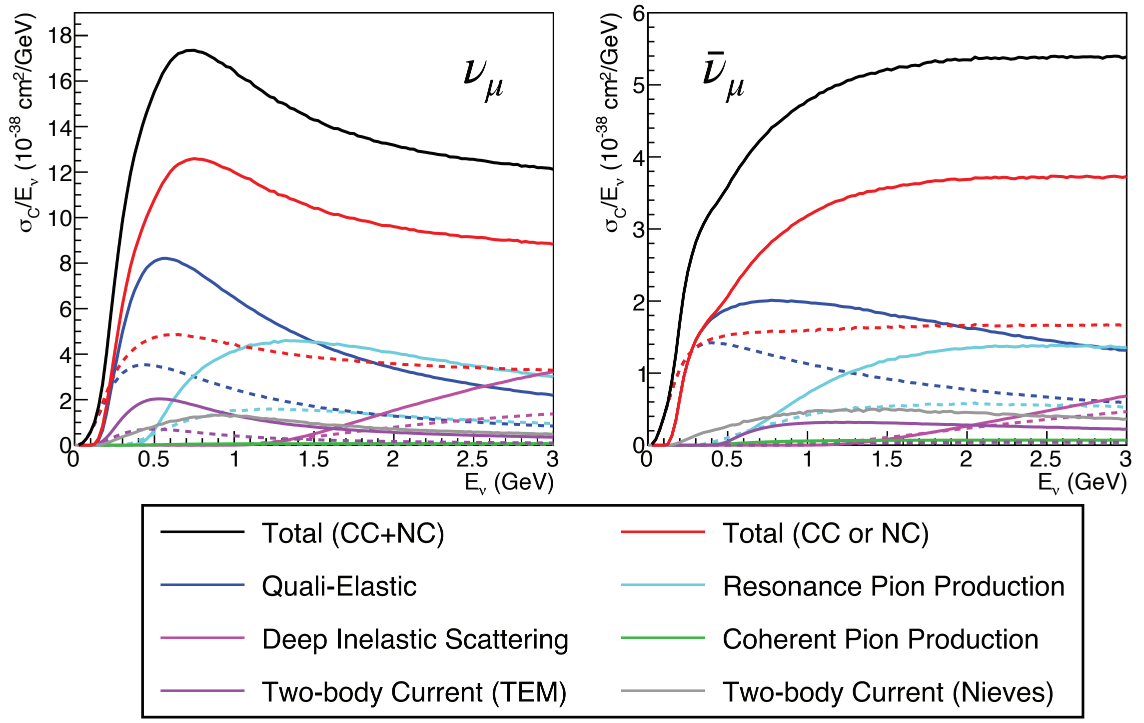

Figure 2.3: Neutrino (left) and antineutrino (right) cross section on carbon as a function of neutrino energy. The solid (dashed) lines represent CC (NC) channels. The figure shows two models for the two-body current: TEM (violet) and Nieves (gray). NC two-body current is only shown for TEM. These results are obtained using NuWro with $M_A = 1.2\,\mathrm{GeV}$ and $g_A^s = 0$ [27].

2.1.1 Charged Current Quasi-Elastic (CCQE) Interaction

The Charged Current Quasi-Elastic (CCQE) interaction is a quasi-elastic scattering with a single nucleon mediated by $W^{\pm}$ bosons.

$$\nu_l + n \to l^- + p, \tag{2.4}$$

$$\bar{\nu}_l + p \to l^+ + n. \tag{2.5}$$

The neutrino energy can be reconstructed from the angle and momentum of the outgoing lepton since it is a two-body reaction if the direction of the incoming neutrino is known. Therefore, accelerator neutrino oscillation experiments use it as the primary signal. Since the CCQE interaction is dominant in $E_\nu \sim 0.5\,\mathrm{GeV}$, the beam flux of accelerator neutrino experiments should have a narrow peak in this energy region.

The Llewellyn-Smith formalism [28] is commonly used to describe the CCQE interaction. The hadronic current is composed of vector part V^λ and axial part A^λ.

$$J^\lambda(p, p') = \bar{u}(p')\Gamma^\lambda u(p) = V^\lambda - A^\lambda, \tag{2.6}$$

where Γ^λ represents the amputated amplitudes of the currents. The vector and axial parts are given as follows:

$$V^\lambda = \bar{u}(p')\left[\gamma^\lambda F_V^1(Q^2) + \frac{i}{2M}\sigma^{\lambda\mu}q_\mu F_V^2(Q^2)\right]u(p), \tag{2.7}$$

$$A^\lambda = \bar{u}(p')\left[\gamma^\lambda\gamma_5 F_A(Q^2) + \gamma_5\frac{q^\lambda}{M}F_P(Q^2)\right]u(p). \tag{2.8}$$

$F_V^{1,2}$ are vector form factors, F_A is an axial form factor, and F_P is a pseudoscalar form factor. These form factors include information on nucleon structure. Note that these form factors are different for CC and NC interactions since the mediator bosons are different. Assuming the Conserved Vector Current (CVC) hypothesis, the vector form factors for CC are written as follows:

$$\left[F_V^i(Q^2)\right]_{\mathrm{CC}} = F_V^{i,p}(Q^2) - F_V^{i,n}(Q^2) \qquad (i = 1, 2). \tag{2.9}$$

where $F_V^{i,p/n}$ represents the electromagnetic form factor for proton/neutron. They can be expressed in terms of the electric $G_E^{p/n}$ and magnetic $G_M^{p/n}$ form factors of proton/neutron.

$$F_V^{1,p/n}(Q^2) = \left(1 + \frac{Q^2}{4M^2}\right)^{-1}\left[G_E^{p/n}(Q^2) + \frac{Q^2}{4M^2}G_M^{p/n}(Q^2)\right], \tag{2.10}$$

$$F_V^{2,p/n}(Q^2) = \left(1 + \frac{Q^2}{4M^2}\right)^{-1}\left[G_M^{p/n}(Q^2) - G_E^{p/n}(Q^2)\right], \tag{2.11}$$

where M is the average of proton and neutron mass. For the axial part, assuming Partially Conserved Axial Current (PCAC) [29], the pseudoscalar form factor F_P is represented by using the axial form factor F_A.

$$F_P(Q^2) = \frac{2M^2}{m_\pi^2 + Q^2}F_A(Q^2). \tag{2.12}$$

Using Eq.2.2, the differential cross section of CCQE interaction can be written as

$$\frac{d\sigma}{dQ^2} = \frac{M^2 G_F^2 \cos^2\theta_c}{8\pi E_\nu}\left[A(Q^2) \pm B(Q^2)\left(\frac{s-u}{M^2}\right) + C(Q^2)\left(\frac{s-u}{M^2}\right)^2\right], \tag{2.13}$$

where s and u are the Mandelstam variables and the sign $+(-)$ is for neutrinos (antineutrinos). $A(Q^2), B(Q^2)$, and $C(Q^2)$ are given as follows:

$$\begin{aligned} A(Q^2) =& \frac{m^2+Q^2}{4M^2}\left[\left(4+\frac{Q^2}{M^2}\right)|F_A|^2-\left(4-\frac{Q^2}{M^2}\right)\left|F_V^1\right|^2+\frac{Q^2}{M^2}\left|F_V^2\right|^2\left(1-\frac{Q^2}{4M^2}\right)\right. \\ &\left.+\frac{4Q^2F_V^1F_V^2}{M^2}-\frac{m^2}{M^2}\left(\left(F_V^1+F_V^2\right)^2+|F_A|^2\right)\right], \end{aligned} \tag{2.14}$$

$$B(Q^2) = \frac{Q^2}{M^2}\left[(F_V^1+F_V^2)F_A\right], \tag{2.15}$$

$$C(Q^2) = \frac{1}{4}\left[\left|F_A^2\right|^2+\left|F_V^1\right|^2+\frac{Q^2}{4M^2}\left|F_V^2\right|^2\right], \tag{2.16}$$

where m is the mass of outgoing lepton. There are several parameterizations of the electric and magnetic form factors of nucleons $G_{E,M}^{p/n}$. A simple parameterization is a dipole form. It can be written as

$$G_E^V(Q^2) = G_E^p(Q^2) - G_E^n(Q^2), \tag{2.17}$$

$$G_M^V(Q^2) = G_M^p(Q^2) - G_M^n(Q^2), \tag{2.18}$$

$$G_E^V(Q^2) = \left(1+\frac{Q^2}{M_V^2}\right)^{-2}, \tag{2.19}$$

$$G_M^V(Q^2) = (1-\xi)\left(1+\frac{Q^2}{M_V^2}\right)^{-2}, \tag{2.20}$$

where $\xi = 3.71$ is the difference of anomalous magnetic moments in units of the nuclear magneton. The vector mass $M_V = 0.84\,\mathrm{GeV}$ is determined by electron scattering experiments. The dipole form factors explain the experiments well for $Q^2 < 2\,\mathrm{GeV}^2$, while it does not work for a higher Q^2 region. Another parameterization called BBBA05, which is tuned to reproduce the measurements, is widely used these days [30].

On the other hand, the axial form factor F_A, which can be measured only by the weak interaction, is commonly parameterized by the dipole form as

$$\left[F_A(Q^2)\right]_{\mathrm{CC}} = g_A\left(1+\frac{Q^2}{M_A^2}\right)^{-2}. \tag{2.21}$$

The axial coupling constant $g_A = 1.2723 \pm 0.0023$ is determined by nucleon β decay experiments [5]. The axial mass M_A determines the Q^2 dependence of the axial form factor. The value of M_A changes the normalization of the total cross section distorting the differential cross section $d\sigma/dQ^2$. For larger values of M_A, the total cross section increases as shown in the left panel of Fig. 2.4. When looking at the area normalized differential cross section (right panel of Fig. 2.4), we can confirm that a large value of M_A lead to a larger differential cross section in a large Q^2 region. Measurement of the total cross section is difficult because of the large normalization uncertainty of neutrino flux. On the other hand, the evaluation based on the differential cross section makes it possible to measure M_A from the shape without using absolute values.

In general, the vector form factors can be precisely determined from high-statistics electron scattering data, while the axial form factors are uncertain because they can be measured only through neutrino interactions.

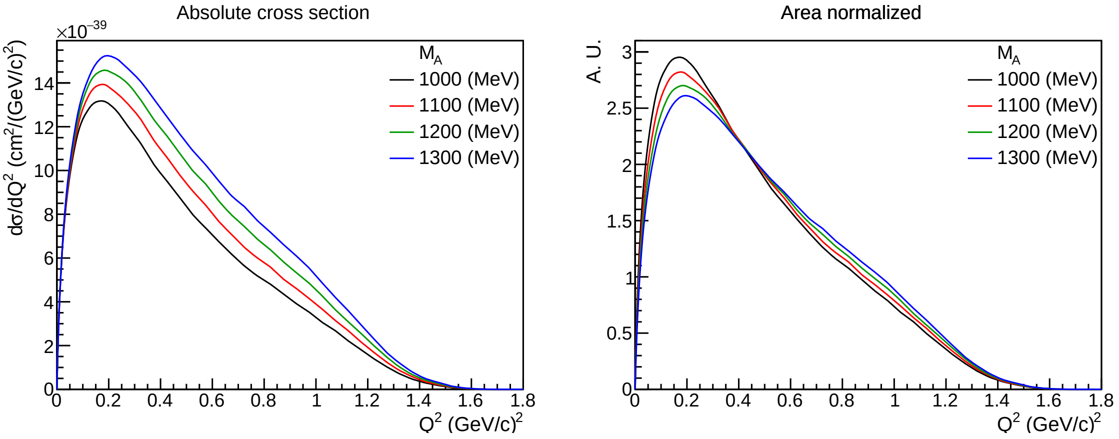

Figure 2.4: Differential cross section per target neutron for ν_μ CCQE on carbon with various values of the axial mass M_A. Monochromatic neutrino energy of 1 GeV is assumed. The left figure shows the absolute cross section, and the right figure shows the area normalized cross section for shape comparison. Larger values of M_A lead to larger total cross sections and larger differential cross sections in a large Q^2 region. This trend is common to NCQE interaction. These results are obtained using NuWro [27].

Experimental Measurements of the Axial Mass M_A

The axial mass M_A has been measured by both methods: total cross section or differential cross section (shape analysis). Various experiments have measured this parameter, but the results differ from experiment to experiment. It has been becoming a significant issue in the field of neutrino-nucleon interaction.

In the 1970s and 1980s, various experiments using deuteron-target bubble chambers appeared to be consistent with obtained results of $M_A \sim 1.0\,\text{GeV}$. A global fit of these experiments once determined $M_A = 1.026 \pm 0.021\,\text{GeV}$. However, recent experiments in the 2000s using carbon and oxygen have found results as large as $M_A = 1.1 - 1.3\,\text{GeV}$, and the discrepancy becomes an issue. Fig. 2.5 shows a summary of M_A measurements. Although errors are large, there is a significant discrepancy between the previous world average and the recent results.

The MiniBooNE experiments obtained a particularly large value of M_A: $M_A = 1.35 \pm 0.17\,\text{GeV}$ [32]. Fig. 2.6a shows the schematic view of the MiniBooNE detector. A 12-m-diameter tank contains 800 tons of pure mineral oil (CH_2), and 1280 (240) 8-inch PMTs are installed for signal (veto) region. It detects Cherenkov light and a little scintillation light. Fig. 2.6b shows the muon neutrino flux at the MiniBooNE having 788 MeV mean energy and a wide distribution. Since it is not a tracker detector, it achieves small dead volume and high acceptance. Fig. 2.7 shows the obtained differential and total cross sections of the CCQE. From the shape-only fit of the differential cross section (Fig. 2.7a), they obtained the result of $M_A = 1.35 \pm 0.17\,\text{GeV}$ giving a large total cross section (Fig. 2.7b).

Tracker detectors such as the MINOS and SciBar with comparable neutrino energies also give consistent results with the MiniBooNE. However, the NOMAD's results show a different trend. The NOMAD detector consists of an active target of drift chambers filled with an Ar(40%)-C_2H_6(60%) with a fiducial mass of 2.7 tons as shown in Fig. 2.8a. The active target is mainly carbon. The neutrino beam has a high energy of about 20 GeV, as shown in Fig. 2.8b. From the fit of the differential cross section as a function of Q^2,

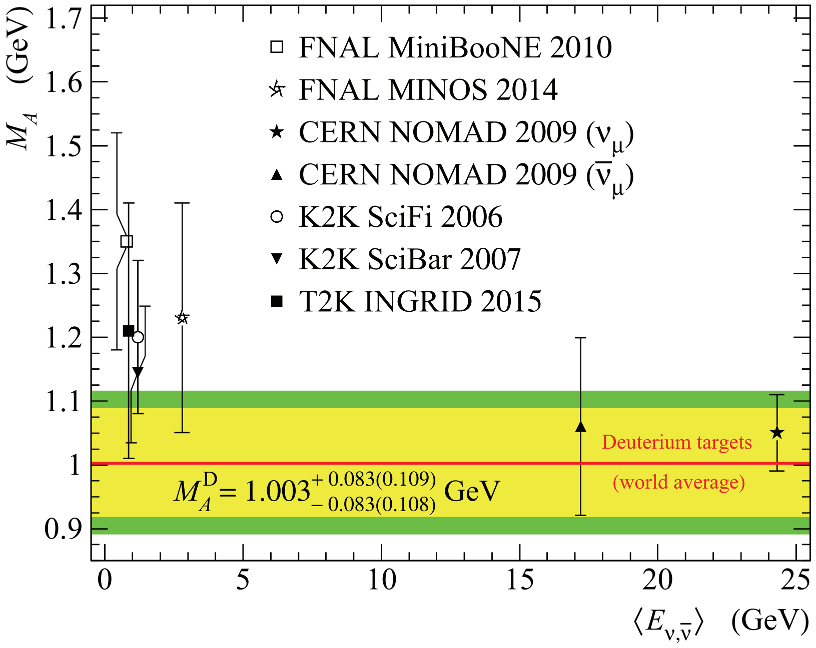

Figure 2.5: Summary of M_A measurements. The yellow and green regions show 1σ and 2σ uncertainties in the world average mainly derived from deuteron-target bubble chambers. The dots represent recent experimental data using carbon targets. The horizontal axis represents the mean neutrino energy. There is a discrepancy between the world average and the recent experiments. The NOMAD experiment also reports somewhat different values from other recent experiments. The figure is from [31].

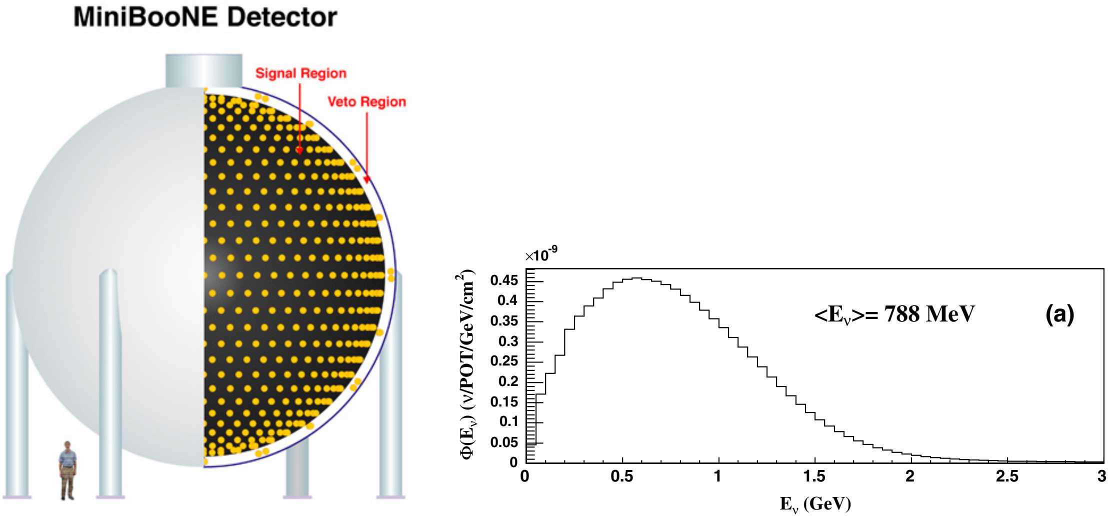

(a) The MiniBooNE detector [33].

(b) Muon neutrino beam flux at the MiniBooNE [32].

Figure 2.6: (a) Schematic view of the MiniBooNE detector. (b) Muon neutrino beam flux at the MiniBooNE. A 12-m-diameter tank contains 800 tons of pure mineral oil (CH_2). The mean neutrino energy is 788 MeV.

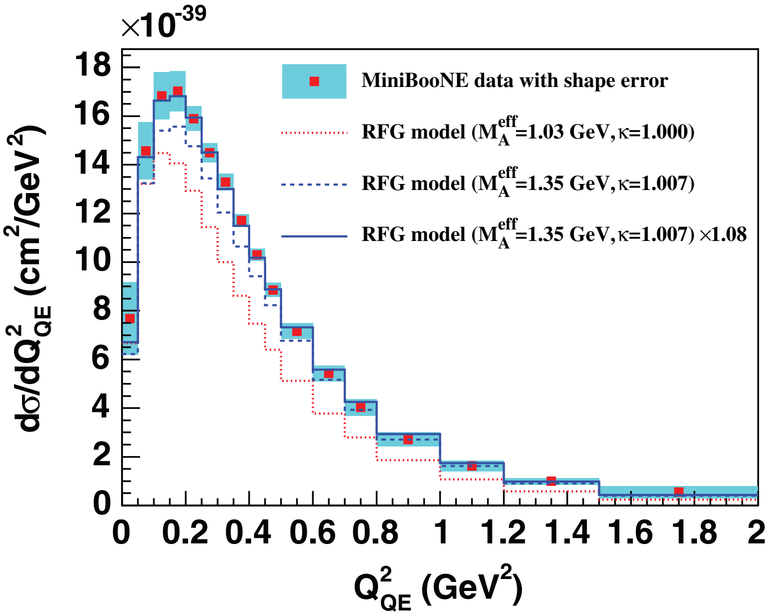

(a) Flux-integrated differential cross section per target neutron. The data leads to $M_A = 1.35 \pm 0.17\,\text{GeV}$ from a shape-only fit.

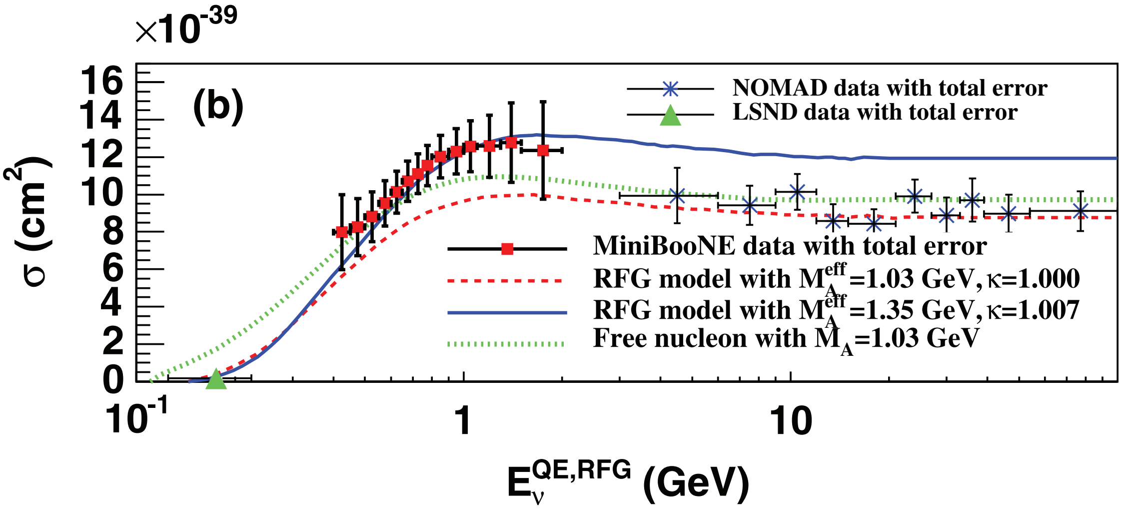

(b) Total CCQE cross section per target neutron as a function of neutrino energy. The result from the MiniBooNE is compared with the NOMAD and LSND. The MiniBooNE data agree with large axial mass with $M_A = 1.35\,\text{GeV}$, as shown in the solid blue line. The cross section with $M_A = 1.03\,\text{GeV}$, similar to the world average, is consistent with the NOMAD but not with the MiniBooNE.

Figure 2.7: ν_μ CCQE cross section per target neutron reported by the MiniBooNE Collaboration. The figure is from [32].

the NOMAD obtained the following results: $M_A = 1.05 \pm 0.02(\text{stat}) \pm 0.06(\text{syst})\,\text{GeV}$ for ν_μ and $M_A = 1.06 \pm 0.07(\text{stat}) \pm 0.12(\text{syst})\,\text{GeV}$ for $\bar{\nu}_\mu$ [34]. These results are consistent with the world average but inconsistent with recent experiments such as the MiniBooNE. The total CCQE cross section obtained from NOMAD is obviously inconsistent with the MiniBooNE's result shown in Fig. 2.7b.

It is becoming clear that a two-body current contribution (2p2h, see Sec. 2.1.6 for detail) must be considered to explain the discrepancy. In the 2p2h, neutrino interacts with a nucleon pair in the nucleus. The 2p2h contribution was absent in the deuteron-target bubble chamber experiments. However, the recent experiments can misidentify the 2p2h interactions as the CCQE interactions, leading to overestimating the CCQE cross sections. While the discrepancy from the deuteron-target bubble chambers can be reasonably explained, it does not explain the one between the NOMAD and MiniBooNE experiments. A vital requirement of the 2p2h model is to explain the NOMAD and MiniBooNE data simultaneously. For example, we expect a model with a large cross section at a few GeV and a smaller one at around 20 GeV. Since we have yet to realize a direct measurement, there is sizeable model-dependent uncertainty. Even if they can explain the MiniBooNE data, the agreement with the NOMAD data is not good. Because of this situation, it is difficult to determine a reasonable constraint on M_A in the current situation.

2.1.2 Neutral Current Quasi-Elastic (NCQE) Interaction

The Neutral Current Quasi-Elastic (NCQE) interaction is also a quasi-elastic scattering with a single nucleon mediated by Z bosons. It does not change the charge of lepton between the initial and final states.

$$\nu(\bar{\nu}) + p \rightarrow \nu(\bar{\nu}) + p, \tag{2.22}$$

$$\nu(\bar{\nu}) + n \rightarrow \nu(\bar{\nu}) + n. \tag{2.23}$$

The formalism of NCQE interaction is more or less the same as that of CCQE interaction except for c_{EW} and form factors. The value of c_{EW} appears in Eq. 2.2 is $1/4$ instead of $\cos\theta_c$. The vector and axial form factors of NCQE interaction differ from those of CCQE (Eq. 2.9 and 2.21) because Z boson mediates the neutral current. Since it does not change the charge of lepton between the initial and final states, it is sensitive to the isoscalar component of weak currents, *i.e.*, the s-quarks existing as sea quarks in nucleons, as shown in the following form factors. The vector form factors for the NCQE interaction are as follows:

$$\left[F_V^i(Q^2)\right]_{\text{NC}}^{p/n} = \pm\frac{1}{2}\left[F_V^i(Q^2)\right]_{\text{CC}} - 2\sin^2\theta_W F_V^{i,p/n}(Q^2) - \frac{1}{2}F_V^{i,s}(Q^2) \qquad (i = 1, 2), \tag{2.24}$$

where θ_W is the Weinberg angle, and the indices p and n represent the proton and neutron, respectively. The proper parameterization of Q^2 dependence for the strange vector form factors, $F_V^{i,s}(Q^2)$, is unknown. A simple one is the dipole form assuming the similar Q^2 dependence as those of the non-strange form factors:

$$F_V^{1,s}(Q^2) = F_V^{1,s} Q^2 \left(1 + \frac{Q^2}{4M^2}\right)^{-1} \left(1 + \frac{Q^2}{M_V^2}\right)^{-2}, \tag{2.25}$$

$$F_V^{2,s}(Q^2) = F_V^{2,s}(0) \left(1 + \frac{Q^2}{4M^2}\right)^{-1} \left(1 + \frac{Q^2}{M_V^2}\right)^{-2}. \tag{2.26}$$

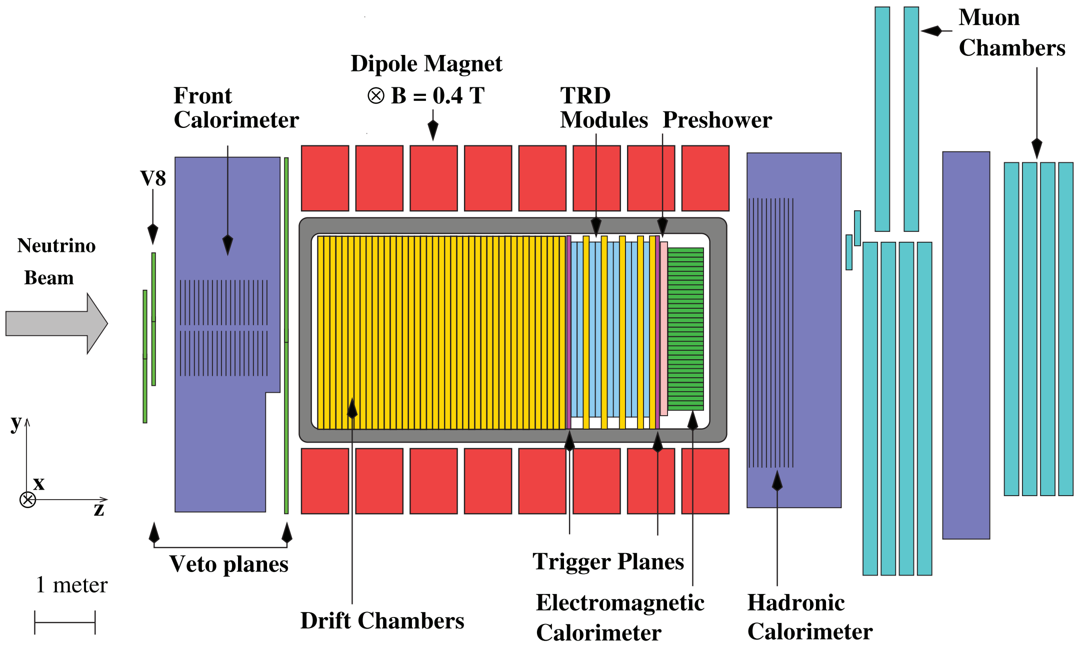

(a) Schematic view of the NOMAD detector

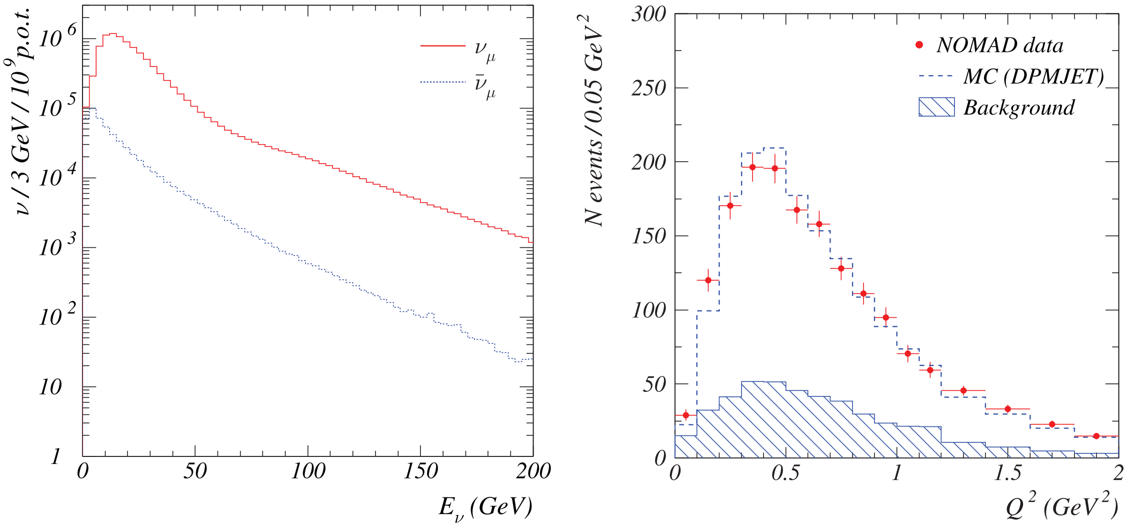

(b) Neutrino beam flux at the NOMAD

(c) Q^2 distribution in CCQE events

Figure 2.8: (a) Schematic view of the NOMAD detector. (b) Neutrino beam flux at the NOMAD. (c) Q^2 distribution in CCQE events. Drift camber has an active target with 2.7 tons, mainly carbon targets. The neutrino beam flux has a wide distribution. The mean energy is 25.9 GeV (17.9 GeV) for ν_μ ($\bar{\nu}_\mu$). The spectrum fit of Q^2 distribution leads to $M_A = 1.05 \pm 0.02(\mathrm{stat}) \pm 0.06(\mathrm{syst})$ GeV for ν_μ and $M_A = 1.06 \pm 0.07(\mathrm{stat}) \pm 0.12(\mathrm{syst})$ GeV for $\bar{\nu}_\mu$. The figures are from [34].

The axial form factors for the NCQE interaction can be written as follows, assuming the dipole form:

$$\left[F_A(Q^2)\right]_{\mathrm{NC}}^{p/n} = \pm\frac{1}{2}\left[F_A(Q^2)\right]_{\mathrm{CC}} - \frac{1}{2}F_A^s(Q^2), \tag{2.27}$$

$$= \frac{1}{2}(\pm g_A - g_A^s)\left(1 + \frac{Q^2}{M_A^2}\right)^{-2}, \tag{2.28}$$

$$F_A^s(Q^2) = g_A^s\left(1 + \frac{Q^2}{M_A^2}\right)^{-2}, \tag{2.29}$$

where the sign $+(-)$ is for proton (neutron), $F_A^s(Q^2)$ represents the strange axial form factor, and $g_A^s = F_A^s(0)$ represents the strangeness axial coupling constant. The strange vector and axial form factors ($F_V^{i,s}$ and F_A^s) represent the electromagnetic (electric charge and magnetic moments) and spin contribution of the strange quarks existing as sea quarks to the nucleon. Polarized electron-nucleon elastic scattering experiments can measure the strange vector form factors. The results are consistent with zero within the uncertainty [35]. On the other hand, the strangeness axial coupling constant g_A^s, which can be measured by the NCQE measurements, is known to prefer negative values. More details about this topic are discussed in Sec. 3.

The strangeness axial coupling constant g_A^s significantly changes the relative proton and neutron NCQE cross sections with little change in the total cross section. Fig. 2.9 shows the NCQE cross section on carbon per nucleon as a function of neutrino energy. For lower values of g_A^s, the neutron contribution to the total cross section becomes smaller while the proton contribution increases. The impact of g_A^s is evident by looking at the neutron cross section as a fraction of the total NCQE cross section, as shown in Fig. 2.10. On the other hand, the value of M_A changes total cross section normalization without changing the fraction of neutron- and neutron-target cross section. Therefore, by measuring both the neutron-target and proton-target cross section, it is possible to measure g_A^s with less dependence on these normalization factors.

2.1.3 Resonace Pion Production (RES)

A channel of resonance pion production (RES) is dominant at the neutrino energy of a few GeV. The RES is an inelastic scattering with a single nucleon producing a single pion via the resonant state of the nucleon. The CCRES interaction becomes a significant background in neutrino oscillation experiments such as the T2K experiment because it is misidentified as a CCQE interaction when the pion is not detected. There are various resonant excitation channels, and the main reactions are as follows: For CCRES,

$$\nu_l + p \to l^- + \Delta^{++} \to l^- + p + \pi^+, \tag{2.30}$$

$$\nu_l + n \to l^- + \Delta^{+} \to l^- + p + \pi^0, \tag{2.31}$$

$$\nu_l + n \to l^- + \Delta^{+} \to l^- + n + \pi^+, \tag{2.32}$$

$$\bar{\nu}_l + p \to l^+ + \Delta^{0} \to l^+ + p + \pi^-, \tag{2.33}$$

$$\bar{\nu}_l + p \to l^+ + \Delta^{0} \to l^+ + n + \pi^0, \tag{2.34}$$

$$\bar{\nu}_l + n \to l^+ + \Delta^{-} \to l^+ + n + \pi^-. \tag{2.35}$$

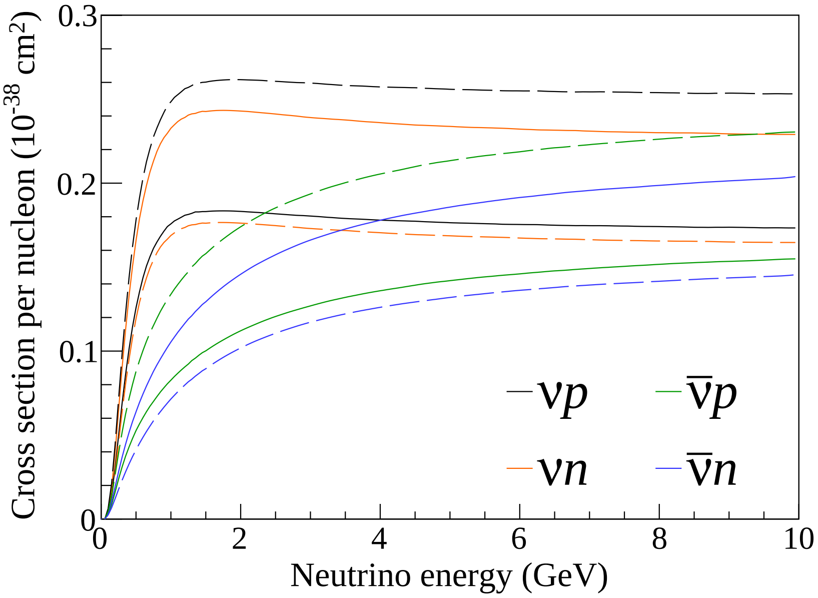

Figure 2.9: NCQE cross section on carbon per nucleon as a function of neutrino energy. The black and red lines represent the neutrino cross sections on protons and neutrons, respectively. The green and blue lines represent the antineutrino cross sections on protons and neutrons, respectively. The solid (dashed) lines are the cross sections with $g_A^s = 0$ (-0.3). These results are obtained using NuWro with $M_A = 1.2\,\text{GeV}$ [27].

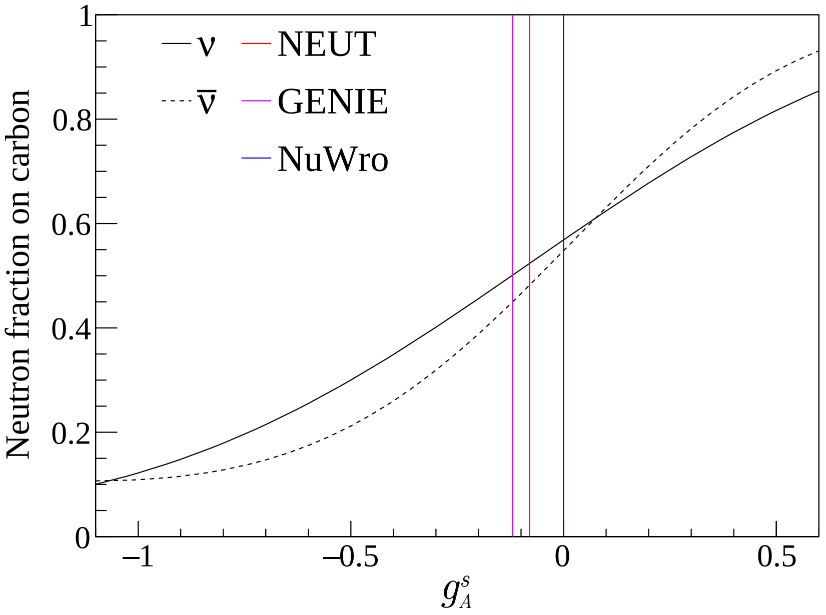

Figure 2.10: Neutron fraction of the total NCQE cross section on carbon as a function of the strangeness axial coupling constant g_A^s. The solid (dashed) line represents the neutrino (antineutrino) cross-section fraction. These results are obtained using NuWro with $M_A = 1.2\,\text{GeV}$ at $0.5\,\text{GeV}$ neutrino energy. The vertical lines in red, violet, and blue represent the default values adopted in neutrino Monte Carlo generators, NEUT [36, 37], GENIE [38], and NuWro [27], respectively. Lower values of g_A^s lead to a lower neutron contribution to the total cross section.

For NCRES,

$$\nu(\bar{\nu}) + p \to \nu(\bar{\nu}) + \Delta^+ \to \nu(\bar{\nu}) + p + \pi^0, \tag{2.36}$$
$$\nu(\bar{\nu}) + p \to \nu(\bar{\nu}) + \Delta^+ \to \nu(\bar{\nu}) + n + \pi^+, \tag{2.37}$$
$$\nu(\bar{\nu}) + n \to \nu(\bar{\nu}) + \Delta^0 \to \nu(\bar{\nu}) + p + \pi^-, \tag{2.38}$$
$$\nu(\bar{\nu}) + n \to \nu(\bar{\nu}) + \Delta^0 \to \nu(\bar{\nu}) + n + \pi^0. \tag{2.39}$$

The region of the invariant mass categorized as RES depends on the models and Monte Carlo event generators.

Rein-Sehgal Model

In the formalism of the RES, the Rein-Sehgal model [39] has long been used. The model is composed of two parts: A part where it generates the resonant state and a part where it decays. The differential cross section is given as

$$\frac{d^2\sigma}{dQ^2 dW} = \frac{1}{32\pi m_N E_\nu} \frac{1}{2} \sum_{spin} |T(\nu N \to l N^*)|^2 \frac{1}{2\pi} \frac{\Gamma}{(W-N)^2 + \Gamma/4}, \tag{2.40}$$

where W is invariant mass of N^*. $T(\nu N \to l N^*)$ describes the amplitude of the resonant state, and $\frac{1}{2\pi}\frac{\Gamma}{(W-N)^2+\Gamma/4}$ is the Breit-Wigner formula which describes the decay of the resonant state. The Rein-Sehgal model considers 18 resonances with $W < 2\,\text{GeV}$. Although the Rein-Sehgal model has been used for a long time because of its simplicity, it became clear that it has a deviation from the data from electron-nucleon scattering experiments.

Graczyk-Sobczyk Model

Several modifications were made to the Rein-Sehgal model, to reduce the discrepancy from the experimental data. Graczyk-Sobczyk [1] provides a new parameterization of form factors based on the Adler-Rarita-Schwinger formalism [40–43]. They introduced three vector form factors C_3^V, C_4^V, and C_5^V based on the dipole form.

$$C_3^V(Q^2) = 2.13 \left(1 + \frac{Q^2}{4M_V^2}\right)^{-1} \left(1 + \frac{Q^2}{M_V^2}\right)^{-2}, \tag{2.41}$$
$$C_4^V(Q^2) = -1.51 \left(1 + \frac{Q^2}{4M_V^2}\right)^{-1} \left(1 + \frac{Q^2}{M_V^2}\right)^{-2}, \tag{2.42}$$
$$C_5^V(Q^2) = 0.48 \left(1 + \frac{Q^2}{4M_V^2}\right)^{-1} \left(1 + \frac{Q^2}{0.776 M_V^2}\right)^{-2}, \tag{2.43}$$

where $M_V = 0.84\,\text{GeV}$. They also introduced four axial form factors C_3^A, C_4^A, C_5^A, and C_6^A.

$$C_3^A(Q^2) = 0, \tag{2.44}$$
$$C_4^A(Q^2) = -\frac{1}{4} C_5^A(Q^2), \tag{2.45}$$
$$C_5^A(Q^2) = C_5^A(0) \left(1 + \frac{Q^2}{M_A^2}\right)^{-2}, \tag{2.46}$$
$$C_6^A(Q^2) = \frac{M^2}{m_\pi^2 + Q^2} C_5^A(Q^2). \tag{2.47}$$

---

[1] Graczyk and Sobczyk are NuWro developers.

The PCAC hypothesis is assumed in Eq. 2.47 and $C_5^A(Q^2)$ is based on the dipole form. Graczyk *et al.* measured the values of $C_5^A(0)$ and M_A by a simultaneous fit of the ANL and BNL neutrino scattering data. $C_5^A(0) = 1.19 \pm 0.08$ and $M_A = 0.94 \pm 0.03\,\mathrm{GeV}$ [43]. Fig. 2.11 shows the best-fit total cross section for $\nu_\mu + p \to \mu^- + p + \pi^+$ together with 1σ uncertaineties. The uncertainty gives about 10% in normalization.

Adler provides an alternative parameterization on the $C_5^A(Q^2)$.

$$C_5^A(Q^2) = C_5^A(0)\left(1 - \frac{1.21Q^2}{2+Q^2}\right)\left(1 + \frac{Q^2}{M_A^2}\right)^{-2}. \tag{2.48}$$

Graczyk *et al.* also provides a fit result under the Adler from factors using the same data set. They obtained $M_A = 1.29 \pm 0.07\,\mathrm{GeV}$ and $C_5^A(0) = 1.14 \pm 0.08$ [43]. Since the fit with the dipole form gives better agreement with the data, NuWro adopts the best-fit result with dipole form factors.

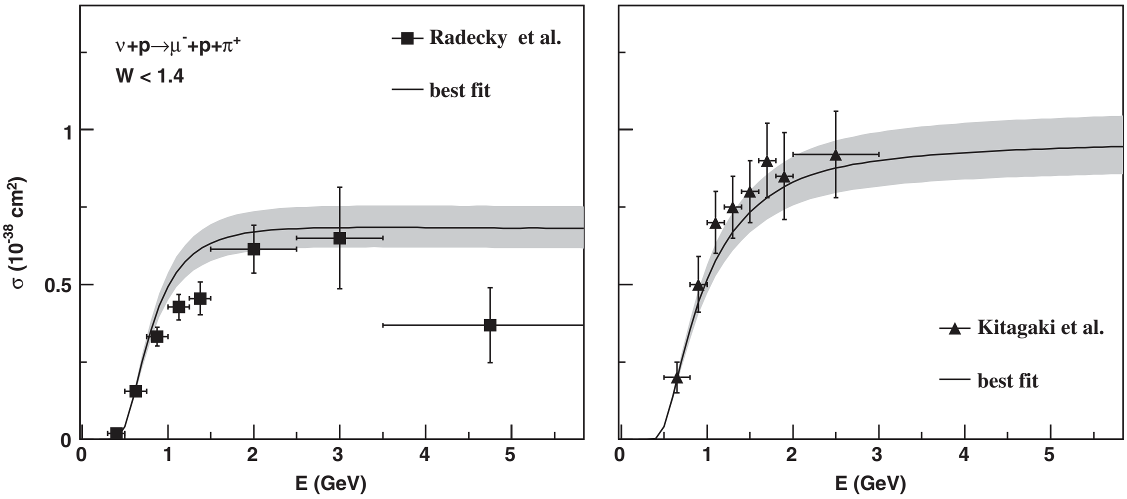

Figure 2.11: Total cross section for $\nu_\mu + p \to \mu^- + p + \pi^+$. In the left panel, the ANL data with the cut $W < 1.4\,\mathrm{GeV}$ are shown, while the right panel shows the BNL data without W cuts. The solid curves and the shaded regions represent the theoretical best-fit and 1σ uncertainties obtained with the dipole forms: $C_5^A(0) = 1.19 \pm 0.08$ and $M_A = 0.94 \pm 0.03\,\mathrm{GeV/c}$. The simultaneous fit of the ANL and BNL data was made in the differential cross section, not in the total cross section shown here. The figure is from [43].

2.1.4 Deep Inelastic Scattering (DIS)

The process that is more inelastic than the RES is categorized as a deep inelastic scattering (DIS). The boundary of RES and DIS is set at $W \sim 2\,\mathrm{GeV}$, but it depends on the models and Monte Carlo event generators. In general, the DIS involves multiple hadrons. The double differential cross section is given as

$$\frac{d^2\sigma}{dxdy} = \frac{G_F^2 m_N E_\nu}{\pi}\left[\left(1 - y + \frac{1}{2}y^2 + C_1\right)F_2(x) \pm y\left(1 - \frac{1}{2}y + C_2\right)xF_3(x)\right], \tag{2.49}$$

$$C_1 = \frac{m_l^2(y-2)}{4m_N E_\nu x} - \frac{m_N xy}{2E_\nu} - \frac{m_l^2}{4E_\nu^2}, \tag{2.50}$$

$$C_2 = -\frac{m_l^2}{4m_N E_\nu x}, \tag{2.51}$$

where x and y are the Bjorken scaling parameters.

$$x = \frac{Q^2}{2m_N(E_\nu - E_l)} + m_N^2, \tag{2.52}$$

$$y = \frac{E_\nu - E_l}{E_\nu}. \tag{2.53}$$

$F_2(x)$ and $xF_3(x)$ are the Parton Distribution Function (PDF), and GRV98 [44] modified by Bodek and Yang [45] is widely used.

2.1.5 Coherent Pion Production (COH)

The coherent pion production (COH) interaction associates a pion without breaking the target nucleus. For CCCOH,

$$\nu_l + A \to l^- + \pi^+ + A, \tag{2.54}$$

$$\bar{\nu}_l + A \to l^+ + \pi^- + A. \tag{2.55}$$

For NCCOH,

$$\nu(\bar{\nu}) + A \to \nu(\bar{\nu}) + \pi^0 + A. \tag{2.56}$$

The differential cross section is given by Rein-Sehgal model [46]. This model differs from the Rein-Sehgal model for RES described in Sec. 2.1.3. It is known to overestimate the cross section in $E_\nu \lesssim 1\,\mathrm{GeV}$. Rein-Sehgal introduced correction factors to get better consistency with experiments in [47]. The Berger-Sehgal model is also provided as an alternative model [48]. The COH has a negligible contribution in this study because of the small cross section.

2.1.6 Two-body Current (2p2h)

The two-body current called "2p2h"[2] or "Meson Exchange Current (MEC)" is an interaction with a nucleon pair produced by the short-range correlation in the nucleus. Various electron scattering experiments have reported evidence of the 2p2h so far [49,50], thus, the neutrino 2p2h is naturally assumed to exist. However, a direct measurement of neutrino 2p2h has not been realized, and there is sizeable model-dependent uncertainty. The direct measurement of neutrino 2p2h and the constraints on the model are among the most important issues in studying the neutrino-nucleon interaction. We need to upgrade detectors to detect short proton tracks and neutron capture gamma rays for direct measurement. In addition, since the contribution of 2p2h is estimated to be only 10−20% of the QE, accurate measurements with high statistics are required.

Fig. 2.12 shows the schematic view of the 2p2h interaction. Due to the short-range nucleon-nucleon correlation, the nucleon pairs tend to have large relative momentum and small center-of-mass momentum. If the struck proton is a part of a nucleon pair, another correlated nucleon with high relative momentum is also recoiled and ejected. Because of the FSI and nuclear de-excitation, not necessarily only two nucleons are emitted. In electron scattering experiments, the 2p2h contribution is dominant in the energy region between the QE and RES, called the dip region. An analogy is expected for neutrino 2p2h interaction with relatively large contributions in the dip region, a few GeV. Therefore, the

---

[2] 2p2h stands for 2-particle-2-hole. In general, 2p2h refers to the one of CC, but here NC is also included.

discrepancy of the M_A measurements shown in Fig. 2.5 may indicate a contribution from the 2p2h interaction. Since the 2p2h is absent in the deuteron-target, it looks straightforward to explain the difference between the world average obtained by deuteron-target bubble chambers and the recent carbon- (oxygen-) target experiments. Therefore, the main issue of the discrepancy is the energy dependence of 2p2h. We need to explain both results of the MiniBooNE ($\sim 1\,\mathrm{GeV}$) and the NOMAD ($\sim 20\,\mathrm{GeV}$) simultaneously. The discrepancy could be explained by the energy dependence of the 2p2h cross section, but model predictions do not agree with the NOMAD's result well in the current situation.

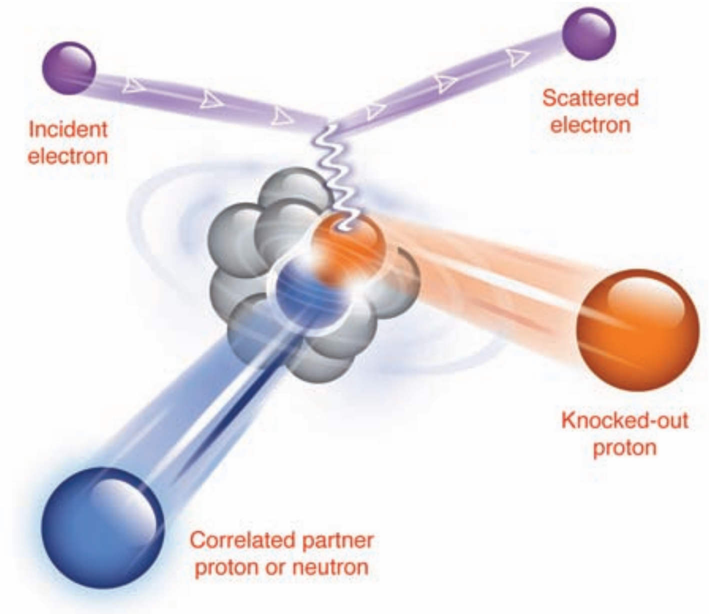

Figure 2.12: Schematic view of the two-body current interaction. This figure shows a case of electron scattering with a *pn* or *pp* pair. If the struck proton is a part of a nucleon pair, another correlated nucleon with high relative momentum is also recoiled and ejected. The figures is from [50]

Cross Section Models

There are several models to describe the 2p2h interaction. Nieves model [51] and Martini model [52] are microscopic calculations that consider some Feynman diagrams for the 2p2h contribution. Since the diagrams considered in the models are different, the cross sections differ by a factor of two, as shown in Fig. 2.13. However, neither the KamLAND data nor the external data are sensitive enough to constrain the 2p2h contribution separately from the QE, and there are still large theoretical uncertainties. Both models predict a monotonic and gradual increasing trend in the higher energy region not shown in Fig. 2.13. As a result, these models overestimate the cross section in the energy region of the NOMAD experiment, about 20 GeV. In addition, because of the complexity of the models, only a model for the CC is available [3]. Since this study measures the NCQE, we must consider the NC 2p2h. Therefore, these models are not suitable for use in this study.

---

[3] The Martini model briefly explains the contribution of NC 2p2h interaction in [52]. However, the model is not implemented in the neutrino Monte Carlo event generators.

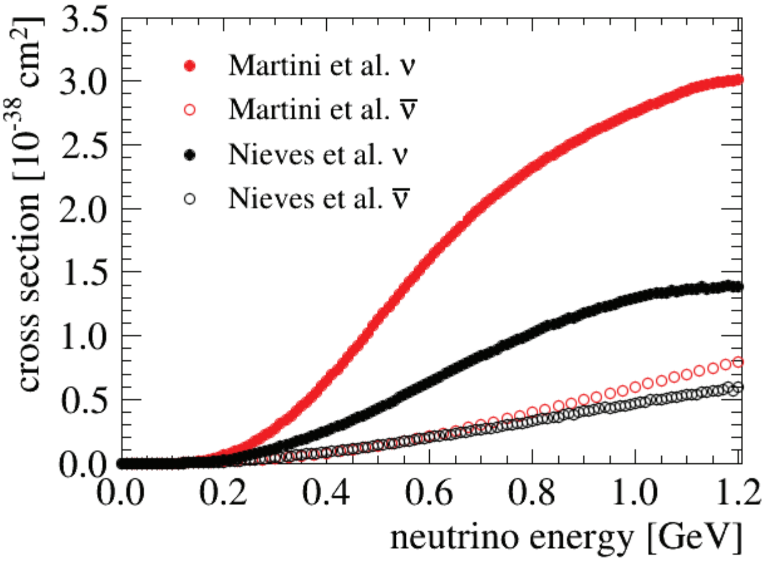

Figure 2.13: Cross section of charged-current two-body contribution on carbon predicted by models of Nieves *et al.* [51] and Martini *et al.* [52]. Both models predict almost comparable cross sections for antineutrino. On the other hand, for neutrino, Martini *et al.* predicts about two times as large as Nieves *et al.* The figure is from [53].

On the other hand, the Transverse Enhancement Model (TEM) [54] is a new approach describing the 2p2h interaction. The TEM only modifies the vector magnetic form factors to give better consistency with the electron scattering data, as shown in Fig. 2.14a. The model is phenomenological, easy to implement in the neutrino Monte Carlo generators, and wholly derived from the electron scattering data. Since the TEM can describe the CC and NC interactions, this study uses the TEM in the analysis. Fig. 2.14b and 2.15 show the cross section of CC and NC 2p2h predicted by the TEM. The TEM CC 2p2h cross section peaks at around 0.8 GeV, gradually decreasing in the higher energy region, leading to better agreement with the NOMAD experiment than other models.

Fractions of Nucleon Pairs

Besides the cross section, the fractions of nucleon pairs (pp, pn, and nn) are uncertain. Considering nuclear forces producing the short-range correlated pairs, np pair, which has opposite isospin, is expected to be dominant, while fractions of pp and nn pairs with the same isospin are comparable.

Electron and proton scattering experiments have measured the fraction of the np pair to np and pp pairs. Since they required at least one proton in the final state, they cannot evaluate the contribution of the nn pair. An electron scattering experiment obtained $96^{+4}_{-22}\%$ [50] and a proton scattering experiment obtained $92^{+8}_{-18}\%$ [49] as summarized in Fig. 2.16a. These consistent results indicate the dominant contribution from the np pair. Fig. 2.16b shows a comprehensive picture of nucleons in carbon obtained from the electron scattering experiment. The results indicate that 80% of the nucleons in carbon are independent (single nucleons), whereas for the 20% of correlated pairs. The np pairs, about 90%, dominate the nucleon pairs. They inferred the same fractions for nn and pp pairs leading to the fraction of about 5% for pp and nn pairs. More detailed investigations

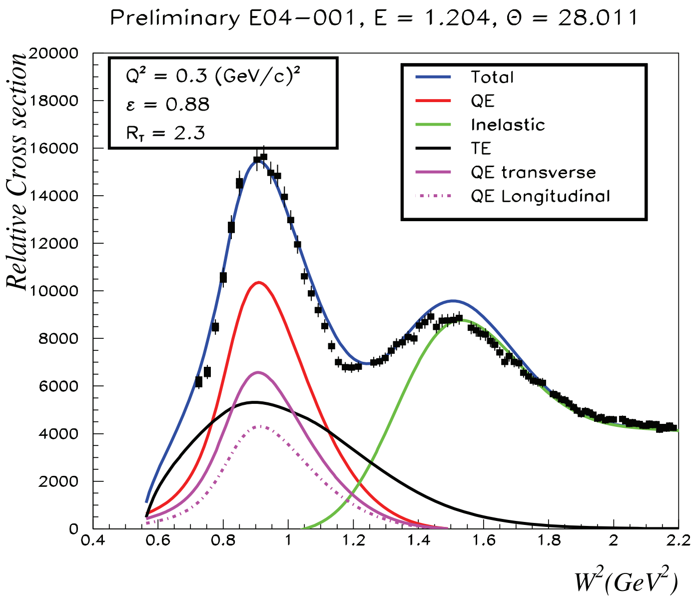

(a) Spectra fitting of electron scattering data. The black dots represent the electron scattering experimental data. TEM contribution, which is written with a solid black line, is fitted to reproduce the data, especially in the dip region. The TEM has a tail near the RES (denoted as "inelastic") region.

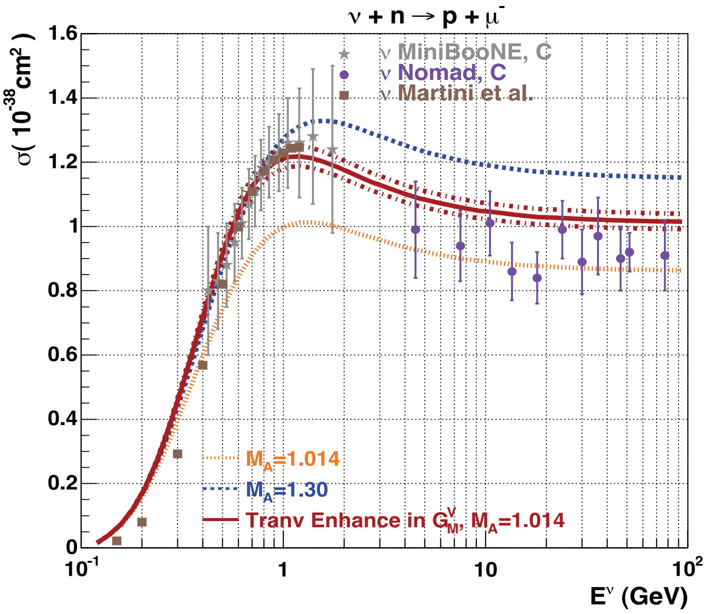

(b) Neutrino CC QE+2p2h cross section per target neutron on carbon. The dotted orange (blue) line represents the pure CCQE interaction with $M_A = 1.014$ (1.30) GeV. The red solid and dashed lines represent the sum (and its uncertainty) of the CCQE interaction with $M_A = 1.014\,\text{GeV}$ and 2p2h interaction. The difference between the orange and red lines denotes the contribution of the 2p2h interaction. The TEM gives relatively good consistency with the data from MiniBooNE (gray) and NOMAD (violet) simultaneously.

Figure 2.14: Spectra fitting of electron scattering data (Fig. 2.14a) and cross section (Fig. 2.14b) in the transverse enhancement model (TEM). The figures are from [54].

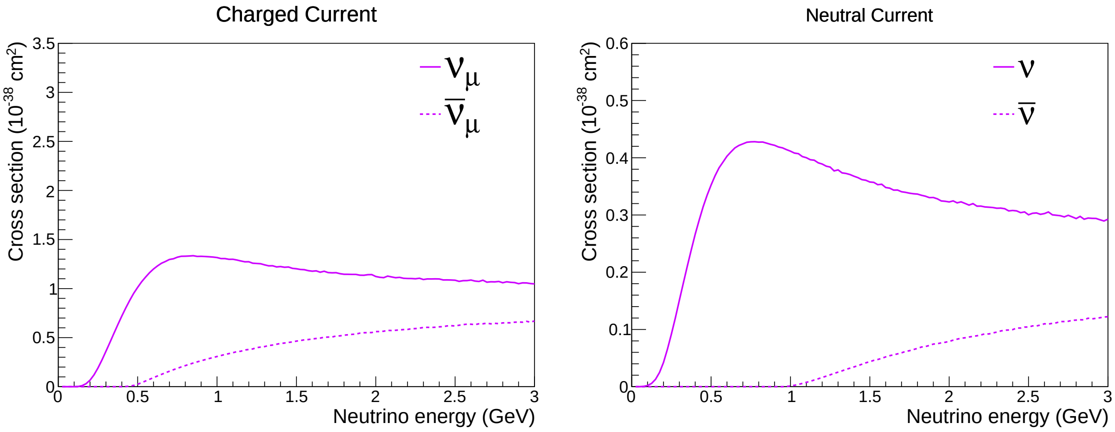

(a) Charged Current (b) Neutral Current

Figure 2.15: Two-body current (2p2h) cross section on carbon predicted by the transverse enhancement model (TEM). The CC 2p2h cross section is similar to that of the Nieves model, but the TEM's cross section gradually decreases in the higher energy region while the Nieves and Martini models do not. These values are calculated with NuWro.s

of these results can be found in [55].

The nucleon pairs are produced by the nuclear forces and do not depend on the incoming particle, such as proton, electron, and neutrino. Therefore, an analogy with electron and proton scattering experiments may hold to some extent for the neutrino interaction. Naturally, verification by direct measurements is an exciting subject of study. The theoretical calculation for neutrino interaction by R. Gran *et al.* [56] predicts the 67% fraction of the *np* pairs, which is slightly smaller than the results from electron and proton scattering experiments.

In this study, we assign the fraction of *np* pairs as $85^{+15}_{-20}\%$, which covers all of the results mentioned above[4].

Toward Direct Measurement

Several experiments are underway for the direct measurement of the 2p2h interaction. Since neutrons are extremely difficult to reconstruct their momentum, these experiments search $\nu + np \to l^- + pp$, identifying two protons. These protons tend to have only a few cm of a track, requiring very high track resolution. Furthermore, protons can also be emitted by FSI and nuclear de-excitation, so an advanced prediction accuracy of these effects is also required. NINJA experiment [57], a 3-kg water target nuclear emulsion detector, aims to measure the 2p2h interaction with dramatically good track resolution.

---

[4] We set this value for “mec_ratio_pp” in NuWro.

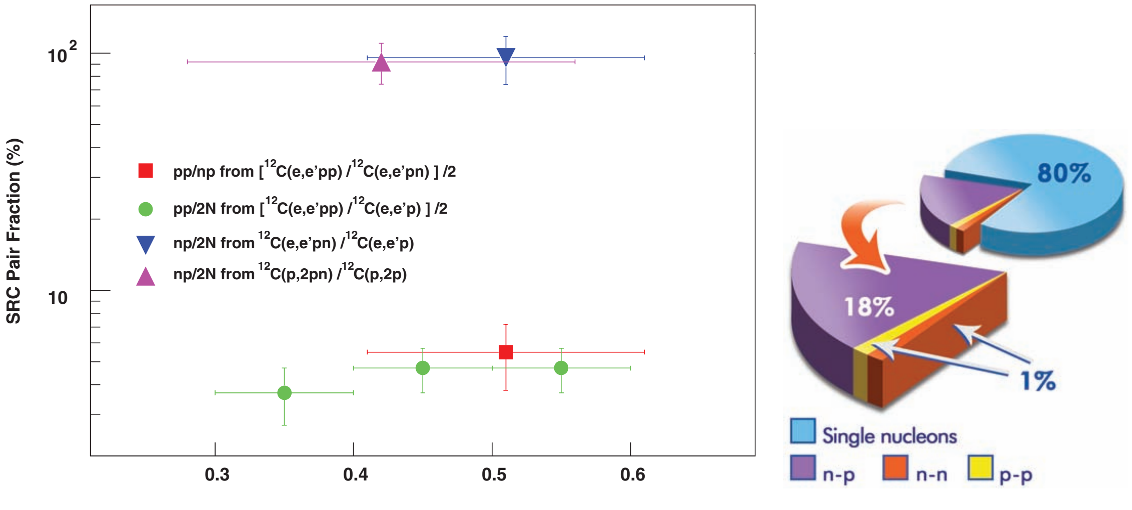

(a) Fraction of correlated nucleon pairs

(b) Fraction of nucleons in the various initial state

Figure 2.16: Fractions of correlated nucleon pairs and a comprehensive picture of nucleons in carbon. (a) The magenta and blue dots represent the fractions of *np* pairs to *np* and *pp* pairs. The red dot represents the fraction of *pp* pairs to *np* pairs and the green dots represent the fraction of *pp* pairs to *np* and *pp* pairs. These four values are consistent, showing the dominant *np* pairs about 90%. (b) The fraction of nucleons was obtained from the inclusive electron scattering data. They inferred the same fractions for *nn* and *pp* pairs. The figures are from [50]

2.2 Nuclear Effects

Neutrino-nucleon interactions have been described so far. However, in practice, neutrino interacts with various nuclei in detectors. Therefore, the formalism of neutrino-nucleon interactions must include nuclear effects. The uncertainty of neutrino-nucleon interaction is mainly from the nuclear effects because of their complex many-body system. The nuclear effects are generally modeled without a nucleon-nucleon correlation under the IA. Several nuclear models have been developed to parameterize the momentum and potential distribution of nucleons bound in a nucleus and the Pauli blocking effects(Sec. 2.2.1). In addition, the RPA is also provided to describe the nucleon-nucleon correlation (Sec. 2.2.2). These nuclear effects significantly impact the low energy and momentum region.

2.2.1 Nuclear Models

Nuclear models describe the energy and momentum distribution of nucleons bound in nuclei. For example, Fig. 2.17 shows the schematic view of ^{12}C nuclear potential [5].

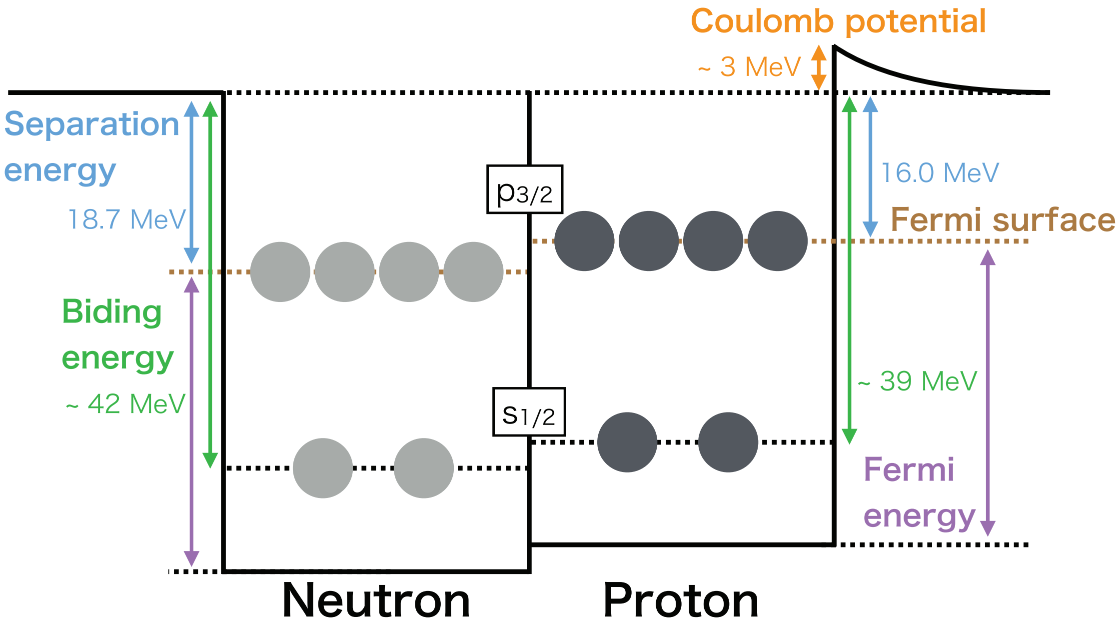

Figure 2.17: ^{12}C nuclear potential for protons and neutrons. In the simple shell model picture, four nucleons are in the $s_{1/2}$ shell level, and two are in the $p_{3/2}$ shell level. The binding energy (green) corresponds to the potential depth for each nucleon, and the separation energy (light blue) equals the minimum binding energy. The maximum value of the nucleon momentum (corresponding to the brown) is called the Fermi surface, and the energy gap to the bottom of the potential (violet) is called the Fermi energy. Protons have the Coulomb potential of about 3 MeV (orange), making protons more shallowly bound in the nucleus than neutrons. Please note that these notations and definitions may differ in documents.

---

[5] The binding energy is sometimes used with the same meaning as the separation energy, but it is confusing. For clarity, we use the terms “binding energy” and “separation energy” strictly interchangeably. We can interpret the separation energy as minimum binding energy. The binding energy is sometimes called missing energy. The binding energy minus the separation energy equals the excitation energy.

In the simple shell model picture, four protons/neutrons are in the $s_{1/2}$ shell level, and two are in the $p_{3/2}$ shell level for ^{12}C. The mass differences uniquely determine the separation energy E_S as follows:

$$E_S = M_{A-1} + M_{p,n} - M_A, \tag{2.57}$$

where M_A, M_{A-1}, and $M_{p,n}$ are the mass of the target nucleus, residual nucleus, and emitted nucleon, respectively. In the case of carbon, it is 18.7 MeV for neutrons and 16.0 MeV for protons. The difference between neutron and proton separation energies is caused by the Coulomb potential, making protons more shallowly bound in the nucleus. The separation energy is equal to the minimum binding energy, namely the binding energy of the $p_{3/2}$ under the simple shell model picture. In practice, the binding energies have finite widths and experimental uncertainty for the $s_{1/2}$ and $p_{3/2}$. The values of these energies, including shell-level occupation, vary with nuclei.

Here, three common models are explained: The relativistic Fermi gas model, the local Fermi gas model, and the spectral function. The potential is discrete with finite width in the spectral function, which considers the shell model picture. On the other hand, it is continuous in the Fermi gas models neglecting the shell model structure. Note that the detailed parameterizations of the models vary slightly among neutrino Monte Carlo generators.

Relativistic Fermi Gas (RFG) Model

The relativistic Fermi gas (RFG) model [58] is the most simple nuclear model. It is parameterized only by the Fermi momentum (also called the Fermi surface) p_F and the separation energy E_S. Because of its simplicity, this model has long been used in the neutrino Monte Carlo event generators so far.

The RFG assumes nucleons are moving in the nucleus below the Fermi momentum with flat distribution in the momentum space. The model also describes the Pauli blocking effect by requiring that the momentum of the final state nucleon emitted from the nucleus is larger than the Fermi momentum. The Fermi momentum p_F is described by

$$p_F = \left(\frac{9\pi Z}{4A}\right)^{1/3} \frac{\hbar}{r_0}, \tag{2.58}$$

assuming a constant nuclear density with a radius $R = r_0 A^{1/3}$, where $r_0 = 1.25\,\mathrm{fm}$. In the case of carbon, the Fermi momentum is $p_F \simeq 220\,\mathrm{MeV/c}$, corresponding to the Fermi energy of $E_F \simeq 25\,\mathrm{MeV}$. The sum of the Fermi energy E_F and the separation energy E_S is the maximum depth of the nuclear potential.

Fig. 2.18 shows the two-dimensional probability distribution of nucleons in carbon based on the RFG. Since the Fermi momentum is constant, there is a one-to-one correspondence between the binding energy and momentum of the nucleons. The average value of E_S is $\langle E_S \rangle = 7 - 9\,\mathrm{MeV}$, but the adopted value varies with the Monte Carlo event generators. Fig. 2.22 shows the projection of Fig. 2.18 onto the x-axis (momentum) and y-axis (biding energy). Since the RFG gives a flat distribution in the momentum space below the Fermi momentum, the probability distribution as a function of momentum (the red line in Fig. 2.22a) is proportional to the squared of the momentum. Because of its simplicity, the RFG is unsuitable for describing low-energy regions with significant nuclear effects.

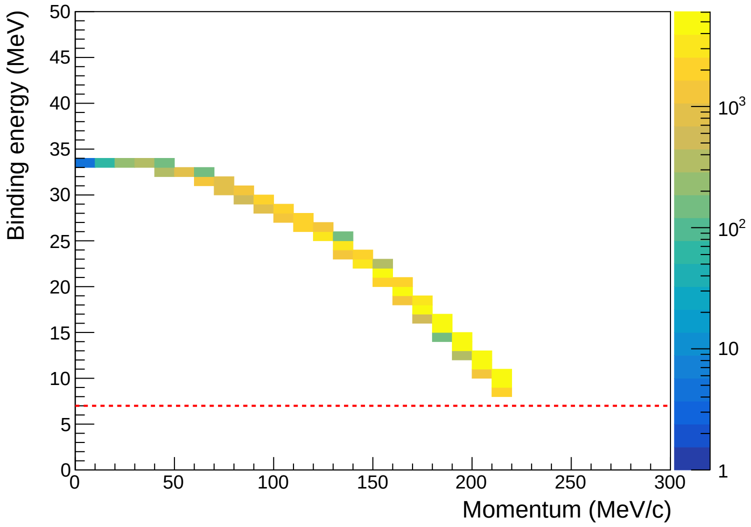

Figure 2.18: Two-dimensional probability distribution of nucleons in carbon based on the RFG model. The red dashed line represents the separation energy of 7 MeV, giving the minimum binding energy. There is a one-to-one correspondence between these parameters. The data is obtained using the NuWro Monte Carlo generator [27].

Local Fermi Gas (LFG) Model

The local Fermi gas (LFG) model is a modified relativistic Fermi gas model that considers nuclear density. Using the nuclear density $\rho(r)$ measured by electron scattering experiments, the Fermi momentum p_F in the LFG is given as

$$p_F = \hbar \left[3\pi^2 \rho(r) \frac{Z}{A} \right]^{1/3}. \tag{2.59}$$

The Pauli blocking effect is considered as well as the RFG. Fig. 2.19 shows the two-dimensional probability distribution of nucleons in carbon based on the LFG. Since the Fermi momentum depends on the radius, there is no one-to-one correspondence. The momentum distribution shown in Fig. 2.22a is similar to the spectral function (SF). The LFG has better reproducibility in the low-energy region than the RFG and has been widely used in various Monte Carlo event generators these days.

Spectral Function (SF)

The spectral function (SF) based on the shell model gives a more accurate description of the nuclear structure. The SF provides a two-dimensional probability density function of nucleons as a function of binding energy and momentum, $P(p, E_B)$. The SF is generally formulated by using electron scattering data. The SF provided by Benhar *et al.* [59], commonly used in various neutrino Monte Carlo event generators, is introduced here. The SF comprises a mean-field part P_{MF} and a correlation part P_{corr}.

$$P(p, E_B) = P_{MF}(p, E_B) + P_{corr}(p, E_B), \tag{2.60}$$

where p and E_B represent nucleons' momentum and binding energy, respectively. The mean-field part P_{MF} assumes that nucleons independently move in a mean-field potential

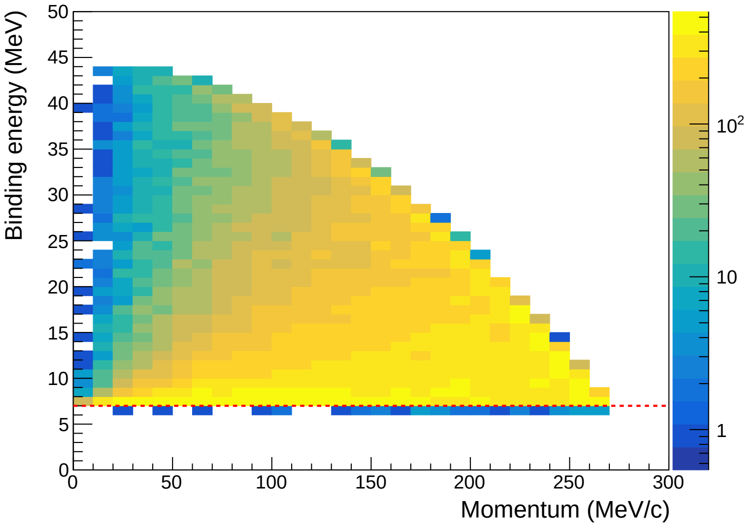

Figure 2.19: Two-dimensional probability distribution of nucleons in carbon based on the LFG model. The red dashed line represents the separation energy of 7 MeV, giving the minimum binding energy. There is no one-to-one correspondence because the Fermi momentum depends on the radius. The data is obtained using the NuWro Monte Carlo generator [27].

within the shell model picture:

$$P_{MF}(p,E) = \sum_n Z_n \left|\phi_n(p)\right|^2 F_n(E - E_n), \tag{2.61}$$

where $F_n(E - E_n)$ represents the binding energy distribution of n-th shell level with E_n as the central value, commonly parameterized by the Lorentzian (the Cauchy distribution), and Z_n represents a spectroscopic factor of n-th shell level, which normalizes the probability of the n-th shell level. Another parameter $\phi(n)$ is the momentum-space wave function normalized to 1. Under the simple shell model picture of carbon, the spectroscopic factors are as follows: $Z_{s_{1/2}} = 1/3$ and $Z_{p_{3/2}} = 2/3$ reflecting the number of nucleons in each shell level.

The correlation part $P_{corr}(p, E_B)$ describes the short-range nucleon-nucleon correlations. The formalism of this part is based on the local nuclear density approximation:

$$P_{corr}(p,E) = \int dr \rho_A(r) P^{NM}_{corr}(p,E;\rho = \rho_A(r)), \tag{2.62}$$

where $\rho_A(r)$ is the nuclear density distribution and $P^{NM}_{corr}(p,E;\rho)$ represents the correlation component of uniform nuclear matter at density ρ. The short-range correlation gives large relative momentum with small center-of-mass momentum. This feature makes the nucleons more deeply bound in the nucleus with larger momentum than those in the mean-field.

Fig. 2.20 shows the raw probability density function of the SF provided by Benhar *et al.* and Fig 2.21 shows the output of NuWro. They show a similar trend: Two clusters in the mean-field part correspond to the $s_{1/2}$ and $p_{3/2}$ shell levels and a high-momentum tail due to the correlations. The respective contributions of the $s_{1/2}$ and $p_{3/2}$ shell levels are evident in the binding energy distribution shown in Fig. 2.22b. The sharp peak around 20 MeV corresponds to $p_{3/2}$, and the broad peak around 40 MeV corresponds to $s_{1/2}$.

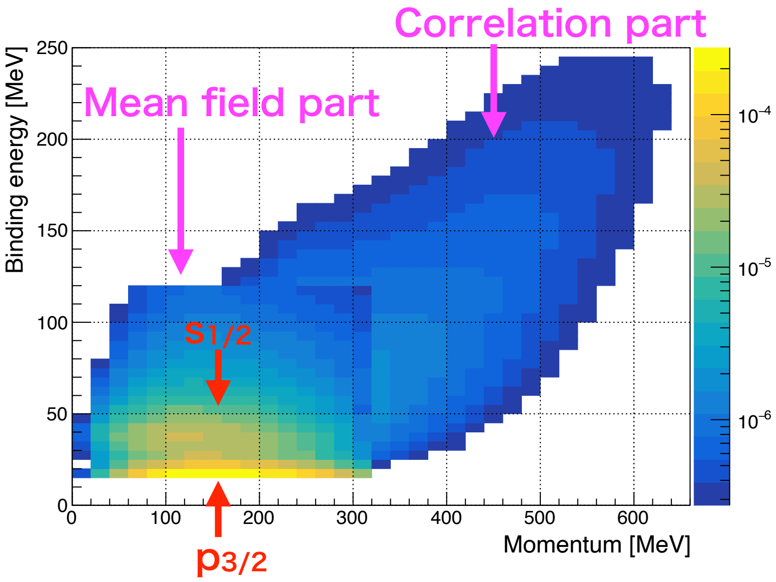

Figure 2.20: Spectral function of carbon provided by Benhar *et al.* [59]. It consists of the mean-field part and the correlation part. Two clusters in the mean-field part correspond to $s_{1/2}$ and $p_{3/2}$ shell levels. The correlation part gives rise to a high-momentum tail.

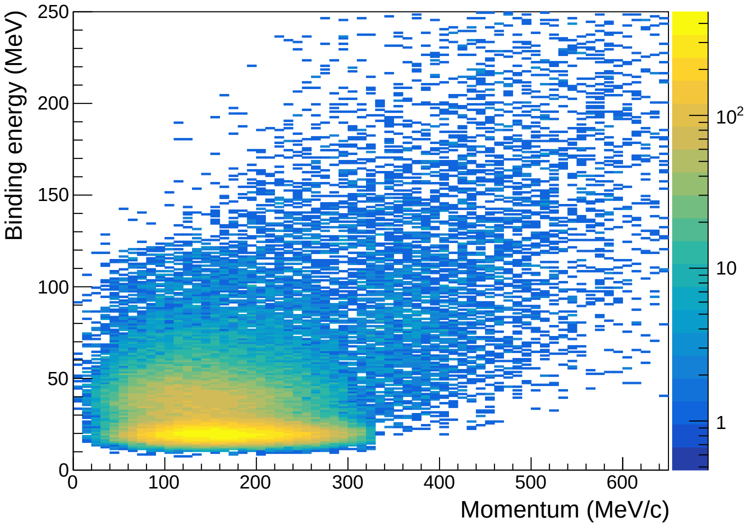

Figure 2.21: Two-dimensional probability distribution of nucleons in carbon based on the SF. One can see a distribution similar to the raw SF shown in Fig. 2.20. The data is obtained using the NuWro Monte Carlo generator [27].

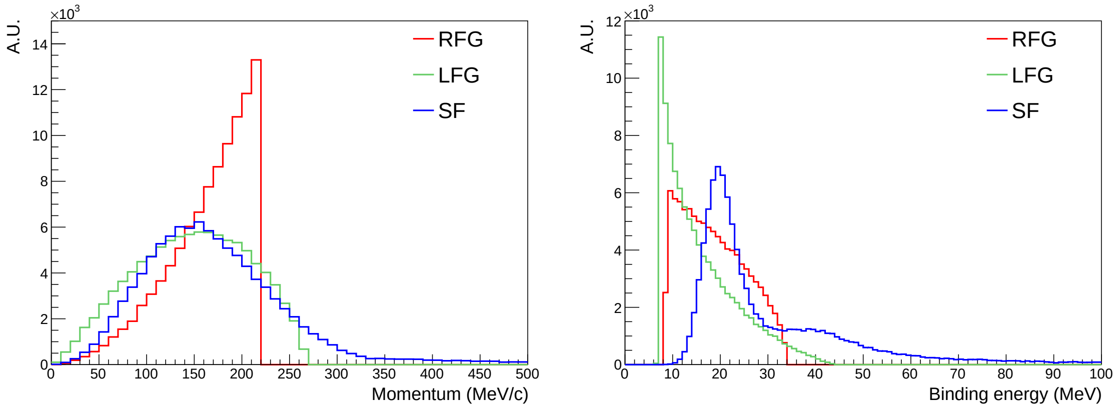

(a) Momentum

(b) Binding energy

Figure 2.22: Momentum and binding energy distributions of ^{12}C. The red, green, and blue lines show the ones of RFG, LFG, and SF, respectively. In the binding energy distribution of the SF, there are two peaks corresponding to the $p_{3/2}$ and $s_{1/2}$ shell levels. It is known that the SF tends to predict the small cross section since the nucleon is more deeply bound in the nucleus. The minimum binding energy corresponding to the separation energy is set to be 7 MeV. The figures are obtained using the NuWro Monte Carlo generator [27].

Although the SF is the model that faithfully describes the nuclear structure, it is not sufficient to simply use it. Neutrino interactions have long been measured and parameterized using the RFG and LFG. Additional corrections for nuclear effects such as RPA have often been modeled based on these Fermi gas models. On the other hand, the SF contains various assumptions about nuclear effects to obtain it, and simply using the SF can be inconsistent in the model overall (e.g., putting nuclear effects on top of each other). Therefore, it is difficult to claim that the SF is good and correct. Nevertheless, further development of the SF is desirable to consider nuclear structure more accurately, including the shell model.

2.2.2 Random Phase Approximation (RPA)

Since the IA neglects the long-range nucleon-nucleon correlation, it is not a good approximation for low-momentum transfer. The Random Phase Approximation (RPA) gives a correction for the correlation formulated considering various Feynman diagrams. It suppresses the cross section in the small energy (momentum) transfer region, as shown in Fig. 2.23. There are several parameterizations of RPA, and the degrees of suppression have large variations because the Feynman diagrams and the correction factors considered vary from model to model [51, 52, 60, 61].

2.3 Final State Interactions (FSI)

The Final State Interactions (FSI) describe the re-scatterings of particles that have gained momentum in the nucleus after the primary interaction. Fig. 2.24 shows the schematic view of the final state interactions. There are several interaction channels: elastic, inelastic, particle production, absorption, and charge exchange. We usually describe the FSI with the cascade model. Particles propagating in the nucleus are moved a little to determine

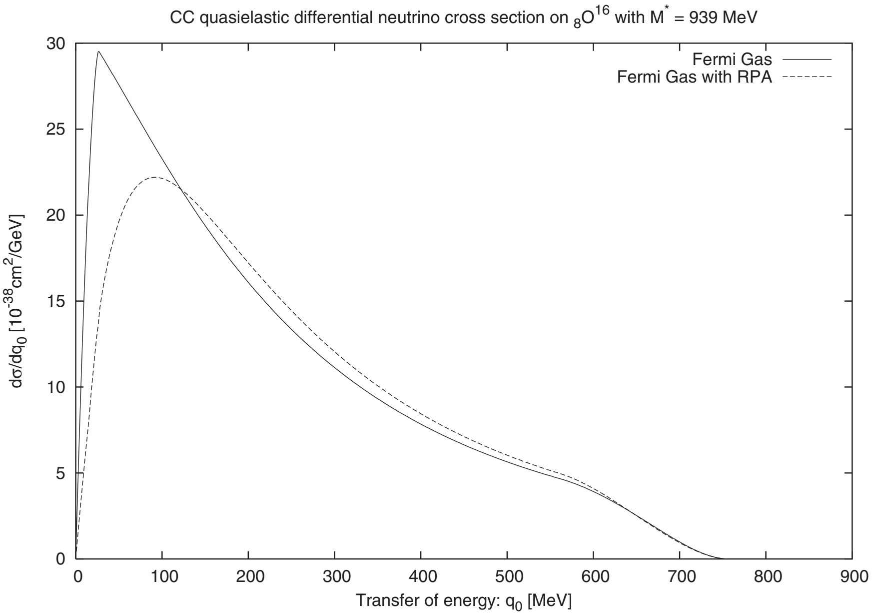

Figure 2.23: Comparison of with and without RPA for differential CCQE cross section on ^{16}O. The solid line is the one without RPA, and the dashed line is the one with RPA. The cross section is highly suppressed in the small transfer energy region. The figure is from [61].

whether they scatter at each step or not. The cascade model repeats this calculation until all particles leave the nucleus. There is a simple model except for the cascade model. In this simple model, once the particle has reacted, it does not handle subsequent re-scatterings. In other words, it does not deal with the movement of a series of particles, namely the cascade. Most neutrino Monte Carlo event generators in use today adopt the cascade model, which provides a more accurate description of the re-scattering.

The cascade FSI model has primarily three parameters to describe the FSI: Step length, cross section, and nuclear density. The nuclear density ρ and cross section σ determine the mean free path λ.

$$\lambda = (\rho\sigma)^{-1}, \tag{2.63}$$

where the cross section data is generally prepared for each particle (proton, neutron, and pion) and interaction channel. The probability of particle propagating over the step length Δx without re-scattering can be written as

$$P(\Delta x) = \exp(-\Delta x/\lambda). \tag{2.64}$$

The step length depends on the neutrino Monte Carlo simulator, but it is about $\Delta x = 0.05 - 0.2$ fm, small enough compared to the size of nuclei. The value of the step length gives no visible impact on the prediction [62]. On the other hand, the cross section and nuclear density, which are based on electron or pion scattering experiments, have large uncertainty and significant impact on the prediction.

The FSI model has been developed by each neutrino Monte Carlo generator, leading to differences in parameters such as the step length, cross section, nuclear density, and corrections for nucleon correlations. As a result, large differences appear in the prediction

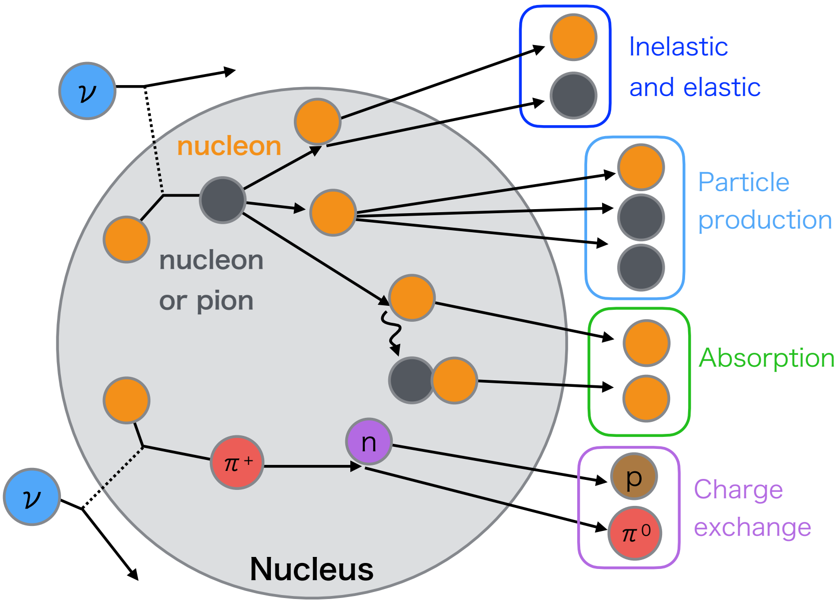

Figure 2.24: Schematic view of final state interaction. Several interaction channels are considered: elastic, inelastic, particle production, absorption, and charge exchange. The absorption is considered only for the pions.

by the FSI models, becoming one of the most uncertain parts of describing neutrino-nucleon interactions. Therefore, further improvement in the accuracy is desired. More details are discussed in Sec. 4.2.

Chapter 3

Strangeness Axial Coupling Constant

This dissertation aims to measure the strangeness axial coupling constant g_A^s, which is an isoscalar component of the axial form factors for the NCQE interaction (Eq. 2.29). The CCQE interaction only involves isovector weak currents, while the NCQE interaction is sensitive to isoscalar weak currents. Therefore, the strange form factors do not appear in the formalism of the CCQE. As can be seen from Eq. 2.28, the extraction of g_A^s generally depends on both g_A and M_A. Since β decay experiments precisely determine g_A, the uncertainty in M_A is the significant issue. Another issue to determine g_A^s is the strange vector form factors (Eq. 2.25 and 2.26). As well as the non-strange form factors, the electron scattering experiments are more accurate for the strange vector form factors than the NCQE measurements. We need to polarize the electrons to measure the parity-violating helicity-asymmetry to see the strangeness contribution.

The strangeness axial coupling constant g_A^s corresponds to the strange quark-antiquark contribution to the nucleon spin, commonly represented by Δs [1]. This parameter has been measured by polarized lepton-nucleon deep-inelastic scattering (polarized l-N DIS) experiments.

The experimental measurements of g_A^s using NCQE interactions are introduced in Sec. 3.1. The measurements of the strange vector form factors from the polarized electron elastic scattering experiment are in Sec. 3.2, and the polarized l-N DIS experiments with a brief theoretical background are in Sec. 3.3.

3.1 Measurements of g_A^s using NCQE interactions

The BNL E734 (Sec. 3.1.1) and MiniBooNE (Sec. 3.1.2) reported the measurements of g_A^s using NCQE interactions.

---

[1] Assuming the naive parton model, the two parameters g_A^s and Δs are the same. It is commonly denoted by g_A^s (Δs) when discussing the NCQE (l-N DIS) interactions. This dissertation follows these notations.

3.1.1 BNL E734 Experiment

First Measurement by Ahrens et al.

The BNL E734 experiment performed the first measurement of g_A^s using the NCQE interactions [63]. They used accelerator neutrinos and measured two NCQE interaction modes: $\nu + p \to \nu + p$ and $\bar{\nu} + p \to \bar{\nu} + p$. Fig. 3.1 shows the schematic view of the BNL E734 detector, a 170-ton high-resolution tracker. The detector mainly consists of liquid-scintillator cells and proportional drift tubes (PDT). The scintillator cells are for the calorimeter, while the PDTs are for high-track resolution. About 80% of the target mass was the liquid scintillator giving about CH_2 composition.

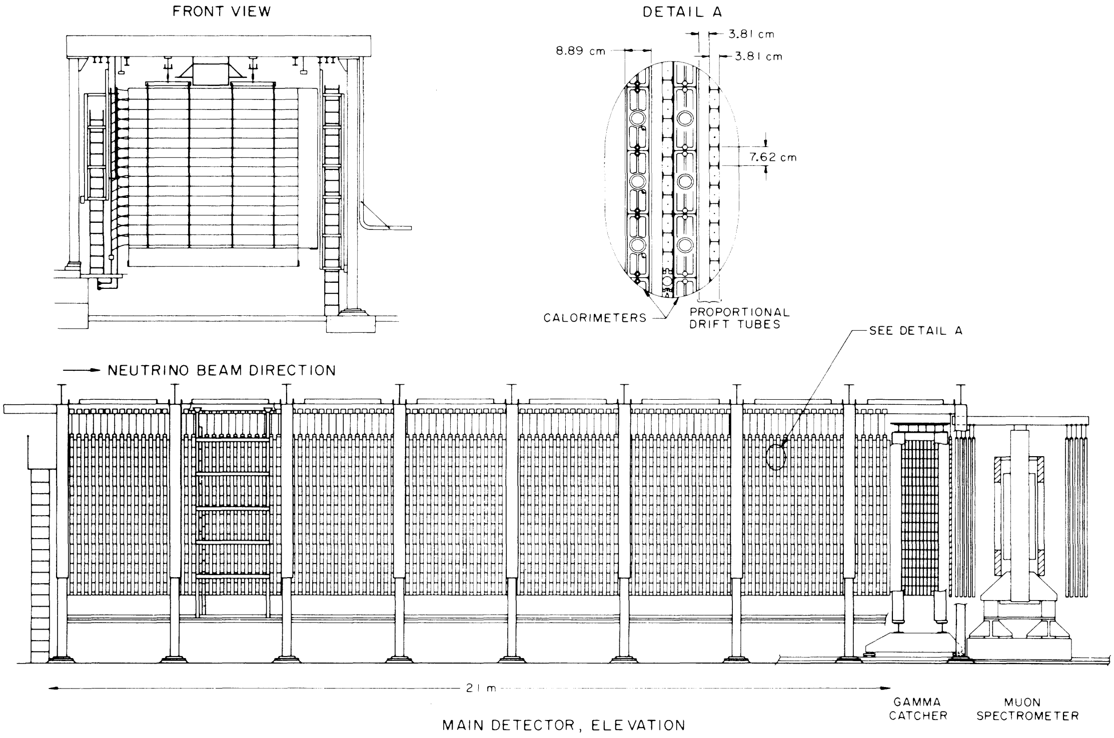

Figure 3.1: Schematic view of the BNL E734 detector. The detector mainly consists of liquid-scintillator cells and proportional drift tubes. The figure is from [63].

The accelerator neutrino at the BNL E734 is generated using 28 GeV proton beams. Electric horns focus on produced pions and kaons. They can switch between neutrino- and antineutrino-dominated modes by changing the horn current. Fig. 3.2 shows the measured and predicted fluxes. The mean neutrino energy is 1.3 GeV (1.2 GeV) for ν_μ ($\bar{\nu}_\mu$).

They measured the differential cross sections as a function of Q^2 for the two modes, as shown in Fig. 3.3. From the simultaneous fitting of the differential cross sections, they obtained

$$g_A^s = -0.12 \pm 0.07, \tag{3.1}$$

with the strong constraint of $M_A = 1.032 \pm 0.036\,\mathrm{GeV}$, the world average at the time. In this analysis, they neglected the strange vector form factors, namely assuming $F_V^{1,s}(Q^2) = F_V^{2,s}(Q^2) = 0$. Since their result had a strong positive correlation between g_A^s and M_A as shown in Fig. 3.4, the M_A constraint was essential to obtain the value of g_A^s.

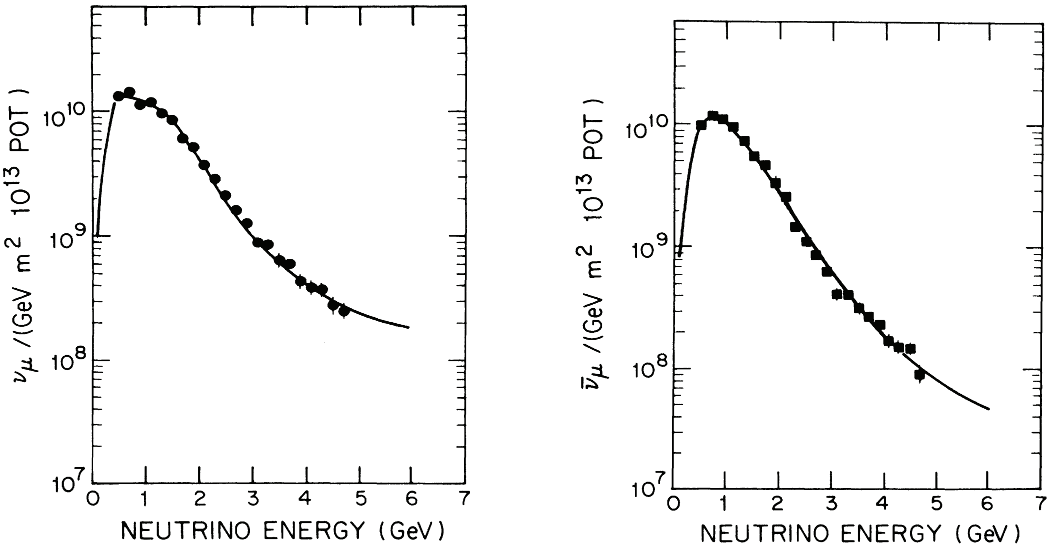

(a) ν_μ flux

(b) $\bar{\nu}_\mu$ flux

Figure 3.2: ν_μ (left) and $\bar{\nu}_\mu$ (right) fluxes at the BNL E734. The dots represent the measured flux, and the solid curves show Monte Carlo predictions. The mean neutrino energy is 1.3 GeV (1.2 GeV) for ν_μ ($\bar{\nu}_\mu$). The figure is from [63].

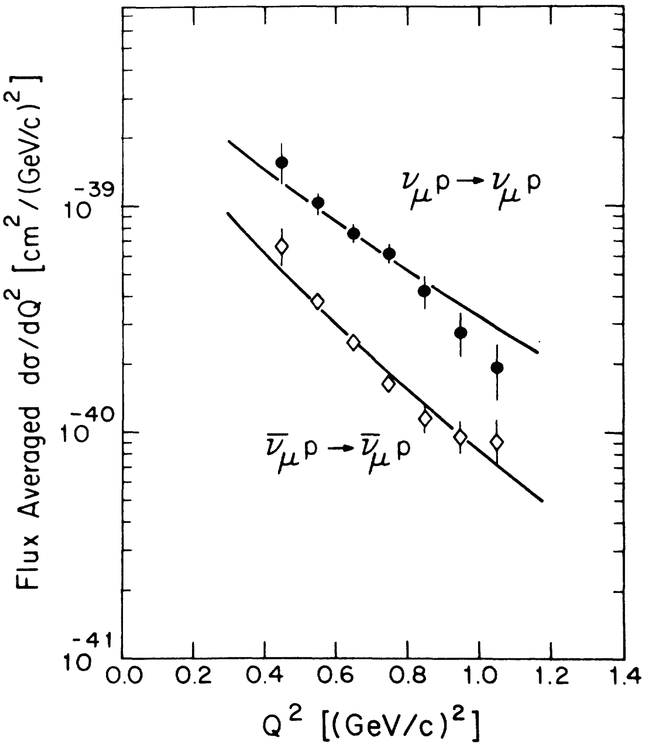

Figure 3.3: Flux-averaged differential cross sections for $\nu_\mu p \to \nu_\mu p$ and $\bar{\nu}_\mu p \to \bar{\nu}_\mu p$. From the simultaneous fitting of the differential cross sections, they obtained $g_A^s = -0.12 \pm 0.07$ with the strong constraint of $M_A = 1.032 \pm 0.036\,\text{GeV}$. The figure is from [63].

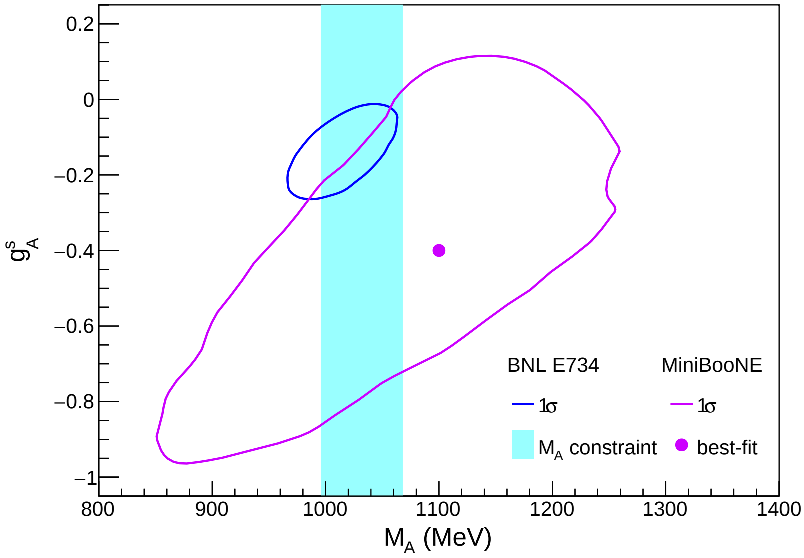

Figure 3.4: Two-dimensional allowed regions for the M_A and g_A^s obtained by the BNL E734 and MiniBooNE experiments. The BNL E734's result (the blue line) was obtained with the strong constraint of M_A (the shaded cyan region) [63]. The MiniBooNE's result (the violet line) was obtained without a M_A constraint [64]. Both results have strong correlations between these parameters.

Re-analysis by Garvey et al.

Garvey *et al.* performed re-analysis using the differential cross sections measured by the BNL E734 [65]. They obtained the following result neglecting the strange vector form factors,

$$g_A^s = -0.15 \pm 0.07, \tag{3.2}$$

with the strong constraint of $M_A = 1.061 \pm 0.026\,\text{GeV}$, which slightly differed from that of Ahrens *et al.* The result was slightly changed from the first measurement but consistent. They also performed the fitting considering the effect of strange vector form factors (Eq. 2.25 and 2.26). They obtained the following results with the same constraint of $M_A = 1.061 \pm 0.026\,\text{GeV}$:

$$g_A^s = -0.13 \pm 0.09, \tag{3.3}$$

$$F_V^{1,s} = 0.49 \pm 0.70, \tag{3.4}$$

$$F_V^{2,s}(0) = -0.39 \pm 0.70. \tag{3.5}$$

The strange vector form factors are consistent with zero, and the effect on g_A^s is small.

Discussion

There are two concerns in the interpretation of the results of the BNL E734. The first point is the strong constraint of M_A. The values of M_A appeared to be consistent with $M_A \sim 1.0\,\text{GeV}$ at that time. However, as discussed in Sec. 2.1.1, now we know that there is a discrepancy between the world average and the recent carbon- and oxygen-target experiments. The situation makes it difficult to determine a reasonable constraint on M_A. The second point is the 2p2h contribution. The 2p2h interaction is a channel that has only recently begun to be discussed and was usually not considered at the time, including these analyses of the BNL E734 experiment. Although the detector achieved good track resolution, the NC 2p2h contamination into the NCQE candidates is expected to be inevitable. Therefore, we require recent experiments to measure g_A^s without M_A constraints considering the 2p2h contribution and verify the BNL's result.

3.1.2 MiniBooNE Experiment

Analysis by the MiniBooNE Collaboration

The MiniBooNE Collaboration measured the flux-averaged NCQE differential cross section [66]. They did not perform a simultaneous fit of M_A and g_A^s and did not include the 2p2h contribution in this analysis. They measured g_A^s assuming two values of M_A,

$$g_A^s = \begin{cases} 0.08 \pm 0.26 & (M_A = 1.35\,\mathrm{GeV}) \\ 0.00 \pm 0.30 & (M_A = 1.23\,\mathrm{GeV}). \end{cases} \tag{3.6}$$

The value of $M_A = 1.35\,\mathrm{GeV}$ is obtained from their CCQE analysis [32]. These results are consistent with the results reported from the BNL E734.

Analysis by Golan et al. using NuWro

Using the data provided by the MiniBooNE Collaboration, an independent simultaneous-fit using the NuWro Monte Carlo event generator [27] was performed by Golan *et al.* [64]. They took into account the 2p2h contribution using the TEM while neglecting the effect of the strange vector form factors: i.e., $F_V^{1,s}(Q^2) = F_V^{2,s}(Q^2) = 0$. This analysis obtained the following results by fixing the 2p2h contribution.

$$M_A = 1.10^{+0.13}_{-0.15}\,\mathrm{GeV}, \tag{3.7}$$

$$g_A^s = -0.4^{+0.5}_{-0.3}. \tag{3.8}$$

Two-dimensional allowed region for M_A and g_A^s is shown in Fig 3.4, confirming a positive correlation between these parameters. The result of g_A^s is consistent with all results mentioned above. The MiniBooNE's data will give a larger error than the BNL's result even if they apply a strong constraint on M_A.

3.2 Polarized Electron Elastic Scattering Experiments

Polarized electron elastic scattering experiments are sensitive to the strange vector form factors. One measures a parity-violating helicity-asymmetry in the scattering by changing the polarization direction. We can extract the strangeness contributions by combining the asymmetries with the non-strange vector form factors. There are various experiments, such as SAMPLE [67], G0 [68], HAPPEX [69], and PVA4 [70]. These experiments use hydrogen-, deuteron-, and ^{4}He-target as summarized in [71]. These studies commonly adopt parameterizations for the strange vector and axial form factors as follows:

$$F_A^s(Q^2) \equiv G_A^s(Q^2) \tag{3.9}$$

$$F_V^{1,s}(Q^2) = \left(1 + \frac{Q^2}{4M^2}\right)^{-1} \left[G_E^s(Q^2) + \frac{Q^2}{4M^2} G_M^s(Q^2)\right], \tag{3.10}$$

$$F_V^{2,s}(Q^2) = \left(1 + \frac{Q^2}{4M^2}\right)^{-1} \left[G_M^s(Q^2) - G_E^s(Q^2)\right] \tag{3.11}$$

The same parameterizations as Eq. 2.10 and 2.11 are assumed here. The G_E^s (G_M^s) represents the strange electric (magnetic) form factor.

3.2.1 Global analysis with the BNL E734

Pate *et al.* performed a global analysis of these polarized electron elastic scattering experiments with the results of the BNL E734 in [35, 72]. Fig. 3.5 shows the experimental data used in the global analysis. All data of the strange magnetic and electric form factors are consistent with zero, but the strange axial form factor prefers a negative value. They performed a global fit with these functions.

$$G_A^s(Q^2) = \frac{\Delta S + S_A Q^2}{\left(1 + Q^2/\Lambda_A^2\right)^2} \tag{3.12}$$

$$G_M^s(Q^2) = \mu_s \tag{3.13}$$

$$G_E^s(Q^2) = \rho_s \frac{Q^2}{4M^2} \tag{3.14}$$

Since the proper parameterization of Q^2 dependence is unknown, they introduced a robust function for G_A^s. Conversely, they introduced simple functions for G_M^s and G_E^s since the data are featureless. Tab. 3.1 shows the best-fit and 1σ uncertainties of the global fit. The best-fit and 70% confidence level results are also shown as the black curves in Fig. 3.5. There are strong constraints on $G_{E,M}^s$, which are consistent with zero. On the other hand, a large uncertainty remained in G_A^s due to the robust Q^2 dependence and experimental uncertainties. Additional measurements of the NCQE interactions in the low Q^2 region of $Q^2 < 0.5\,\mathrm{GeV}^2$ are expected to reduce the uncertainty effectively. The MicroBooNE experiment [73], a 170-ton liquid-argon time projection chamber detector, aims to measure g_A^s in this Q^2 region [2]. Since the nuclear effects become relatively large in the low Q^2 region, the accuracy of the nuclear models will be important.

3.3 Polarized Lepton-Nucleon Deep-Inelastic Scattering Experiments

The strangeness axial coupling constant g_A^s corresponds to the strange quark-antiquark contribution to the nucleon spin, commonly represented by Δs. The experiments of the polarized lepton-nucleon deep-inelastic scattering (polarized l-N DIS) have measured the Δs. The theoretical formalism and experimental measurements are introduced in this section.

---

[2] In a Ph. D dissertation by Katherine Woodruff, they obtained $-1.8 < g_A^s < 3.8$ with 95% confidence level and $-1.0 < g_A^s < 2.6$ with 68% confidence level [74]. The results are not published yet.

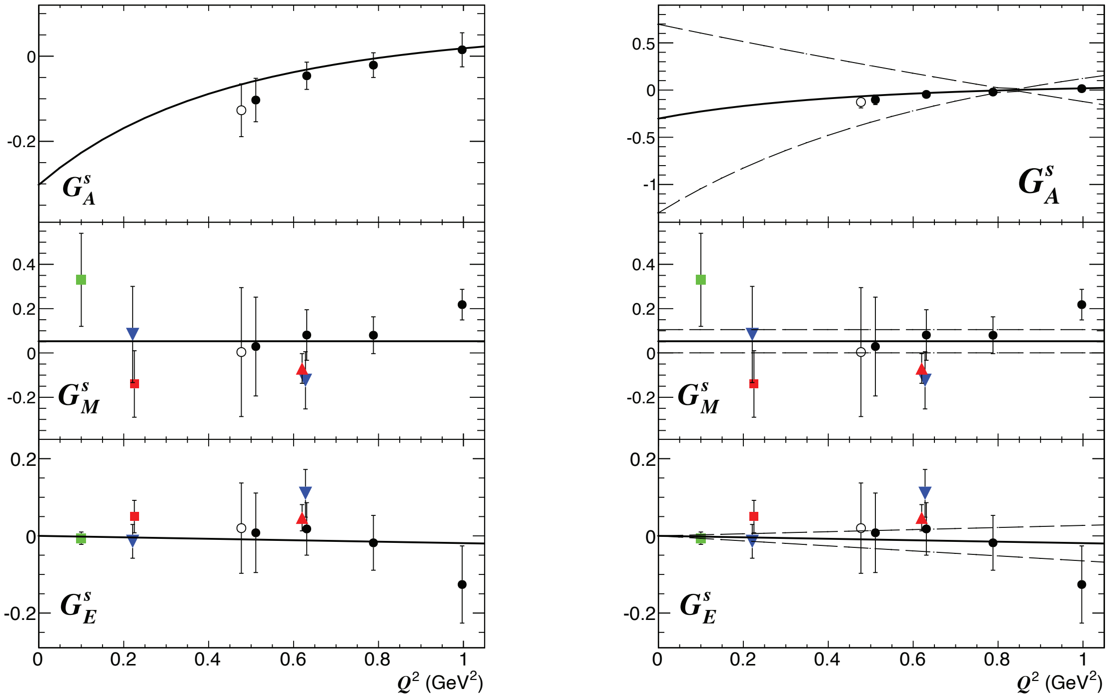

Figure 3.5: Measurements of the strange form factors G^s_A, G^s_M, and G^s_E as a function of Q^2. The green squares are from another global analysis by Liu *et al.* [71]. The blue inverted triangles represent the results of the G0 [68], the red triangles show the results of the HAPPEX [69], and the red squares denote the results of the PVA4 [70]. The black open (closed) circles represent a combined analysis using BNL E734 and HAPPEX (G0) [35]. The dashed curves shown in the right panel are the 70% confidence level for the fit. The vertical scale of the top right panel for G^s_A was adjusted to see all confidence levels. While strange magnetic (G^s_M) and electric (G^s_E) form factors are consistent with zero, the strange axial form factor (G^s_A) prefers a negative value. The figure is from [72].

Table 3.1: The best-fit and 1σ uncertainties of the global fit analysis using the BNL E734, HAPPEX, SAMPLE, G0, and PVA4 [72].

Parameter	Value
ρ_s	-0.071 ± 0.096
μ_s	0.053 ± 0.029
ΔS	-0.30 ± 0.42
Λ_A	1.1 ± 1.1
S_A	0.36 ± 0.50

3.3.1 Quark Contributions to the Nucleon Spin and the First Moment

The cross section of the polarized l-N DIS is characterized by the spin structure function $g_1^N(x, Q^2)$ [75,76]. Here, $x = Q^2/2pq$ and $Q^2 = -q^2$, where p is the momentum of the initial nucleon, q is the four-momentum transfer, and N represents the target (p, n, and d). The measurements of the asymmetry in the polarized l-N DIS make it possible to determine the spin structure function $g_1^N(x, Q^2)$.

From the theoretical point of view, the important quantity is the first moment $\Gamma_1^N(Q^2)$ of the spin structure function:

$$\Gamma_1^N(Q^2) = \int_0^1 g_1^N(x, Q^2)dx \quad (N = p, n, d) \tag{3.15}$$

In the region $Q^2 \lesssim 10\,\mathrm{GeV}^2$, the main contribution to the first moment comes from the light quarks: u, d, and s. In the naive parton model, assuming the isospin symmetry of proton and neutron, the first moment can be expressed as

$$\Gamma_1^p = \frac{1}{2}\left(\frac{4}{9}\Delta u + \frac{1}{9}\Delta d + \frac{1}{9}\Delta s\right), \tag{3.16}$$

$$\Gamma_1^n = \frac{1}{2}\left(\frac{1}{9}\Delta u + \frac{4}{9}\Delta d + \frac{1}{9}\Delta s\right), \tag{3.17}$$

$$\Gamma_1^d = \frac{1}{4}\left(\frac{5}{9}\Delta d + \frac{5}{9}\Delta u + \frac{2}{9}\Delta s\right), \tag{3.18}$$

where

$$\Delta q = \int_0^1 [q_{\rightarrow}(x) - q_{\leftarrow}(x)]\,dx \quad (q = u, d, s). \tag{3.19}$$

The Q^2 dependence is omitted in these equations. $q_{\rightarrow(\leftarrow)}(x)$ represents the q-quark and q-antiquark distribution that are parallel (opposite) to the nucleon spin. Therefore, the Δq denotes the contribution of q-quarks and q-antiquarks to the nucleon spin. The first moment of deuteron Γ_1^d is the average of the proton and neutron. The first moment can also be written regarding the hadronic matrix elements: a_3, a_8, and a_0. For example, the first moment of the proton is as follows:

$$\Gamma_1^p = \frac{1}{12}\left(a_3 + \frac{1}{3}a_8 + \frac{4}{3}a_0\right), \tag{3.20}$$

$$= \frac{1}{12}\left(a_3 + \frac{5}{3}a_8 + 4\Delta s\right), \tag{3.21}$$

$$a_0 = \Delta u + \Delta d + \Delta s, \tag{3.22}$$

$$a_3 = \Delta u - \Delta d, \tag{3.23}$$

$$a_8 = \Delta u + \Delta d - 2\Delta s, \tag{3.24}$$

The matrix element a_0 represents the total quark contributions to the nucleon spin and the matrix element a_3 corresponds to the axial coupling constant, which is known to high precision from β decay as already introduced in Sec. 2.1.1:

$$a_3 = g_A = 1.2723 \pm 0.0023. \tag{3.25}$$

The matrix element a_8 can be obtained from hyperon β decay under the assumption of the $SU(3)_f$ flavor symmetry. The fit of the experimental data [77] gives

$$a_8 = 3F - D = 0.585 \pm 0.025. \tag{3.26}$$

From Eq. 3.21, 3.25, and 3.26, we can obtain the value of Δs. An important aspect of this Δs calculation is the necessity to assume the $SU(3)_f$ flavor symmetry. The symmetry is known to be violated by a maximum of 20%, affecting the value of Δs. Details are discussed in Sec. 3.3.3.

For example, Fig. 3.6a shows the spin structure functions multiplied by x measured by the HERMES experiment [78]. Although we can calculate the first moment by integrating the measured functions as in Eq. 3.15, there is a limit to the region of x that the experiments can measure practically. Fig. 3.6b shows the integral values of the functions of proton, neutron, and deuteron from x to 0.9. For $x \lesssim 0.05$, the variation of the integral value is relatively small. The integrals in the region from 0.9 to 1 are also considered to obtain the final result.

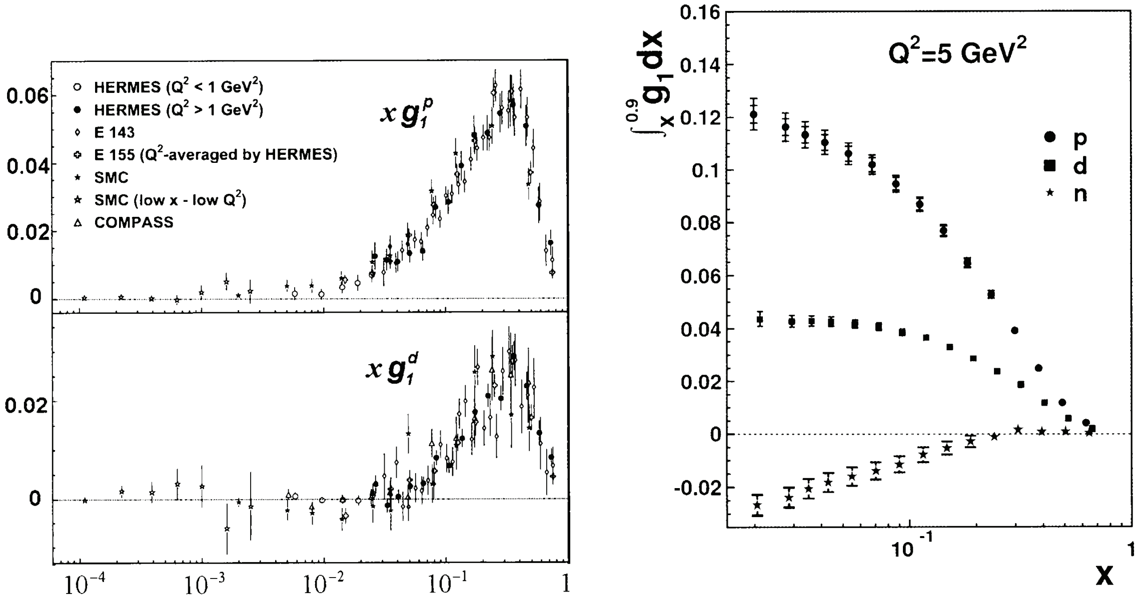

(a) The spin structure functions multiplied by x as a function of x. The upper panel shows one of a proton, while the lower panel shows one of a deuteron.

(b) The integral values of the spin structure function from x to 0.9. The HERMES provided the data for proton, neutron, and deuteron. The results at the smallest x approximately correspond to the first moments.

Figure 3.6: The spin structure functions and their integral values reported from the HERMES experiment. The figures are from [79], slightly modified the original figures from the HERMES experiment [78].

3.3.2 Experimental Results of Δs

The EMC experiment measured the first moment of proton at $Q^2 = 10.7\,\mathrm{GeV}^2$ [75, 80]:

$$\Gamma_1^p(10.7\,\mathrm{GeV}^2) = 0.126 \pm 0.010(\mathrm{stat.}) \pm 0.015(\mathrm{syst.}), \tag{3.27}$$

leading to the negative value of Δs:

$$\Delta s = -0.18 \pm 0.05. \tag{3.28}$$

For others, the HERMES [78] and COMPASS [81] reported the following resutls:

$$\Delta s = -0.085 \pm 0.018 \quad (\text{HERMES}, Q^2 = 5\,\text{GeV}^2), \tag{3.29}$$

$$\Delta s = -0.08 \pm 0.02 \quad (\text{COMPASS}, Q^2 = 3\,\text{GeV}^2). \tag{3.30}$$

These consistent results prefer negative values with small statistical and systematic uncertainties. A negative Δs is reasonably explained by the current experimental measurements of the hadronic matrix elements [82]. Compared to the g_A^s measurements by the NCQE interactions introduced in Sec. 3.1.1 and 3.1.2, the results from these polarized l-N DIS experiments have smaller uncertainties.

3.3.3 Impact of the $SU(3)_f$ Flavor Symmetry Violation on the Δs

In calculating Δs from the first momentum, we assumed the $SU(3)_f$ flavor symmetry obtaining the value of a_8. While the isospin symmetry is not in doubt, there are some questions in assuming the $SU(3)_f$ flavor symmetry. The symmetry is broken by a maximum of 20% [82], in which case the results of Δs are shifted by ±0.04 [81]. This uncertainty is approximately equal to or larger than the statistical and systematic errors of the experiments. It is clearly of interest to measure $g_A^s(\Delta s)$ in a way independent of $SU(3)_f$ flavor symmetry, i.e., by measuring the NCQE interactions.

3.4 Significance of This Study

The characteristics and significance of this study are summarized in this section. Fig. 3.7 shows a summary of $g_A^s(\Delta s)$ measurements. The measurements of g_A^s (Δs) using the NCQE interactions are very interesting as an independent method from the $SU(3)_f$ flavor symmetry, although the current uncertainties are larger than those of the polarized l-N DIS scattering experiments.

One challenge in measuring g_A^s using the NCQE interaction is the strong correlation with M_A as introduced in Fig. 3.4. In the BNL E734 and MiniBooNE experiments, proton target NCQE is primarily used as a signal because of the difficulty of measuring neutron target NCQE. Since the g_A^s changes the relative fraction of proton and neutron targets in the NCQE cross section on ^{12}C, the measurement of only the proton target (or neutron target) highly depends on the normalization factors such as M_A. Conversely, when measuring the ratio of interactions on the proton target and the neutron target, normalization cancels out, and we can measure g_A^s with a slight dependence on M_A. In practice, nucleons measured by detectors are affected by the FSI, secondary interaction, and nuclear de-excitation. The nucleons measured by detectors are affected by these processes, so it is impossible to strictly identify the target nucleons on an event-by-event basis. However, by measuring nucleon multiplicity, it is possible to statistically separate the contribution of target nucleons using the distribution within the uncertainty of these nuclear effects. This method requires high nucleon detection efficiency. KamLAND is suitable for measuring the NCQE interactions as it can detect nucleon recoils with low energy thresholds and can measure neutron multiplicity (see Sec. 9.2). KamLAND atmospheric neutrino data, including information on neutron multiplicity associated with the NCQE interaction, makes

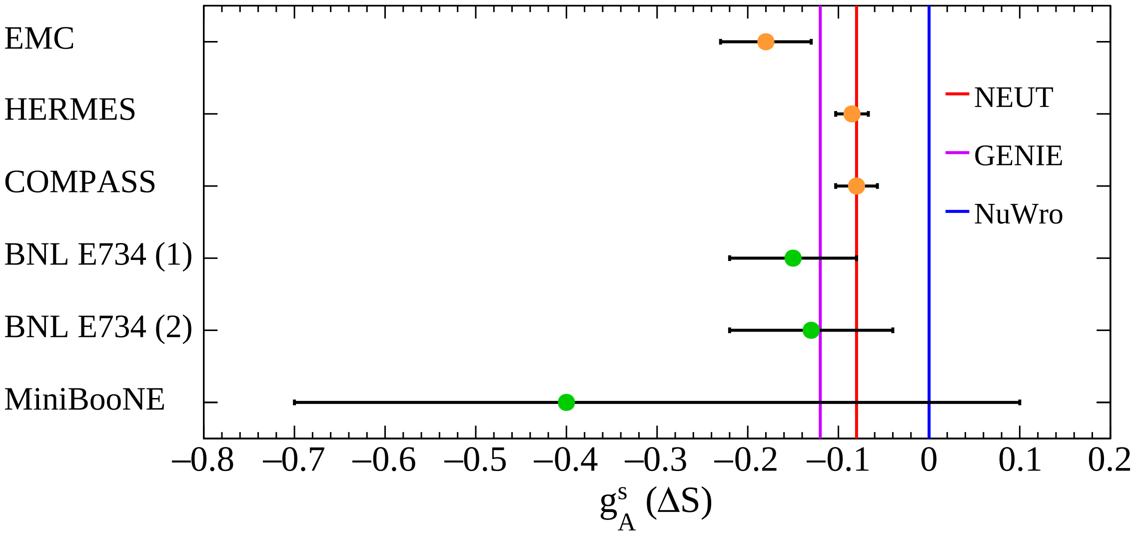

Figure 3.7: Summary of g_A^s (Δs) measurements. The results from the EMC [75, 80], HERMES [78], COMPASS [81], BNL E734 [65], and MiniBooNE [64] are also shown. The orange symbols are the results of polarized lepton deep-inelastic scattering experiments, and the green symbols are that of NCQE scattering experiments. Two results of the BNL E734 are shown, wherein (1) the strange vector form factors are assumed to be zero ($F_V^{1,s}(Q^2) = F_V^{2,s}(Q^2) = 0$), and in (2), they are also treated as fit parameters. The red, violet, and blue vertical lines represent the values adopted in neutrino Monte Carlo generators in default.

it possible to measure g_A^s with a suppressed dependence on M_A. Our result is the first measurement of g_A^s by using the neutron multiplicity and gives the most accurate value without M_A constraints (see Sec. 11.4).

The Q^2 dependence of the strange axial form factor is not certain, but the NCQE measurements usually assume the dipole form (Eq. 2.29) and use exactly the same value of the axial mass M_A as that of non-strange axial form factors. This study is based on the same assumptions. Since the polarized electron elastic scattering experiments show zero consistent strange vector form factors, we assume that these are exactly zero in this analysis. We consider the 2p2h interaction assuming the TEM. Since the TEM is the only model that can describe the NC 2p2h, there is no other choice currently. Note that these analysis conditions about the strange vector form factors and 2p2h (TEM) are the same as those of the MiniBooNE's analysis.

Chapter 4

Neutrino Monte Carlo Event Generators

Neutrino Monte Carlo (MC) event generators simulate neutrino interactions implementing the theoretical models. Since the detector response of neutrino interactions is commonly estimated by using the generators, their prediction accuracy directly affects the sensitivity of observations. Several MC generators have been developed: NuWro [83], NEUT [36], GENIE [38], NUANCE [84], and GiBUU [85]. Their overall rough scheme to describe the interaction is the same. They are composed of three parts: primary interaction, nuclear effect, and FSI. However, since different groups have developed them, they adopted different models and parameters, and the output results sometimes differ significantly. We cannot claim the appropriate generator for all experiments since they have strengths and weaknesses in the energy region and nuclear models. This chapter discusses features and the comparisons of generators focusing on NuWro, NEUT, and GENIE, which are particularly common.

4.1 Model Configurations

NuWro (Sec. 4.1.1), NEUT (Sec. 4.1.2), and GENIE (Sec. 4.1.3) are especially famous generators. These generators cover a wide neutrino energy range from several tens of MeV to several hundreds of TeV. In addition, various target nuclei, such as carbon, oxygen, argon, and iron, are available.

Model parameters, such as M_A and g_A^s, need to be easily changed for analysis. We generally perform such analysis using a package called reweight. NuWro and GENIE provide tools with the reweight package, but NEUT does not. GENIE has reported bugs in the recent version and some puzzling behavior of nuclear effects. Based on these situations, we decided to use NuWro as the main generator in this study.

4.1.1 NuWro

NuWro [83] is developed by a group of theorists at Wroclaw University. It is an open source based on C^{++} and shared in [86]. In addition, they provided the so-called reweight package for changing the model parameters and estimating systematic uncertainties. It is rarely used as the main generator in the analysis of experiments while very frequently used as a sub-generator for validation and comparison. One of NuWro's unique features is providing various nuclear models such as RFG, LFG, and SF. We can easily switch these models. This feature makes it easy to evaluate various nuclear models. We use version 21.09, released in September 2021, as the main generator in this dissertation.

Tab. 4.1 shows the model configurations of NuWro. The default settings are adopted except for the 2p2h model. In default, NuWro adopts the Nieves model to describe the CC 2p2h. However, the TEM selected to consider the CC and NC 2p2h in this study. As for the nucleon FSI, NuWro uses a relatively new cross section model by Niewczas *et al.* [87]. This model fits the experimental nucleon-nucleon scattering data to improve the agreement with the PDG data set. As a result, it gives good agreement in the nucleon transparency with experimental data, as shown in Fig. 4.1. The probability of FSI [1] in the typical nucleon momentum from NCQE 0.5 GeV is about 0.25 ± 0.07. This error in the probability corresponds to 28% relative uncertainty. On the other hand, for the pion FSI, NuWro uses a relatively old cross section model by Scalcdo *et al.* [88]. Since the model is not tuned to experimental data, there is large uncertainty of about 50% as shown in Fig. 4.2.

Table 4.1: Model configuration in NuWro. (V)FF represents (vector) form factor. The Nieves model is adopted in default to describe the CC 2p2h.

Channel	Model	Parameter	
CCQE	Llewellyn-Smith	M_A	1.03 GeV
		VFF	BBBA05
		RPA	Graczyk *et al.* [61]
NCQE	Llewellyn-Smith	M_A	1.03 GeV
		g_A^s	0
		VFF	BBBA05
		strange VFF	Neglected
CC and NC RES	Graczyk-Sobczyk	FF	Dipole form
		M_A	0.94 GeV
		$C_5^A(0)$	1.19
		RES/DIS boundary	$W = 1.6$ GeV
CC and NC DIS	GRV98 PDF	with modification by Bodek and Yang	
CC and NC 2p2h	TEM		
CC and NC COH	Modified Rein Sehgal		
Nuclear model	LFG	Separation energy	7 MeV
FSI	NuWro cascade	Step length	0.2 fm
		Nucleon cross section	Niewczas *et al.* [87]
		Pion cross secction	Scalcedo *et al.* [88]

4.1.2 NEUT

NEUT [36] was first developed for Kamiokande experiments and has been continuously developed and used in the experiments in Japan, such as Super-Kamiokande, K2K, and T2K experiments. The primary target was oxygen, but other nuclei, such as carbon, argon, and iron, have been available for use in other detectors. The code is based on Fortran, and it is not open source. We use NEUT version 5.4.0.1, provided by Y. Hayato, the lead developer of NEUT. Since we did not receive a reweight package, we have not been

---

[1] (FSI probability) = 1 − (Transparency)

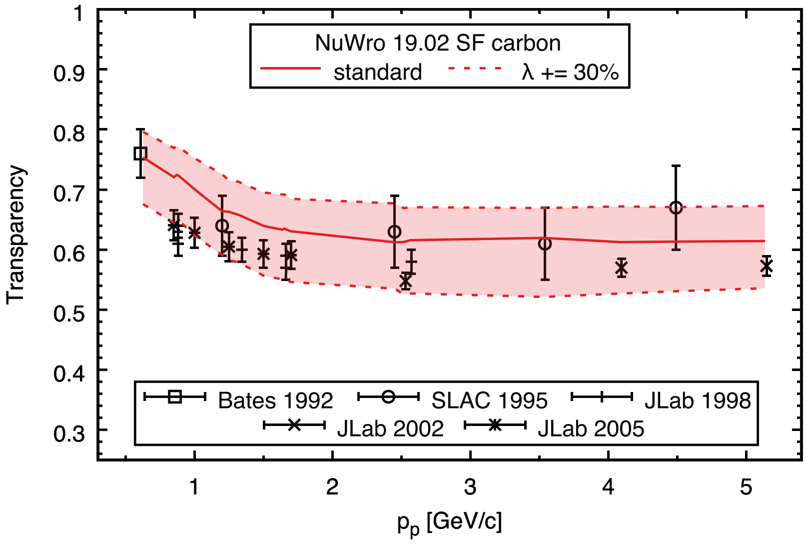

Figure 4.1: Proton transparency for carbon as a function of momentum. The dots represent experimental data, the solid line represents the result of NuWro, and the dashed lines represent 1σ uncertainty corresponding to the scale of the mean free path λ by ±30%. At the typical nucleon momentum of NCQE interactions of 0.5 GeV, the transparency is 0.75 ± 0.07. The figure is from [87].

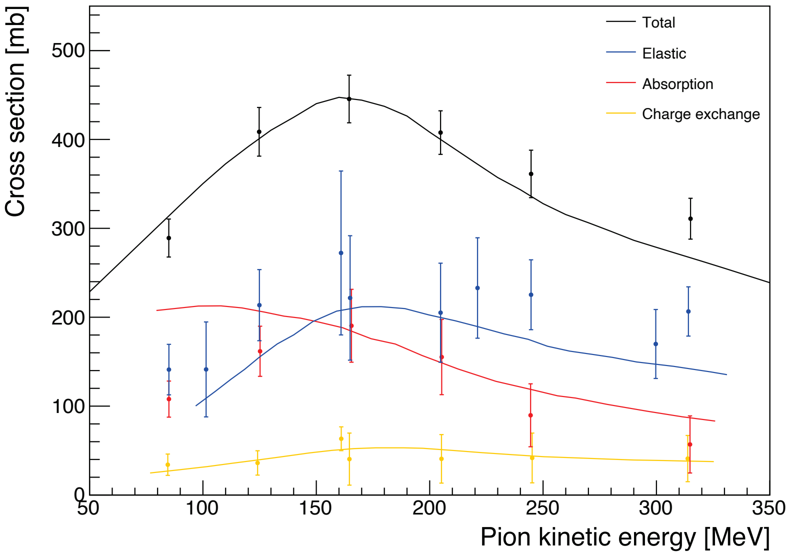

Figure 4.2: Pion-Carbon cross section in NuWro FSI model as a function of pion kinetic energy. The solid lines represent the model by Salcedo *et al.* and dots are the experimental data. The data is reproduced from [88].

able to perform any analysis, such as estimating systematic uncertainties with changing parameter values.

Tab. 4.2 shows the model configurations of NEUT. The default settings are adopted. In the formalism of the CCQE interaction, a model by Gran *et al.* is adopted. This model is suitable for use with the Nieves 2p2h model. The model by Ankowski *et al.* describes the NCQE interaction. The SF is used to calculate the cross section, but the RFG is used to describe nucleon kinematics. In the RFG model, the separation energy is set to be precisely zero. This configuration is unsuitable for experiments that measure nucleon kinematics of the NCQE interaction. Particles emitted by the de-excitation from the residual nucleus are also considered only for ^{16}O, not for other nuclei, such as carbon. For pion FSI, NEUT uses a cross section model by Pinzon *et al.* [89]. In this model, energy-dependent normalization factors were introduced for the cross section model by Scalcede *et al.* to improve the agreement with experimental data. Fig. 4.3 shows the model by Pinzon *et al.*. Compared with Salcedo *et al.*, the data provided by Pinzon *et al.* gives better agreement with experimental data.

Table 4.2: Model configuration in NEUT. (V)FF represents (vector) form factor.

Channel	Model	Parameter	
CCQE	Gran *et al.* [56]	M_A	1.21 GeV
		VFF	BBBA05
		Nuclear model	LFG
NCQE	Ankowski *et al.* [37,90]	M_A	1.21 GeV
		g_A^s	-0.08
		VFF	BBBA05
		strange VFF	Neglected
		Nuclear model	RFG
CC and NC RES	Graczyk-Sobczyk	FF	Dipole form
		M_A	0.95 GeV
		$C_5^A(0)$	1.01
		RES/DIS boundary	$W = 2.0$ GeV
CC and NC DIS	GRV98 PDF	with modification by Bodek and Yang	
CC and NC 2p2h	Nieves *et al.*		
CC and NC COH	Berger-Sehgal		
FSI	NEUT cascade	Step length	0.2 fm
		Nucleon cross section	Bertini *et al.* [91]
		Pion cross secction	Pinzon *et al.* [89]

4.1.3 GENIE

While most generators are developed by a specific experimental or theoretical group, GENIE [38] is being developed to create a comprehensive simulator for various experiments. GENIE provides more available target nuclei than other generators, libraries describing dark-matter-nucleus scatterings, and a reweight package. It is used as the main generator in experiments at Fermi National Accelerator Laboratory, such as NOvA [13] and MINERvA [92]. It is an open source based on C^{++} and shared in [93]. We use version 3.0.6, released in July 2019, in this dissertation. GENIE offers various sets of models and parameters called the tune. Tune G18_10a_02_11a, considered the most common, is

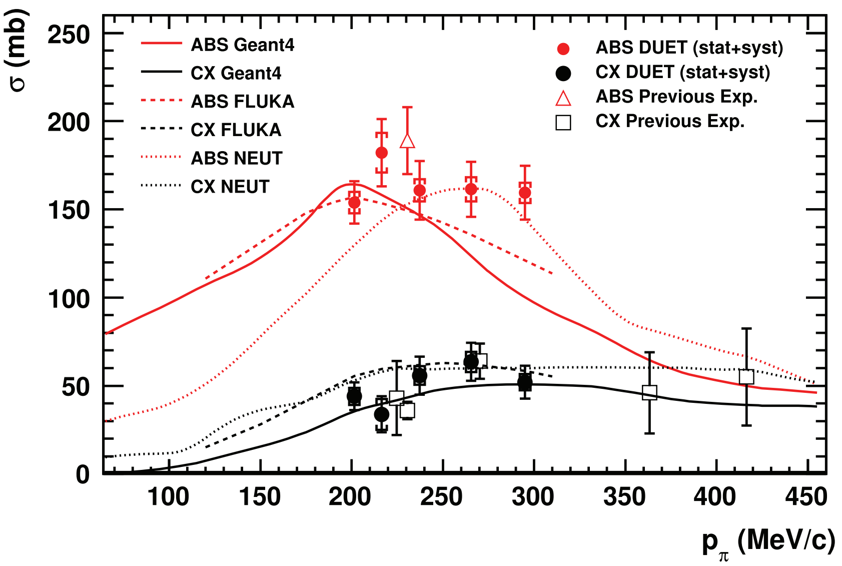

Figure 4.3: Pion-Carbon cross section in NEUT FSI model as a function of pion momentum. The dotted lines denote the cross section model used in NEUT. The model is tuned to reproduce the data by introducing energy-dependent normalization factors. The figure is from [89].

used in this dissertation. It has been reported that versions before version 3.0.6 have several bugs in the description of quasi-elastic scattering. In addition, the results often differ significantly from those of other generators, especially in the nuclear model and FSI. Therefore, many experiments use modifications of GENIE. In this dissertation, we dare not make any changes and use GENIE only as a comparison reference.

Tab. 4.3 shows the model configurations of GENIE. All of them are the default setting. GENIE uses INTRANUKE hA 2018 as the FSI model, which is not the cascade model. This model only calculates a single interaction instead of calculating a cascade. A problem has been reported where the FSI releases a huge number of nucleons with zero momentum. It is also reported that the momentum and binding energy of nucleons bound in the nucleus shows an improper distribution. Threre is an altenative FSI model called INTRANUKE hN. It is similar to NuWro and NEUT cascade models.

4.2 Comparison of Final State Interaction (FSI) models

Dytman *et al.* compared the FSI models implemented in these MC event generatros [62]. They compared two parameters to evaluate FSI models: Cross section and transparency. Since the transparency depends on the nuclear density and corrections, this parameter provides an alternative validation method. They used the following versions: NuWro version 19.01, NEUT version 5.4.0.1, GENIE version 3.0.6 for INTRANUKE hA and hN, and version 3.2.0 for INCL++. The version of GENIE and NEUT is the same as Sec. 4.1. The version of NuWro slightly differs from that used in our analysis, but the FSI model is not considered to be significantly different.

Table 4.3: Model configuration in GENIE. (V)FF represents (vector) form factor. Some parameters were unknown, so we wrote what we could find out.

Channel	Model	Parameter	
CCQE	Nieves *et al.*		
NCQE	Llewellyn-Smith	M_A	0.96 GeV
		g_A^s	-0.12
CC and NC RES	Berger-Sehgal	FF	Dipole form
		M_A	1.12 GeV
		RES/DIS boundary	$W = 2.0$ GeV
CC and NC DIS	GRV98 PDF	with modification by Bodek and Yang	
CC and NC 2p2h	Nieves *et al.*		
CC and NC COH	Berger-Sehgal		
Nuclear model	LFG		
FSI	INTRANUKE hA 2018 [38]	Step length	0.05 fm

4.2.1 Nucleon FSI

Fig. 4.4 shows the comparison of total reaction cross section and transparency for proton-carbon. When looking at the cross section (Fig. 4.4a), all FSI models give similar values for $T_p \gtrsim 0.1$ GeV. However, below that energy, NEUT and GENIE INCL++ show small values, clearly disagreeing with experiments. When looking at the transparency (Fig. 4.4b), only NuWro disagrees with data overestimating the transparency, while the others predict almost the same value. The difference is considered to be caused by differences in the nuclear density and nucleon-nucleon short-range correlation.

The trend of NuWro that predicts slightly larger transparency can also be confirmed in Fig. 4.1. The figure shows that the differences between NuWro and others are within the uncertainty. Based on the above, the FSI probability in NuWro is expected to be 0.25 ± 0.07 at the typical nucleon energy from NCQE, corresponding to 28% relative error.

4.2.2 Pion FSI

Fig. 4.5 shows the comparison of total reaction cross section and transparency for π^+-carbon. Unlike the nucleon, one can see a variation in the cross section data in Fig. 4.5a. NEUT agrees well with experimental data because they use the optimized cross section model by Pinzon *et al.* [89]. The deviation of cross section is about ±20% at $T_{\pi^+} = 0.2$ GeV, where corresponding to the excitation of Δ (so-called Δ region). One can see sizable variations also in the transparency (Fig. 4.5b). One concern here is the relationship between the cross section and transparency. Since the transparency follows Eq. 2.63, the larger cross section tends to give the smaller transparency. However, in the pion of $T_{\pi^+} \gtrsim 0.4$ GeV, the relationship does not hold. The correction may cause this situation, but further investigation is desired.

Compared to nucleon, the pion FSI appears to have much room for improvement. First, the reaction cross section needs to be optimized. The transparency after the optimization might be an interesting study because it needs to be validated, including correction effects. Experimental data are still scarce and have sizable errors (Fig. 4.2 and 4.3). It should be effective in obtaining additional experimental data and validating the models. In this study, a large relative error of 50% is assigned to the pion FSI probability, considering

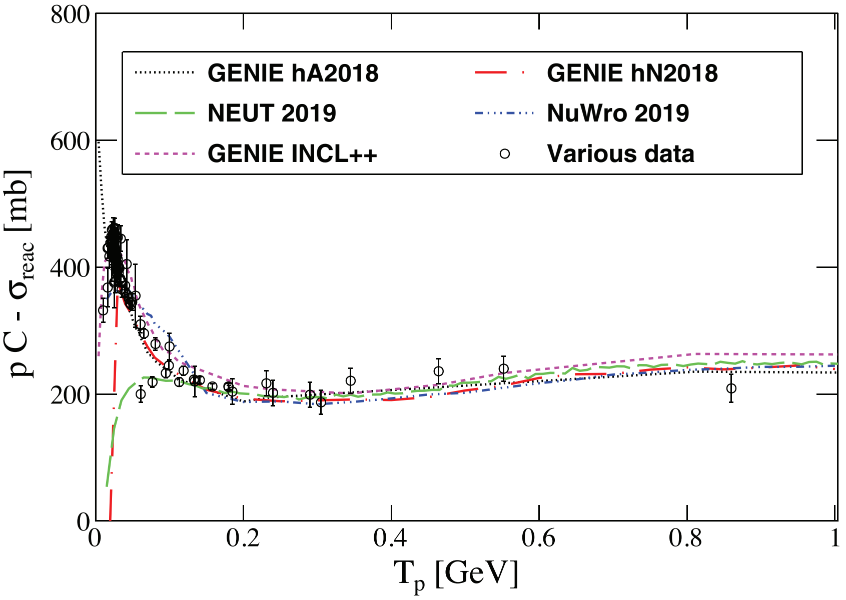

(a) Total reaction cross section

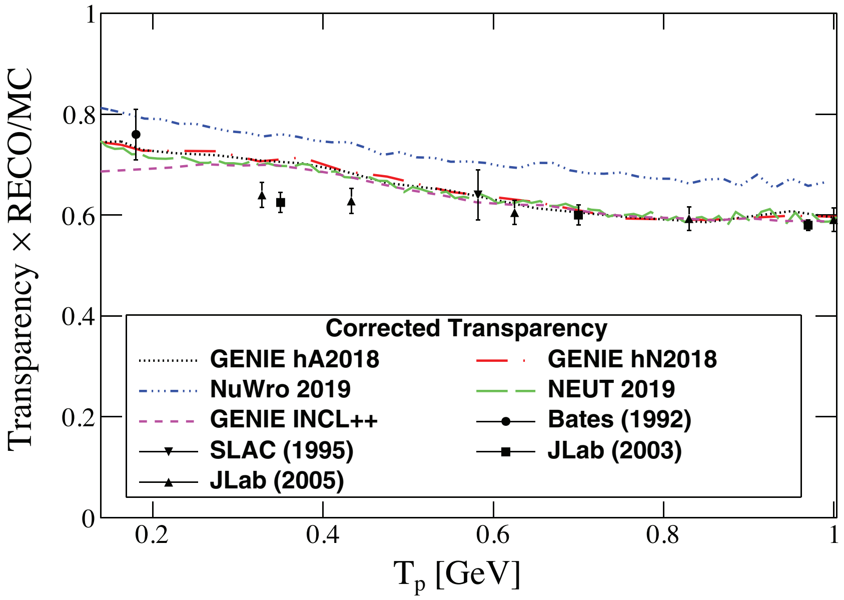

(b) Transparency

Figure 4.4: Total reaction cross section and transparency for proton-carbon as a function of proton kinetic energy. (a) All FSI models give a similar cross section for $T_p \gtrsim 0.1\,\mathrm{GeV}$, while NEUT and GENIE INCL++ give a small cross section below that energy. (b) NuWro predicts large transparency than others even though the cross section is almost the same. The difference is considered to be caused by differences in the nuclear density and nucleon-nucleon short-range correlation. The figure is from [62].

the differences between the models and the experiments and the large errors in the experimental data. Reducing this uncertainty is expected to greatly improve the prediction accuracy of NCRES, which is a part of the background events of the NCQE.

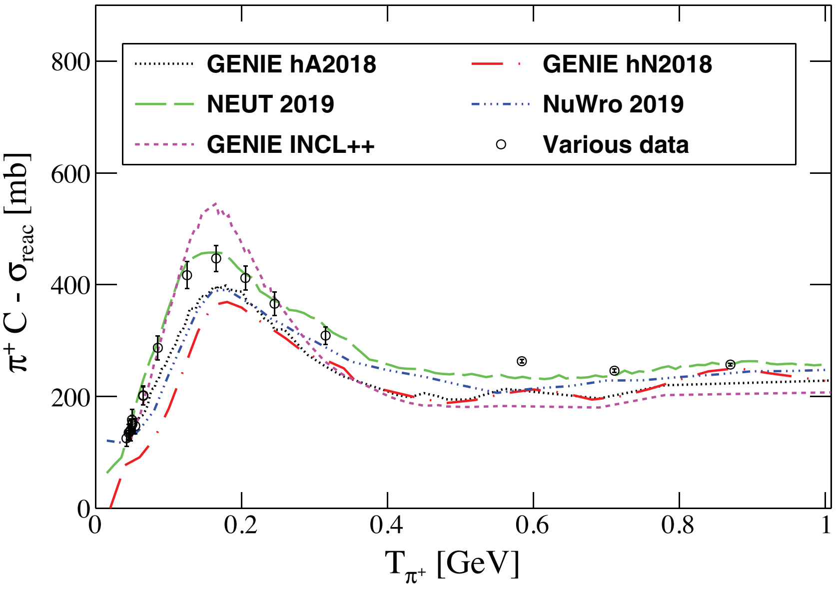

(a) Total reaction cross section

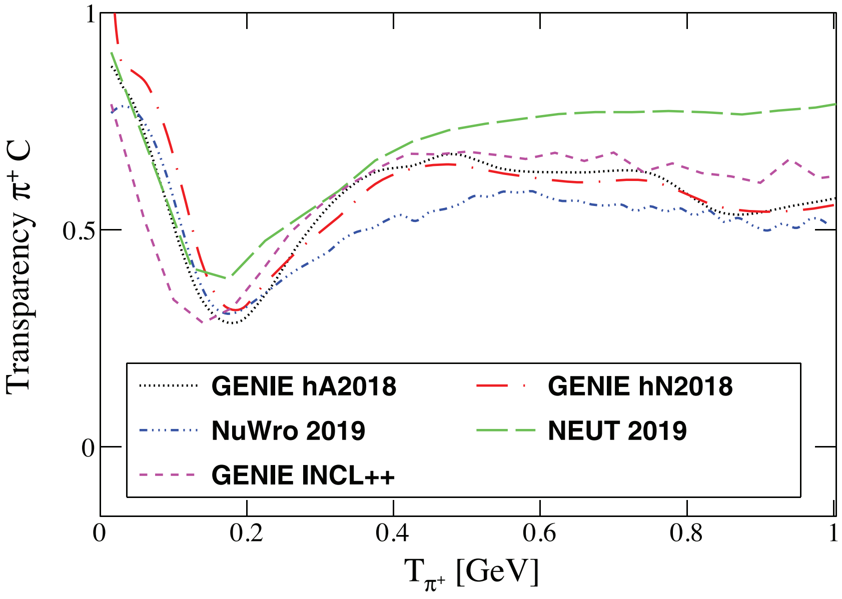

(b) Transparency

Figure 4.5: Total reaction cross section and transparency for π^+-carbon as a function of pion kinetic energy. A peak (dip) in the cross section (transparency) around 0.2 GeV corresponds to excitation of Δ, so-called the Δ region. (a) NEUT agrees well with experimental data because they use the optimized cross section model by Pinzon *et al.* [89] The figure is from [62].

Chapter 5

Nuclear De-excitation

Nuclear de-excitation associated with neutrino-nucleon interactions often occurs after the FSI. For example, in the case of ^{12}C target, the typical excitation energy is about 20 MeV, which is higher than the separation energies of various particles such as neutron, proton, and α. Therefore, the nuclear de-excitation process can emit various particles. It is significant to predict this process, especially for experiments measuring neutron multiplicity or low-energy neutrino interaction below several tens of MeV. However, all the neutrino MC generators introduced in Chap. 4 do not consider the nuclear de-excitation [1].

A systematic method to predict nuclear de-excitation, which can be used with the results of neutrino MC event generators, is established [94]. This chapter describes the prediction methods and results. Since this study is intended for liquid scintillator detectors, including KamLAND, the ^{12}C target is only discussed.

5.1 Overview of the Prediction

Neutrino Monte Carlo generators are event-by-event simulations. Therefore, a de-excitation simulation in the way of event-by-event simulation is required. This simulation uses two simulation software packages, TALYS version 1.95 [95] and modified Geant4 version 10.7.p03 [96] in this prediction.

TALYS is an open-source software package for the simulation of nuclear reactions based on the Fortran and shared in [97]. It provides a comprehensive and accurate nuclear reaction simulation up to 200 MeV energies, including fission, scattering, and compound reactions. Given any nucleus and excitation energy, it provides the branching ratios of all nuclear de-excitation processes. Although TALYS provides branching ratios, it does not perform event-by-event simulations.

Geant4, a widely-used software package for simulating the passage of particles through matter, makes it possible to do the event-by-event simulation. Within the Geant4 tool package, "G4RadioactiveDecay" simulates nuclear de-excitation and radioactive decays. An event-by-event simulation of de-excitation decay chains is performed by loading the branching ratios obtained from TALYS into G4RadioactiveDecay with several modifications.

In addition to the branching ratios from TALYS, various parameterizations related to the shell model, including excitation energies and spectroscopic factors, are necessary for the simulation (see Sec. 5.2).

---

[1] NEUT deals with the nuclear de-excitation only for oxygen, but not for carbon.

5.2 Shell Model Picture of ^{12}C

5.2.1 Shell-Level Occupation and Spectroscopic Factors

Fig. 5.1 shows the schematic view of the shell level occupation of neutrons for ^{12}C. In the simple shell model picture, two nucleons lie in the $s_{1/2}$ shell, four nucleons lie in the $p_{3/2}$ shell, and no nucleon lies in the $p_{1/2}$ shell. The difference between protons and neutrons is only in the absence and presence of the Coulomb potential of about 3 MeV (see Fig. 2.17), and there is no difference in the shell-level occupation. When a nucleon in the $p_{3/2}$ shell disappears, the excitation energy is zero, leading to no de-excitation. Contrarily, when a nucleon in the $s_{1/2}$ shell disappears, the excitation energy becomes about 23 MeV, corresponding to the energy gap between $p_{3/2}$ and $s_{1/2}$ levels.

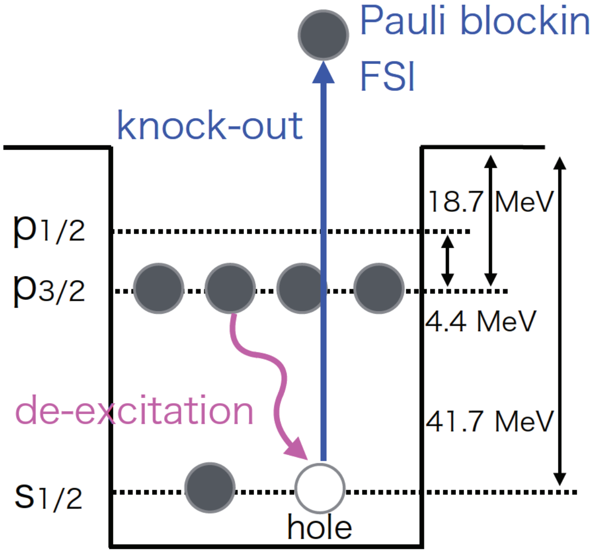

Figure 5.1: Shell-level occupation of neutrons for ^{12}C ground state in the simple shell model picture. In a more precise shell model calculation, the $p_{1/2}$ shell level just ~ 4 MeV above the $p_{3/2}$ is filled with a nucleon pair in a certain probability (see Sec. 5.3 for detail). When a neutron disappears from the $s_{1/2}$, an excitation energy of 23 MeV is produced. The occupation of protons is the same as neutrons.

The spectroscopic factors represent the probabilities of knocking out a nucleon from a specific shell level. Assuming the same probability for all nucleons, the spectroscopic factors for $s_{1/2}$ and $p_{3/2}$ are 1/3 and 2/3. However, the electron scattering experiment by Lapikás *et al.* shows that the spectroscopic factor of $s_{1/2}$ becomes smaller than this value because it is more deeply bound than $p_{3/2}$ [98]. Therefore, the following results obtained by the experiments are adopted: 0.296 for $s_{1/2}$ and 0.704 for $p_{3/2}$.

5.2.2 Excitation Energy Distribution

While the mass difference uniquely determines the separation energies, the binding energies have finite widths and experimental uncertainty. Fig. 5.2 shows the missing (binding) energy spectrum of carbon obtained from the electron scattering experiment at the Jefferson Lab [99]. The width of $s_{1/2}$ level tends to be larger than that of $p_{3/2}$ level.

The missing energy distribution is commonly parameterized with the Lorentzian (Cauchy

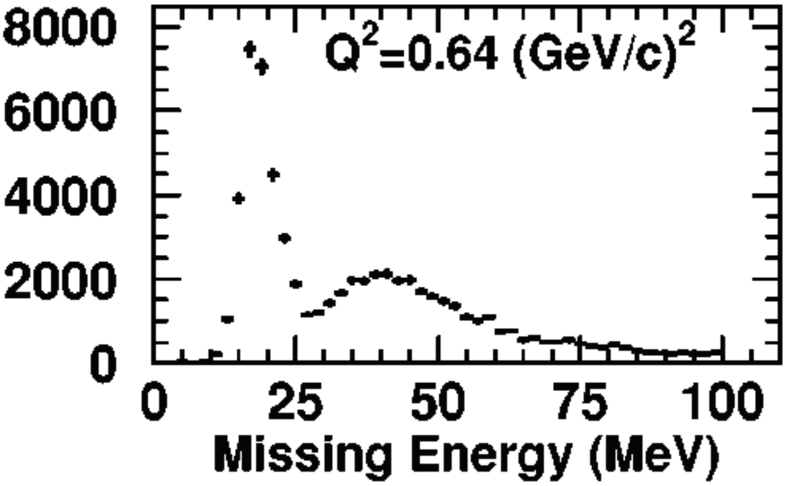

Figure 5.2: Measured missing energy distribution of single proton disappearance from ^{12}C. There are two peaks: A peak near 18 MeV corresponds to the $p_{3/2}$-hole state, and another peak near 40 MeV corresponds to $s_{1/2}$-hole state. Both peaks have finite widths, but the $s_{1/2}$ has a larger width than $p_{3/2}$. Missing energy is a sum of separation energy and excitation energy and is the same meaning as the binding energy under the notation of this dissertation. Therefore, this figure has the same meaning as Fig. 2.22b. The binding energy distribution of the SF model in Fig. 2.22b (blue line) has a similar distribution to this figure. The figure is from [99].

distribution), which has a heavier tail than the Gaussian.

$$f(E) = \frac{\Gamma/2}{\pi\left[(E - E_{\text{mean}})^2 + (\Gamma/2)^2\right]}, \tag{5.1}$$

where E_{mean} represents the mean and Γ represents the width in FWHM. Tab. 5.1 shows a summary of experimental measurements of the missing energy distribution for single proton disappearance from ^{12}C. There are experimental uncertainties, especially in width. A theoretical calculation predicts 12 MeV in FWHM for $s_{1/2}$ [100]. From these experimental and theoretical results, this simulation adopts $E^{\text{proton}}_{\text{mean},s} = 39 \pm 1\,\text{MeV}$ and $\Gamma^{\text{proton}}_{s} = 14^{+10}_{-2}\,\text{MeV}$ for parameterizing the proton missing energy distribution for the $s_{1/2}$-hole state. Considering the absence of the Coulomb potential of 2.7 MeV, the neutron missing energy distribution can be given as $E^{\text{neutron}}_{\text{mean},s} = 41.7 \pm 1\,\text{MeV}$ and $\Gamma^{\text{neutron}}_{s} = 14^{+10}_{-2}\,\text{MeV}$. There is no difference in the width between protons and neutrons. Finally, the excitation energy distribution of protons and neutrons is obtained by subtracting the separation energy (18.7 MeV for neutrons and 16.0 MeV for protons) from the missing energy.

$$E_{\text{mean},s} = 23 \pm 1\,\text{MeV}, \tag{5.2}$$

$$\Gamma_s = 14^{+10}_{-2}\,\text{MeV}. \tag{5.3}$$

Since the Coulomb potential changes the overall potential depth, the excitation energy corresponding to the difference in energy levels is considered to be common to protons and neutrons. We briefly mention how the uncertainty of these values affects the branching ratios at the end of this chapter. Appendix A.1 contains information on separation energies.

Table 5.1: Measurements of mean and width of missing energy for single proton disappearance from ^{12}C. The Lorentzian is commonly used to parameterize the missing energy distribution. The values are in units of MeV, and the widths are written as FWHM.

Experiment	p shell		$s_{1/2}$ shell	
	Mean $E_{\mathrm{mean},p}$	Width Γ_p	Mean $E_{\mathrm{mean},s}$	Width Γ_s
Tokyo [101]	15.5 ± 0.1	6.9 ± 0.1	36.9 ± 0.3	19.8 ± 0.5
Saclay [102]	17.5 ± 0.4	-	38.1 ± 0.1	-
Lapikás *et al.* [98]	-	-	39 ± 1	24 ± 6

5.3 Disappearance from the p shell

In the simple shell model, the $p_{1/2}$ level just 4 MeV above the $p_{3/2}$ level is always empty. In a more precise shell model picture, the $p_{1/2}$ shell is partially occupied by a nucleon pair due to nucleon-nucleon correlation. From various shell model calculations, this partial occupation, called the pairing effect, is expected to occur with a probability of $40 \pm 10\%$ [100] Therefore, $20 \pm 5\%$ of the time, the disappearance of a single nucleon from the $p_{3/2}$ or $p_{1/2}$ shell will leave the residual nucleus in an excited state with spin-parity $J^\pi = 1/2^-$. The energy gap between $p_{1/2}$ and $p_{3/2}$ is a few MeV. In this energy region, there is only one excited state in both ^{11}C and ^{11}B. It decays to the ground state by emitting one γ with an energy of 2.0 MeV for ^{11}C and 2.1 MeV for ^{11}B. See Fig. A.1 and A.2 in Appendix A.2 for energy level diagrams of ^{11}C and ^{11}B.

5.4 Disappearance from the $s_{1/2}$ shell

Nucleon disappearance from the $s_{1/2}$ shell is more complicated than the p-hole state. Because of the high excitation energy, typically more than the separation energies, various particle emissions should be considered, including multi-step processes as well as single-step de-excitations. This simulation considers seven de-excitation modes: γ, α, n, p, deuteron (d), triton (t), and ^{3}He. All the branching ratios, including the full decay chains of the daughter nuclei, are extracted from TALYS. Since the excitation energy of an $s_{1/2}$-hole is large, the impact of the pairing effect is neglected in this case.

5.4.1 Branching Ratios in TALYS

Fig. 5.3 shows the branching ratios of ^{11}B* and ^{11}C* decays as a function of excitation energy. The spin-parity is $J^\pi = 1/2^+$ for single nucleon disappearance from the $s_{1/2}$ shell. At the typical excitation energy of 23 MeV, neutron emission accounts for about 65% of de-excitations. This process strongly affects the neutron multiplicity associated with neutrino-nucleon interactions. In contrast, the neutron branching ratio for ^{11}C* decay at a 23 MeV excitation energy is about 6%. This branching ratio is similar to that of proton emission for ^{11}B*. For both nuclei, the minimum separation energy is for α: 8.66 MeV for ^{11}B* and 7.54 MeV ^{11}C*. Below the energy, only γ rays can be emitted. The α branching ratio accounts for almost 100% at just above the α separation energy.

Kamyshkov *et al.* reported a calculation of the branching ratio of ^{11}C using SMOKER code [100]. This calculation neglected decay modes of d, t, and ^{3}He, which account for about 20% in the branching ratio according to TALYS. The trends are approximately

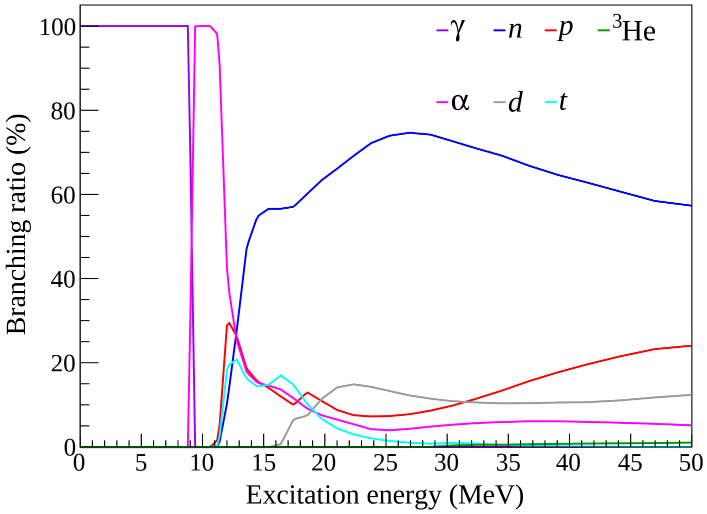

(a) ^{11}B*

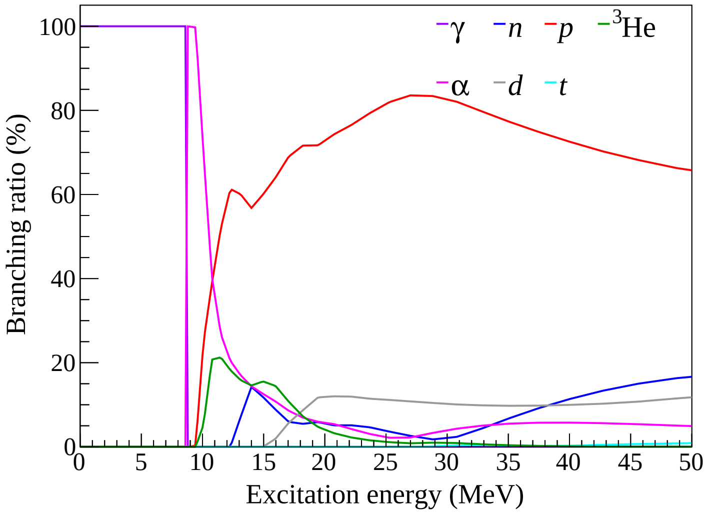

(b) ^{11}C*

Figure 5.3: Branching ratios of ^{11}B* and ^{11}C* with $J^{\pi} = 1/2^{+}$ as a function of excitation energy. These values are calculated with TALYS [95]. Neutron emission is dominant in ^{11}B* while it is minor in ^{11}C*. ^{3}He emission for ^{11}B* and triton emission for ^{11}C* are negligible since they are neutron- and proton-rich, respectively.

consistent comparing our results and SMOKERE's results (see Appendix A.3). This simulation, which considers all decay modes including t, d, and ^{3}He, is considered to be more accurate.

Multi-Step De-excitation

In the case of high excitation energies of $s_{1/2}$-hole state, multi-step de-excitation must be considered. Fig. 5.4 shows the schematic view of the multi-step de-excitation decays. If it has high excitation energy, one-step de-excitation (a single de-excitation process) rarely leads to the ground state. In other words, it frequently transits to the excited state of other nuclei. If the excited state is lower than the separation energies, it simply goes to the ground state with gamma-ray emissions. Otherwise, it undergoes an additional de-excitation process (multi-step de-excitation) going to another nucleus with particle emission other than gamma rays.

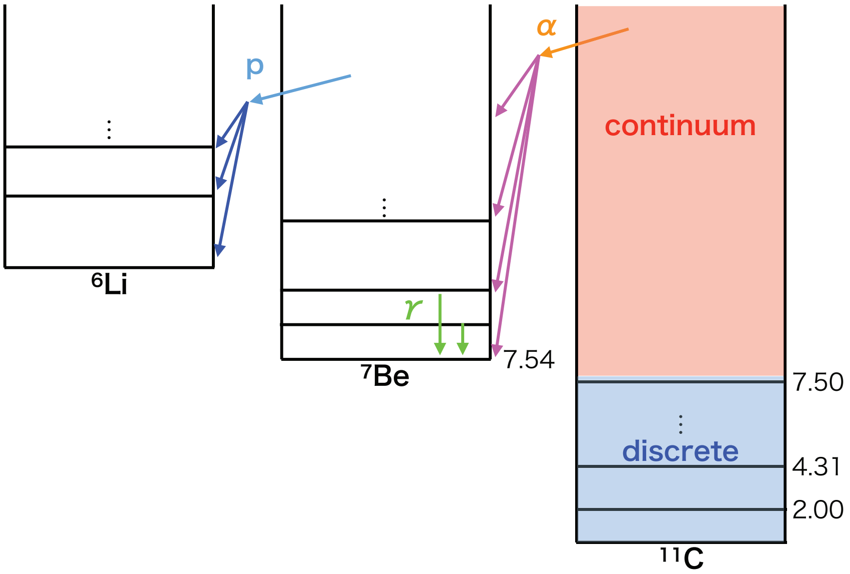

Figure 5.4: Schematic view of multi-step de-excitation. As an example, a decay chain of $^{11}\mathrm{C}^* \rightarrow ^7\mathrm{Be}^* \rightarrow ^6\mathrm{Li}^*$ is shown. First, an α particle is emitted from a certain excited state of $^{11}\mathrm{C}^*$ and transitions to $^7\mathrm{Be}^*$. It frequently goes to the excited state of $^7\mathrm{Be}^*$. If the excited state of $^7\mathrm{Be}^*$ is below the separation energies, it emits only gamma rays and goes to the ground state of ^{7}Be. If it is above the separation energies, it goes to another nucleus with particle emission except for gamma rays. In this figure, it transits to $^6\mathrm{Li}^*$ with a proton emission.

The branching ratios of the primary nuclei are already introduced in Fig. 5.3. However, it does not include the excitation energy distribution of the daughter nuclei. For a comprehensive prediction of multi-step de-excitation, this simulation also calculates and extracts the excitation energy distribution of the daughter nuclei. The distribution depends on complex nuclear effects such as spin-parity. In this study, a huge amount of information about the multi-step de-excitation is calculated by using TALYS. Although the process of de-excitation twice is shown as an example in Fig. 5.4, this study does not set an upper limit on the number of decay chains.

As examples, Fig. 5.5 shows the excitation energy distribution of the daughter nuclei when specific excitation energy of about 23 MeV is given for ^{11}B and ^{11}C. The maximum excitation energy of the daughter nucleus is the excitation energy of the primary nucleus minus the separation energy. It can be seen that the distribution varies greatly from particle to particle. The distribution shows that, in many cases, it does not go to the ground state but through the excited states of the daughter nuclei. The excitation energy of the daughter nuclei is typically around 10 MeV. This excitation energy is generally below or slightly above the proton and neutron separation energies. Therefore, more stable particles such as α and d mainly contribute to multi-step de-excitation.

The trouble with considering multi-step de-excitation is that the branching ratios of the daughter nuclei vary slightly with the parent nucleus. For example, $^{10}\mathrm{B}^*$ generated via $^{11}\mathrm{C}^* \to p + ^{10}\mathrm{B}^*$ and $^{11}\mathrm{B}^* \to n + ^{10}\mathrm{B}^*$ have differenct branching ratios (see Appendix A.4). The difference is considered to be caused by the difference in spin-parity. The spin-parity of primary nucleus ($^{11}\mathrm{C}^*$ and $^{11}\mathrm{B}^*$) is common to be $J^\pi = 1/2^+$, but it would be differ in $^{10}\mathrm{B}^*$. In order to consider the difference, this simulation calculates the branching ratio comprehensively using TALYS and uses the branching ratio independently for the primary nucleus. In other words, this simulation adopts different branching ratio data of the daughter nuclei used in the simulation of the primary nucleus, such as $^{11}\mathrm{C}^*$ and $^{11}\mathrm{B}^*$.

5.4.2 Event-by-event Simulation using a Modification of Geant4

The event-by-event simulation is performed by using Geant4, loading the branching ratios obtained from TALYS. Geant4 version 10.7.p03, released on 19th November 2021, is used in this simulation. In the original code, the de-excitation modes of triton, deuteron, and ^{3}He are not implemented. The code is modified so as to implement these decay modes. The kinematics of the de-excitation process, such as momentum and energy conservation, separation energies, and nuclear recoil, are properly considered.

The excitation energy can be calculated from the binding energy obtained from the neutrino MC generators, as shown in Fig. 2.22b. However, the excitation energy distribution with the Lorentzian introduced in Sec. 5.2.2 is assumed to obtain generator-independent results.

5.5 Copmparison with Experimental Data and Other Predictions

The predicted results with this simulation are compared with experimental data and other predictions. Sec.5.5.1 and 5.5.2 shows the comparison of $^{11}\mathrm{B}^*$ and $^{11}\mathrm{C}^*$, respectively. For $^{11}\mathrm{B}^*$, some experimental data are available to confirm the validity of the simulation developed in this study. However, some channels show deviations from the experimental data, and further discussion is required, such as additional experiments and model evaluations. On the other hand, we could not find experimental data for $^{11}\mathrm{C}^*$, so we are forced to compare between predictions only. Although the contribution of neutron emission is small for $^{11}\mathrm{C}^*$, it is desired to obtain experimental data and compare it with the predictions.

5.5.1 Comparison of $^{11}\mathrm{B}^*$

As inferred from Fig. 5.3a, the s-hole state of $^{11}\mathrm{B}^*$ has a large contribution of neutron emission with $\sim 65\%$. Therefore, this is the most critical de-excitation mode when measuring neutron multiplicity associated with neutrino interactions.

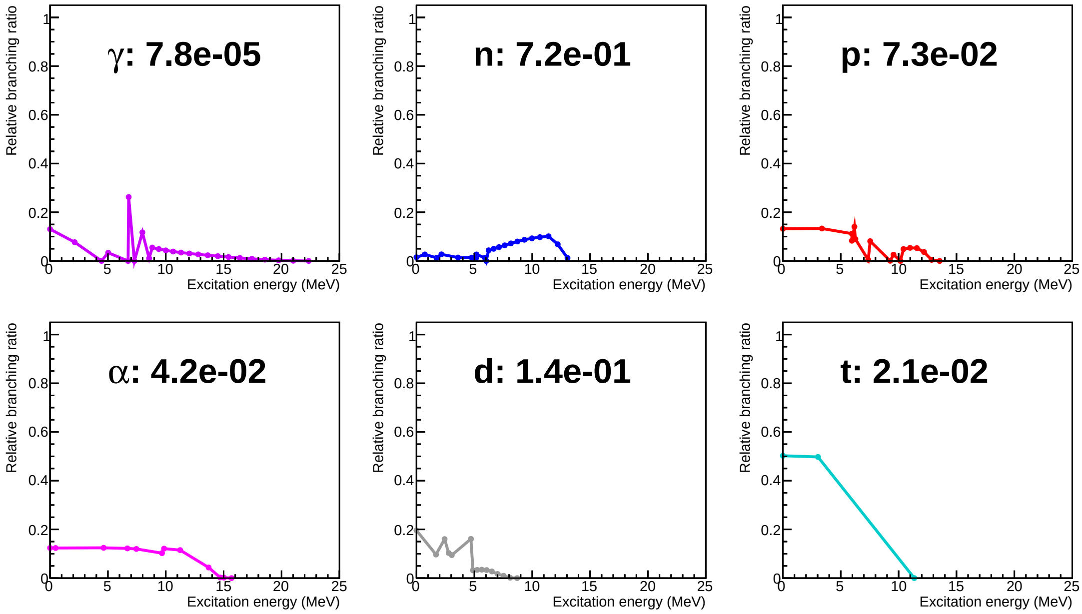

(a) ^{11}B* with 23.8 MeV excitation energy.

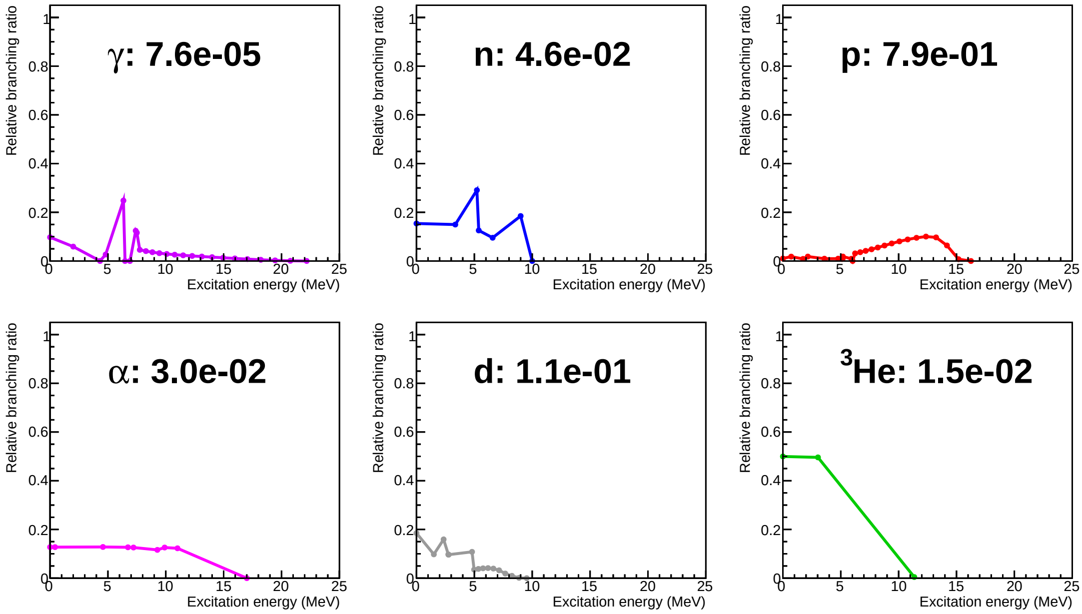

(b) ^{11}C* with 23.7 MeV excitation energy.

Figure 5.5: Branching ratios of ^{11}B* and ^{11}C* with $J^{\pi} = 1/2^{+}$ as a function of excitation energy of daughter nuclei. The values in each panel represent the absolute branching ratio for each de-excitation mode. The colored lines represent the relative branching ratio as a function of the excitation energy of the daughter nucleus for each mode. The data shows that, in many cases, it frequently goes to the excited states of daughter nuclei. The branching ratio of ^{3}He (triton) for ^{11}B* (^{11}C*) is zero due to the high separation energy and is not shown in the figure. (a) The neutron branching ratio of ^{11}B* is 0.72 and the excitation energy of the daughter nuclei ^{10}B* (denoted as the blue line) peaks at around 10 MeV.

Fig. 5.6 shows a comparison of the relative branching ratios of n and d/α for $^{11}\mathrm{B}^*$ with excitation energies of 16−35 MeV. The experimental data are from Panin *et al.* [103], which measured three single-step de-excitation modes:

$$^{11}\mathrm{B}^* \to n +^{10}\mathrm{B}, \tag{5.4}$$

$$^{11}\mathrm{B}^* \to d +^{9}\mathrm{Be}, \tag{5.5}$$

$$^{11}\mathrm{B}^* \to \alpha +^{7}\mathrm{Li}. \tag{5.6}$$

The published result does not distinguish between d and α, so for comparison, the relative branching ratios of n and d/α are calculated. Another prediction result from Hu *et al.* uses TALYS version 1.95 [104], the same version used in our analysis. The excitation energy and spin-parity configurations may cause the difference between Hu's result and ours. The branching ratio to n is the most important parameter in this analysis. Our result agrees with the experimental data within a relative uncertainty of 20%.

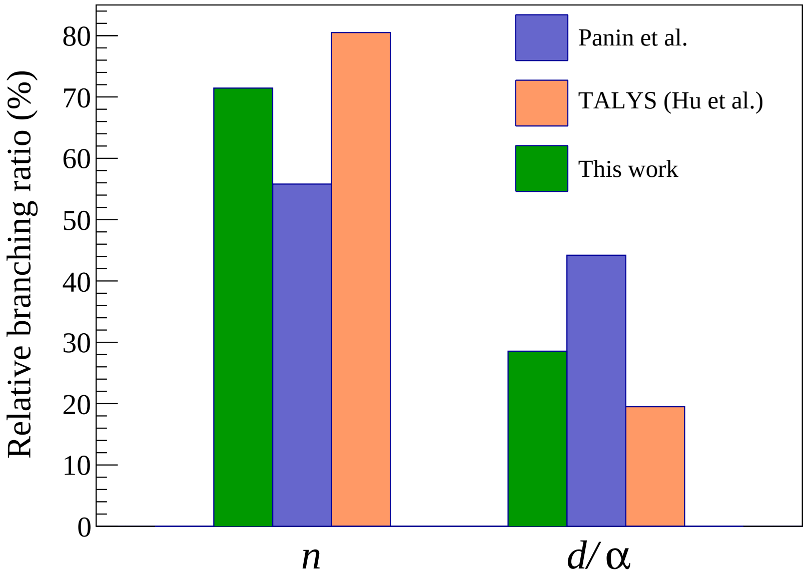

Figure 5.6: Comparison of measured and predicted relative branching ratios of n and d/α for $^{11}\mathrm{B}^*$ with 16−35 MeV excitation energy. The experimental data, in blue, are from Panin *et al.* [103]. The orange histograms show the predicted results from Hu *et al.* using TALYS [104], and the greens represent our results. Our result agrees with the experimental data within a relative uncertainty of 20%.

Fig. 5.7 compares the measured and predicted branching ratios for $^{11}\mathrm{B}^*$ in the same excitation energy range with the experimental result from Yosoi *et al.* [105]. The experiment by Yosoi *et al.* measured the branching ratio for p, α, d, and t. The $^{3}\mathrm{He}$ branching ratio is not shown because it is less than 1%. The n branching ratios are consistent within a 20% relative uncertainty. There is a large difference in the single-step decay of triton, where the experimental result has a much larger value than the predictions. Fig. 5.8 shows the measured excitation energy spectra as a function of excitation energy measured by Yosoi *et al.* It is similar to TALYS prediction (Fig. 5.3a) in that proton has a relatively large contribution at lower excitation energies, and deuteron appears to have a contribution at larger excitation energy near 25 MeV. However, the triton contribution appears to be the most dominant mode over a wide range of excitation energies, which is clearly inconsistent with TALYS. The authors also discussed this issue in their paper. They provided the predicted result using the CASCADE code (the blue histograms in Fig. 5.7). Even this prediction shows a large discrepancy with the experimental data. The causes of this discrepancy are still unclear. Therefore, further investigations are needed, such as validation experiments and model evaluations.

In addition, a large difference can be confirmed in the multi-step α decay. Our result gives almost 0% while others show about 5%. The α emission process is dominant at low excitation energies around 10 MeV, which lead to low α kinetic energies and low excitation energies of the daughter nuclei. Since the neutron separation energy of ^{7}Li is as high as 7.3 MeV, multi-step α de-excitations do not contribute significantly to neutron emission. All these differences between our prediction and experimental results and with other predictions are considered model-dependent uncertainties.

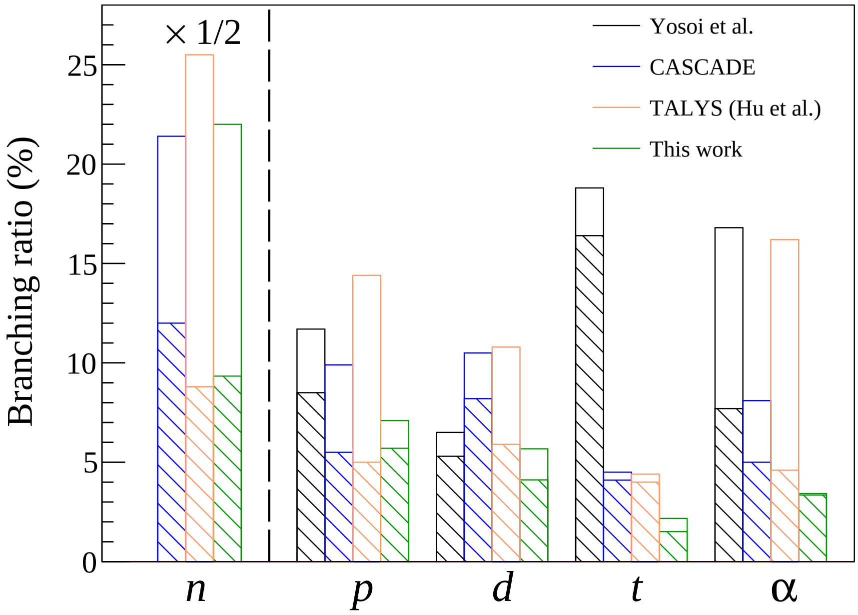

Figure 5.7: Comparison of measured and predicted branching ratios of n, p, d, t, and α for ^{11}B* with 16−35 MeV excitation energy. The branching ratios of n are multiplied by a factor of 1/2. The green histograms represent our result using TALYS, and the orange histograms represent the prediction by Hu *et al.* using TALYS [104]. The experimental data in black are from Yosoi *et al.*, and the authors also provide the predicted result using the CASCADE code [105]. The hatched histograms represent the branching ratios for single-step decays, and the open histograms represent those from multi-step decays.

5.5.2 Comparison of ^{11}C*

The branching ratios of ^{11}C* are also compared with another prediction by Kamyshkov *et al.* using SMOKER [100]. The SMOKER code does not consider the de-excitation modes of d, t, and ^{3}He. We therefore only compare the n, p, and α branching ratios. In contrast to ^{11}B*, neutron emission is a minor de-excitation mode, while proton emission is a major one. The total branching ratio for single-step and multi-step neutron decays is

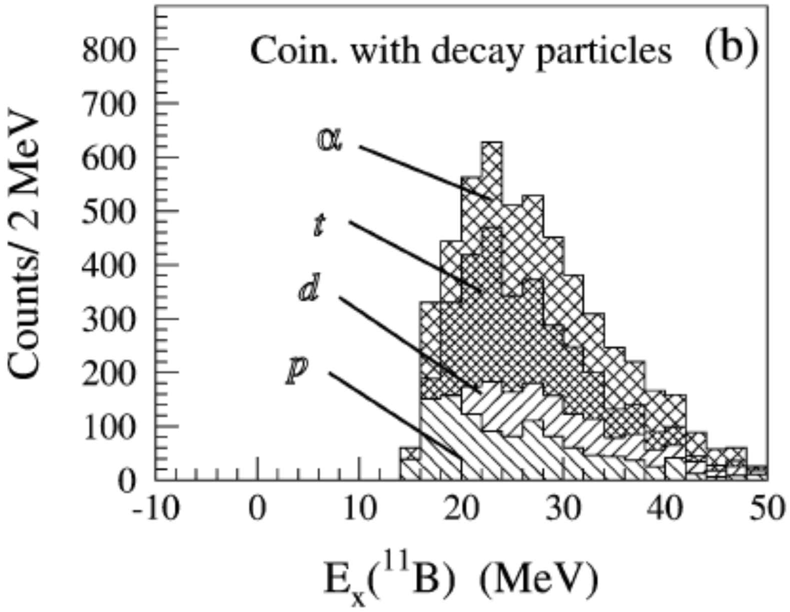

Figure 5.8: Excitation energy spectra of $^{11}B^{*}$ as a function of excitation energy measured by Yosoi *et al.* The triton contribution appears to be the most dominant mode over a wide range of excitation energies, which is clearly inconsistent with TALYS shown in Fig. 5.3a. The figure is from [105].

5.7%, while SMOKER predicts 13.8%. This difference is also treated as a model-dependent uncertainty.

5.5.3 Impact of Uncertainties in the Excitation Energy Distribution

Finally, the impact of the mean and width of the excitation energy distribution on the branching ratios is investigated. The excitation energy distribution is changed within Eq. 5.2 and 5.3 to check the relative change in the branching ratios. The relative changes in the branching ratios are within 15%. This uncertainty from the excitation energy is assigned in addition to the model-dependent uncertainty derived from Fig. 5.6 and 5.7.

5.6 Multi-Nucleon Disappearance

The single nucleon disappearances such as $^{11}B^{*}$ and $^{11}C^{*}$ are discussed so far. There are cases where multiple nucleons are released through neutrino-nucleon interactions by 2p2h interaction or FSI effects. These cases (denoted as multi-nucleon disappearance in this dissertation) undergo highly complex processes because it can have higher excitation energies and requires considering a combination of shell levels that can be the holes. The simulation for the multi-nucleon disappearance is also established under various simplifications, similar to some of the other predictions introduced in Sec. 5.5. A comparison with experimental data has not been realized. Therefore, the predictions are entirely model-dependent and must be given a significant degree of uncertainty. The improvement in simulation based on more accurate descriptions and comparison with experimental data is one of the key issues for the future.

5.6.1 Assumption and Simplification

Nucleon-Nucleon Correlation and Spin-Parity

This study ignores the nucleon-nucleon correlation in the multi-nucleon disappearance. For example, since the 2p2h interaction is a channel that reacts with two nucleons in short-range correlation, one can expect that these nucleons tend to be in the same shell level, particularly in $s_{1/2}$ shell. The FSI might likely emit nucleons of the same shell for the same reason. However, the correlation effect is not certain and challenging to parameterize at this time. Therefore, the effect is neglected in this simulation. This simplification allows us to assume that the spectroscopic factor and de-excitation energy distribution are independent for all nucleons, i.e., all nucleons having equal contributions (probabilities). The paring effect is also neglected due to the correlation mentioned in Sec. 5.3. This gives that the shell-level occupancy of $p_{1/2}$ becomes zero, and the excitation energy of the $p_{3/2}$-hole state also becomes zero.

This study uses the value of spin-parity automatically set by TALYS for the multi-nucleon disappearance, while it properly considers the spin-parity for single nucleon disappearance. In the configuration, TALYS gives all excitation energies with all spin-parity with equal probabilities. This simplification reduces complexity in considering combinations of shell levels that would be holes. At high excitation energies, the spin-parity dependence is not so large because of the continuous distribution of excited states with various spin parities.

Spectroscopic Factor

For the spectroscopic factor, the same probability for all nucleons is assumed, neglecting the nucleon-nucleon correlations. In the case of two nucleon disappearance $^{10}\mathrm{C}^*$ and $^{10}\mathrm{Be}^*$, which corresponds to two neutrons and proton disappearance, respectively, the spectroscopic factors are as follows.

$$(\text{Spectroscopic factor}) = \begin{cases} 1/15 & (\text{two holes in } s_{1/2}) \\ 8/15 & (\text{one holes in } s_{1/2} \text{ and one holes in } p_{3/2}) \\ 6/15 & (\text{two holes in } p_{3/2}) \end{cases} \tag{5.7}$$

This will be slightly changed in a case of $^{10}\mathrm{B}^*$ corresponding to one neutron and one proton disappearance as follows:

$$(\text{Spectroscopic factor}) = \begin{cases} 1/9 & (\text{two holes in } s_{1/2}) \\ 4/9 & (\text{one holes in } s_{1/2} \text{ and one holes in } p_{3/2}) \\ 4/9 & (\text{two holes in } p_{3/2}) \end{cases} \tag{5.8}$$

For three or more nucleon disappearances, a simple probability calculation is performed in the same way.

Excitation Energy Distribution

The excitation energy distribution is also calculated simply neglecting the correlations. The excitation energy is calculated as the sum for each hole: If a nucleon in the $s_{1/2}$ disappears, the excitation energy according to the Lorentzian with $E_{\mathrm{mean,s}} = 23\,\mathrm{MeV}$ and $\Gamma_s = 14\,\mathrm{MeV}$ is added, and if a nucleon in the $p_{1/2}$ disappears, the zero excitation energy is added. Since the Lorentzian has the reproductive property, if two nucleons disappear from the $s_{1/2}$, the excitation energy distribution can be expressed using the Lorentzian with $E_{\mathrm{mean,s}} = 46\,\mathrm{MeV}$ and $\Gamma_s = 28\,\mathrm{MeV}$.

5.6.2 Comparison with Other Prediction

The predicted branching ratios of ${}^{10}\mathrm{C}^*$ in the case of two-nucleon disappearance from $s_{1/2}$ shell is compared with the prediction by Kamyshkov *et al.* using SMOKER [100]. Our result of the branching ratio of the neutron is 7.2%, while SMOKER predicts 12.2%. The difference corresponding to the model-dependent uncertainty is comparable to that of ${}^{11}\mathrm{C}^*$. However, the result shows a large difference in the neutron emission via the multi-step de-excitation, such as ${}^{10}\mathrm{C}^* \to p + n +^{8}\mathrm{B}$. It is 49.8% in our result, while the SMOKER predicts 0%. Therefore, a large model-dependent uncertainty for neutron emission probability must be applied.

Comparing the total neutron emission probability from ${}^{10}\mathrm{C}^*$, a large and conservative uncertainty is applied: 120% for two-nucleon disappearance, 180% for three- or more-nucleon disappearance on the neutron emission probability.

Part III

KamLAND Experiment

Chapter 6

KamLAND Detector

KamLAND (**Kam**ioka **L**iquid scintillator **A**nti-**N**eutrino **D**etector) is a 1-kton ultra-pure liquid scintillator detector located in the Kamioka mine, Gifu Prefecture, Japan [106]. We have achieved stable physics data acquisition since 2002. The details of the KamLAND detector are described in this chapter.

6.1 KamLAND Site

The KamLAND site is almost 1000 m underground from the top of Mt. Ikenoyama, as shown in Fig. 6.1. The 2,700 m water equivalent overburden reduces the cosmic muon flux by a factor of 10^{-5} to the surface flux.

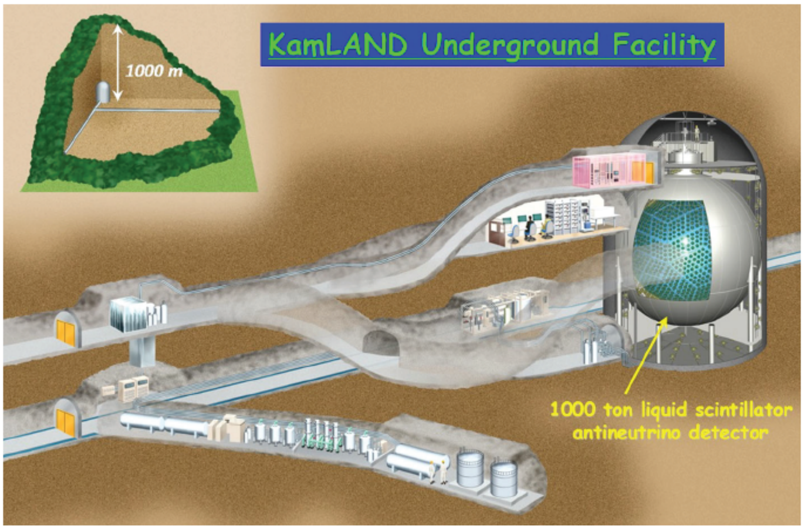

Figure 6.1: KamLAND site

6.1.1 Cosmic Muon Flux at KamLAND Site

The cosmic muon flux at the KamaLAND site is estimated using MUSIC simulator [107]. The simulation considers the three-dimensional geometrical feature of Mt. Ikenoyama shown in Fig. 6.2. Fig. 6.3a shows the predicted muon flux as a function of muon energy. The mean muon energy is 260±8 GeV. Fig. 6.3b shows the predicted muon arrival direction.

There is clear azimuth and zenith angle dependence. The south side of Ikenoyama has more muon flux because the rock is thinner than the north side. The simulation agrees well with the KamLAND data. The cosmic muon event rate at the KamLAND detector is about 0.34 Hz.

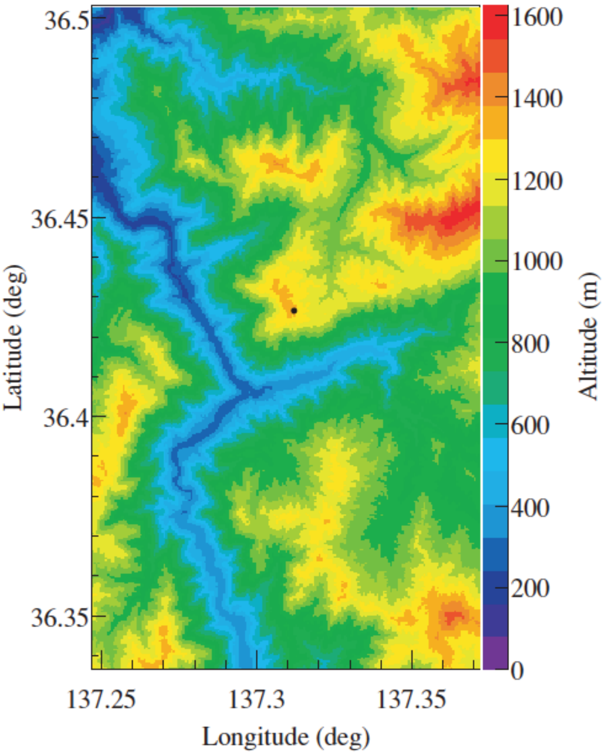

Figure 6.2: Ikenoyama topological profile. The black dot shows the location of the KamLAND. The figure is from [108].

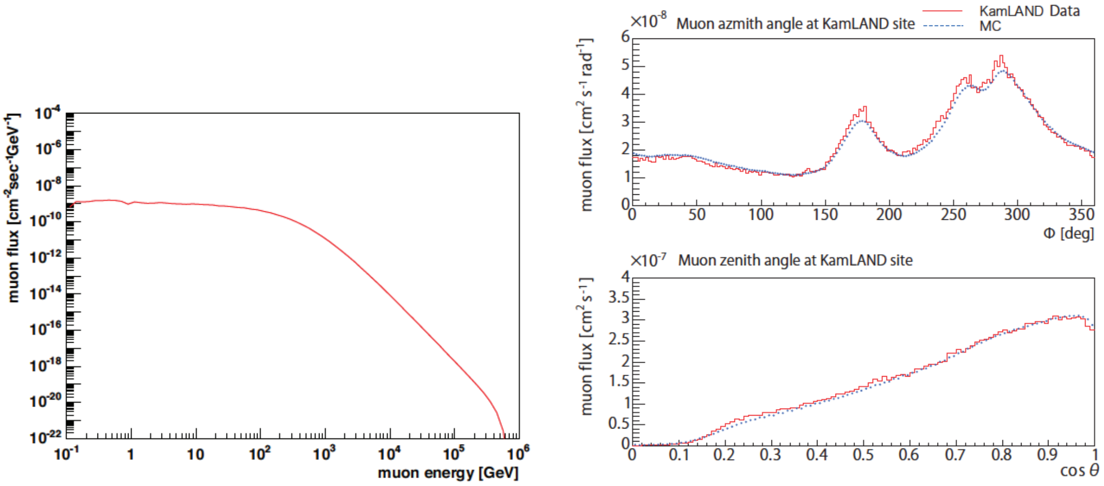

(a) Muon energy

(b) Muon arrival direction

Figure 6.3: Muon flux at the KamLAND predicted with MUSIC [107]. The mean muon energy is 260 ± 8 GeV.

6.2 Detector Components

KamLAND consists of the inner detector (ID) and the outer detector (OD). The ID refers to the inside of an 18 m diameter spherical stainless steel tank. The OD refers to the outside of it. The ID is for detecting neutrino reactions, while the OD is for a cosmic muon veto counter. Photo Multiplier Tubes (PMT) are installed in the ID and OD to detect light. Fig. 6.4 shows the schematic view of the KamLAND detector. In the upper part of the KamLAND, there is a space called the "dome area" where people can enter. The dome area contains calibration devices, a clean room, and an electronics hut. The calibration devices can be installed from the chimney, located in the center of the upper part of the KamLAND.

The coordinate system in KamLAND is defined with the detector center as $(x, y, z) = (0, 0, 0)$. The $+z$ direction is defined as the vertical up, and the $+y$ direction as the magnetic north.

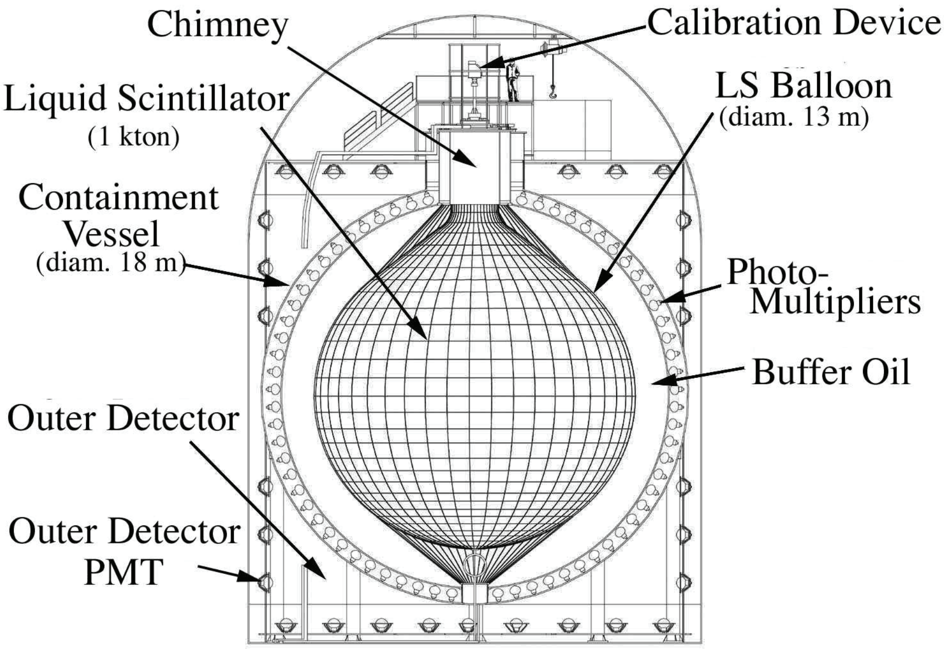

Figure 6.4: Schematic view of the KamLAND detector.

6.2.1 Inner Detector (ID)

The ID consists of an 18 m diameter spherical stainless steel tank, acrylic plates, a 13 m diameter outer balloon filled with 1000-ton of liquid scintillator, 1325 17-inch PMTs, and 554 20-inch PMTs.

KamLAND Liquid Scintillator (KamLS)

KamLAND has a 1000-ton liquid scintillator (LS) in the outer balloon. The KamLS is made of dodecane, pseudocumene, and PPO, as shown in Tab. 6.1. Pseudocumene is used as the solvent, and PPO as the solute (luminescent agent). Dodecane is not involved in the scintillation process but plays a role in adjusting density and preventing transparency loss. The elemental composition of KamLS is approximately CH_2 with negligible amounts of nitrogen and oxygen, as shown in Tab. 6.2. The density of the KamLS is 0.778 g/cm^3 at 15°C. The light emission spectrum of KamLS peaks at 375 nm wavelength with ∼8000 photon/MeV of light yield. The light emission wavelength must be in a region where the PMT quantum efficiency and the LS transparency are sufficiently high. The KamLS composition is adjusted to satisfy these conditions as shown in Fig. 6.5.

Table 6.1: Components of KamLAND liquid scintillator

Material	Molecular formula	Density [g/cm^3]	Volume ratio
Dodecane	$C_{12}H_{26}$	0.749	80%
Pseudocumene	C_9H_{12}	0.875	20%
PPO	$C_{15}H_{11}NO$	-	1.36 [g/L]

Table 6.2: Elemental composition of KamLAND liquid scintillator. The hydrogen-to-carbon ratio was verified by elemental analysis by ±2%.

Element	Stoichiometry	Number of targets per kiloton
Carbon	$\equiv 1$	4.30×10^{31}
Hydrogen	1.97	8.47×10^{31}
Nitrogen	$(1-6) \times 10^{-4}$	$(5-30) \times 10^{27}$
Oxygen	1×10^{-4}	5×10^{27}

The refractive index of the KamLS was measured using the Abbe refractometer. In this measurement, the wavelength and temperature dependence of the refractive index was investigated. The measurable wavelength region is limited to the visible light range of 400−680 nm. The refractive index of the KamLS, 300−380 nm, is complemented by the following equation.

$$f(\lambda) = a + \frac{b}{\lambda^2} + \frac{c}{\lambda^4} \tag{6.1}$$

where λ represents the wavelength. Fig. 6.6 shows the measured refractive index of the KamLS as a function of wavelength. In the actual temperature of the KamLS of 11.5°C, the refractive index is about 1.465 at $\lambda = 380$ nm.

Fig. 6.7 is measured attenuation length and the Rayleigh scattering length of the KamLS. The wavelength dependence of the Rayleigh scattering length is parameterized by the fourth power of the wavelength, shown as the orange line in the figure: 23.3 m Rayleigh scattering length at 400 nm wavelength. At $\lambda = 380$ nm, the attenuation length is about 11 m, and the Rayleigh scattering length is about 18 m. It can be seen that the scattering length is sufficiently larger than the attenuation length. Since the scattering process worsens vertex resolution, this is another essential performance required for scintillators.

Scintillators have the property of re-emission. In general, re-emission occurs with a certain probability when a solute absorbs scintillation light, has a specific time constant and is converted to light with a longer wavelength. The solute determines the probability and time constant, and there is also a slight influence on the solvent. In the case of KamLS, the absorption by PPO is dominant in the wavelength below 350 nm. The re-emission probability of PPO has been measured to be 80% at maximum, as shown in Fig. 6.8. The re-emission time constant has also been measured to be about 1.8 ns [111]. This time constant is smaller than the primary light of about 5 ns.

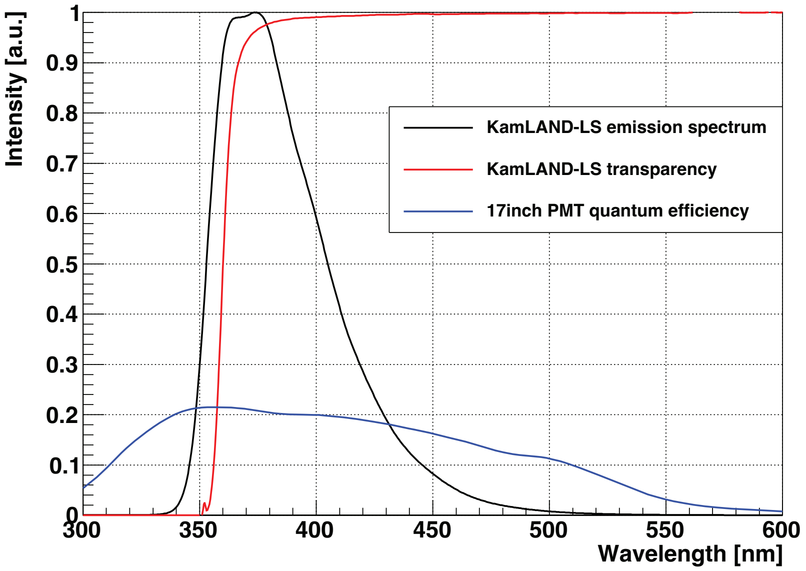

Figure 6.5: Emission spectrum and transparency of KamLAND liquid scintillator and quantum efficiency of 17-inch PMT. The black line represents the KamLAND liquid scintillator light emission spectrum, the red line represents the transparency of the KamLAND liquid scintillator at 9 cm, and the blue line represents the quantum efficiency of the 17-inch PMT used at KamLAND. The emission spectrum peaks at 375 nm wavelength where the PMT quantum efficiency and the KamLS transparency are high.

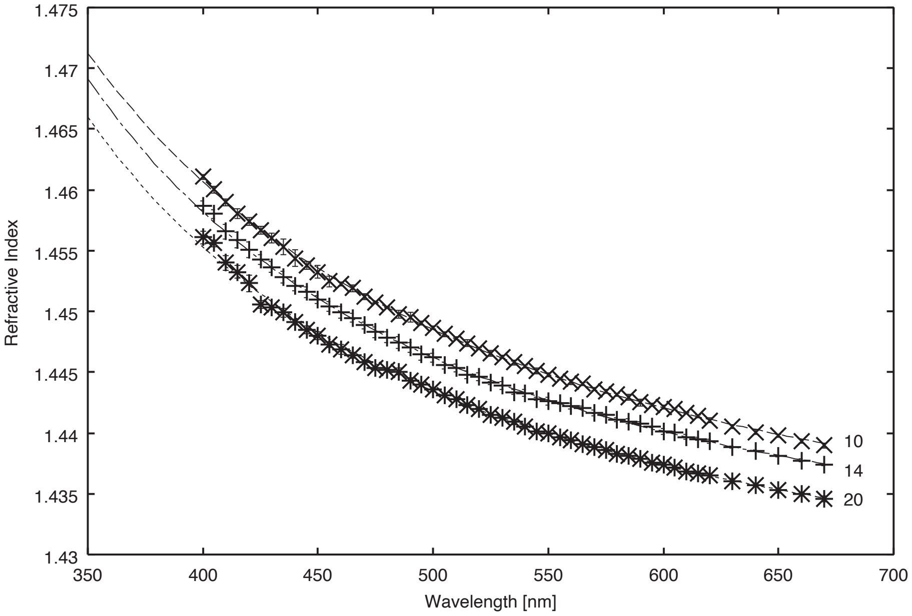

Figure 6.6: Refractive index of KamLAND liquid scintillator as a function of wavelength. The dots in 400−680 nm represent the measured values with different temperatures 10°C, 14°C, and 20°C. The black lines represent the fitting result with Eq. 6.1. The figure is from [109].

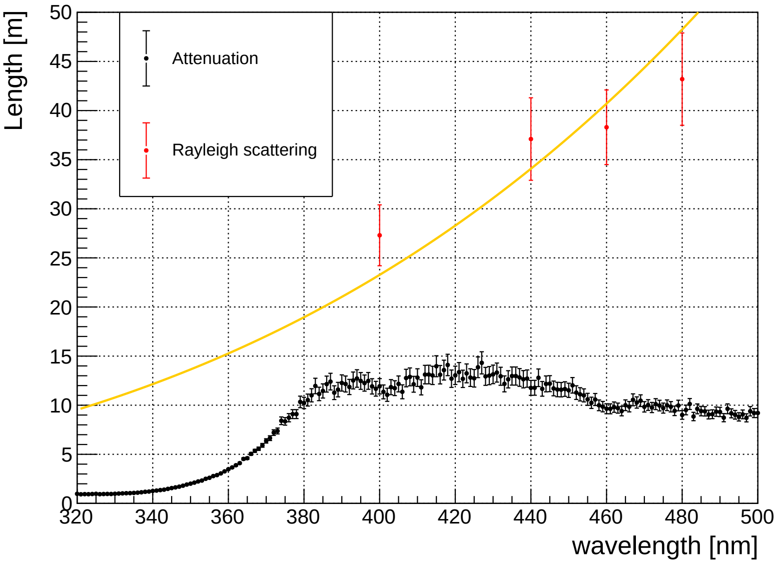

Figure 6.7: Attenuation length and Rayleigh scattering length of KamLAND liquid scintillator as a function of wavelength. The black dots show the attenuation length, and the red dots show the Rayleigh scattering length. These parameters are measured in the laboratory [110, 111]. The orange line is the fit result of the Rayleigh scattering length, assuming it is proportional to the fourth power of the wavelength: 23.3 m Rayleigh scattering length at 400 nm wavelength.

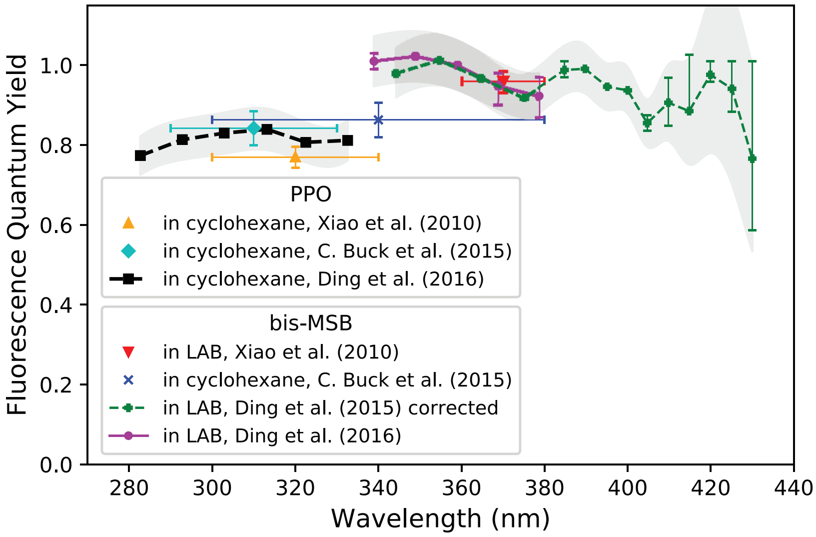

Figure 6.8: Measurments of fluorescence quantum yield of PPO and bis-MSB as a function of wavelength. It is almost 80% for PPO. The value is almost equivalent to the re-emission probability. The bis-MSB is another solute frequently used for scintillators. The figure is from [112].

Outer Balloon, Buffer Oil, and Acrylic Plate

The outer balloon consists of five layered transparent films with a 135 μm total thickness. The layer is composed of (EVOH/nylon/nylon/nylon/EVOH). The balloon is supported and suspended by 44 Kevlar ropes. The top and bottom parts of the balloon are densely covered with supporting systems, such as the Kevlar ropes. Therefore, the observed charge is relatively small around these parts by shadow effects. The shadow effects are corrected in the energy reconstruction.

The outside of the outer balloon is filled with buffer oil (BO). It is to shield external gamma rays from the radioactive impurities in the detector material, such as the stainless steel tank and PMTs. The BO consists of mineral oil as shown in Tab. 6.3, and the density is adjusted to be 0.04% lower than the KamLS. The BO emits a slight scintillation light of about 5% of the KamLS (~400 photon/MeV). The attenuation length of the BO is almost equal to the KamLS.

Acrylic plates are inserted just inside the PMT surfaces. The buffer oil on the inner side of these plates (outer balloon side) is called the inner buffer (IB), and one on the outer side (stainless tank side) is called the outer buffer (OB), These plates prevent radioactive impurities from PMTs and the stainless tank from entering the inner buffer. The Refractive indices of the BO and acrylic plate are shown in Fig. 6.9.

Table 6.3: Components of buffer oil

Material	Molecular formula	Density [g/cm^3]	Volume ratio
Dodecane	$C_{12}H_{26}$	0.749	53%
Isoparaffin	C_nH_{2n+2}	0.795	47%

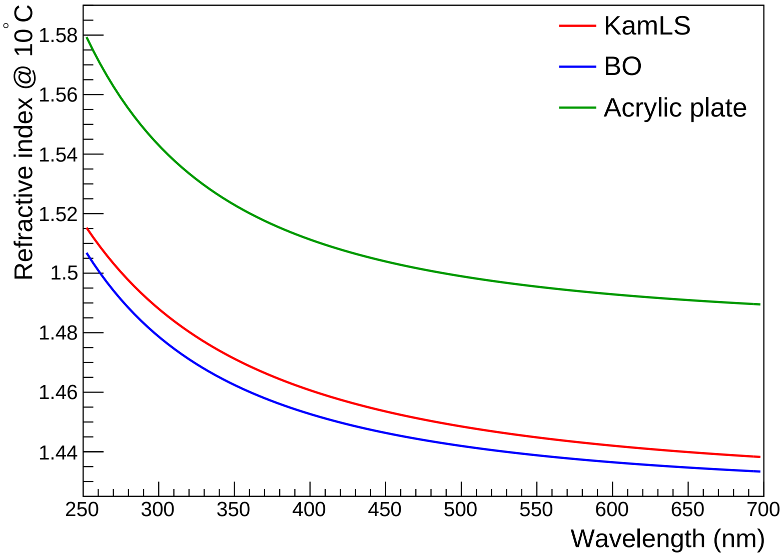

Figure 6.9: Best-fit refractive index of the KamLAND liquid scintillator, buffer oil, and acrylic plate as a function of wavelength at 10°. These are obtained by fitting the data with Eq. 6.1. The data is reproduced from [109].

ID PMTs

ID has 1325 17-inch PMTs, and 554 20-inch PMTs mounted on the stainless steel tank. The 20-inch PMTs were used in the Kamiokande experiment, while 17-inch PMTs were developed for the KamLAND. The 20-inch PMTs shown in Fig. 6.10c have Venetian blind type dynode. The 17-inch PMTs shown in Fig. 6.10a and 6.10b have box & line type dynode, which gives better timing resolution and charge linearity than the Venetian blind type. These two types of PMT have the same glass structure, but the outer radius region with poor timing resolution is masked for the 17-inch PMTs. The Transit Time Spread (T.T.S) is 3.5 ns in FWHM for 17-inch PMTs, while it is 7.7 ns for 20-inch PMTs. The Quantum Efficiency (QE) of the photo-cathode is 21% at 375 nm wavelength, as shown in Fig. 6.5. The total detector photo coverage is 34% with all ID PMTs and 22% with 17-inch PMTs only.

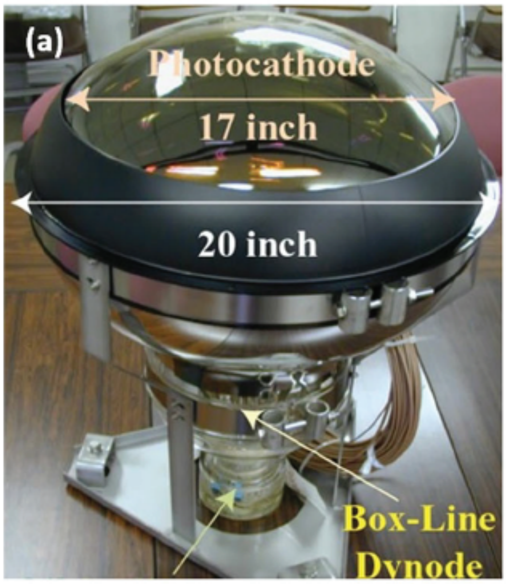

(a) Picture of 17-inch PMT

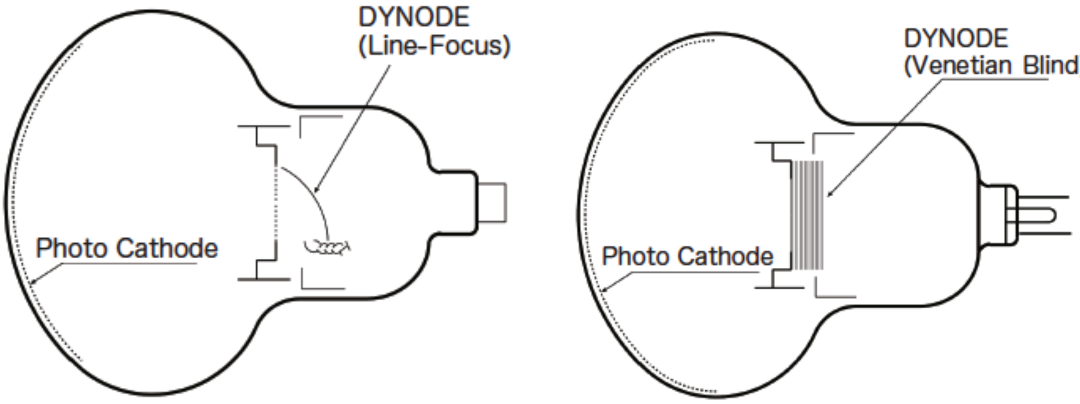

(b) 17-inch box & line PMT

(c) 20-inch Venetian blind PMT

Figure 6.10: Picture and schematic view of ID PMTs. (a) The mask that covers the outer radius region of 17-inch PMT is shown.

The charge linearity of 17-inch PMTs was measured using a dye laser in the laboratory. The result shows that the charge linearity is maintained up to about 1000 p.e., although there are individual differences [113]. At higher charges, the output tends to amplify without saturation, although the linearity is lost.

Besides the signal pulse, some phenomena can create spurious pulses smearing the timing information. These spurious pulses are classified as pre-pulse, after-pulse, and late-pulse and have typical time shifts in the hit timing. Fig. 6.11 shows the schematic view of these spurious pulses. A pre-pulse is generated when a photon passes through the photocathode and produces a photo-electron at the dynode. Since there is no process drifting the photo-electron in the PMT, the pre-pulse appears at an earlier time of about several ns than the signal pulse. An after-pulse is generated when a photo-electron ionizes residual gas (I^+), and the ions additionally generate photo-electrons at the photocathode. Since the ion takes time to drift into the photocathode, the after-pulse appears a few μs or more later than the signal pulse. The time difference is larger than the event time window of KamLAND. Therefore, it is reconstructed as a separate event. A late-pulse is caused by elastic or inelastic scattering of photo-electrons at the dynode. It produces a delay of several ns to several hundred ns from the timing of the signal pulse, being reconstructed as the same event.

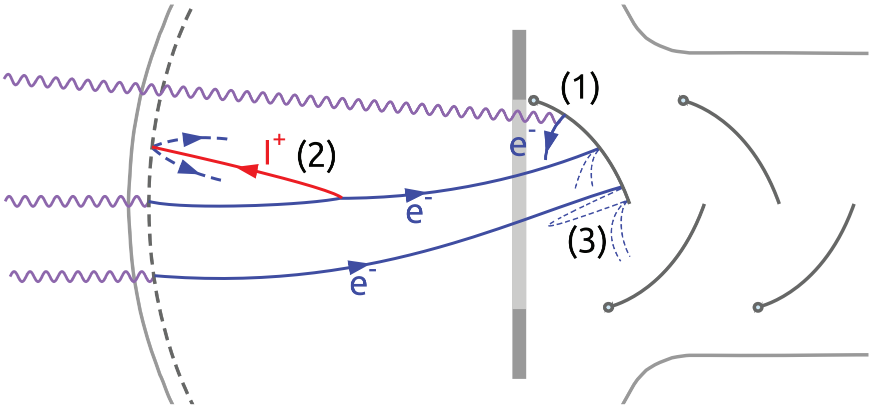

Figure 6.11: Schematic view of the pre-pulse, after-pulse, and late-pulse in a PMT. A pre-pulse (1) is generated when a photon passes through the photocathode and causes a photo-electron production at the dynode. An after-pulse (2) is generated when a photo-electron ionizes residual gas (I^+), and the ions additionally generate photo-electrons at the photocathode. A late-pulse (3) is caused by elastic or inelastic scattering of photo-electrons at the dynode. The figure is from [114].

Immediately after high-charge signals, a phenomenon called overshoot frequently happens. This phenomenon shifts in the baseline caused by the capacitors in the circuit being discharged. Fig. 6.12 shows the typical waveform of the overshoot. The baseline has shifted upward for several hundred μs, and small downward signals from the after-pulse also appear. The baseline shift effectively raises the threshold for hit discrimination so that a dead time occurs immediately after high-charge events, such as cosmic muons. The overshoot time depends on the signal intensity and PMTs, but it is maintained up to about 2 ms for particularly high-charge cosmic muons, called showing muons.

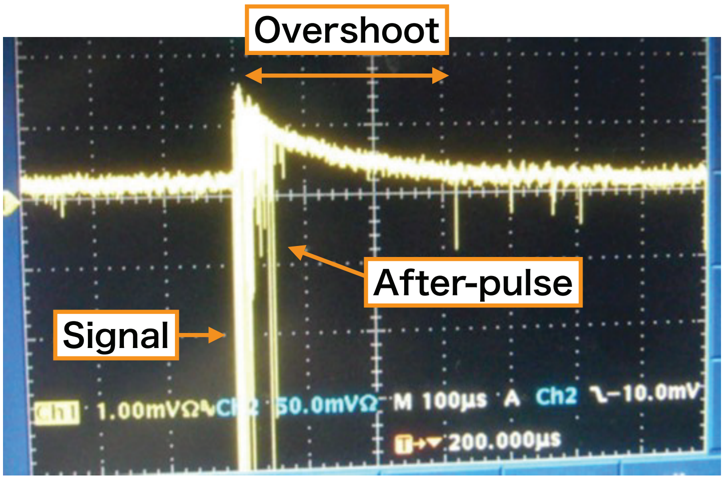

Figure 6.12: Typical waveform of overshoot. After a high-charge signal, the PMT waveform baseline shifts upward for about 300 μs. The after-pulses cause fine downward structures during the overshoot.

6.2.2 Outer Detector (OD)

The OD is a cylindrical water Cherenkov veto detector surrounding the stainless steel tank. The OD contains about 3000 m^3 of pure water. The rock cavern and stainless steel tank surface are covered with the Tyvek sheet to increase light collection efficiency.

An OD refurbishment campaign was carried out between Jan.−Jun. 2016 [115]. Since approximately 65% of the OD 20-inch PMTs had failed in 2016, the PMTs were replaced, and their arrangement was changed. Fig. 6.13 shows the changes made by the OD refurbishment. The new model of PMTs with high QE was newly installed. The boundary Tyvek, which was laid horizontally at $z = \pm 8.5$ m was removed to increase the area where the PMTs are sensitive. In order to cover the equator with the narrowest space and poorest veto efficiency, the angles of the PMTs near the equator, called rings 3 and 4, were changed.

OD 20-inch PMTs

Before the refurbishment, the number of OD 20-inch PMTs was 225; since then, it has been 140. The PMTs used from the beginning of KamLAND were also used in the Kamiokande experiment. These were replaced with new PMTs in the refurbishment since almost 65% of them died in 2016. The new PMTs have Venetian blind type dynode, high QE of 32%, and 5.8 ns T.T.S. in FWHM. The total number of OD PMTs was reduced because simulation studies have shown that the new PMTs can achieve sufficiently high veto efficiency even with the small number of PMTs.

OD 8-inch and 5-inch PMTs

In addition to the 20-inch PMTs, OD has sixteen 8-inch PMTs and six 5-inch PMTs. These PMTs are arranged to veto cosmic muon passing through the chimney, which is difficult to detect with the OD 20-inch PMTs only. 8-inch PMTs are located in the upper part of the buffer oil region, and 5-inch PMTs are located at the top of KamLAND and

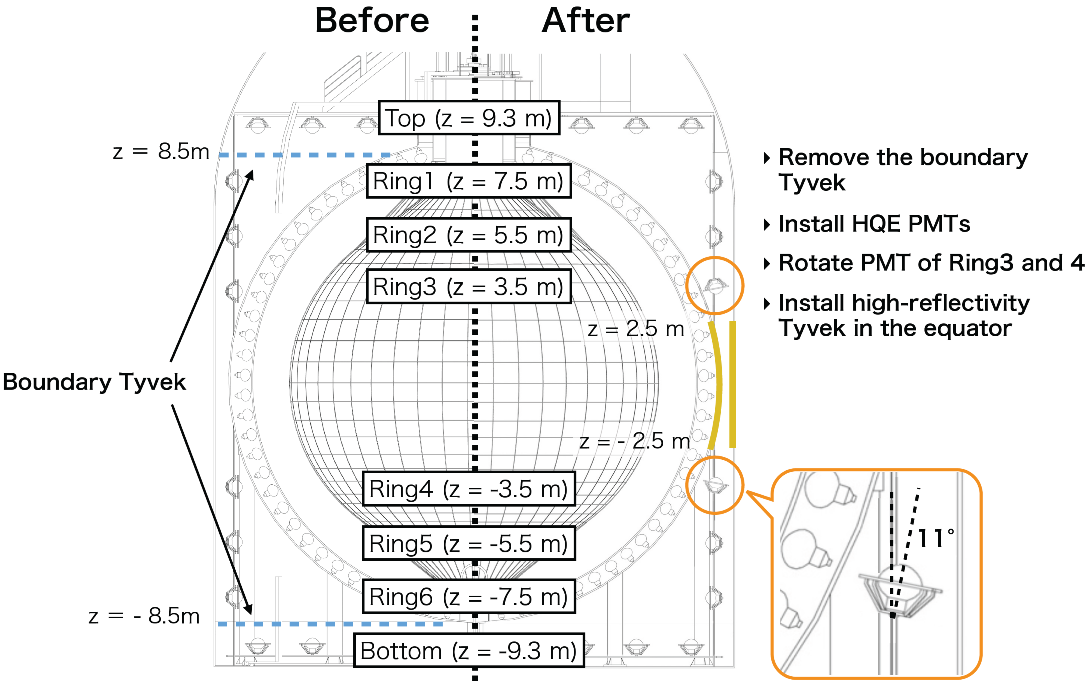

Figure 6.13: Major changes in OD refurbishment. The left (right) side shows the schematic view of OD before (after) the OD refurbishment. The PMTs are labeled top, ring 1 – 6, and bottom according to each z position. The boundary Tyvek located at $z = \pm 8.5$m was removed. New High QE PMTs and high-reflectivity Tyvek were installed. The angle of PMTs at rings 3 and 4 was also changed. The total number of OD PMTs was reduced.

detect scintillation light in the chimney as shown in Fig. 6.14. Although these PMTs are located in the ID, they are classified as OD PMTs for this purpose.

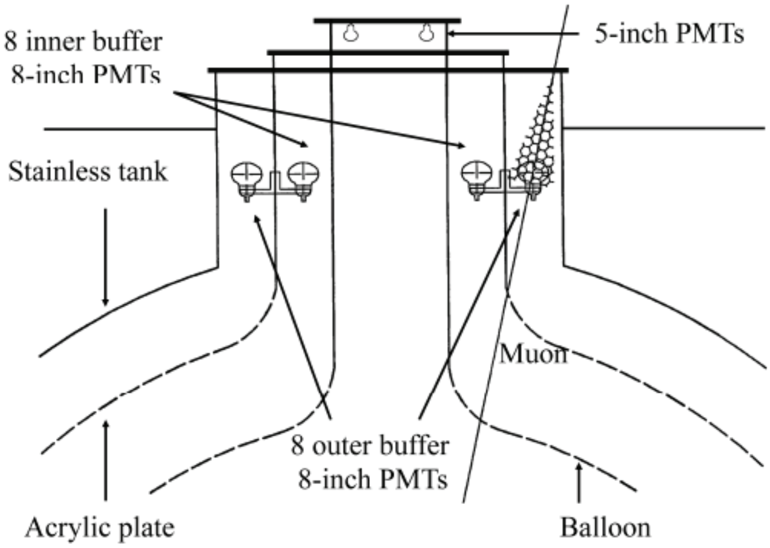

Figure 6.14: Arrangement of 8-inch PMTs and 5-inch PMTs. The 8-inch PMTs are in the buffer oil region. The 5-inch PMTs are at the top of the detector.

6.2.3 LS Purification

In the region of a few MeV, the primary target of the KamLAND, natural radioactive impurities in the KamLS were critical backgrounds. Two LS purification campaigns have been carried out to reduce these backgrounds. The first purification was performed in 2002 with a water extraction method. In the water extraction method, the polarized water molecule trapped heavy ions such as uranium and thorium in the LS. However, non-negligible contamination still remained. The second purification was performed in 2007 with a distillation method. The distillation method can remove the contamination more efficiently than the water extraction method. These two LS purification campaigns significantly and successfully reduced the radioactive background in a low-energy region of $\lesssim 1\,\mathrm{MeV}$.

6.2.4 KamLAND-Zen Detector

A project to search for the neutrinoless double-beta decay using ^{136}Xe at KamLAND, called the KamLAND-Zen experiment, was started in 2011. In this experiment, a nylon balloon filled with a xenon-loaded liquid scintillator was installed at the center of KamLAND, as shown in Fig. 6.15. In order to distinguish from the outer balloon, the balloon for the KamLAND-Zen experiment is called the mini-balloon (MIB). The KamLAND-Zen experiment has two phases: KamLAND-Zen 400 and KamLAND-Zen 800. The KamLAND-Zen 400 is from November 2011 to December 2015 [116], and the KamLAND-Zen 800 is from May 2019 to current. During the period between the KamLAND-Zen 400 and 800, there is no MIB in the detector, i.e., the detector status is the same as in the normal KamLAND experiment. The numbers 400 and 800 indicate the xenon amount in kg. The size of the MIB and the composition of the xenon-loaded liquid scintillator are different.

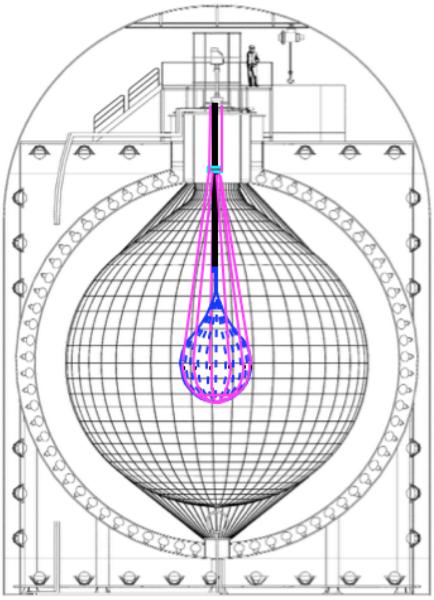

Figure 6.15: Schematic view of KamLAND-Zen experiment. A 154- or 192-cm radius nylon balloon filled with a xenon-loaded liquid scintillator is installed at the center of the KamLAND.

KamLAND-Zen 400

From November 2011 to December 2015, the KamLAND-Zen 400 experiment was carried out by installing a 154 cm radius nylon balloon filled with a xenon-loaded liquid scintillator at the center of the KamLAND. The MIB is made of the nylon-6 film with 25 μm. The components of the xenon-loaded liquid scintillator (XeLS) are shown in Tab. 6.4. The amount of PPO is higher than the KamLS because the quenching effect of xenon gives a smaller light yield. The XeLS still emits about 10% less light than the KamLS. The contribution of the neutrino-xenon interaction is small and negligible since the solubility of xenon is 2.9wt%, and the total amount of XeLS is about two orders of magnitude smaller than that of the KamLS.

Table 6.4: Components of xenon-loaded liquid scintillator for KamLAND-Zen 400

Material	Molecular formula	Density [g/cm^3]	Volume ratio
Decane	$C_{10}H_{22}$	0.735	82.3%
Pseudocumene	C_9H_{12}	0.875	17.7%
PPO	$C_{15}H_{11}NO$	-	2.7 [g/L]
Xenon	-	-	2.9% by weight

KamLAND-Zen 800

In August 2016, the KamLAND-Zen 800 experiment, an upgraded version of the KamLAND-Zen 400, was once started. KamLAND-Zen 800 has a larger MIB with a 192 cm radius and increases the exposure. However, after the installation, leakage on a MIB was found. The MIB was extracted on November 2016 without data taking of the KamLAND-Zen 800. This period, from August to November 2016, is called KamLAND-Zen failed 800.

After that, we again prepared a new MIB with the same design and installed it in May 2019. Since no leakage was found, the data taking of KamLAND-Zen 800 successfully started in January 2020. The XeLS components slightly differ from that of the KamLAND-Zen 400. This study does not deal with data from the KamLAND-Zen 800 period. Thus, detailed explanations are omitted.

6.3 Data Acquisition

In KamLAND, two DAQ (Data AcQuisition) systems are acquiring data in parallel. One is KamDAQ, which uses KamFEE (KamLAND Front End Electronics). It has been working since the beginning of KamLAND. Most physics analyses use data acquired by the KamDAQ. The other is MogDAQ, which uses MoGURA (Module for General Use Rapid Application). It was developed to reduce the dead time after cosmic muons. The basic design of both KamDAQ and MogDAQ are the same. The DAQ system comprises Front End Electronics (FEE) and a trigger circuit. The FEE is for data acquisition, while the trigger circuit determines data acquisition based on hit information. This study only uses the KamDAQ data, not uses MogDAQ data.

6.3.1 KamDAQ (KamFEE)

The KamDAQ uses KamFEE in data collection. The KamFEE is a VME board that can connect up to 12 PMTs and runs with a 40 MHz clock. Fig. 6.16 shows the schematic diagram of KamFEE. The PMT waveforms are divided into two paths: The path that sends the hit information to the trigger circuit and the path that acquires the waveform. On the path to recording the waveform, there are three amplifiers (gains) with different amplification factors to achieve dynamic range: $\times 20$, $\times 4$, and $\times 0.5$ as design values. They are called H (High), M (Middle), and L (Low) gain, respectively. The amplified waveform is digitized by ATWD (Analog Transient Waveform Digitizer) with 10-bit, 1.49 ns intervals, and 128 times sampling. Since it takes about 30 μs for ATWD to digitize the signal, the dead time is reduced by preparing two ATWDs (A and B) on each channel. On the other hand, the path that sends the hit information to the trigger circuit has a hardware threshold corresponding to about 0.3 p.e. by the discriminator. If the waveform height exceeds the threshold, hit information is sent to the trigger circuit for 125 ns.

The trigger circuit sums the hit information ($Nsum$) sent from the KamFEE boards. If the $Nsum$ exceeds a certain threshold, a trigger is issued, and the ATWDs digitize the waveform. There are various trigger types in KamFEE shown in Appendix B.

6.3.2 MogDAQ (MoGURA)

The MogDAQ uses MoGURA (Module for General Use Rapid Application) as a FEE. The MoGURA was developed to reduce the dead time after cosmic muon caused by high-rate afterpulses and overshoots. The BLR (BaseLine Restorer), installed before the MoGURA board, reduces the overshoot after high-charge events. As a result, the detection efficiency of neutron capture events after cosmic muon events is higher than that of KamFEE. It runs with a 50 MHz clock, and there are three types of gain to achieve dynamic range: $\times 120$, $\times 24$, $\times 2.4$, and $\times 0.24$ as design values.

The data calibration of MoGURA is still under research and development. Recently, the calibration of vertex reconstruction has been advanced, and the accuracy has been greatly improved. In the future, it will be necessary to develop a method to identify

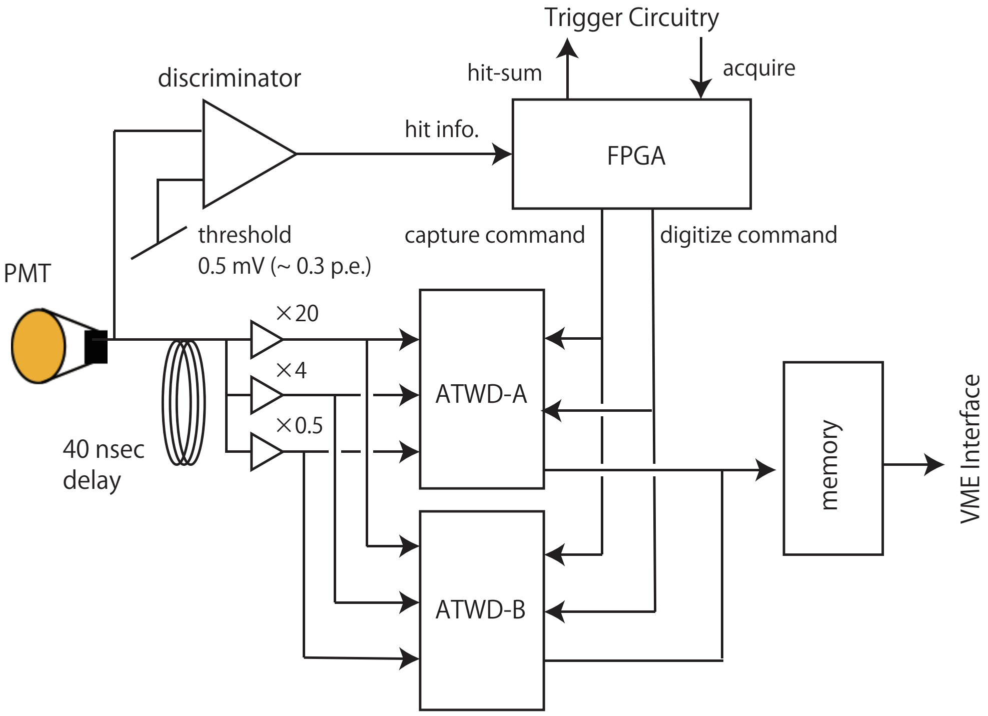

Figure 6.16: KamFEE diagram. There are three different gains (H, M, and L gains) and two ATWDs (A and B) for each PMT. If the waveform height exceeds the threshold, hit information is sent to the trigger circuit for 125 ns.

the dead time during data taking that could not be performed correctly due to hardware troubles.

6.4 Calibration System

Various radioactive sources, lasers, and diffuser balls have been developed to calibrate and validate the KamLAND data. The radioactive sources have been used to calibrate vertex and energy reconstruction for events of a few MeV (Sec. 6.4.1). There are two types of calibrations using the source: Z-axis and 4π calibrations. In the Z-axis calibration, the source is placed along various z positions. The 4π calibration includes full volume. On the other hand, calibration using a laser and diffuser ball (referred to as “dye-laser calibration”) aims to calibrate the timing response and the charge linearity.

6.4.1 Radioactive Source Calibration

Tab. 6.5 shows a summary of the radioactive sources used in KamLAND. Level diagrams of these sources are summarized in Appendix C. The energy dependence of event reconstruction quality is investigated by using various sources. In addition to the radioactive sources, ^{40}K and neutron capture events during physics data are frequently used. The ^{40}K is mainly from radiation impurities of balloons and has very high statistics. Neutrons produced by cosmic muon spallations or neutron emissions from ^{8}He/^{9}Li are used for neutron capture. As seen in Tab. 6.5, the energy range covered by the radioactive sources is up to a few MeV. The dye-laser calibration is performed for higher energy regions as described in Sec. 6.4.2. The beta decay of ^{12}B and ^{12}N is also used to check the validity of the energy around 15 MeV[1].

Table 6.5: Calibration radioactive sources used in KamLAND. The last two columns, ^{40}K and neutron capture, are not radioactive sources but are used for calibration. The ^{40}K is mainly from radiation impurities of ballons. For neutron capture, neutrons produced by cosmic muon spallations are mainly used.

Source	Particle type	Energy (MeV)	Hallf life
^{203}Hg	γ	0.2792	46.61 days
^{137}Cs	γ	0.6616	30.07 years
^{65}Zn	γ	1.1116	244.3 days
^{68}Ge	γ	0.511× 2	270.8 days
^{60}Co	γ	1.1732, 1.3325	5.271 years
^{241}Am^{9}Be	$\gamma,\ n$	γ: 4.4, $n : < 10$	432 years
^{210}Po^{13}C	$\gamma,\ n$	$\gamma : 6.13$, $n : < 7.5$	22 years
^{40}K	e^-	1.3111	-
$np \rightarrow d\gamma$	γ	2.2246	-

Z-axis Calibration

In the Z-axis calibration, the source is installed from the chimney and placed along the z-axis. The X and Y positions of the source are fixed at the center, i.e., $(x, y) = (0, 0)$. The source is typically placed every 50 cm from -5.5 m to $+5.5$ m along the z-axis. A composite source, in which multiple sources are placed in a single holder, was frequently used. The composite source has the advantage of avoiding misalignments by reinstallation. In addition, since it does not need to restart the DAQ, data with the same detector response can be obtained. These two features make it possible to evaluate the energy and vertex reconstruction quality stably. In the composite source data analysis, the energy spectra are used to separate the contribution of each source. Therefore, if there is a source whose intensity is weaker than the others, there is a disadvantage in that the influence of the spectra of the other sources cannot be neglected.

Tab. 6.5 shows a summary of major Z-axis calibration campaigns. We choose campaigns representing the four periods used in this study. In the campaign in 2015 during the KamLAND-Zen 400 period, the composite source was installed into the inside of the MIB. Fig. 6.17 shows obtained energy spectra of the composite source in 2009 and 2018. Both data show weak ^{68}Ge intensity, leading to large errors in the estimations of vertex and energy deviation for ^{68}Ge. Furthermore, the energy peak of ^{68}Ge is strongly influenced by the tail of ^{137}Ce. This influence biases the energy resolution for ^{68}Ge. The details are discussed in Sec. 7.6.4.

4π Calibration

Full-volume calibrations, so-called the 4π calibration, have also been performed [117,118]. Fig. 6.18 shows the schematic view of the 4π calibration. A pole was installed into the KamLAND. The radioactive sources are attached at various points on the pole. The event reconstruction quality throughout the fiducial volume was calibrated and estimated by

---

[1] These signals are not used for calibration.

Table 6.6: Summary of major Z-axis calibration campaigns. We choose campaigns representing the four periods used in this study. In 2018 and 2015, a composite source with three sources with ^{137}Cs/^{68}Ge/^{60}Co was installed. For others, a single ^{137}Cs source and a composite source with ^{68}Ge/^{60}Co was used. The intensity of ^{68}Ge was weak in 2009 and 2018.

Date	Detector status	Source
Sep. 2006	Before purification	^{137}Cs and ^{68}Ge/^{60}Co
Jul. 2009	After purification	^{137}Cs and ^{68}Ge/^{60}Co
Feb. 2011	Before KamLAND-Zen 400	^{137}Cs and ^{68}Ge/^{60}Co
Oct. 2015	During KamLAND-Zen 400	^{137}Cs/^{68}Ge/^{60}Co
Jan. 2018	After OD refurbishment	^{137}Cs/^{68}Ge/^{60}Co

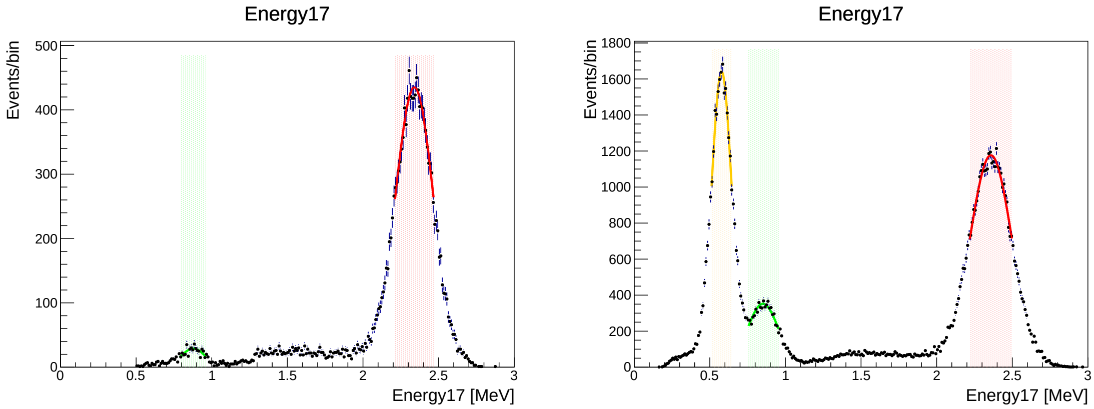

(a) After purification (Jul. 2009)

(b) After OD refurbishment (Jan. 2018)

Figure 6.17: Visible energy spectra of a composite source in 2009 and 2018. We used a composite source of ^{68}Ge/^{60}Co(/^{137}Cs) in 2009 (2018).
(a) There are two peaks corresponding to ^{68}Ge (green) and ^{60}Co (red). The intensity of ^{68}Ge is weak, but the bias due to the tail of ^{60}Co is not critical.
(b) There are three peaks corresponding to ^{137}Cs (orange), ^{68}Ge (green), and ^{60}Co (red). Since the intensity of ^{68}Ge is weak, the energy peak of ^{68}Ge is strongly influenced by the tail of ^{137}Cs. This biases the energy resolution of ^{68}Ge as shown in Fig. 7.25d.

adjusting the orientation and length of the pole. The 4π calibration was carried out in 2006 and 2011.

6.4.2 Dye-Laser Calibration

A dye-laser calibration was also carried out to investigate the timing response and charge linearity. Fig. 6.19 shows a schematic view of dye-laser calibration. This calibration used a dye-laser with 500 nm wavelength less affected by re-emission, scattering, and absorption. The laser output is stable within about 10%. A diffuser ball that diffuses the light isotropically was installed in the center of KamLAND. By changing the ND filter, data with various light intensities of $\mathcal{O}(1-10^3)$ p.e./PMT can be obtained.

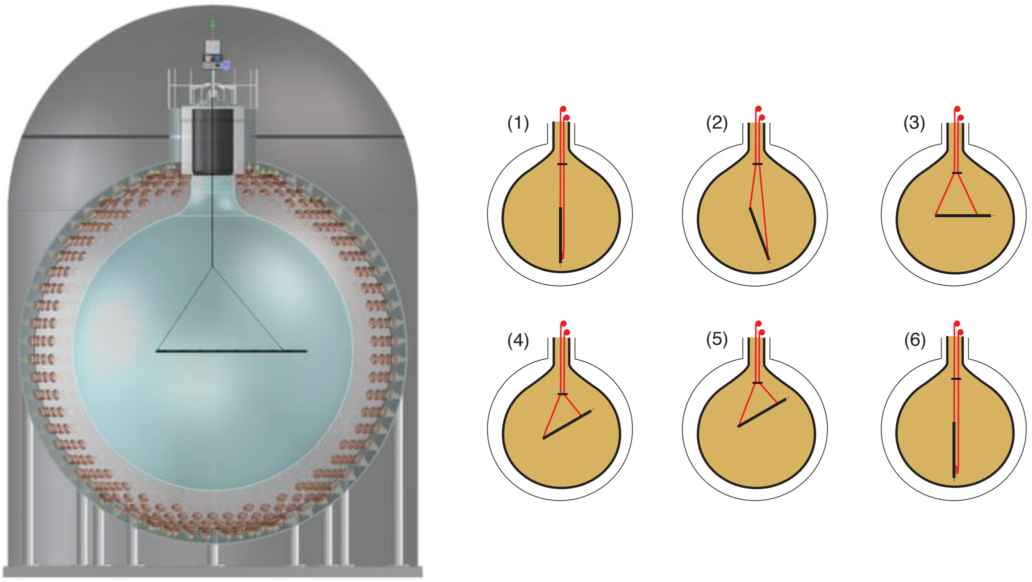

Figure 6.18: Schematic view of 4π calibration. The event reconstruction quality throughout the fiducial volume was calibrated and estimated by adjusting the orientation and length of the pole. The figure is from [117].

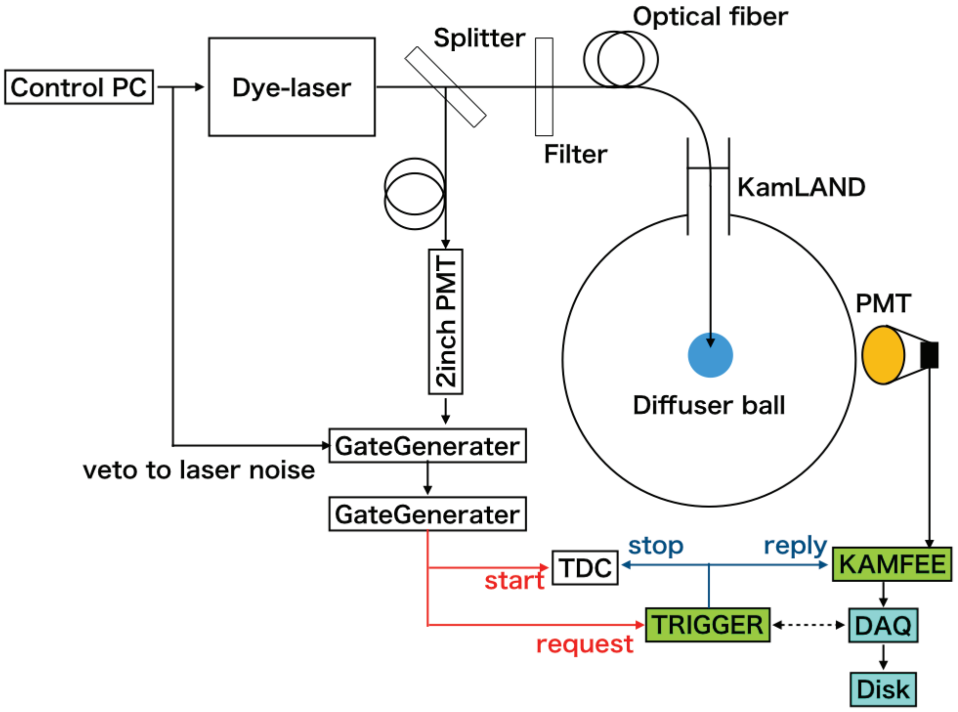

Figure 6.19: Schematic view of dye-laser calibration. The wavelength of the dye-laser is 500 nm which is less affected by re-emission, scattering, and absorption. The pulse width is 1.2 ns. The light intensity can be easily changed by using a rotating ND filter. The figure is from [119].

Chapter 7

Event Reconstruction and Detector Calibration

KamLAND has two data acquisition systems as described in Sec. 6.3. This chapter only discusses event reconstruction using the KamDAQ (KamFEE) since the MogDAQ (MogURA) is not used in the analysis. We extract various physics parameters, such as vertex and visible energy, from the acquired PMT waveforms through the following sequential event reconstruction processes.

1. Waveform analysis (Sec. 7.1)

   Hit timing and charge information are extracted from acquired PMT waveforms.

2. Charge and Time correction (Sec. 7.2 and 7.3)

   Various corrections for the obtained time and charge are made to consider individual differences in the PMTs and KamFEE channels. In addition, to improve the quality of the event reconstruction, PMTs that have bad responses are identified, and those are masked in the following processes.

3. Muon track reconstruction (Sec. 7.4)

   Tracks of cosmic muons are reconstructed.

4. Vertex reconstruction (Sec. 7.5)

   Event vertices are reconstructed assuming the point source.

5. Energy reconstruction (Sec. 7.6)

   Visible energies are reconstructed using the vertices determined in the previous process.

While the ID uses time and charge information in the event reconstruction, OD uses only hit information. Various corrections are made to consider individual differences in the PMTs and KamFEE channels. For clarity, we should distinguish between the corrections for each PMT and those for each ATWD or gain since there is one amplifier but two ATWDs for one PMT. This dissertation uses the term “PMT” or “cable” when only the PMT needs to be distinguished and the term “channel” when the ATWD (A/B) needs to be distinguished.

7.1 Waveform Analysis

At first, time and charge information is extracted from PMT waveforms acquired by the ATWDs. The digitized waveform has 128 samplings with 1.49 ns intervals. The time width of the sampling bins is calibrated by using 40 MHz clock, as shown in the left panel of Fig. 7.1. This calibration is performed for each channel at the beginning of each run.

The PMT waveforms have particular offsets called the pedestal. In order to evaluate this offset, 50 pedestal waveforms are obtained for each channel at the beginning of each run. After subtracting the pedestal, the waveform is smoothed using its running-averaged first derivatives to avoid high-frequency noises. The baseline is adjusted event by event to concentrate at zero because the baseline can shift event by event due to overshoots. The rise and peak of pulses are determined from the derivatives. The rise of the pulse, called the "leading edge", corresponds to the hit timing of the pulse. The leading edge of the first pulse is used as the hit timing of the first arrival photon at the PMT. The charge is defined as the total area of the waveform in the unit of [ADC counts]. The value is normalized by the area of one photo-electron (p.e.) pulse.

In the following event reconstruction, only two parameters obtained from the waveform analysis are used: The hit timing of the first arrival photon and the total charge for each PMT. If multiple p.e. signals are in a single waveform, the hit timing of the first arrival photon and the total p.e. counts are used. We have developed a more sophisticated waveform analysis that separates multiple p.e. signals and determines the hit time and charge for each signal. However, it is not used in this study.

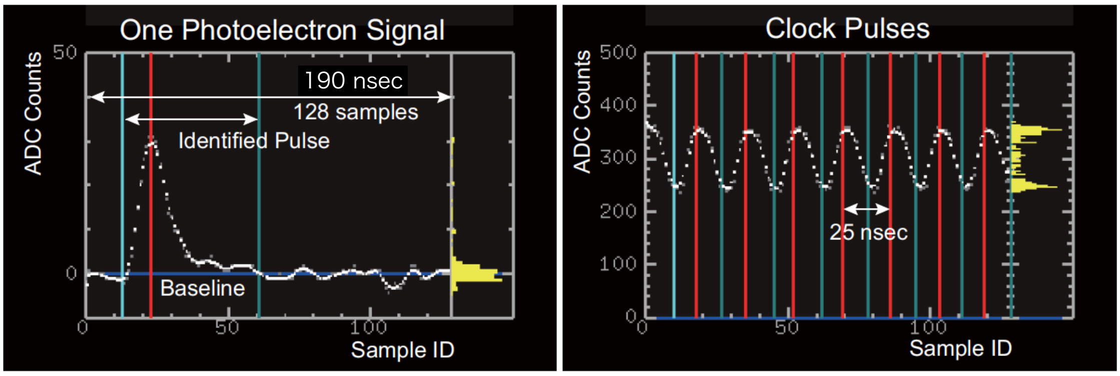

Figure 7.1: Typical one photo-electron waveform (left) and pulse of 40 MHz clock (right). The vertical red lines represent the peak position, and the vertical cyan lines are the start and end of the pulses. Derivatives of the waveform determine the timing information. The horizontal blue lines represent the baseline. The total waveform sampling width is 190 ns.

7.2 Charge Calibration

The charge calibration is important for improving energy reconstruction quality. The charge is defined as the following equation.

$$(\text{Charge [p.e.]}) = \frac{(\text{ADC sum [counts]})}{(\text{ADC sum of one p.e. [counts/p.e.]})} \times (\text{Gain correction factor}), \quad (7.1)$$

where the gain correction factor can be given as follows in design values.

$$\text{(Gain correction factor)} = \begin{cases} 1.0 & \text{(H gain)} \\ 4.86 & \text{(M gain)} \\ 41.86 & \text{(L gain).} \end{cases} \tag{7.2}$$

The ADC sum is calculated as the total area of the waveform in the previous process, waveform analysis. The ADC sum of one p.e. signal has individual differences and time variations. This parameter is calibrated run by run using physics data (Sec. 7.2.1). The gain correction factor corresponds to the amplification factor of the amplifier of the Kam-FEE. As shown in Fig. 6.16, FEE has three amplifiers, H, M, and L gains, with different factors. The values shown in Eq. 7.2 are the design values, which differ from actual values. Furthermore, there are individual differences in amplifier and transmission distance, so these factors are needed to be calibrated. Since the ADC sum of one p.e. is calibrated using data acquired by the H gain, the factor of the H gain is defined as 1. The dye-laser calibration calibrates those of the M and L gains (Sec. 7.2.2).

The M gain covers middle charge regions such as $50 - 200\,$p.e., while the L gain covers high charge regions above 200 p.e. The charge linearity of the 17-inch PMT itself is confirmed to be maintained up to about 1000 p.e. by the laboratory measurement. Therefore, the accuracy of the gain correction factors is essential for the charge linearity of the KamLAND data.

7.2.1 One photo-electron (p.e.) Gain Correction

The ADC sum of one p.e. is corrected run by run and channel by channel using physics data. The one p.e. events are selected with the following criteria to obtain one p.e. charge distribution. These criteria aim to select low-energy events far from the PMT to reduce multi-p.e. contributions.

- Run time $\geq 10\,$hours
- Muon veto and 2 msec veto after muon
- $100\,\mu$s veto after all events
- $120 < ((Number of hit ID PMTs) < 230$
- (Distance between PMT and the event) $\geq 5.6\,$m
- Single peak in the waveform

Fig. 7.2 shows the typical one p.e. distributions of the 17-inch and 20-inch PMTs. When obtaining the distributions, a certain constant ADC sum of one p.e is assumed. There is a clear peak corresponding to the one p.e. signals for the 17-inch PMT, while it is not in the 20-inch PMT due to the poor charge resolution. For the 17-inch PMT, the peak position is determined with the Gaussian fitting and calibrate the one p.e. gain by multiplying a factor so that the peak position equals one [1].

---

[1] Therefore, strictly speaking, the ADC sum of one p.e. in Eq. 7.1 is defined as

$$\begin{aligned}\text{(ADC sum of one p.e. [counts/p.e.])} =& \text{(A certain constant ADC sum of one p.e. [counts/p.e])} \\ & \times \text{(The peak position of the Gaussian fitting).}\end{aligned} \tag{7.3}$$

On the other hand, for the 20-inch PMTs, an alternative method is prepared because it does not have a clear one p.e. peak. The relative charge from neighbor 17-inch PMTs to the 20-inch PMT (Q_{Ratio}) is defined as

$$Q_{Ratio} = \frac{\text{Charge of the 20-inch PMT}}{\text{Average charge of neighbor eight 17-inch PMTs}} \left(\frac{17}{20}\right)^2, \tag{7.4}$$

where the factor $(17/20)^2$ corresponds to the difference in the photo-cathode area. By fitting the charge distribution of Q_{Ratio}, the one p.e. calibration for the 20-inch PMTs is made.

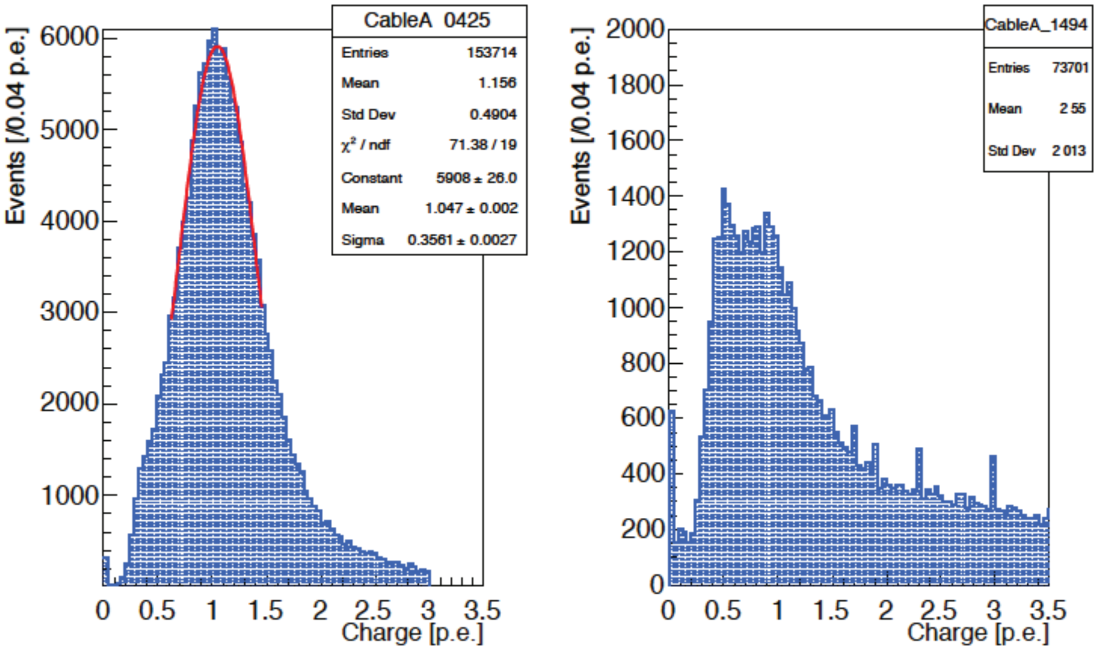

Figure 7.2: Typical one p.e. distribution of the 17-inch (left) and 20-inch (right) PMTs. The 17-inch PMT shows a clear peak, but the 20-inch PMT does not due to the poor charge resolution. The red line shown in the 17-inch PMT represents the fitting result with the Gaussian. The figure is from [119].

7.2.2 Calibration of Gain Correction Factors using Dye-Laser

The gain correction factors of M and L gains are calibrated channel by channel using the dye-laser calibration data (see Sec. 6.4.2 for detailed setup). We established this calibration to improve the charge linearity. The 20-inch PMTs have poor charge resolution and linearity and are not used to analyze high-energy events. Therefore, this calibration is performed only for the 17-inch PMTs.

Fig. 7.3 shows a relation between the observed charge and event time obtained by a certain channel. The data by 12 ND filter settings giving different light intensities were acquired. The observed charge shown here is calculated assuming the design values of the gain correction factor. This calibration uses the data acquired within the period represented by the red and violet lines in the figure. These periods correspond to 0.6 hours for the 1st ND filter setting and 0.05 hours for others.

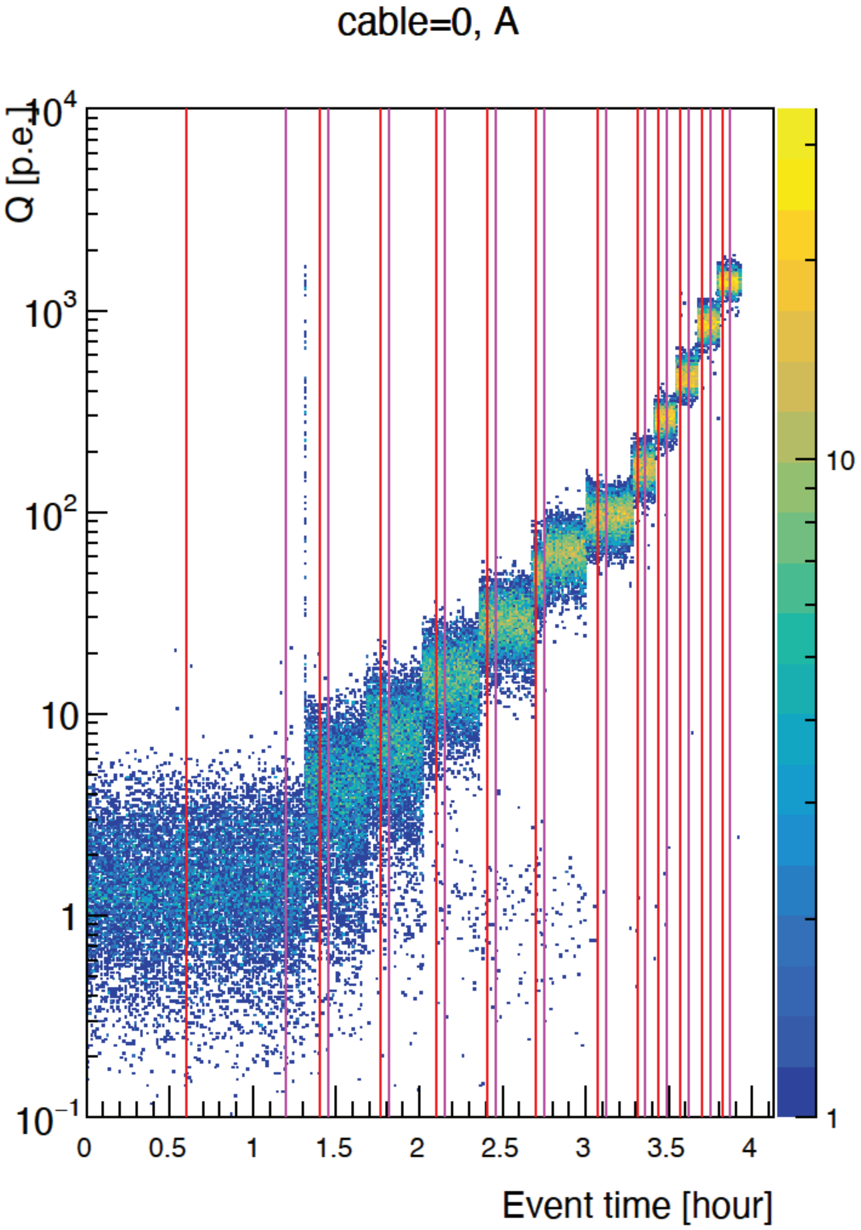

Figure 7.3: Charge and event time in the dye-laser calibration data acquired by a certain channel (A channel of cable number 0). There were 12 ND filter settings, giving different light intensities. Y-axis shows the observed charge by the channel, assuming the design values of the gain correction factor. All channels show similar trends. The data acquired within the red and violet lines are used in the calibration.

This calibration optimizes the gain correction factors for the M and L gains by finding the relation between the observed and expected charge for each filter setting. The observed charge is simply determined by the average of the observed charge over each filter setting. On the other hand, the expected charge is calculated through several steps: From the data of the filter setting with the lowest light intensity, the hit probability is calculated and converted to the expected charge using a model. The expected charge is then scaled using the filter transmittance, considering the threshold effects and obtaining those for the other filter settings.

Although the amplifiers are common to A and B channels, we found systematic differences between A and B, probably due to differences in the transmission paths of A and B channels on the board. Therefore, this calibration is performed for each channel.

Parameterize the No-hit Probability

By using low-energy events that do not saturate the hit, the relation between the hit (or no-hit) probability and the expected charge can be modeled ¿ At first, the relation between no-hit probability and the expected charge is parameterized using physics data. The expected charge is calculated from the reconstructed vertex considering the geometric structure of detectors (See Sec. 7.6.3 for detail). Note that the threshold effect is not considered in this calculation.

Fig. 7.4 shows the typical relation between the expected charge and no-hit probability calculated from physics events for a certain PMT. We have developed three parameterizations of the no-hit probability as a function of the expected charge $P_{no-hit}(\mu)$.

$$P_{no-hit}(\mu) = (1+\epsilon\mu)e^{-\mu} \qquad (\epsilon = 0.10), \tag{7.5}$$

$$P_{no-hit}(\mu) = (1+\epsilon\mu)e^{-\mu} \qquad (\epsilon \text{ is fitted as a free parameter}), \tag{7.6}$$

$$P_{no-hit}(\mu) = \left(1+\epsilon_1\mu+\epsilon_2\frac{\mu^2}{2!}+\epsilon_3\frac{\mu^3}{3!}\right)e^{-\lambda\mu}, \tag{7.7}$$

where μ represents the expected charge. Eq. 7.5 and 7.6 assume that the number of observed photo-electron follows the Poisson distribution, and inefficiency (ϵ) occurs only for one p.e., i.e., the inefficiency for multi-p.e. is neglected. The difference between Eq. 7.5 (blue line in the figure) and 7.6 (magenta line in the figure) is whether ϵ is fixed at 0.10 or obtained by fitting. Eq. 7.7 is an empirical extension proposed by Miyake [120]. There are four free parameters: ϵ_1, ϵ_2, ϵ_3 and λ. The Miyake model gives a better description of the data than others, so this analysis adopts the Miyake model shown as the red line in Fig. 7.4. The no-hit probability for each 17-inch PMTs is parameterized with the Miyake model using the physics data immediately before the dye-laser calibration campaign.

Convert the No-hit Probability to the Expected Charge

When determining the expected charge using the no-hit probability, it is necessary to use a region where the no-hit probability is large enough, i.e., the hits are not saturated. The no-hit probability is calculated using the period of the first filter setting with the lowest light intensity during the dye-laser calibration data. Then, the no-hit probability is converted to the expected charge using the Miyake model.

The expected charge obtained here does not include the threshold effect, which is negligible in the high-charge region, but not in the one p.e. region. Since the laser calibration data is about one p.e. in the first filter setting, the threshold effect should be

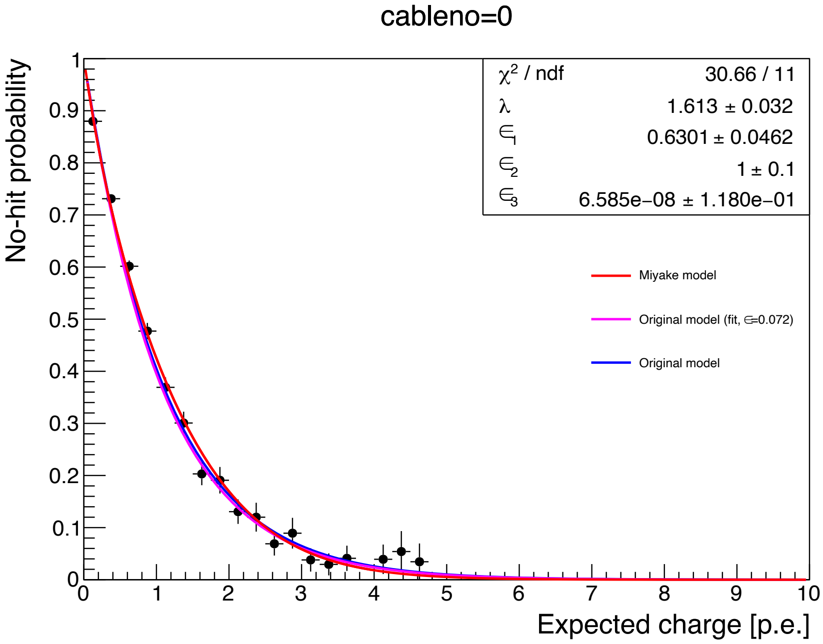

Figure 7.4: Typical relation between no-hit probability and expected charge. The expected charge without threshold effect is shown in the X-axis. We have developed several parameterizations of the no-hit probability as a function of the expected charge (Eq. 7.5, 7.6, and 7.7). This analysis uses the Miyake model (the red line) [120], which gives better agreement with the data than others.

additionally applied for this period. On the other hand, it can be neglected for other filter settings, which have more than five p.e. The threshold effect is parameterized using the radioactive source calibration data:

$$\frac{Q_{expected}}{Q_{expected-no-threshold}} = [1 - \delta \times \exp(Q_{expected-no-threshold})] \,, \tag{7.8}$$

where $Q_{expected(-no-threshold)}$ represents the expected charge with (without) the threshold effect, and $\delta = 0.05$ is determined from the calibration data. Fig. 7.5 shows the relation between $Q_{expected}$ and $Q_{expected-no-threshold}$ with $\delta = 0.05$. Finally, the expected charge for the first filter setting, i.e., $Q_{expected}$, is obtained using the Eq. 7.8 As for others, neglecting the threshold effect, the expected charge for the first filter setting is scaled with the transmittance of the ND filter (Fig. 7.6).

Relation between the Observed and Expected Charge

Fig. 7.7a shows the typical relationship between the observed and expected charge with design values of the gain correction factor. The errors are calculated from the laser stability (10%) and statistical uncertainty in obtaining the no-hit probability. When we assume the design values, there are clear gaps at the boundaries of gains, making the charge linearity worse. Furthermore, although the amplifiers are common, we found systematic differences between A and B channels. The differences were found in the cable shown in Fig. 7.7 and in many other cables. We consider that the geometrical difference in the transmission paths to the ATWD A and B channels causes the differences.

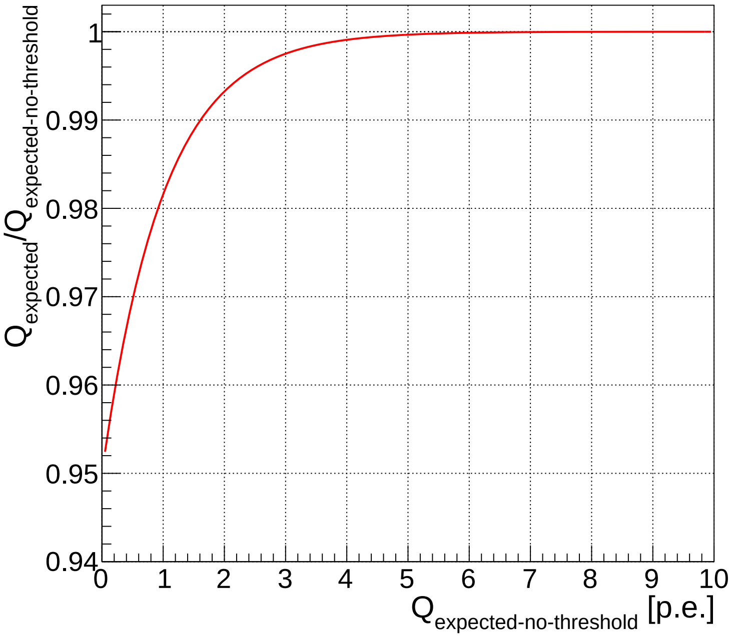

Figure 7.5: Relation between the expected charge with ($Q_{expected}$) and without ($Q_{expected-no-threshold}$) threshold effect. The relation is parameterized by Eq. 7.8 with $\delta = 0.05$.

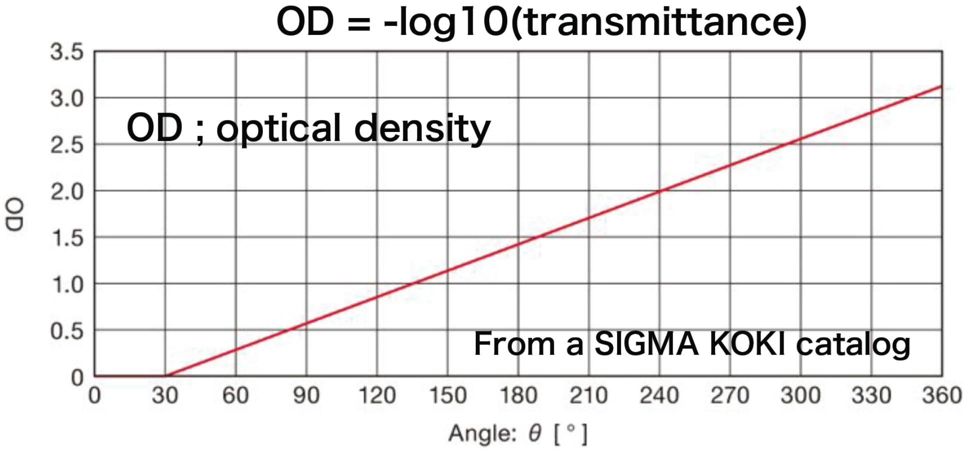

Figure 7.6: Relation between the optical density (OD) and rotation angle of the rotating ND filter used in the dye-laser calibration. The relation between the optical density and the transmittance is as follows: (optical density) $= -\log_{10}$(transmittance). The figure is from [121]

In order to reduce the charge non-linearity, the gain correction factors are calibrated by minimizing the Chi-squared from $Q_{obs}/Q_{exp} = 1$ for each channel. Fig. 7.7b shows the relation between observed and expected charge after the calibration. The same cable (cable number zero) as in Fig.7.7a is shown. The best-fit gain correction factors are as follows:

$$
(\text{Gain correction factor}) = \begin{cases} 3.99 & (\text{M gain, A channel}) \\ 34.59 & (\text{L gain, A channel}) \\ 4.00 & (\text{M gain, B channel}) \\ 28.93 & (\text{L gain, B channel}) \end{cases} \tag{7.9}
$$

Almost all cables and channels were found to prefer smaller values than the design values. By adopting the best-fit factors, the gaps that appear in Fig. 7.7a are reduced, and the charge linearity is maintained up to about 1000 p.e. within the uncertainty.

The observed charge of 1000 p.e. for 17-inch PMTs corresponds to ∼ 6 GeV in visible energy, assuming an event at the center of KamLAND. In this study, events below 1 GeV within a 5 m radius are selected, giving negligible contribution of observed charge higher than 1000 p.e.

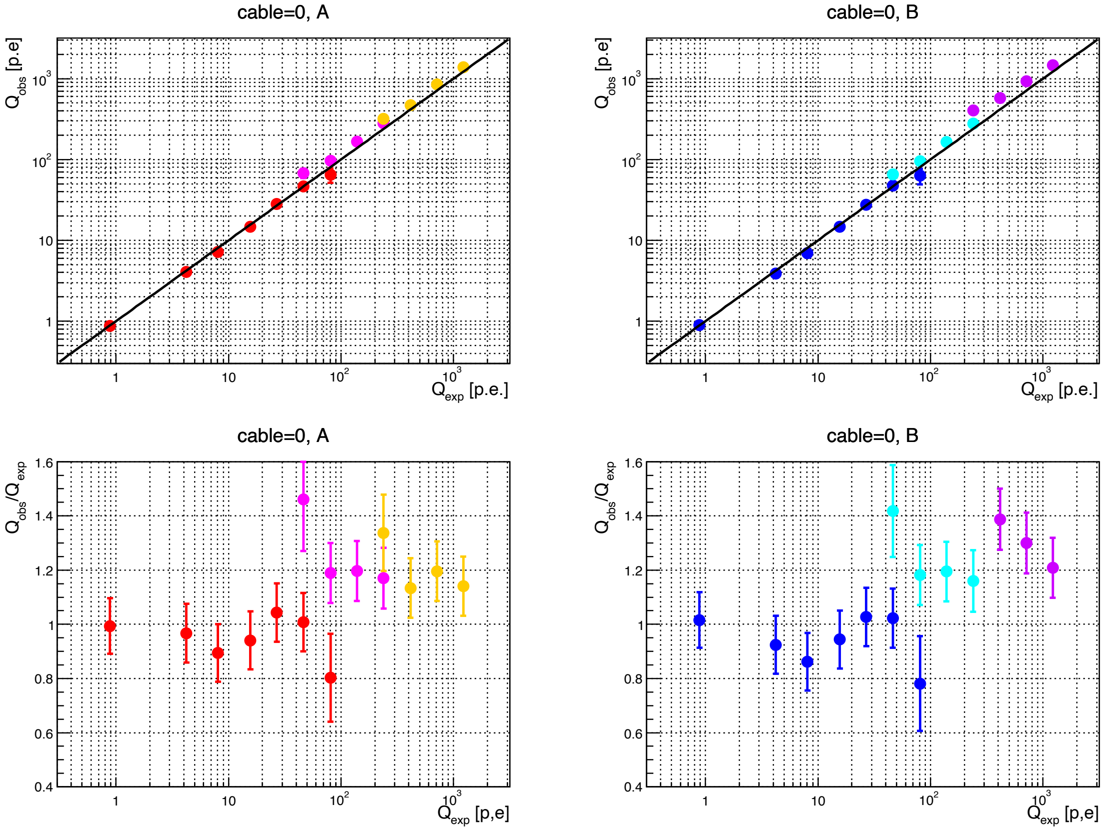

(a) Typical relation between observed and expected charge with designed gain correction factors. There are clear gaps at the boundaries of gains, particularly between the H and M gains, making the charge linearity bad. We also found systematic differences between A and B channels. Since the amplifiers are common to channels, we consider that the geometrical difference in the transmission paths to the ATWDs causes the differences.

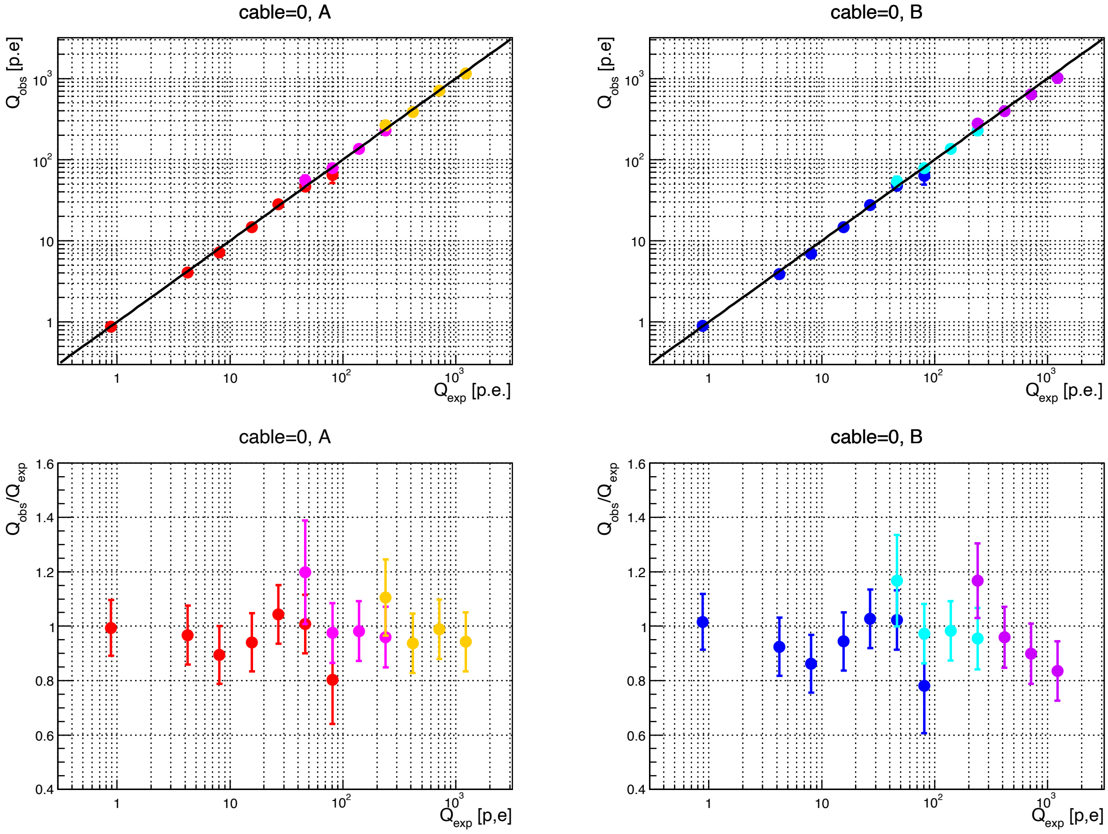

(b) Typical relation between observed and expected charge with best-fit gain correction factors. By fitting the gain correction factors minimizing the Chi-squared from $Q_{obs}/Q_{exp} = 1$, the best-fit amplification factors are determined. The gaps appeared in Fig. 7.7a are greatly reduced by the fitting, and the charge linearity is maintained up to about 1000 p.e. within the uncertainty. In order to reduce the systematic differences between A and B channels, the gain correction factors are determined independently for each channel.

Figure 7.7: Typical relation between observed and expected charge with designed (a) and best-fit (b) gain correction factors. The data of cable number 0 is shown. The left (right) figure shows the data acquired by the A (B) channel. The red (blue) dots show the data acquired by the H gain, the magenta (cyan) dots show the data acquired by the M gain, and the orange (violet) dots show the data acquired by the L gain. The error bars are calculated from the laser light stability and statistical uncertainty in determining the expected charge from the no-hit probability. The solid black lines shown in the upper figures represent $Q_{obs} = Q_{exp}$.

7.2.3 Bad Channel Selection

The KamLAND uses many PMTs, but some of them have bad responses. These PMTs (or channels), called “bad channels”, could be caused by various factors: Dead PMT, unstable High-Voltage applied to the PMTs, and unstable cable connections. Since the bad channels may bias and worsen the event reconstruction, These channels are identified and masked in the reconstruction process. The selection criteria to judge the bad channels for the ID PMTs are as follows.

- The number of hits is less than 600 in 10,000 events.

  The low hit rate PMTs are selected.

- The number of no-hits is more than 1,000 in 10,000 events.

  The low hit rate PMTs are selected.

- The number of hits is less than 80 in 100 high-charge muon events.

  The low response channels for high charge are selected.

- The number of hits is less than 480 in 10,000 events except for muon events.

  The low response channels for low charge are identified.

- The difference in hit rates between ATWD A and B channels is larger than 25% in 10,000 events.

  The channels that have a failure of electronics are identified.

- The i-th PMT that satisfies the following equation.

  $$\frac{1}{N_i}\sum_{j=1}^{N_i}\frac{(Q_i - Q_j)^2}{Q_j} > 1,000\,\text{p.e.} \qquad (j;\ \text{neighbor PMTs}) \tag{7.10}$$

  where Q_i is a charge of i-th PMT.

  The channels with large charge differences from neighbor PMTs.

- The PMT satisfies the following conditions about the gain.

  $$(\text{gain}) < 0.4\,\text{p.e.} \parallel (\text{gain}) > 4\,\text{p.e.} \qquad (\text{17-inch PMTs}), \tag{7.11}$$
  $$(\text{gain}) < 0.4\,\text{p.e.} \parallel (\text{gain}) > 6\,\text{p.e.} \qquad (\text{20-inch PMTs}), \tag{7.12}$$

  where the “gain” represents the Gaussian mean value evaluated by one p.e. events in Sec. 7.2.1.

On the other hand, one selection criteria described below for the OD bad channels is applied. However, this information is not used in the event reconstruction.

- The number of hits is less than 5 in 10,000 events.

  The low response channels are selected.

Fig. 7.8 shows the time variations of the number of bad channels. For the ID 17-inch PMTs, the number of bad channels increased from 2011 to 2019. The maximum number has reached 360, and many PMTs have been treated as bad channels. Since 2020, the number of 17-inch bad channels is gradually decreasing due to the installation of amplifiers. The descriptions about the amplifiers are omitted since the data used in this analysis is before the amplifier installation. The number of bad channels for the ID 20-inch PMTs is almost constant. For the OD 20-inch PMTs, the number of bad channels decreased drastically by the OD refurbishment campaign in 2016.

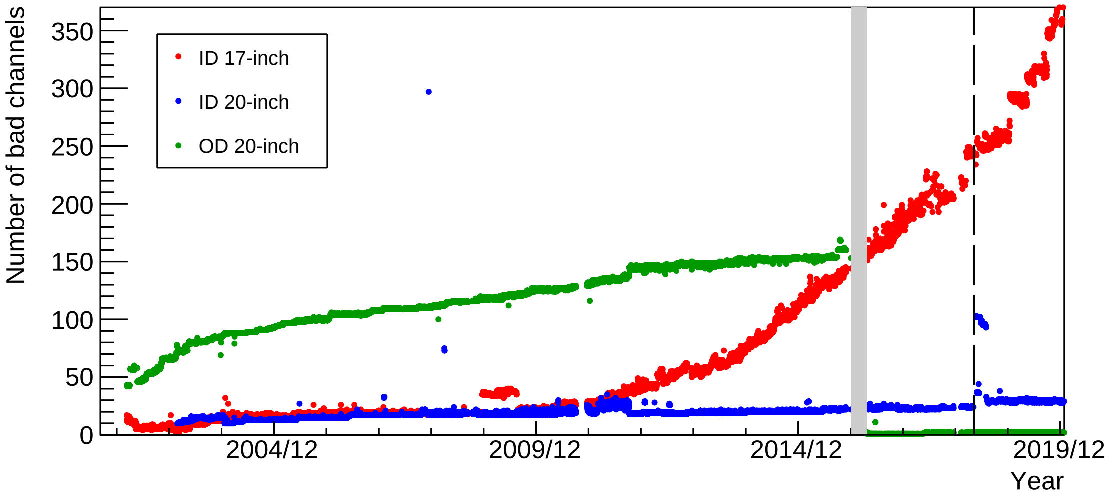

Figure 7.8: Time variations of the number of bad channels. The red, blue, and green dots represent the ID 17-inch, ID 20-inch, and OD 20-inch PMTs, respectively. The number of 17-inch bad PMTs gradually increased from 2011 to 2020. We are installing amplifiers to 17-inch PMTs in stages from 2020. It decreases the number of bad channels of 17-inch PMTs. The number of bad OD PMTs drastically decreased in 2016 due to the OD refurbishment represented by the gray-shaded region. The data used in this analysis is up to May 2018, represented by the long dashed line.

7.2.4 Dark Charge Estimation

PMT has an accidental dark charge via thermal electrons emitted from the photo-cathode and radioactivities in the glass. The dark charge rate depends on the temperature and values of HV. The dark charge contribution is estimated run by run and PMT by PMT using an off-time window, where there is no correlation with physics events.

The events within a radius of 200 cm except for muons and 2 ms after muons are selected. Fig. 7.9 shows the typical hit timing distribution of 17-inch PMT for the selected events. Using the off-time window ($-100 < t < -50$ ns), where the effect of physical events is negligible, the hits and charge rates are calculated. Fig. 7.10 shows the time variation of the total dark charge rate of the 17-inch PMTs. The dark charge rate is $2-4$ p.e./50 ns, except during the LS purification. High dark rates were observed during the purification due to the LS convections and temperature changes.

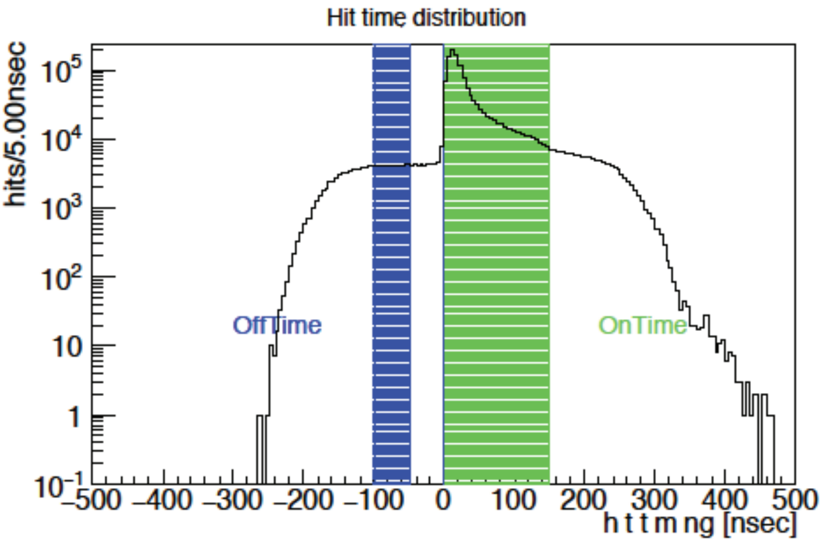

Figure 7.9: Hit timing distribution of 17-inch PMT. The green shaded region ($0 < t < 150\,\text{ns}$) represents on-time window, where the hit due to physical events are dominant. The blue shaded region ($-100 < t < -50\,\text{ns}$) represents off-time window, where the hit is not affected by physical events. The dark charge contribution is estimated using the hits and charges in the off-time window. The figure is from [119].

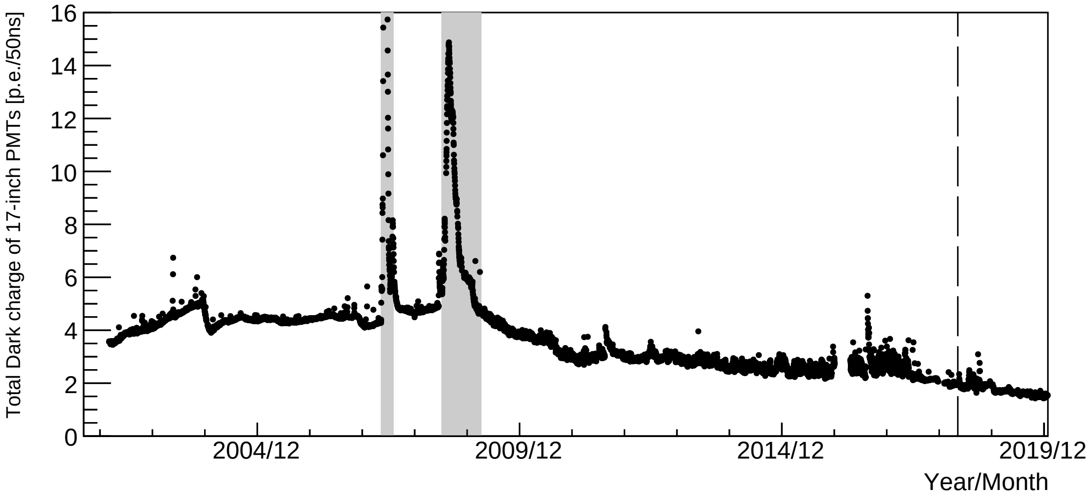

Figure 7.10: Time variations of the dark charge rate of 17-inch PMTs. High dark charge rates were observed during the purification campaigns (gray-shaded region) caused by convection and temperature changes of LS. The data used in this analysis is up to May 2018, represented by the long dashed line.

7.3 Timing Calibration

The timing is also calibrated channel by channel to improve vertex reconstruction. The charge dependence of the timing response is calibrated by using the dye-laser calibration data (Sec. 7.3.1). The time variation of the timing response is also evaluated by using ^{60}Co calibration and ^{40}K data (Sec. 7.3.2 and 7.3.3).

7.3.1 Calibration of Charge Dependent Timing Response

The timing response depends on the charge because of the transit time spread in a PMT (T.T.S.) and slewing effects. The first arrival photon tends to have a smaller delay for the high-charge pulse due to the photon statistics. Furthermore, the amplifiers (H, M, and L gains) have individual differences in the timing response. These effects are calibrated by using the dye-laser calibration data.

Fig. 7.11 shows typical correlations between time and charge for the 17-inch and 20-inch PMT. The correlation is parameterized by a function $T(Q)$ channel by channel.

$$T(Q) = P_0 + P_1 \times \log_{10} Q + P_2 \times (\log_{10} Q)^2 \tag{7.13}$$

where Q corresponds to the observed charge in the ADC counts, P_0, P_1, and P_2 are fitting parameters.

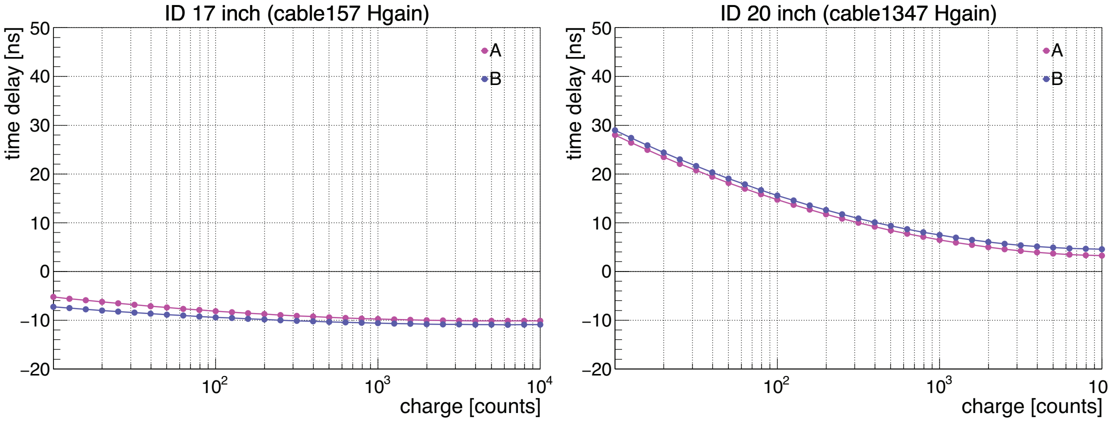

Figure 7.11: Typical correlation between time and charge for 17-inch and 20-inch PMTs. The left (right) figure shows the 17-inch (20-inch) PMT. The first arrival photon tends to have a smaller delay for the high charge due to the photon statistics. The 20-inch PMT has a larger delay than the 17-inch because of poor time resolution. The figure is from [122].

7.3.2 Correction with ^{60}Co Calibration

Time variation of the timing response is monitored and calibrated by using ^{60}Co source calibration data. The data of ^{60}Co installed in the center of the KamLAND is used in this calibration. This calibration was performed regularly at an interval of two weeks in the early period of KamLAND in the 2000s. However, it has been reduced to once every few years since the MIB was installed for the KamLAND-Zen experiment. Therefore, an alternative correction using ^{40}K on the PEEK cylinder described below is carried out to evaluate the time variation.

7.3.3 Run by Run Correction with ^{40}K on the PEEK Cylinder

Time variation of the timing response during the KamLAND-Zen experiment is monitored and calibrated by using ^{40}K events on the PEEK cylinder. The PEEK cylinder is one of the support apparatuses of the MIB located at $(x, y, z) = (0, 0, 5.5\,\mathrm{m})$, and contains many ^{40}K. Therefore, the relative time change can be corrected using the hit time of the ^{40}K events from the PEEK cylinder run by run and channel by channel. This calibration can be performed without installing any sources during the physics data taking.

At first, the reference hit timing functions are prepared using the ^{40}K events on the PEEK cylinder. The functions are prepared for 16 groups classified by PMT z position, as shown in Fig. 7.12. The lower PMTs tend to have broader shapes due to the influence of re-emission and scattering. The hit timing of each PMT obtained from the physics data is fitted with the reference as shown in Fig. 7.13. The fitting process gives the relative time change.

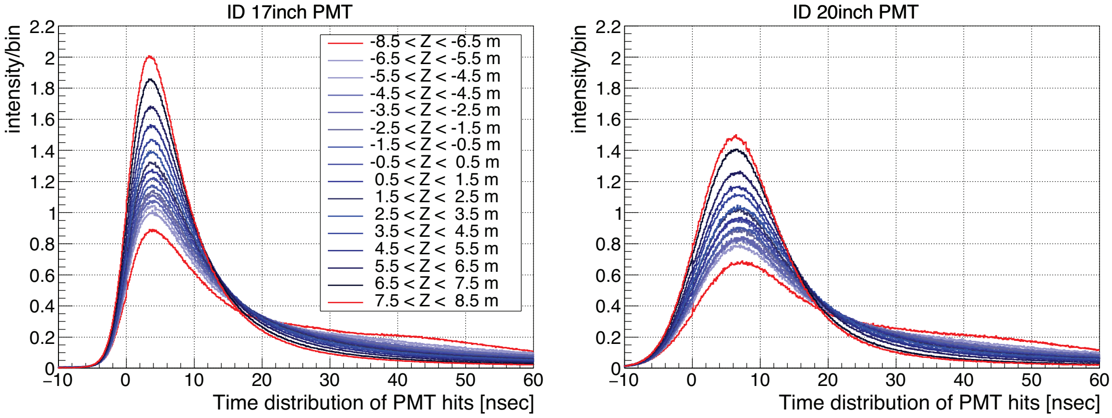

Figure 7.12: Reference hit timing functions for PEEK cylinder ^{40}K events. The left (right) panel shows the references for 17-inch (20-inch) PMTs. The lower PMTs tend to have broader shapes. The figure is from [122].

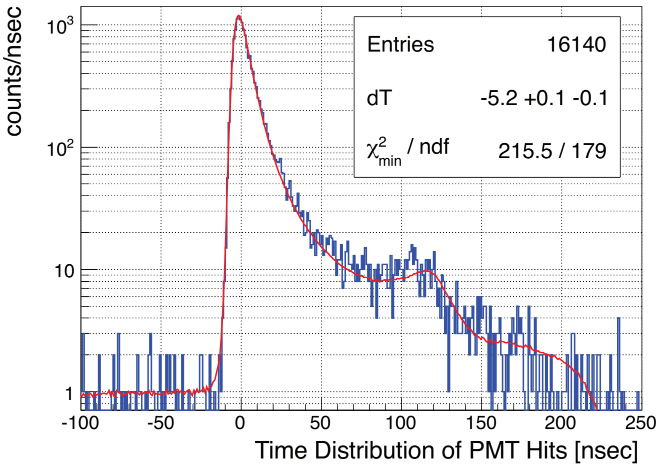

Figure 7.13: Fit with the reference hit timing function. The red line shows the best fit, determining the relative time change. The figure is from [122].

7.4 Muon Track Reconstruction

Compared to the ground, the cosmic muon flux at the KamLAND is attenuated to 10^{-5}. However, it remains at about 0.34 Hz. They frequently undergo nuclear spallations in the LS, producing enormous radioactive isotopes and neutrons. These radioactive isotopes are the severe background of low-energy neutrino studies at the KamLAND. Since a method of using spatial correlation to the muon track can effectively veto these backgrounds, a track reconstruction algorithm for the cosmic muons has been developed.

7.4.1 Muon Selection Criteria

The selection criteria for cosmic muons are as follows. Here, N_{200OD} represents the maximum number of OD PMT hits within a 200 ns time window, and Q_{17} represents the total observed charge of the 17-inch PMTs.

- $Q_{17} \geq 8500\,\mathrm{p.e.}$

  Muons going through the ID called "through going muons" are selected. This charge threshold corresponds to $\gtrsim 50\,\mathrm{MeV}$ in visible energy.

- $Q_{17} \geq 500\,\mathrm{p.e.} \wedge N_{\mathrm{200OD}} \geq 5\ (9)$

  Muons going through the OD with little through the ID called "clipping muons" are selected. The OD hit threshold changes from 5 to 9 hits after the OD refurbishment, so that veto efficiencies are equal.

Since the linearity of the 20-inch PMTs is not as good as the 17-inch PMTs, the charge information of the 20-inch PMTs is not used in the muon track reconstruction. Fig. 7.14 shows the event selection of muons, and Fig. 7.15 shows the muon charge distribution. There are two peaks in the $\log_{10} Q_{17}$ distribution. The first peak at $\log_{10} Q_{17} \simeq 4.3$ corresponds to the minimum ionization of muons through the BO. The second peak at $\log_{10} Q_{17} \simeq 5.6$ corresponds to the minimum ionization of muons through the LS. The muon categories shown in Fig. 7.15 are explained in Sec. 7.4.3.

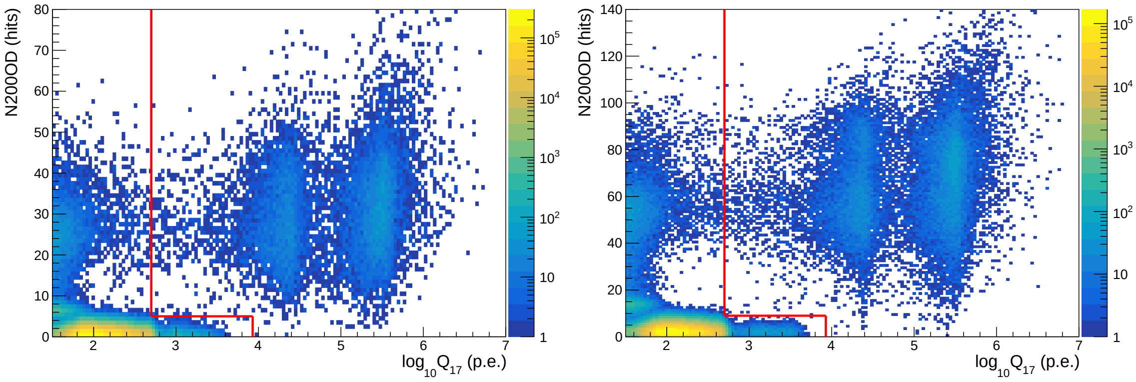

(a) Before OD refurbishment

(b) After OD refurbishment

Figure 7.14: Distribution of N_{200OD} and $\log_{10} Q_{17}$ (a) before and (b) after OD refurbishment. The red lines show the muon selection criteria. In order to equal the veto efficiency, the different thresholds are set for N_{200OD} before and after the OD refurbishment.

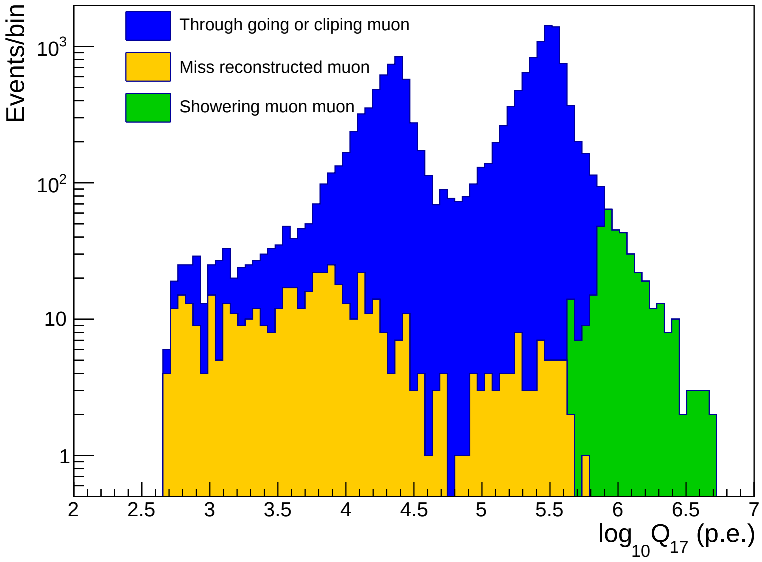

Figure 7.15: Muon charge distribution. The blue, orange, and green shaded regions show the categories of cosmic muons described in the text. The peak at $\log_{10} Q_{17} \simeq 4.3$ (5.6) corresponds to the minimum ionization of muons through the BO (LS).

7.4.2 Track Reconstruction Algorithm

The track reconstruction uses the timing of the first arrival photon of PMTs. The Cherenkov light is emitted at a constant angle called the Cherenkov angle θ_C. On the other hand, the scintillation light is emitted isotropically. As discussed below, the first arrival photon for each PMT is the one emitted in the Cherenkov angle for either Cherenkov or scintillation light. Thus, there is no need to distinguish between the Cherenkov and scintillation lights.

We here assume that the cosmic muons are ultra-relativistic and the speed of light. The Cherenkov angle is given as follows using the refractive index of medium n.

$$\cos\theta_C = \frac{1}{n}, \tag{7.14}$$

where the refractive index of the KamLS and BO is $n \simeq 1.465$ corresponding to $\theta_C \simeq 47°$. Fig. 7.16 shows the schematic view of the muon track reconstruction and notations. We denote the angle between the muon track and the scintillation light that earliest reaches a certain PMT as θ. Here, a term t_0 represents the time at which the muon entered the ID, and a term t represents the time at which the scintillation light arrives the PMT. The relation between t_0 and t can be written as

$$\begin{aligned} t &= t_0 + \frac{l}{c} + \frac{z-l}{\cos\theta} \times \frac{n}{c}, & (7.15) \\ &= t_0 + \frac{l}{c} + \sqrt{(z-l)^2 + \rho^2} \times \frac{n}{c}. & (7.16) \end{aligned}$$

The condition of θ that minimize t can be calculated from Eq. 7.16 with $dt/dl = 0$, and it leads to

$$\cos\theta = \frac{1}{n}. \tag{7.17}$$

This angle θ is the same as the Cherenkov angle θ_C. Thus, it allows the simplification of the algorithm by using only the first hit timing.

In the reconstruction, the entrance is firstly searched for by looking for the first hit PMT. Second, the exit is searched for by looking for the PMT with a high charge and late hit timing. Then, using Eq. 7.16, the entrance and exit are optimized to obtain a more precise track. Since this algorithm assumes that a single muon penetrates the detector, it is unsuitable for muon bundles, stopping muons, and neutrino interactions. A new algorithm for these muons is now under development.

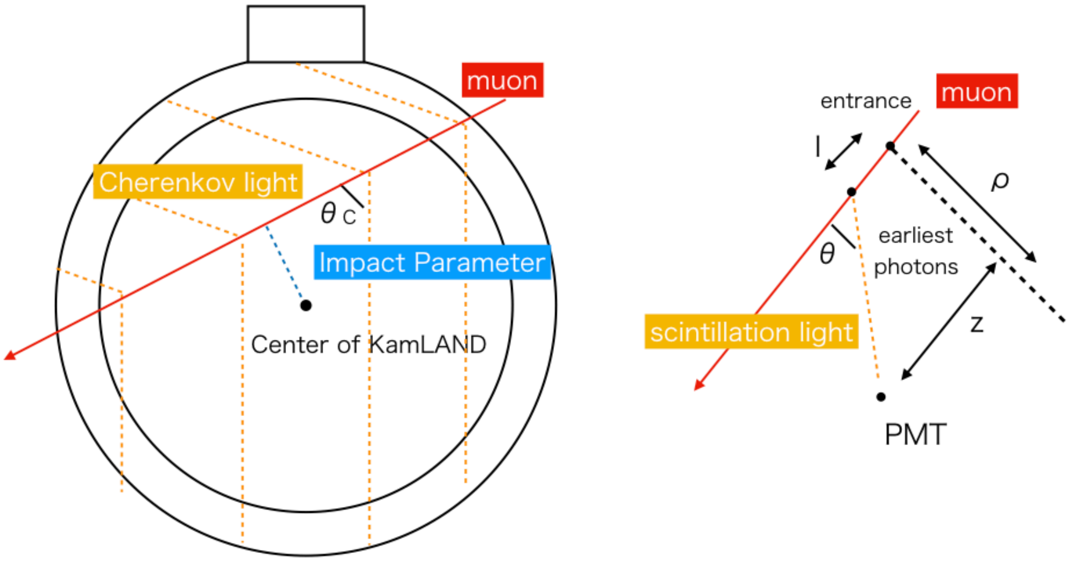

Figure 7.16: Schematic view of muon track reconstruction. The “entrance” represents the position where the muon entered the ID. The term l represents the distance from the entrance to the scintillation emission point, the term ρ represents the distance from the muon track to a certain PMT, and the term z represents the distance from the entrance to the PMT projected onto the muon track. The figure is from [119].

7.4.3 Tracking Performance

Fig. 7.17 show the correlation between the total charge of the 17-inch PMTs (Q_{17}) and the impact parameter, The impact parameter is defined as the distance between the center of the KamLAND and the reconstructed muon track. A clear gap appears at 650 cm in the impact parameter corresponding to the boundary of the LS and BO. There is a correlation between the total charge and muon track length. The correlation can be expressed as the light yield per unit length in LS and BO as follows.

$$\left(\frac{dQ}{dX}\right)_{\rm BO} \equiv \frac{Q_{17}}{L_{\rm BO}}, \tag{7.18}$$

$$\left(\frac{dQ}{dX}\right)_{\rm LS} \equiv \frac{Q_{17} - L_{\rm BO}\langle\frac{dQ}{dX}\rangle_{\rm BO}}{L_{\rm LS}}, \tag{7.19}$$

where $L_{\rm LS(BO)}$ is the track length in the LS (BO) calculated using the reconstructed track. Fig. 7.18 shows the distribution of $(dQ/dX)_{\rm LS,BO}$. The peaks in the distributions can be interpreted as charge intensity per unit length due to the minimum ionization of muons. By the Gaussian fitting, the peak position, corresponding to the charge intensity of minimum ionization, can be determined with an accuracy of a few percent. Here, the Gaussian mean values determined by the fitting are denoted as $\langle dQ/dX \rangle_{\mathrm{LS,BO}}$. These values are calculated run by run to check the stability of the light yield and gains for high-charge regions.

The expected charge corresponding to the minimum ionization of muon can be calculated from these values and the reconstructed track. The difference between the expected and observed charges (ΔQ) can also be defined as

$$\Delta Q \equiv Q_{17} - L_{\mathrm{BO}} \langle \frac{dQ}{dX} \rangle_{\mathrm{BO}} - L_{\mathrm{LS}} \langle \frac{dQ}{dX} \rangle_{\mathrm{LS}}. \tag{7.20}$$

The ΔQ called the residual charge can be interpreted as the charge of shower contribution. The muons satisfying $\Delta Q > 0.75 \times 10^6$ p.e. are categorized as the showering muons. The showering muons are considered to have produced enormous neutrons and radioactive isotopes by showers, i.e., nuclear spallations.

A parameter called *Badness* is also defined as an indicator of the accuracy of the muon reconstruction. *Badness* is determined by various factors but mainly by the following two points. First, if the residual charge ΔQ is negative, a large *Badness* is assigned. The energy deposit by muons is never less than that of the minimum ionization. In other words, a negative ΔQ strongly suggests the failure of the reconstruction. Second, if the expected hit timing from the reconstructed track differs from what is actually observed, a large badness is also given. The muons satisfying $Badness > 100$ are categorized as miss-reconstructed muons. As shown in Fig. 7.15, miss-reconstructed muons account for a few percent of all muons.

As mentioned in Sec. 6.2.1, the buffer oil in KamLAND emits a scintillation light. The light yield per unit length in BO $(dQ/dX)_{\mathrm{BO}}$ includes both scintillation and Cherenkov light, and it is about 25 p.e./cm. According to simulation studies, the contributions of scintillation light and Cherenkov light are roughly equivalent.

7.5 Vertex Reconstruction

There are two vertex reconstruction algorithms at KamLAND: “LT vertex”’ and “V2 fitter”. The LT vertex based on a numerical calculation using simple geometric elements performs a rough estimation. The V2 fitter based on the maximum likelihood method performs vertex reconstruction with better accuracy. The V2 fitter has better accuracy than the LT vertex but has the disadvantage of being computationally time-consuming. To compensates for this disadvantage by reducing the computation time, the V2 fitter uses an output of the LT vertex as the initial values in the likelihood minimization. All physics analyses in KamLAND use the results of the V2 fitter.

Both fitters assume the event vertex as the point source. This assumption is reasonable for low-energy events but not ideal for high-energy events since they tend to have a track with some length. Fig. 7.19 shows the schematic view of the surface of the first arrival photos of a fully contained event with some track length. In scintillator detectors, the first arrival photons create a surface with a characteristic shape called the Fermat surface. The Fermat surface consists of only scintillation light outside the Cherenkov angle. Contrary, there is scintillation and Cherenkov light inside the angle. As described in Sec. 7.4.2, it is not necessary to distinguish between the Cherenkov and scintillation light when looking

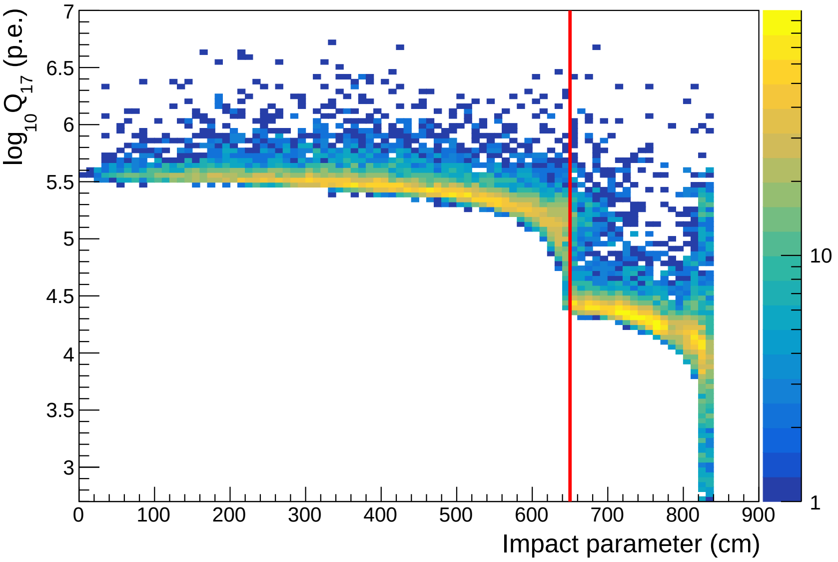

Figure 7.17: Correlation between the total charge of the 17-inch PMTs and reconstructed impact parameter. A clear gap at 650 cm corresponds to the balloon edge shown as the red line. There is a correlation between these parameters, which corresponds to the minimum ionization of muons.

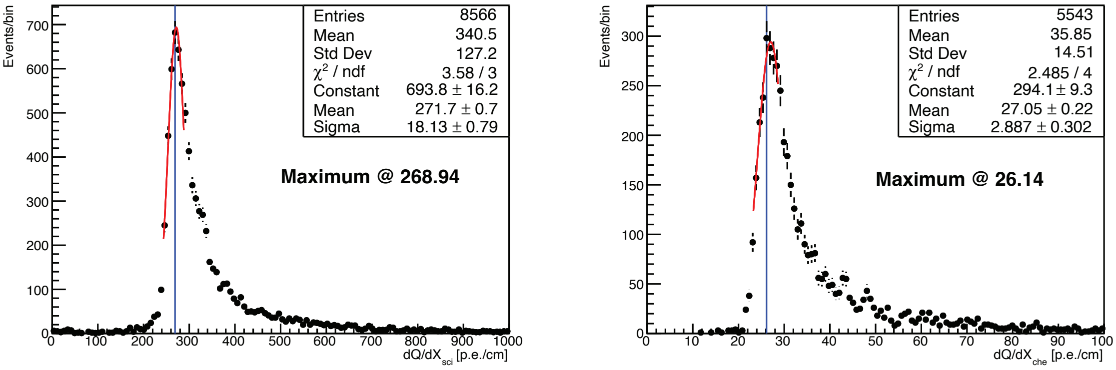

Figure 7.18: Muon charge per reconstructed muon track length in LS (left) and BO (right). The X-axis value of the bin that takes the maximum is written as text and a blue vertical line. The distribution is fitted with the Gaussian shown as the red line. The Gaussian fitting determines the mean value corresponding to the light yield of muon minimum ionization with a few percent accuracy.

at the first arrival photons. The refractive index of the liquid scintillator determines the angle of the cone part corresponding to the Cerenkov angle. As shown in Fig. 7.19, the center of the observed charge will naturally be very close to the middle of the track [2]. The center of the observed time of the first arrival photons will be located along the track but is slightly biased to the start of the track because many PMTs observe the scintillation light emitted from the start point first. [3] Since the LT vertex and V2 fitter use the time of the first arrival photon as the PMT hit time, the vertices of events having a track with some length are slightly biased to the start point of the track.

In order to precisely investigate high-energy neutrino events at KamLAND, we need to reconstruct the start and end points for fully or partially contained events. However, the muon and vertex fitters currently used in KamLAND cannot reconstruct those parameters. We are now developing a new fitter to achieve these reconstructions.

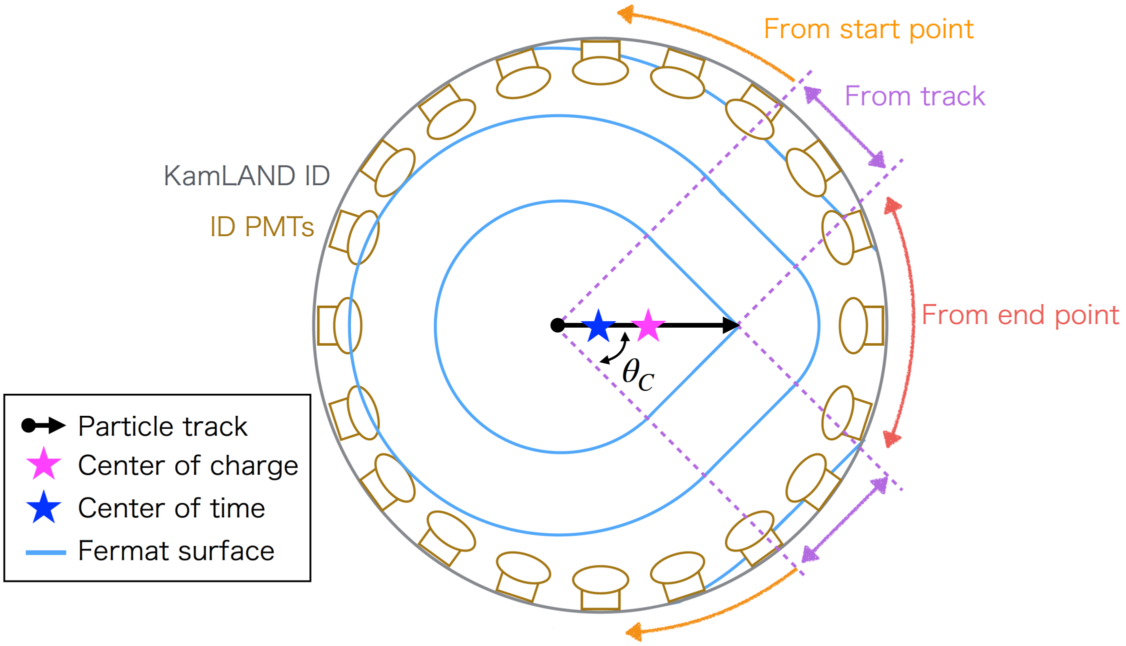

Figure 7.19: Schematic view of the first arrival photons for a fully contained event with some track length. The black arrow represents a track of a charged particle. The cyan lines represent the three-dimensional surface, the Fermat surface, created by the first arrival photons. The center of observed charge, shown as a magenta star, will naturally be very close to the middle of the track. On the other hand, the center of observed time, shown as a blue star, will be located along the track but is slightly biased to the start of the track.

7.5.1 Vertex Reconstruction Algorithm

LT Vertex

The LT vertex is based on a numerical calculation using simple geometric elements, such as the hit timing, charge, and positions of PMTs. Here, $\boldsymbol{r} = (x, y, z)$ denotes the vertex

---

[2] Strictly speaking, the particles are presumed to be slightly off-center because of the difference in their stopping power at the start and end points.

[3] If we calculated the center of the time of all photons, it would be middle or slightly biased to the end of the track due to the Cherenkov light.

of an event. The photon emission time $t_i(\boldsymbol{r})$ can be written as follows.

$$t_i(\boldsymbol{r}) = T_i - ToF_i(\boldsymbol{r}), \tag{7.21}$$

where T_i is the hit timing of i-th PMT and $ToF_i(\boldsymbol{r})$ is the time of flight to the i-th PMT. The $Tof_i(\boldsymbol{r})$ can be calculated as follows using the position of i-th PMT (x_i, y_i, z_i):

$$ToF_i(\boldsymbol{r}) = \frac{\sqrt{(x-x_i)^2 + (y-y_i)^2 + (z-z_i)^2}}{c/n_{\text{eff}}}, \tag{7.22}$$

where n_{eff} is the effective refractive index of the LS. Therefore, c/n_{eff} corresponds to the effective speed of light in the LS. It is measured by using the radioactive source calibration data $c/n_{\text{eff}} = 16.95\,\text{cm/ns}$.

The fitter calculates the photon emission time t_i for all PMTs and then searches for the vertex that minimizes the deviation of t_i. Ideally, when the fitter chooses the true vertex, the minimum value of the deviation would be zero. Since the t_i and its derivatives dt_i/dx are considered to be independent, the covariance of these two parameters $\text{Cov}(t_i, dt_i/dx)$ should be zero.

$$\text{Cov}(t_i, dt_i/dx) = \frac{1}{\sum_i w_i} \sum_i w_i (t_i - \langle t_i \rangle) \left(\frac{dt_i}{dx} - \langle \frac{dt_i}{dx} \rangle \right), \tag{7.23}$$

$$\frac{dt_i}{dx} = -\frac{n_{\text{eff}}(x-x_i)}{c\sqrt{(x-x_i)^2 + (y-y_i)^2 + (z-z_i)^2}}, \tag{7.24}$$

where $\langle t_i \rangle$ and $\langle dt_i/dx \rangle$ are the mean values of t_i and dt_i/dx respectively. Another parameter w_i is a weighting factor depending on ToF_i, giving a large weight for the close distance between the PMT and vertex $\boldsymbol{r}$. For better convergence, the fitter searches the vertex until Eq. 7.23 converges to zero. The same things are also calculated for y and z.

V2 Fitter

Using the maximum likelihood method, the V2 fitter gives a more accurate reconstruction quality than the LT vertex. The V2 fitter uses the output of the LT vertex as initial values in the minimization. The likelihood $\mathcal{L}(\boldsymbol{r}, t)$ consists of the PDF (Probability Density Function) $f(t)$ of the PMT hit timing created using the radioactive source calibration data. Once the temporal vertex $\boldsymbol{r} = (x, y, z)$ is determined, the ToF subtracted hit timing $\tau_i(\boldsymbol{r}, t)$ can be calculated as

$$\tau_i(\boldsymbol{r}, t) = t_i - t - ToF_i(\boldsymbol{r}), \tag{7.25}$$

where t_i is the hit timing of i-th PMT, t is the time of the event, and ToF_i is the time of flight from the event vertex $\boldsymbol{r}$ to the i-th PMT. $\tau_i(\boldsymbol{r}, t)$ would be zero ideally. The likelihood is defined as

$$\mathcal{L}(\boldsymbol{r}, t) = \prod_{i \in hit} \phi(\tau_i(\boldsymbol{r}, t)), \tag{7.26}$$

with

$$\phi = \psi/N, \tag{7.27}$$

$$\psi = \mu \times f(t) + D, \tag{7.28}$$

where N is a normalization factor, D is the contribution of dark noise, and μ is a factor adjusting the ideal PDF to fit the real data. In the actual maximization, log-likelihood is used because of its convenience:

$$\log(\mathcal{L}) = \sum_{i \in hit} \log \phi(\tau(\boldsymbol{r}, t)). \tag{7.29}$$

The maximum log-likelihood time and vertex are determined as the solution of the following four-dimensional equations:

$$\frac{\partial}{\partial \mathrm{x}} \log \mathcal{L} = \sum_{i \in hit} \frac{d(\log \mathcal{L})}{d\tau_i} \frac{\partial \tau_i}{\partial \mathrm{x}} = 0 \quad (\mathrm{x} = x, y, z, t). \tag{7.30}$$

7.5.2 Vertex Reconstruction Quality

We regularly monitor the vertex reconstruction quality, such as vertex bias, resolution, and miss-reconstruction probability by the Z-axis and 4π calibrations.

Vertex Bias

Fig. 7.20 shows the vertex deviation obtained from the Z-axis calibration. The z deviation is defined as a difference in the reconstructed z vertex and source z position. Calibration for outer events is challenging because they are more affected by detector components that have complex structures, such as balloons and straps. As a result, the vertex deviation tends to be larger in the outer region. The magnitude of the deviation is period-dependent due to the time variation of detector responses. In the $-550 < z < 550$ cm, the deviation is within ±6.5 cm corresponding to 3.6% fiducial volume uncertainty.

The 4π calibration is useful to check the vertex bias for the full volume. The vertex bias was ±3 cm at 550 cm in 2006 and ±6.5 cm at 550 cm in 2011. These results are consistent with the Z-axis calibration.

Vertex Resolution

The vertex resolution is also evaluated based on the source calibration data. Since gamma rays of several MeV spread tens of centimeters in the detector, the reconstructed vertex is affected by the dispersion of the light emission point. This effect is estimated by simulation and subtracted to obtain the vertex resolution. Fig. 7.21 shows the result: $11.7 \pm 2.2\,\mathrm{cm}/\sqrt{E(\mathrm{MeV})}$ before purification and $13.8 \pm 2.3\,\mathrm{cm}/\sqrt{E(\mathrm{MeV})}$ after purification.

Vertex Miss-Reconstruction Probability

The miss-reconstruction probability is evaluated using ^{60}Co source calibration data. The probability is defined as the percentage of events where the distance between the reconstructed vertex and the source position is greater than a certain distance. This evaluation sets a sufficiently long distance where the gamma rays attenuated as the selection criteria for the distance, 300 cm. The result was 0.2% [123], which is small enough to be negligible in this study.

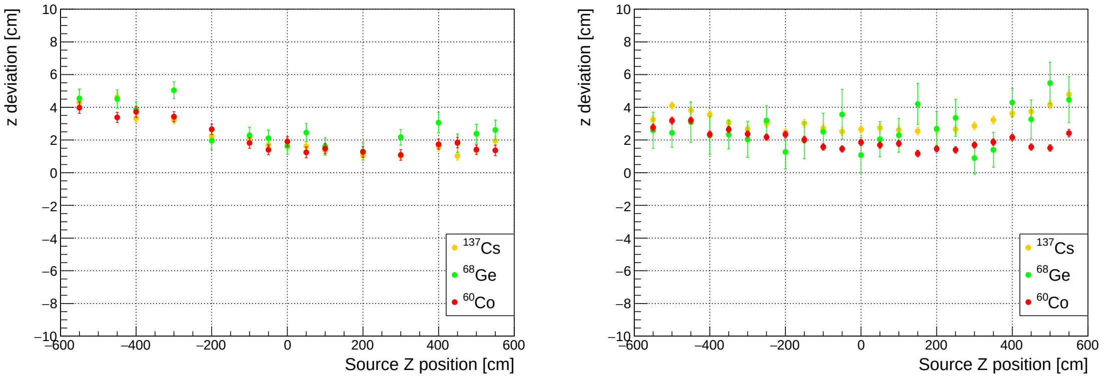

(a) Before purification (Sep. 2006)

(b) After purification (Jul. 2009)

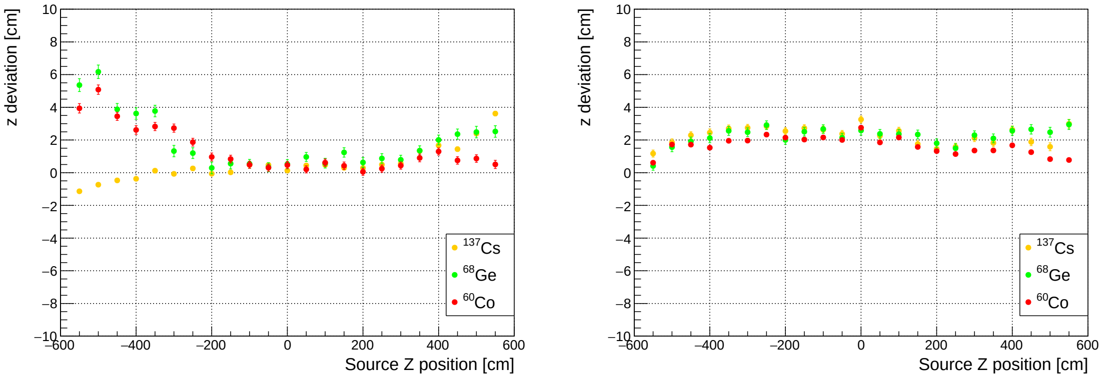

(c) Before KamLAND-Zen 400 (Feb. 2011)

(d) After OD refurbishment (Jan. 2018)

Figure 7.20: Vertex deviations between reconstructed z and source z position. The deviations are within 6.5 cm for all periods, although it depends on the period. (b) The uncertainty of ^{68}Ge is large because of the weak intensity. (c) It is known that the source position of ^{68}Ge and ^{60}Co were slightly misarranged during the data taking of $-550 < z < -150$ cm.

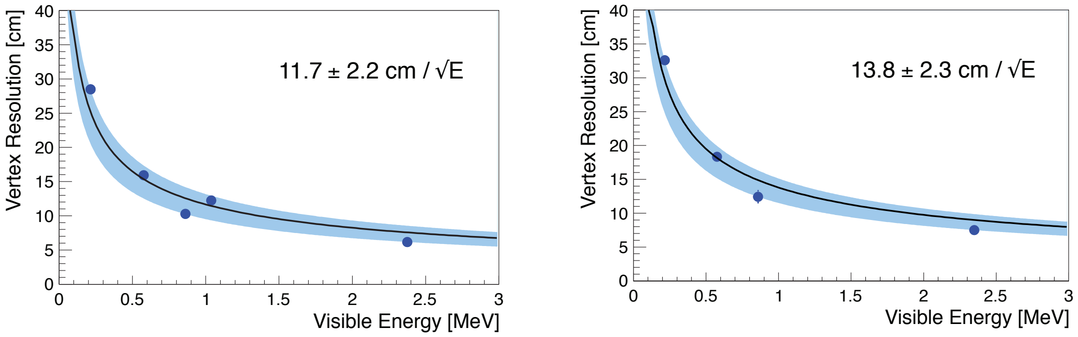

(a) Before purification (Sep. 2006)

(b) After purification (Jul. 2009)

Figure 7.21: Vertex resolution before and after purification as a function of visible energy. The blue dots represent the estimated vertex resolution. From the lowest to highest energy, data for ^{203}Hg, ^{137}Cs, ^{68}Ge, ^{65}Zn, and ^{60}Co are shown. After purification, there is no data of ^{65}Zn. The solid black lines show the best-fit vertex resolution, and blue shaded regions show the error. The figure is from [123].

7.6 Energy Reconstruction

There are two energy reconstruction algorithms at KamLAND: “KatEnergy” and “EnergyA2”. Both algorithms use the vertex reconstructed by the V2 fitter in the calculations. The EnergyA2 is based on the maximum likelihood method and uses information about the presence or absence of the PMT hits as well as the charge information. As a result, the EnergyA2 gives better resolution in the low-energy region of a few MeV than the KatEnergy. However, the EnergyA2 loses the linearity above several tens of MeV, where the hit saturates. Therefore, this study uses the KatEnergy.

Both fitters calculate two energies: energy reconstructed from the 17-inch PMTs only and that using all ID PMTs. In the low-energy region of a few MeV, the energy reconstructed using all ID PMTs gives better resolution because of the increase in photon statistics. However, since the 20-inch PMTs have poor charge linearity, the energy that also uses the 20-inch PMTs is not proper for high-energy analysis. Therefore, this study uses the energy reconstructed by the KatEnergy using the 17-inch PMTs only, frequently denoted as “Energy17”. Correction factors common to both algorithms are described in Sec. 7.6.1 and 7.6.2. The details of each algorithm are explained in Sec. 7.6.3.

7.6.1 Correction Factors

The visible energy in KamLAND uses all basic calibrations and corrections, such as the gain, bad channels, and dark charge explained in Sec. 7.2. The bad channels are removed in the reconstruction, and the contribution of the dark charge is subtracted. In addition, there are several corrections for more precise energy reconstruction, as described below.

Shadow Effects

The shadow effects of balloons and kevlar ropes reduce the charge observed by the PMTs around the bottom and chimney regions. The effects was estimated using ^{60}Co source calibration data and it is corrected in the reconstruction as shown in Fig. 7.22

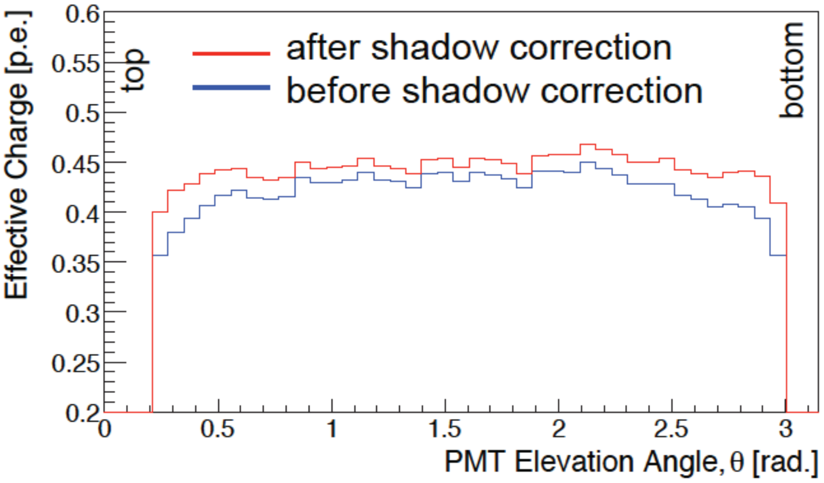

Figure 7.22: Shadow effects estimated using ^{60}Co source calibration data. Before the correction, there is a large polar angle θ dependence because the ballon straps densely cover the top and bottom regions. The correction made from the source calibration data reduces the angle dependence.

Attenuation Length

The attenuation length is one of the important parameters to estimate the light yield because most of the emitted light is absorbed by LS. Different attenuation lengths were prepared for each of the three periods with the changes in the detector.

- Before finishing the second purification: Start of the KamLAND – Apr. 8th, 2009 (run008501)

  The attenuation length estimated with neutron capture gamma rays is used. Fig. 7.23 shows a schematic view of the estimation. It uses the distance between the PMT and the event vertex.

- After the second purification and before the OD refurbishment: Apr. 9th, 2009 (run008502) – Dec. 15th, 2015 (run013404)

  The attenuation length estimated with ^{60}Co source calibration data in Jul. 2009 is used.

- After the OD refurbishment: Dec. 16th, 2015 (run013405) – Current

  The attenuation length estimated with ^{60}Co source calibration data in Feb. 2018 is used.

The LS purification most changed the optical properties of the KamLS. Therefore, a large difference is found before and after the purification. On the other hand, the difference between the second and third periods is relatively small.

Softrware Discriminator Threshold

In order to reduce the accidental dark hit and noise, a software charge threshold is applied at 0.3 p.e. This software threshold is higher than the hardware threshold implemented in KamFEE. This correction yields an additional non-linearity factor.

7.6.2 Non-linearity Factors

The relation between the visible energy and the real deposited energy has non-linear effects because of various factors such as the dark charge, detection inefficiency, the quenching effect, and the Cherenkov light. The major factors that generate the non-linearity are explained below.

One p.e. Inefficiency

The inefficiency of one p.e. due to the hardware and the software threshold causes the non-linear bias for the visible energy. When we consider one p.e. detection efficiency ϵ, the probabilities of zero p.e., one p.e., and N p.e. (N$\geq$2) observation can be written as follows with the Poisson distribution.

$$\begin{aligned}
P_i(0) &= e^{-\mu_i} + (1-\epsilon)\mu_i e^{-\mu_i}, && (7.31)\\
&= e^{-\mu_i}[1 + (1-\epsilon)\mu_i], && (7.32)\\
P_i(1) &= \epsilon\mu_i e^{-\mu_i}, && (7.33)\\
P_i(N) &= \frac{\mu_i^N}{N!}e^{-\mu_i}, && (7.34)
\end{aligned}$$

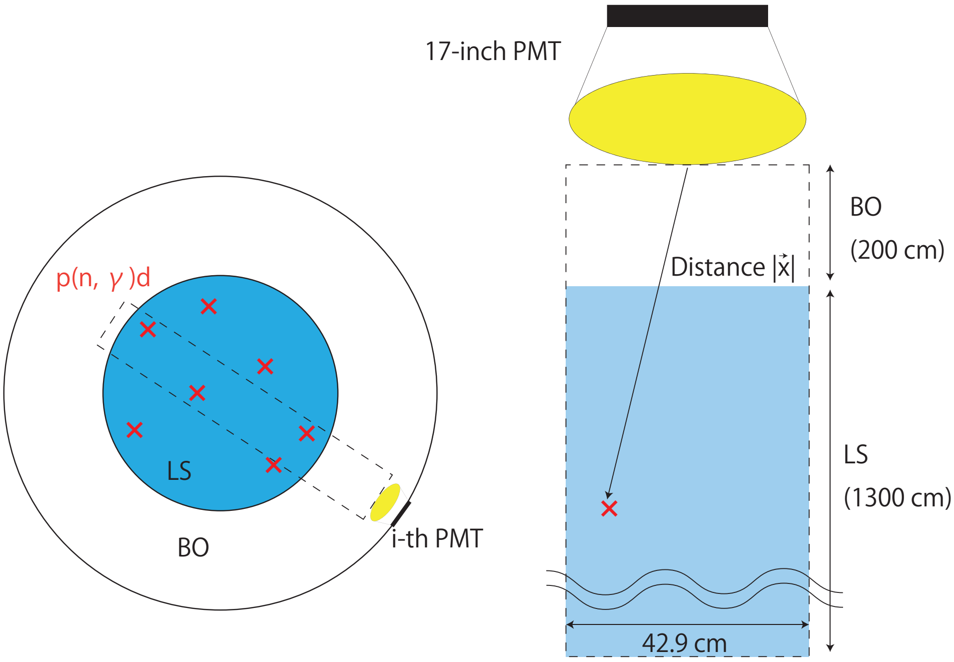

Figure 7.23: Schematic view of the attenuation length estimation using neutron capture gamma rays. In order to reduce the contributions of re-emission and scattering, events within a 42.9 cm diameter of a perpendicular cylinder from each PMTs are selected. The figure is from [119].

where $P_i(m)$ represents the probability of m p.e. observation of i-th PMT and μ_i represents the mean number of photo-electrons of j-th PMT. The expected charge of i-th PMT, $Q_i^{expected}$ is calculated by summing up these charges as follows:

$$Q_i^{expected} = q_i(1) \times P_i(1) + \sum_{N\geq 2} [q_i(N) \times P_i(N)], \tag{7.35}$$

where $q_i(N)$ represents the mean charge of N p.e. with the threshold effect. If there is no threshold effect, the expected charge $Q_i^{expected-no-threshold}$ can be written as

$$\sum_{N\geq 1} [q_i(N) \times P_i(N)] = \mu_i q_1 \equiv Q_i^{expected-no-threshold}, \tag{7.36}$$

where q_1 is the mean charge of one p.e. without threshold effect. Assuming that only one p.e. signal is affected by the threshold effect, Eq. 7.35 is converted to

$$\begin{aligned} Q_i^{expected} &= \mu_i q_1 - \mu_i e^{-\mu_i} q_1 + q_i(1)\epsilon\mu_i e^{-\mu} && (7.37)\\ &= \mu_i q_1 \left[1 - e^{-\mu_i} + \frac{q_i(1)}{q_1}\epsilon e^{-\mu_i}\right] && (7.38)\\ &= Q_i^{expected-no-threshold}\left[1 - e^{-\mu_i}\left(1 - \frac{q_i(1)}{q_i}\epsilon\right)\right]. && (7.39)\end{aligned}$$

The mean charge of one p.e. with threshold effect of i-th PMT, $q_i(1)$, can be written with $q_{i,loss}$, which is the mean charge under the threshold.

$$q_1 = q_i(1)\epsilon + q_{i,loss}(1-\epsilon). \tag{7.40}$$

Therefore, from Eq. 7.39 and 7.40, the expected charge of i-th PMT is given as

$$Q_i^{expected} = Q_i^{expected-no-threshold}(1 - e^{\mu_i}\delta), \tag{7.41}$$

$$\delta \equiv \frac{q_{i,loss}}{q_i}(1 - \epsilon). \tag{7.42}$$

The parameter δ is measured to be 0.05 for KatEnergy and 0.03 for EnergyA2 from the radioactive source calibration data. Fig. 7.5 shows the relation between $Q_i^{expected}$ and $Q_i^{expected-no-threshold}$ with KatEnergy ($\delta = 0.05$).

Cherenkov light and Quenching Effect

Although the scintillation light of LS dominates the light emission in KamLAND, Cherenkov light has some contribution. The direct contribution is negligible because of the high absorption probability in the short wavelength region. However, the re-emission contributes to the visible energy.

The number of scintillation photons is proportional to the energy deposit in the first order. However, there is a non-negligible dependence on the ionization density called the "quenching effect". The most popular way to describe the quenching effect is using Birk's formula [124],

$$\frac{dL}{dx} = \frac{L_0\left(\frac{dE}{dx}\right)}{1 + k_B\left(\frac{dE}{dx}\right)}, \tag{7.43}$$

where L_0 is a normalization factor, k_B is the Birk's constant, dE/dx is the ionization density, and dL/dx is the light intensity per unit length. The effects of these non-linearity factors are estimated from various sources as described in Sec. 7.6.4.

7.6.3 Energy Reconstruction Algorithm

KatEnergy

KatEnergy is an algorithm to calculate visible energy from the vertex and the observed charge. There is a linear correlation between the light yield and the visible energy. The visible energy E is calculated by the following equation.

$$E = E_0 \times \frac{\sum_i Q_i^{observed} - \sum_i d_i}{\sum_i Q_i^{expected}}, \tag{7.44}$$

where E_0 is a constant value, $Q_i^{observed}$ is the observed charge of i-th PMT, d_i is the dark charge of i-th PMT, and the $Q_i^{expected}$ is the expected charge for i-th PMT. E_0 is determined with the neutron capture gamma rays. Since the observed charge and dark charge are determined from the real data, the accuracy of predicting $Q_i^{expected}$ determines the quality of the energy reconstruction. In the KatEnergy fitter, the expected charge of i-th PMT is calculated by

$$Q_i^{expected} = \frac{e^{-L_i/\lambda}}{4\pi L_i^2}\eta_i\xi_i\cos\theta_i, \tag{7.45}$$

where L_i is the distance between the reconstructed vertex and the PMT, λ is the attenuation length (Sec. 7.6.1), η_i is the correction factor for the shadow effect (Sec. 7.6.1), ξ_i is the threshold effect of the FEE discriminators, and θ is the angle of incidence to the PMT.

EnergyA2

EnergyA2 calculates visible energy using the maximum likelihood method. It achieves better resolution than the KatEnergy in the low energy region of a few MeV by incorporating information on the presence or absence of PMT hits as well as the charge into the likelihood function. However, the EnergyA2 loses the charge linearity above several tens of MeV, where the hit saturates. Therefore, this study does not use EnergyA2.

The likelihood function comprises the PDF (Probability Density Function) of hit, charge, and time information for each PMT.

$$\mathcal{L} = \prod_{i \in \text{no-hit}} P(\text{no-hit}|\mu_i) \times \prod_{i \in \text{hit}} P(\text{hit}|\mu) P(q_i|\mu_i) \eta(t_i|\mu_i), \tag{7.46}$$

where μ_i is the expected charge, q_i is the observed charge, and t_i is the hit timing of i-th PMT. $P(\text{no-hit}|\mu_i)$ is the no-hit probability while $P(\text{hit}|\mu_i)$ is the hit probability. $P(q_i|\mu_i)$ is the PDF for the charge and $\eta(t_i|\mu_i)$ is the one for the hit timing. In practice, the fitter maximizes the log-likelihood $\log \mathcal{L}$ to determine the visible energy.

7.6.4 Energy Reconstruction Quality

We evaluated the energy reconstruction quality, such as deviation, resolution, and non-linearity, using the Z-axis calibrations. This section discusses the energy reconstructed by the KatEnergy using the 17-inch PMTs only, which is used in this study (Energy17). The atmospheric neutrino events are high-charge, and their energy spectrum has a very gradual curve, close to flat. In addition, the final analysis is based on a comparison of observed data and simulations. The resolution and accuracy are sufficiently good and have little impact on the final results. On the other hand, it is essential to understand the uniformity of the energy scale in the fiducial volume and the non-linearity and to reproduce these factors in the simulation.

Energy Deviation

Fig. 7.24 shows the results of energy deviation: Since the ^{68}Ge had weak intensity in 2009 and 2018, the uncertainty was large in 2009, and they were slightly biased in 2018. As well as the vertex, the outer side tends to have a larger deviation, and the quality varies from period to period. In the $-550 < z < 550$ cm, the deviation is within ±3.5%.

Energy Resolution

Fig. 7.25 shows the results of energy resolution at various z positions. The resolution is the best before purification, at about 7%. Thereafter, it gradually worsened, about 8% in 2009 and 2011 and about 9% in 2018. The main reason for the poor resolution is the increase in the number of bad channels as described in Sec. 7.2.3. The z-dependence of the resolution does not appear to be visible.

Energy Non-Linearity

The energy non-linearity is parameterized by using source calibration data. Fig. 7.26 shows two-dimensional allowed regions of the Cherenkov contribution and Birk's constant, which are the dominant factors of non-linearity estimated by simulations. Fig. 7.27 shows the best-fit model of the relation between visible energy and real energy. In the case of gamma

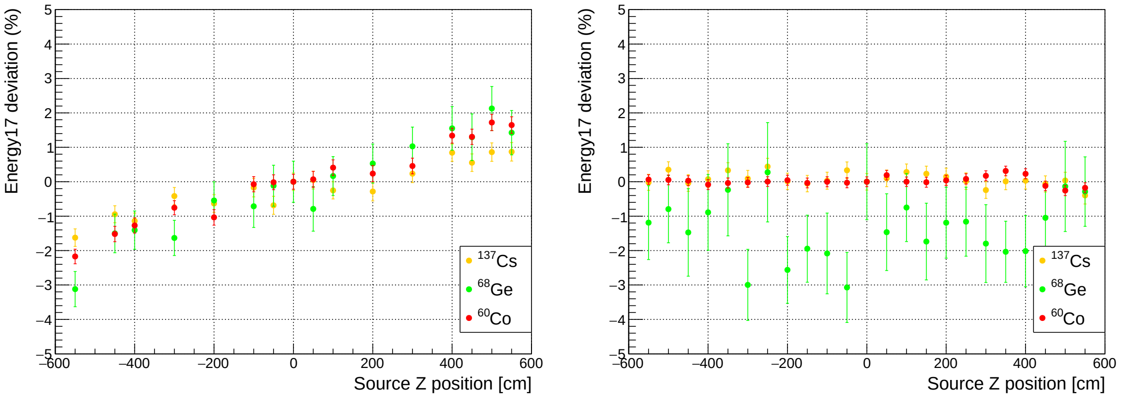

(a) Before purification (Sep. 2006)

(b) After purification (Jul. 2009)

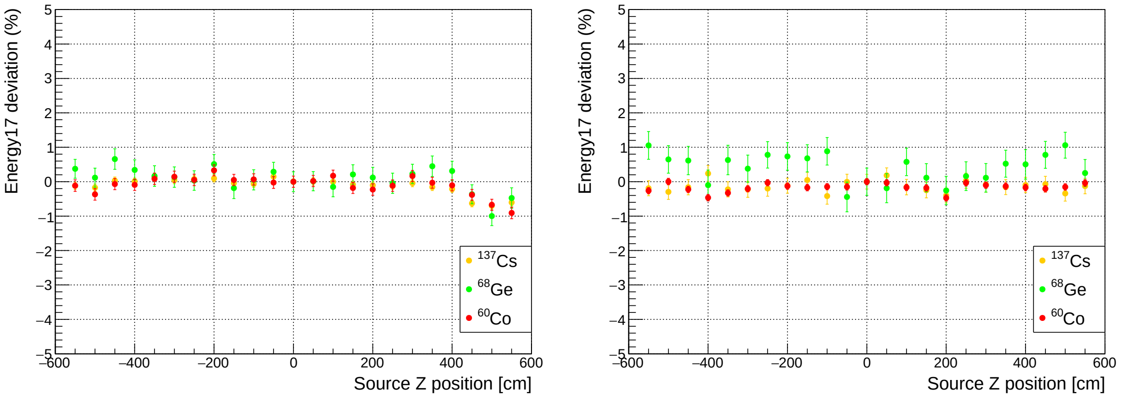

(c) Before KamLAND-Zen 400 (Feb. 2011)

(d) After OD refurbishment (Jan. 2018)

Figure 7.24: Z dependence of energy deviation for various sources. The deviation is defined based on the value obtained at the center of the detector. (b) The uncertainty of ^{68}Ge is large due to its weak intensity. (d) A composite source of ^{137}Cs, ^{68}Ge, and ^{60}Co, was used as shown in Fig. 6.17b. The peak of ^{68}Ge was strongly influenced by the tail of ^{137}Cs because of the the weak intensity, making the apparent deviation look bad.

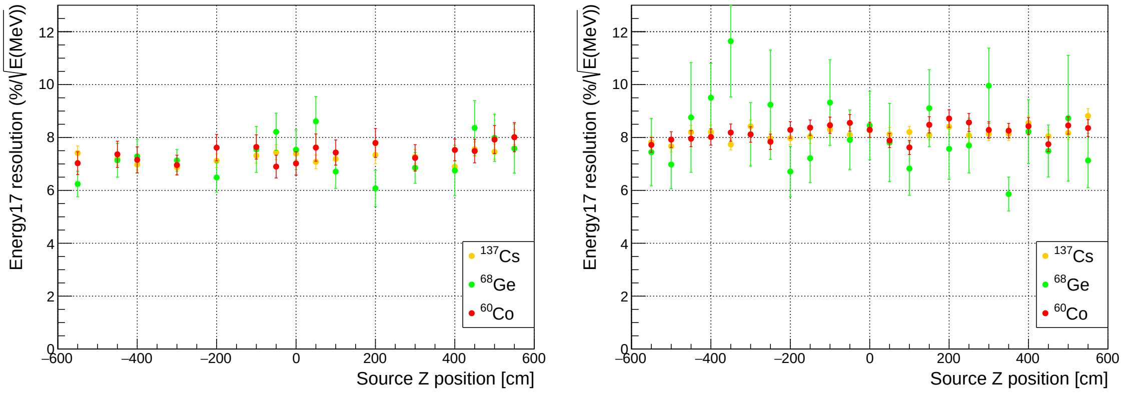

(a) Before purification (Sep. 2006)

(b) After purification (Jul. 2009)

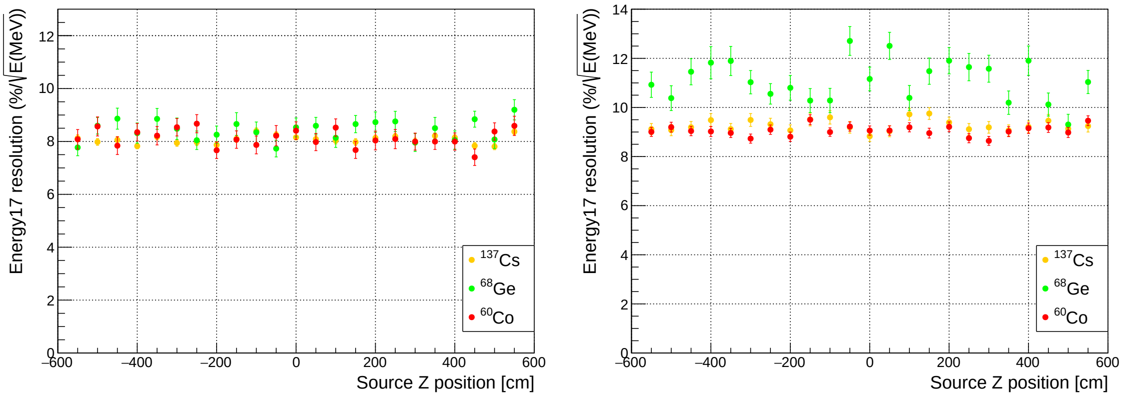

(c) Before KamLAND-Zen 400 (Feb. 2011)

(d) After OD refurbishment (Jan. 2018)

Figure 7.25: Z dependence of energy resolution for various sources. (b) The uncertainty of ^{68}Ge is large due to its weak intensity. (d) The peak of ^{68}Ge was strongly influenced by the tail of ^{137}Cs because of the weak intensity, making the apparent resolution look bad.

rays, the real and visible energies are equal to around 2.2 MeV. In the region above 5 MeV, the visible energy is several percent larger than the real energy, and the ratio is almost constant because the quenching effect is negligible.

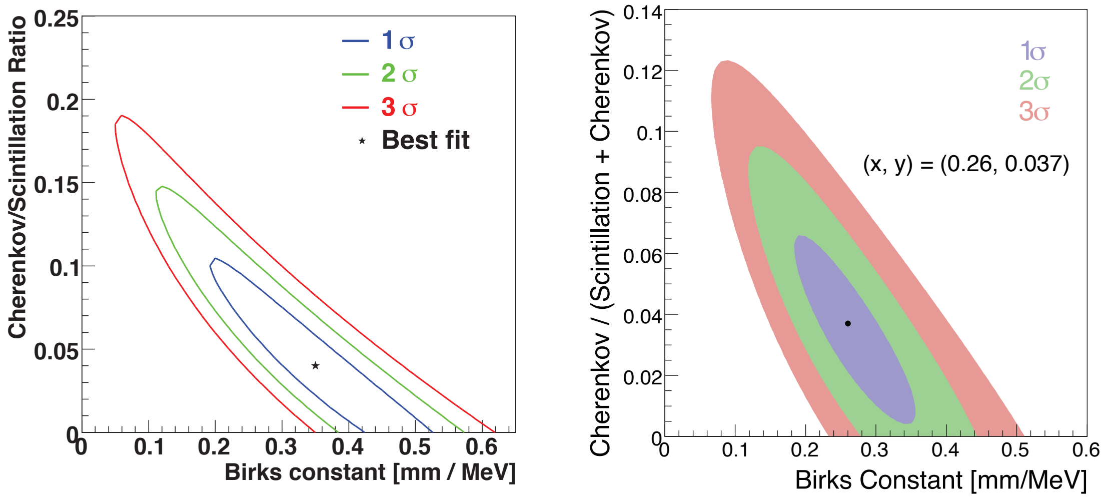

(a) Before the purification [118]

(b) After the purification [125]

Figure 7.26: Uncertainty of two parameters among the Birk's constant and the Cherenkov contribution before/after LS purification. These two parameters are inversely correlated.

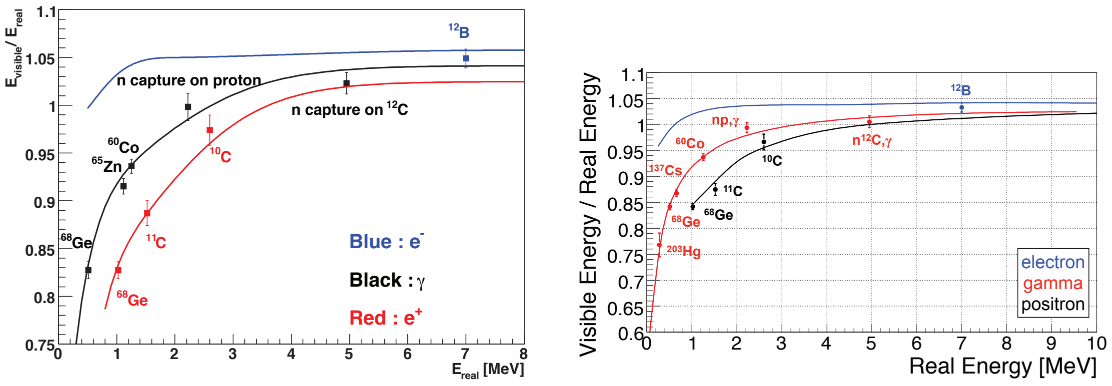

(a) Before the purification [118]

(b) After the purification [125]

Figure 7.27: Energy non-linearity correction before/after the LS purification. The blue, red, and black lines show the electron, the gamma-ray, and the position energy scale, respectively. The data points are calibration data.

Chapter 8

Detector Monte Carlo Simulation

A Geant4-based full optical detector simulator called “KLG4” (KamLAND Geant4) is used to estimate the detector response of neutrino interaction in KamLAND. We have developed highly accurate KLG4 over a wide energy range for multipurpose use. The KLG4 developed in this study has been widely used in various studies: Cosmic muons, neutrino interactions, and developing new fitters with neural networks. This chapter describes the details of the KLG4.

The Geant4 version and the configuration of the physics lists are described in Sec. 8.1. The cross section data and neutron production yield in Geant4 are evaluated in Sec. 8.2. The KLG4 structure, such as geometry, scoring, and event reconstruction, are explained in Sec. 8.3. The tuning of optical parameters and their quality are summarized in Sec. 8.4.

8.1 Geant4 Version and Physics List

The KLG4 uses Geant4 version 9.6.p04, released on 30th January 2015 [96]. This version is the last of version 9 and fixes bugs that existed prior to this one. Geant4 can handle various physics processes at various energies from eV to PeV. However, since no model can comprehensively describe all energy regions, Geant4 provides various models for each physics process and its energy. Therefore, users must choose the appropriate combination of models. This combination is called the physics list.

Tab. 8.1 shows a summary of the physics list adopted in the KLG4. This configuration employs the appropriate models in the low-energy region of sub-GeV energy. The features of these models are described in the following sections.

Table 8.1: Configuration of the physics list in the KLG4

Interaction process	Name of package
Hadronic interaction	Modified QGSP_BIC_HP
Electromagnetic interaction	G4EmLivermorePhysics
Decay process	G4DecayPhysics, G4RadioactiveDecayPhysics
Extra process	G4IonPhysics, G4MuonNuclearProcess, G4StoppingPhysics
Optical photon process	G4Cerenkov, KLG4 original scintillation model, Modified G4OpBoundaryProcess, Modified G4OpAbsorption,

8.1.1 Hadronic Interaction

As hadronic interactions, a modification of the "QGSP_BIC_HP" package is used. Geant4 recommends using this package to simulate low-energy regions, particularly below 200 MeV. This package is composed of a combination of four models: The Quark-Gluon String model (QGS) for quark-gluon interactions, the Binary cascade model (BIC) for nucleon and meson interactions, the Precompound model (P) for nuclear reactions, and the precise thermal neutron transport model (HP).

For the quark-gluon interactions, the Fritiof Parton String model (FTF) is provided in addition to the QGS. The Bertini cascade model (BERT), similar to the BIC adopting the cascade model, is also provided for the nucleon meson interactions. Because we found that the QGS gives better agreement with the KamLAND data in cosmic muon spallation than the FTF, the QGS is used in the KLG4. On the other hand, there was no apparent difference between the BIC and BERT in the cosmic muon spallation simulation. The BIC model is adopted since it is said to be more suitable for low-energy simulation. Because this study measures neutrons, the neutron transport model employed in KLG4 is important. The KLG4 additionally considers a highly accurate neutron transport model below 20 MeV called the HP model.

Since there was an improper implementation of the QGSP_BIC_HP model where a part registers the BIC for pions, we modified the code. See Appendix D.1 for detail.

8.1.2 Electromagnetic Interaction

As electromagnetic interactions, the KLG4 uses the "G4EmLivermorePhyics", a combination of the standard model (G4EmStandardPhysics) and the Livermore model. The Livermore model is for low-energy regions up to 1 GeV and is suitable for studying MeV−GeV physics. The G4EmStandardPhysics is a standard model that can handle up to 100 TeV.

8.1.3 Decay and Extra Processes

The KLG4 adopts G4DecayPhysics and G4RadioactiveDecayPhysics to describe particle and radioactive decay. The KLG4 also considers "G4IonPhysics" to describe scattering with ions such as deuteron and alpha, "G4MuonNuclearProcess" describes muon spallation, and "G4StoppingPhysics" describes muon and pion capture.

8.1.4 Optical Photon Process

For the optical photon generation process, the KLG4 uses G4Cerenkov and the KamLAND original scintillation model together. The G4Cherenkov is provided by the Geant4. In order to describe the scintillation process accurately, the KamLAND original scintillation model has been established. The KLG4 also uses a modification of G4OpBoundaryProcess and G4OpAbsorption to describe the propagation of optical photons, such as absorption, scattering, and reflection.

Modification of G4OpBoundaryProcess and G4OpAbsorption

We slightly modified G4OpBoundaryProcess and G4OpAbsorption to make it easier to handle. This modification inherits the original code and does not change the physical process or model. Reflection and refraction are considered for the process at the boundary of materials, while diffraction is not. For the process in the material, absorption, and Rayleigh scattering are considered. Geant4 also provides tools to describe the Mie scattering, which is elastic scattering that occurs when the wavelength is as large as the scatterer. The KLG4 neglects the Mie scattering because the KamLS was purified with a fine enough filter.

KLG4 Original Scintillation Model

KLG4 implements original scintilaltion generation model. The light yield is calculated from the ionization density (dE/dx) and quenching effect. The ionization density can be calculated using Geant4. The model describes the quenching effect according to Birk's formula (Eq. 7.43). The Birk's constant (k_B) and the normalization factor (L_0) are tuning parameters. However, Birk's formula is known to give poor agreement for heavier charged particles such as protons. Chou proposed an alternative formula that extends Birk's formula empirically [126].

$$\frac{dL}{dx} = \frac{L_0\left(\frac{dE}{dx}\right)}{1 + k_B\left(\frac{dE}{dx}\right) + C\left(\frac{dE}{dx}\right)^2}, \tag{8.1}$$

where C is an adjustable constant for high-order correction. Compared with Birk's formula (Eq. 7.43), Chou's formula (Eq. 8.1) adds a second-order term of dE/dx to the denominator.

The quenching effects for protons and carbons of the KamLS were measured using a monochromatic neutron beam [127]. Fig. 8.1 shows the measured quenching factor for proton as a function of proton energy. The quenching factor is fitted with three functions: Birk's, Chou's, and another complicated formula. The description of another formula is omitted since it is not used in this study. The result shows that Birk's formula gives poor agreement with the experimental data, while Chou's formula agrees well. The best-fit parameters of Chou's formula are given as follows:

$$k_B = (7.79 \pm 0.13) \times 10^{-3}\,(\mathrm{g/cm^2/MeV}), \tag{8.2}$$

$$C = (1.64 \pm 0.05) \times 10^{-5}\,(\mathrm{g/cm^2/MeV})^2. \tag{8.3}$$

When we consider a density of the KamLS $\rho = 0.78\,\mathrm{g/cm^3}$, these values are expressed as

$$k_B = 0.0999\,(\mathrm{mm/MeV}), \tag{8.4}$$

$$C = 2.70 \times 10^{-3}\,(\mathrm{mm/MeV})^2. \tag{8.5}$$

The normalization factor L_0 is defined as 0.982 times that of Birk's formula determined by the quenching effect of gamma rays. KLG4 uses Chou's formula to describe the quenching effect of proton and carbon. In addition to the quenching effect, various factors, such as time constants of light emission and re-emission, are also considered based on measurements.

8.2 Cross Section Data and Neutron Production Yield

The detector response of the particles produced by the neutrino interactions is estimated using the KLG4. Because the neutron multiplicity observed in KamLAND is affected by the secondary interactions in the detector, the reproducibility of the physics process in Geant4, particularly the hadronic interactions, is important.

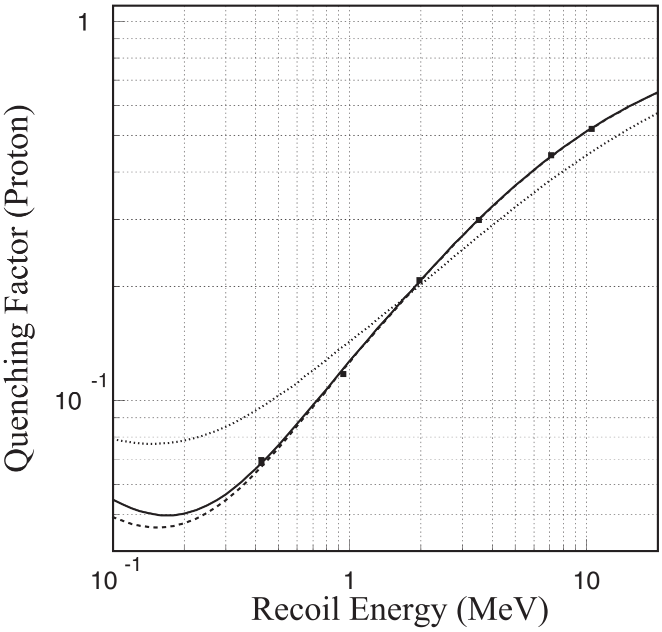

Figure 8.1: Measured quenching effect for proton as a function of proton energy in the KamLAND liquid scintillator. The dots represent the experimental data, the dotted curve represents the best-fit of Birk's formula (Eq. 7.43), the dashed curve shows the best-fit of Chou's formula (Eq. 8.1), and the solid line is another fit result of a more complicated formula. The figure is from [127].

The quality of the neutron transport model is checked in Sec. 8.2.1. The channels that could contribute to neutron production are also investigated: Neutron-carbon, pion-carbon, and muon-carbon interactions. For neutrons and pions, the cross section data for carbon in Geant4 is compared with experimental data in Sec. 8.2.2. For muons, the neutron production yield obtained by Geant4 is compared with experimental data in Sec. 8.2.3.

8.2.1 Neutron Transport Model

We check the mean capture time and travel distance of thermal neutrons in KamLS to verify the neutron transport models in Geant4. While the neutron production depends on the QGS and BIC models, these parameters mostly depend on the HP model, which describes the low-energy region below 20 MeV. While the measured capture time is $207.5 \pm 2.8\,\mu$s [108], Geant4 version 9.4.p04 gives $200.6 \pm 0.6\,\mu$s (stat. error only). There is a slight difference, but it is acceptable to estimate the neutron capture event rate using Geant4.

We also check the travel distance of neutrons associated with atmospheric neutrino events at KamLAND. The result shows a good agreement between simulation and real data. This consistency means that Geant4 predicts neutron transportation precisely. Details are described in Sec. 9.4.2.

8.2.2 Nucleon and Pion Cross Sections on Carbon

Inelastic scatterings of nucleons and pions on carbon play an essential role in neutron production as a secondary interaction in detectors. The nucleon and pion cross sections on ^{12}C in Geant4 are compared with experimental data.

Fig. 8.2 shows ^{12}C-neutron elastic and inelastic cross sections as a function of neutron kinetic energy. It can be seen that the trend is different at the 20 MeV boundary. A fine structure below 20 MeV corresponds to the excited state of ^{12}C. On the other hand, above 20 MeV, there is only a gradual decrease. This trend difference is because the cross section models in the QGSP_BIC_HP are described by the HP model below 20 MeV and the BIC model above 20 MeV. As for the inelastic scattering, it has a threshold because it requires separation energy. Geant4 cross section data agrees well with various experimental data, both elastic and inelastic scatterings. There is a ±7% normalization uncertainty, considered an uncertainty of the secondary interaction by nucleons.

Fig. 8.3 shows the ^{12}C-π^+/π^- inelastic cross section as a function of pion kinetic energy. The cross section of pions has a characteristic peak around 200 MeV, called the Δ region. Compared to the nucleons, the error in the experimental data is large. There is a ±14% normalization uncertainty, which is considered as an uncertainty of the secondary interaction by pions.

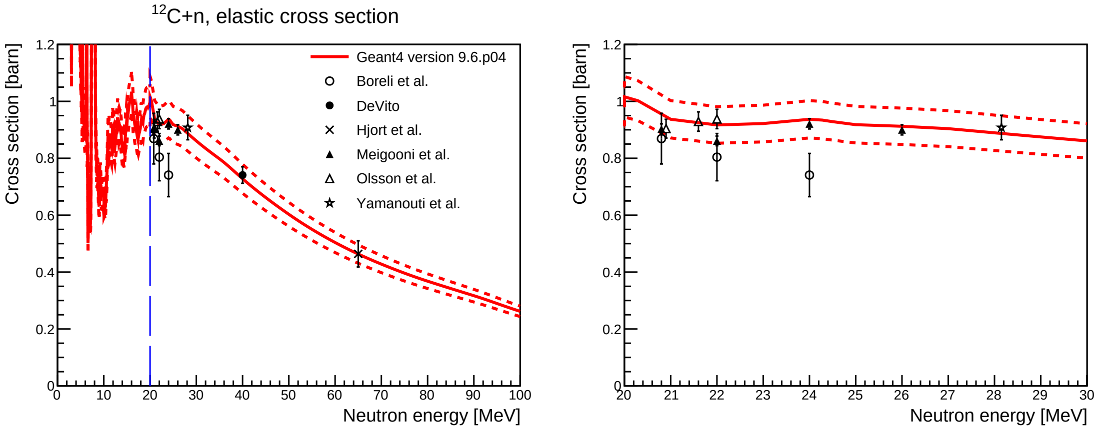

(a) Elastic cross section

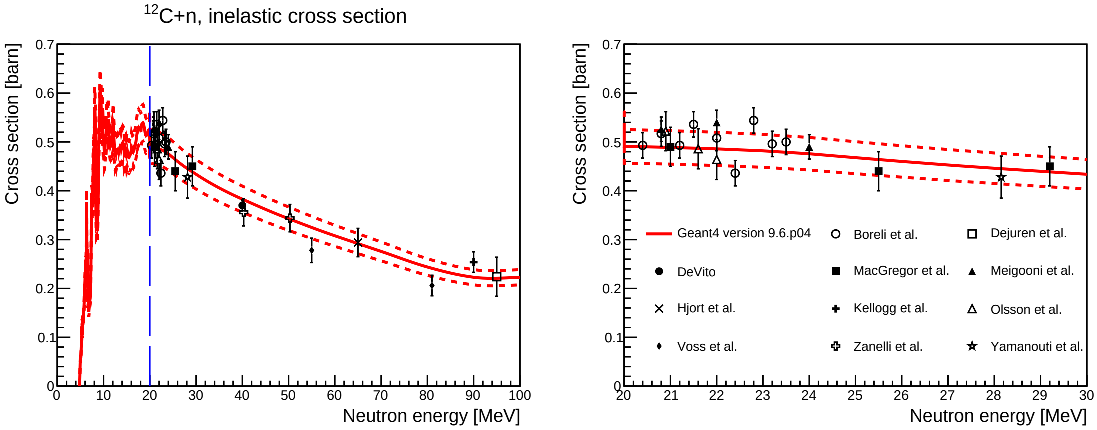

(b) Inlastic cross section

Figure 8.2: ^{12}C-neutron (a) elastic and (b) inelastic cross section as a function of neutron energy. The solid red lines represent the cross section in Geant4 version 9.6.p04, and the red dashed lines represent those with scaling factor by ±7% corresponding to 1σ uncertainty. The long dashed blue line shows the energy boundary of the BIC and HP models. The right figure is an enlarged view of the $20-30$ MeV. The experimental data are from [128–137], and they are tabulated in [138].

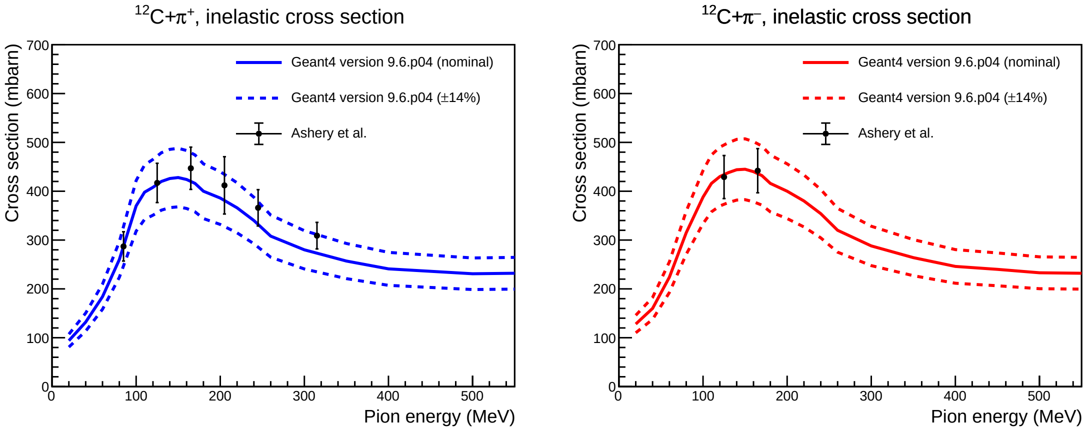

Figure 8.3: ^{12}C-π^+/π^- inelastic cross section as a function of pion energy. The left (right) figure shows π^+ (π^-). The black dots show the experimental data from Ashery *et al.* [139]. The solid lines represent the cross section in Geant4 version 9.6.p04, and the dashed lines represent those with scaring factor by ±14% corresponding to 1σ uncertainty. The inelastic cross section is the sum of the absorption, charge exchange, and inelastic scattering cross sections.

8.2.3 Neutron Production Yield of Muons

The neutron production yield of muons in Geant4 is compared with experimental data. Fig. 8.4 shows the neutron production yield Y_n as a function of muon energy in C_nH_{2n}. Geant4 simulation reproduces the experimental data well, except for LVD data in a wide energy range. The LVD data with 270 GeV mean muon energy gives the following result [140].

$$Y_n = 1.5 \pm 0.4 \times 10^{-4}\,/\mu/(\mathrm{g/cm^2}), \tag{8.6}$$

while the KamLAND data with 260 GeV mean muon energy [108] leads to

$$Y_n = 2.8 \pm 0.3 \times 10^{-4}\,/\mu/(\mathrm{g/cm^2}). \tag{8.7}$$

Geant4 simulation with 260 (270) GeV muon energy predicts the following results.

$$Y_n = \begin{cases} 2.9 \times 10^{-4}\,/\mu/(\mathrm{g/cm^2}) & (260\,\mathrm{GeV\ muon\ energy}), \\ 3.0 \times 10^{-4}\,/\mu/(\mathrm{g/cm^2}) & (270\,\mathrm{GeV\ muon\ energy}). \end{cases} \tag{8.8}$$

The Geang4 data is consistent with the KamLAND data but disagrees with the LVD data. The sizeable systematic uncertainty cannot easily explain the difference between the LVD and KamLAND data. Fig. 8.5 shows the energy spectrum of muon-induced neutrons produced in C_nH_{2n}. Since the LVD data gives a smaller neutron production yield, it is scaled by 2.0 to make it consistent. The spectrum shape of Geang4 is almost consistent with the scaled LVD data.

Neutron production by muons frequently occurs in cosmic muons with energy as high as 200 GeV. However, at the energies of a few hundred MeV observed in this study, it does not significantly contribute. Considering the density of the KamLS, for 10 GeV muons, the production yield is $\sim 1.6 \times 10^{-5}\,/\mu/\mathrm{cm}$. This value is significantly small compared to the ones via strong interactions, such as nucleons and pions. Thus, the uncertainty of this contribution is neglected in this study.

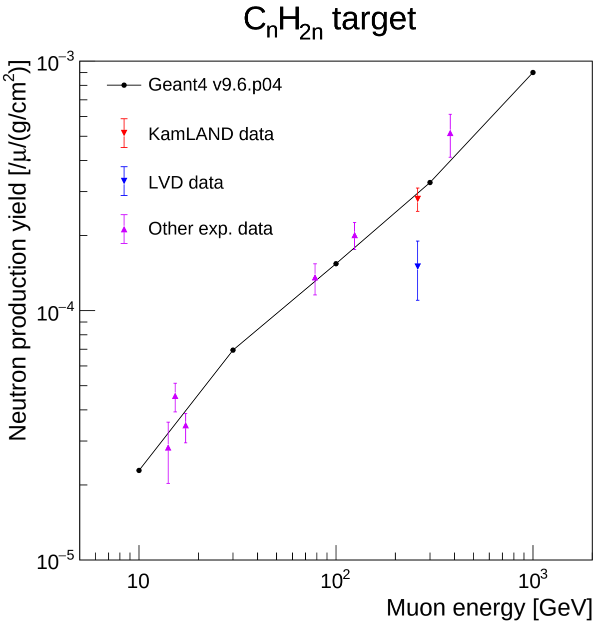

Figure 8.4: Neutron production yield as a function of muon energy in C_nH_{2n}. The black dots show the results of Geant4 version 9.6.p04. The red and blue dots represent experimental data by KamLAND [108] and LVD [140], respectively. The violet dots represent other experimental data [141]. LVD data is about two times smaller than Geant4 and KamLAND. Geant4 simulation is consistent with experimental data except for LVD data.

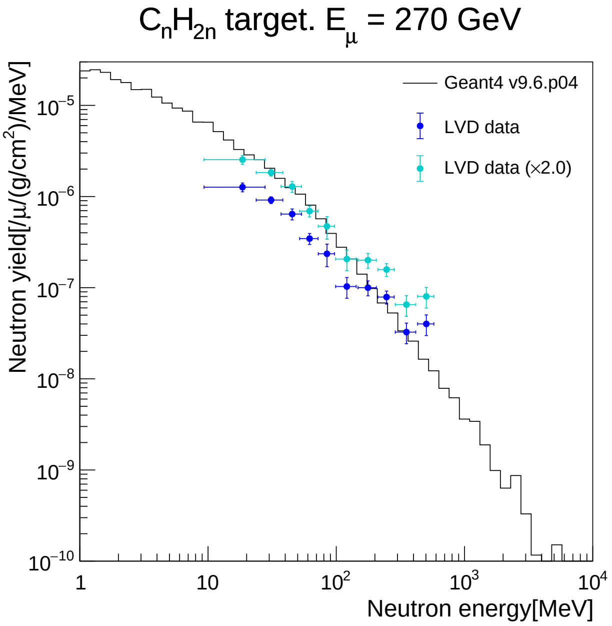

Figure 8.5: Energy spectrum of muon-induced neutrons produced in C_nH_{2n} at 270 GeV muon energy. The black line represents the results of Geant4 version 9.6.p04, and the blue dots represent the data of the LVD experiment [140]. The cyan dots represent the LVD data scaled by 2.0 so that the neutron production yield is consistent with Geant4. The scaled LVD data agrees with the Geant4 simulation.

8.3 Geometry, Scoring, and Event Reconstruction in KLG4

The KLG4 faithfully reproduces the KamLAND geometry. In addition, by considering the QE of the PMT photocathode when judging the hit of the optical photon, it can simulate various factors, such as photo coverage and light collection efficiency. There are several volumes with complex structures for ID, especially on the outside, such as outer balloon supporting straps and acrylic plates. Since the OD refurbishment changed the PMTs arrangement, we prepared two geometries before and after the OD refurbishment. See Appendix D.2 for more details.

KLG4 involves three processes to get the final physics parameters, such as vertex and energy. The first is the simulation of Geant4. In this process, the particle propagation, including the optical photon, is simulated. Then the time and charge information at which the optical photon hits the PMT are stored. Here, the information is the raw output of the simulation and does not include the detector responses. The time information is described by the global time in Geant4, and the charge information is the number of photons hit, a natural number. The PMTs are given the role of so-called "sensitive detectors" to save the hit information. The photon detection efficiency, including photo coverage, is accurately simulated by applying the quantum efficiency of the photocathode in the hit judgment.

In the second process, the detector response is added to the raw output of the simulation to reproduce the KamLAND real data. For example, the T.T.S. (time resolution), one p.e. inefficiency, the charge resolution, and the dark charge are considered. These detector responses are determined generally data-driven. After adding these detector responses, the charge of each PMT and the hit time of the first photon are calculated. This information is equivalent to those obtained by waveform analysis and time and charge correction on the KamLAND real data.

The events are reconstructed with the time and charge information in the third process. The muon, vertex, and energy fitter used in KLG4 are exactly the same as those used in the KamLAND real data analysis. Note that Geant4 is only involved in the first process, and only KamLAND analysis tools are involved in the second and third processes.

8.4 Tuning of Optical Parameters and Detector Responses

The accuracy of optical parameters and detector responses determine the quality of the KLG4. Many optical parameters of detector components have been measured in the laboratory. Most detector responses can be derived from laboratory measurements or the KamLAND real data. However, these parameters have uncertainties, and some of the optical parameters are not (or cannot be) measured. These uncertainties leave a large degree of freedom in the parameters. Therefore, we need to tune these optical parameters and detector responses to achieve better reproducibility.

KLG4 is tuned separately for the following four periods divided by activities that change the detector component and response.

- KLG4 period I: Before the first purification

  This is the period from the beginning of KamLAND to just before the start of the purification. Since the purification changed the optical properties, this period is divided from others. This period corresponds to "period I" in atmospheric neutrino analysis.

- KLG4 period II: After the second purification – before the KamLAND-Zen 400

This is the period from the end of the purification to just before the start of KamLAND-Zen 400. This period is separated because the mini-balloon was installed for the KamLAND-Zen 400. This period corresponds to "period II" in atmospheric neutrino analysis.

- KLG4 period III: During KamLAND-Zen 400

  This is the period during KamLAND-Zen 400. The mini-balloon geometry is implemented in KLG4 during this period. This period corresponds to "period III" in atmospheric neutrino analysis.

- KLG4 period IV: After KamLAND-Zen 400 and OD refurbishment − before the KamLAND-Zen 800

  This is the period after the KamLAND-Zen 400 and OD refurbishment and just before the start of KamLAND-Zen 800. A different OD geometry is implemented in this period, as shown in Appendix D.2. Note that there is no mini-balloon in this period. This period corresponds to "period IV" in atmospheric neutrino analysis.

The purification period during the KamLS light yield was changing is excluded. The KamLAND-Zen 800 period, outside of the data set in this study, is not included.

8.4.1 Radioactive Source Calibration

We primarily use the radioactive source calibration data of ^{137}Cs, ^{68}Ge, and ^{60}Co to tune the optical parameters. The geometries of the source holder and supporting equipment are prepared to consider the attenuation of gamma rays in the holder and the shadow effects. These radioactive decay events are generated in the KLG4, and the number of hits, total charge, and reconstructed vertices and energies are compared with the KamLAND data.

Note that there are two significant points in this tuning. The first is to use three or more sources with different energies. If only one or two sources are used, the quenching effect would be explained by the scaling of the absolute light yield, making it difficult to determine the Birk's constant. Conversely, using three or more sources, the quenching effect, namely the Birk's constant, can be determined separately from the absolute light yield. In the case of this tuning, ^{137}Cs emits one gamma-ray of 0.6616 MeV, while ^{68}Ge emits two gamma rays of 0.511 MeV via the positron annihilation. Thus, ^{68}Ge suffers the strongest quenching effect of the three sources. The second is to reproduce the real data for various z positions. For example, when tuning only the data when the source is at the center of KamLAND, it does not have the sensitivity to determine the attenuation length of the LS and BO. It is because there is no difference in optical path length for all ID PMTs, which can be explained by the scaling of the absolute light yield. On the other hand, if we use data where the source is located at 5 m, for example, there is a difference in optical path length, making it sensitive to the attenuation length. Furthermore, since the LS and BO regions of the KamLAND are slightly z-asymmetric, it is possible to see the difference in the attenuation length between the LS and BO by looking at the z-asymmetry in the calibration data,

This section shows the results of tuning for the KLG4 period IV. The reproducibilities for other periods (KLG4 period I−III) are almost the same, and they are summarized in Appendix D.3.

Hit, Charge, and Energy Quality

We first check the distributions of the number of hit PMTs (Nhit17 and NhitID), total charge (TotalCharge17 and TotalChargeID), and reconstructed energy (Energy and Energy17) of the sources. Fig. 8.6 shows the distributions of the composite source at the center of KamLAND during the KLG4 period IV. This study uses the energy reconstructed by 17-inch PMTs (Energy17), but the parameters that include 20-inch PMTs (NhitID, TotalChargeID, and Energy) are also tuned. In all of the six parameters, there are three peaks corresponding to the ^{137}Cs, ^{68}Ge, and ^{60}Co sources, and the peak distributions agree with the KamLAND real data.

We then check the peak positions of these distributions obtained by fitting the peak with the Gaussian at various z positions. The z-asymmetry of the peak positions caused by the difference in optical path length is susceptible to the attenuation length. Fig. 8.7 shows the deviation of the peak positions of the six parameters at various z positions. The deviation is defined as

$$\frac{(\text{Peak position in KLG4}) - (\text{Peak position in data})}{(\text{Peak position in data})}. \tag{8.9}$$

Comparing with the deviation of Energy17 in the KamLAND real data (Fig. 7.24d), there is a larger deviation in the KLG4, indicating some optical parameters or detector responses are not entirely reproduced. Nevertheless, over a wide z range of $-550 < z < 550\,\mathrm{cm}$, the peak positions agree within 3.5% for 17-inch PMTs only and 4.0% for ID PMTs. When targeting high-energy events, as in this study, the charge scale in the high-charge region is the main source of the uncertainty as studied in Sec. 8.4.2. Thus, the deviation in the low-energy region shown here is not much of a problem, and this quality is sufficient to meet the requirements [1].

Vertex Qualitiy

The vertex reproducibility depends on the effective light speed in LS and BO, which is determined by the Rayleigh scattering length and the refractive index parameterizing the light speed in the medium. The refractive indices were measured with good accuracy in the laboratory, including wavelength dependence (Fig. 6.6 and 6.9). On the other hand, the Rayleigh scatterings length has a large error in the measurements (Fig. 6.7). In this tuning, we vary the Rayleigh scattering length within the error, and a value that is in good agreement with the data is adopted.

Fig. 8.8 shows the vertex deviation between reconstructed z and source z positions in the KLG4. The deviation is less than 2.5 cm in a wide z range $-550 < z < 550\,\mathrm{cm}$, which is much better than that of KamLAND real data shown in Fig. 7.20.

Hit Timing Quality

The PMT hit timing is also checked and tuned. It depends on many parameters, such as the Rayleigh scattering length, the time constant of scintillation light, re-emission, and PMT T.T.S. In addition, there are complicated effects of detector-specific spurious pulses such as pre-pulse and late-pulse. Therefore, we need advanced tuning to achieve high

---

[1] In a KLG4 used in KamLAND-Zen analysis, the deviation of the charge peak position is less than 2% within a narrow z range $-250 < z < +250\,\mathrm{m}$. The KLG4 developed here is slightly worse than the quality: 2.5% within the z range. However, the KLG4 developed here has been found to have better quality than the KamLAND-Zen analysis for the outer regions.

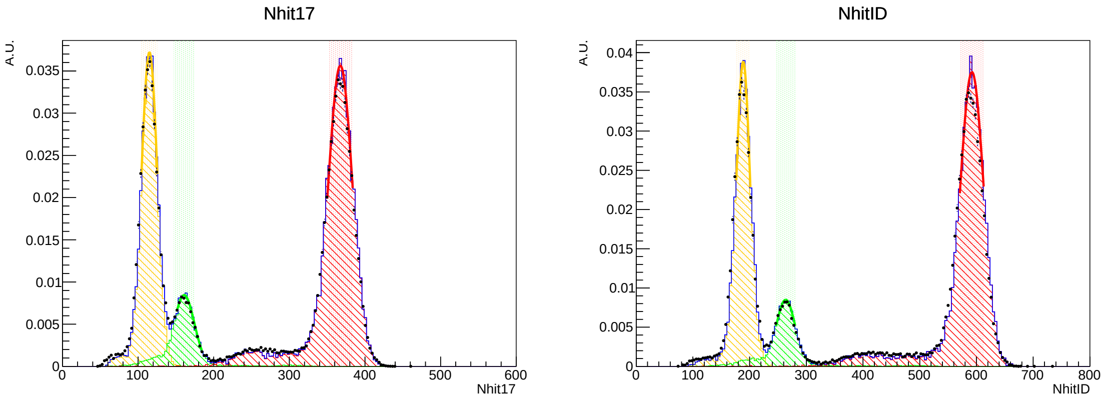

(a) The number of hit 17-inch PMTs (Nhit17) (b) The number of hit ID PMTs (NhitID)

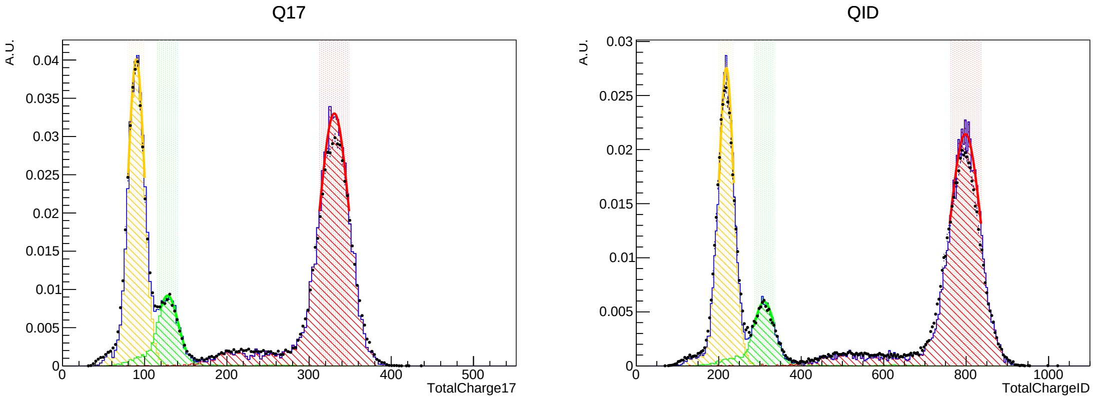

(c) Total charge of 17-inch PMTs (TotalCharge17)

(d) Total charge of ID PMTs (TotalChargeID)

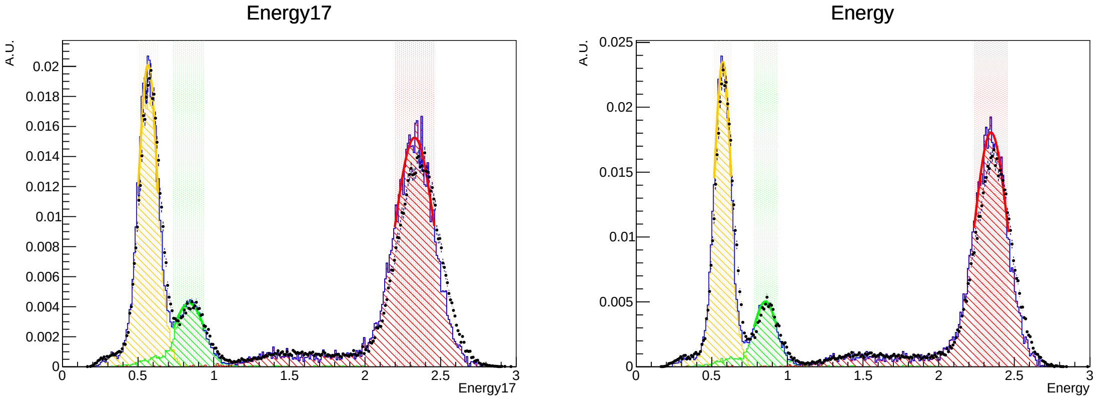

(e) Reconstructed Energy of 17-inch PMTs (Energy17)

(f) Reconstructed Energy of ID PMTs (Energy)

Figure 8.6: Distributions of the number of hit PMTs, total charge, and reconstructed energy of the composite source (^{137}Cs/^{68}Ge/^{60}Co) at the center of KamLAND. The data for the KLG4 period IV is shown. The black dots represent the KamLAND real data. The orange, green, and red shaded histograms represent the contributions from ^{137}Cs, ^{68}Ge, and ^{60}Co, respectively. The colored solid lines represent the fitting of peaks with the Gaussian, and the colored shaded boxes denote the $\pm 1\sigma$ region of the Gaussian.

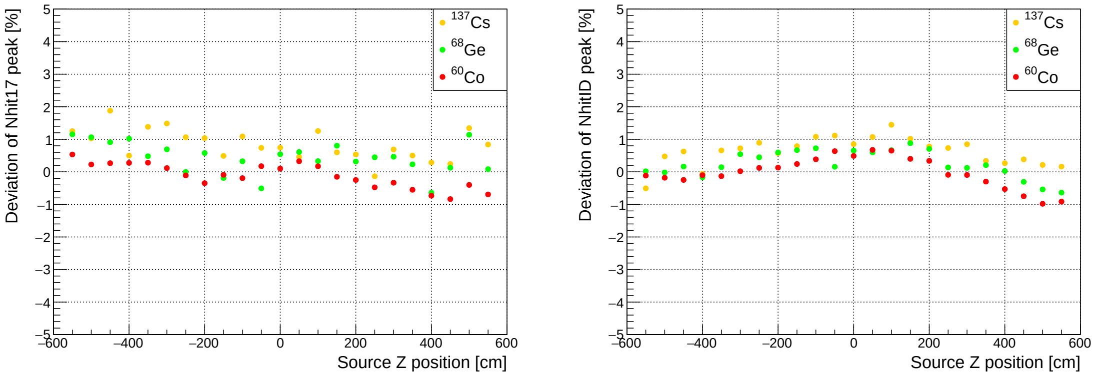

(a) The number of hit 17-inch PMTs (Nhit17) (b) The number of hit ID PMTs (NhitID)

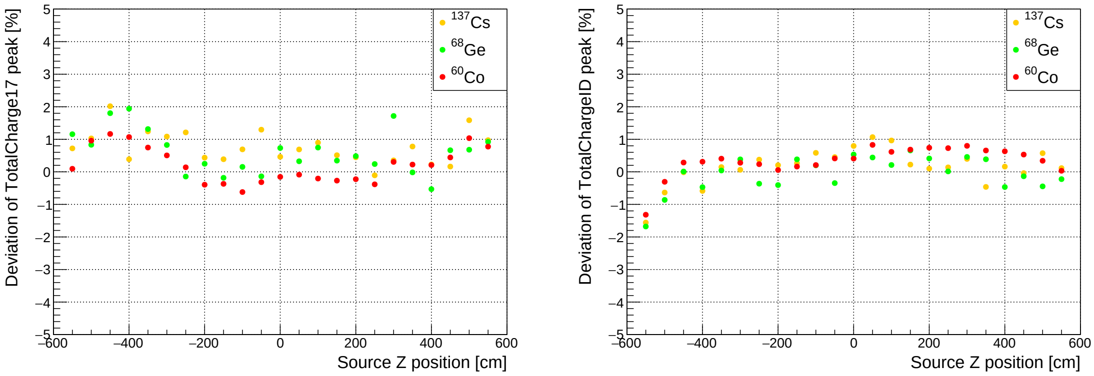

(c) Total charge of 17-inch PMTs (TotalCharge17)

(d) Total charge of ID PMTs (TotalChargeID)

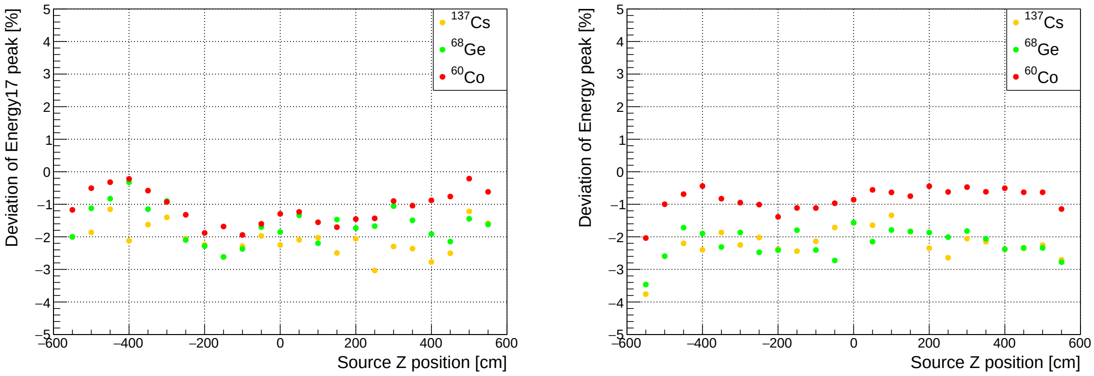

(e) Reconstructed Energy of 17-inch PMTs (Energy17)

(f) Reconstructed Energy of ID PMTs (Energy)

Figure 8.7: Deviations of the peak positions in the hits, charge, and energy distributions at various z positions. The data for the KLG4 period IV is shown. These parameters agree with the KamLAND real data within 3.5% (4.0%) for 17-inch PMT only (with 20-inch PMTs).

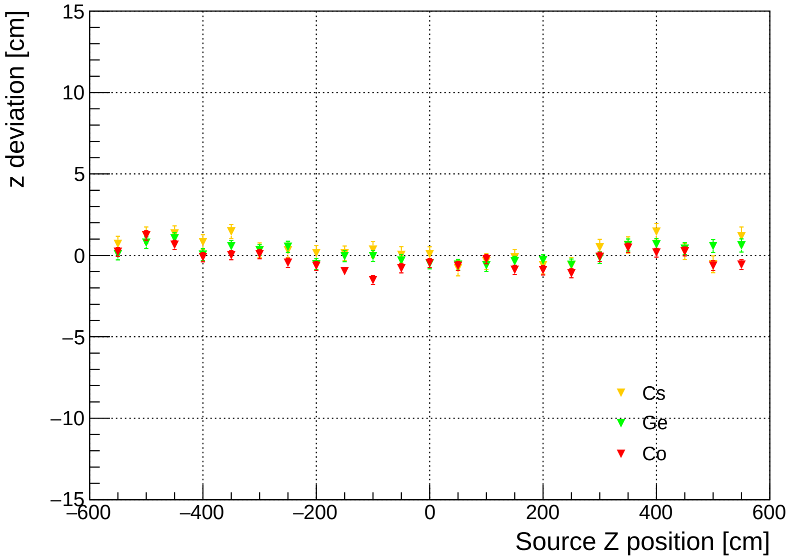

Figure 8.8: Vertex deviation between reconstructed z and source z position in the KLG4 period IV. The vertex deviation is less than 2.5 cm in all sources and z positions, which is much better than that of KamLAND real data shown in Fig. 7.20.

reproducibility for the hit timing. It should be noted that the KLG4 developed in this study has not yet implemented the pre-pulse.

Fig. 8.9 shows the hit timing distribution of 17-inch and both 17-inch and 20-inch PMTs. KLG4 generates pseudo dark hits using dark hit rates estimated with the real data, agreeing with the data and simulation in the dark hit region, $-100 \lesssim$ (hit timing) $\lesssim -50$ ns. In the most important signal region ($-10 \lesssim$ (hit timing) $\lesssim 40$ ns), the curve shapes are in good agreement, which strongly depends on the time constant of the scintillation light. The rise of the signal peak ((hit timing) $\simeq -20$ ns) is the typical time window of the pre-pulses. Since the current KLG4 does not consider the effect of pre-pulse, there is a discrepancy between the data and the simulation. Although it is not so important in event reconstruction, it may be possible to improve the accuracy of hit timing distribution by modeling and implementing the pre-pulse. After the signal region ((hit timing) $\gtrsim 40$ ns), the component of a long time constant of the scintillation light, late-pulse, and the Rayleigh scattering affects the distribution significantly. Although we have some laboratory measurements for these parameters, they tend to have large uncertainty. The probability and time delay of the late pulse are complicated to model. The discrepancy between data and simulation in this region becomes larger than that of the signal region. This region is not so important in the event reconstruction, but it is one of the future issues to be addressed.

8.4.2 Cosmic muon

The reproducibility of the high-energy region is also investigated and tuned using cosmic muons. The cosmic muon events are simulated in the KLG4 according to the flux profile introduced in Sec. 6.1.1. The source calibration data determines well the optical parameters related to the KamLS but is not so sensitive to the parameters related to the BO. In

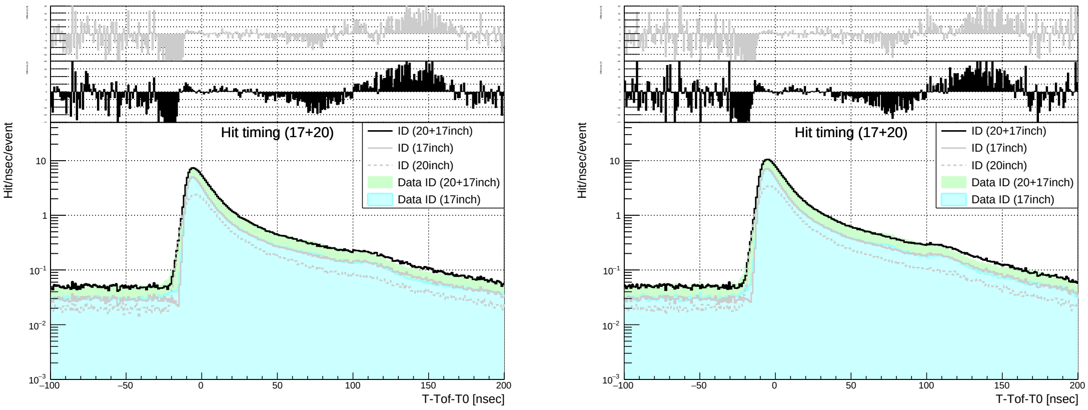

(a) ^{137}Cs (b) ^{68}Ge

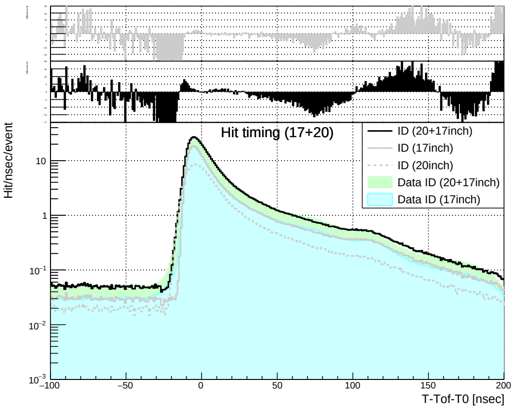

(c) ^{60}Co

Figure 8.9: Hit timing distribution of 17-inch and both 17-inch and 20-inch PMTs. The bottom panel shows the hit timing distribution of data and simulation, and the middle panel shows the deviation of 17-inch and 20-inch PMTs, and the top panel shows the deviation in 17-inch PMTs only. The data for the KLG4 period IV is shown.

particular, it is not sensitive to the light yield of weak scintillation light emitted by BO [2]. Therefore, the main parameters to be tuned here are those related to the BO.

Fig. 8.10 shows the muon total charge distribution obtained from the simulation compared with the KamLAND data. Two peaks in the charge distribution correspond to the minimum ionization of muon in the LS and BO. The peak position is determined by the light yield of the LS and BO and is compared with the data to tune the simulation and estimate the charge scale uncertainty. The charge distribution of the simulation is consistent with the real data, including the peak positions. The peak positions defined by fitting with the Gaussian agree with the real data within 6% (8%) for LS muons (BO muons) in all KLG4 periods.

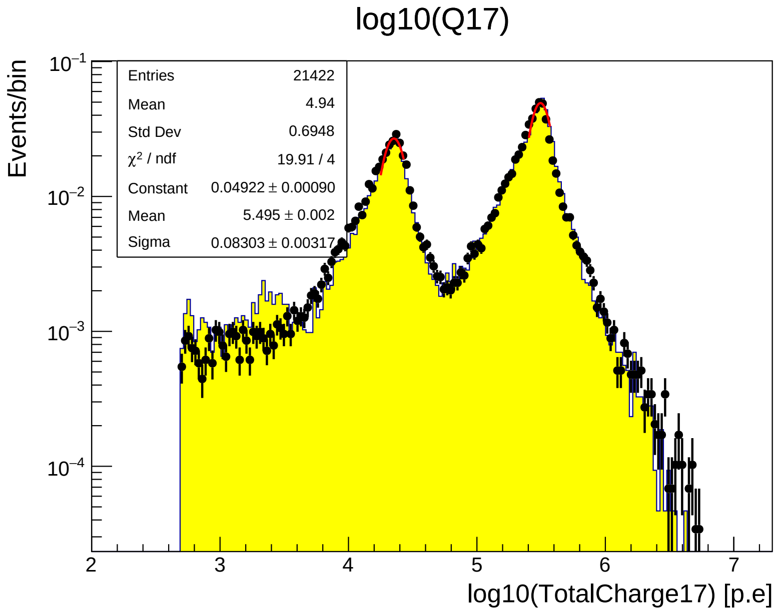

Figure 8.10: Muon total charge distribution of data and simulation. The black dots denote the KamLAND real data, while the yellow-shaded region represents the simulation results. The peak positions, corresponding to the charge via the minimum ionization of muon in BO and LS, are in good agreement between the data and simulation. The solid red lines represent the fit of these peaks with the Gaussian using simulation result. The data for the KLG4 period IV is shown.

Fig. 8.11 shows the muon charge per reconstructed muon track length in the LS and BO. These parameters are defined as Eq. 7.18 and 7.19. The total charge mentioned above is a simple sum of the observed charge, but this parameter depends on the reconstruction quality of the muon fitter. Since the reconstruction quality depends on various factors, such as timing and charges observed by each PMT, this parameter allows the advanced cross-check of the tuning quality. The peak shown in Fig. 8.11 corresponds to the light

---

[2] The fact that the BO produces weak scintillation light was found from simulation studies of cosmic muons using KLG4. We initially thought that the BO, composed of mineral oil, does not emit scintillation light, and KLG4 did not confer scintillation light emission on the BO. However, when we simulated cosmic muons that passed through the BO, we found that the charge was more than half less than the real data and that the PMT hit distribution also had a much less isotropic component. Subsequent detailed simulation studies revealed that the BO has a scintillation emission capability of ~400 photons/MeV, corresponding to ~ 5% of that of the KamLS. The mineral oil composing the BO has no luminescence performance, but some additives may have it.

yield of the minimum ionization of muon in LS and BO. The peak positions determined by Gaussian fitting agree with the real data within 6% (8%) for LS muons (BO muons) in all KLG4 periods.

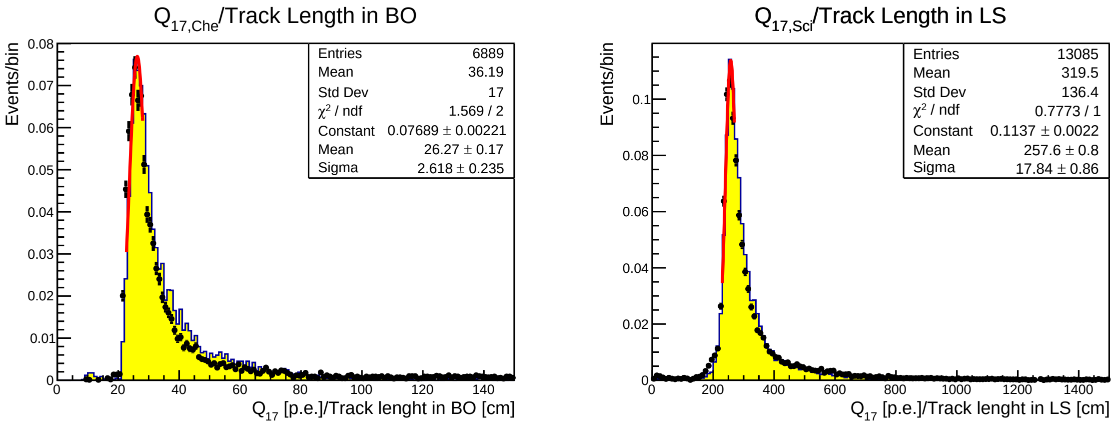

Figure 8.11: Muon charge per reconstructed muon track length in LS (right) and BO (left) of data and simulation. The black dots denote the KamLAND real data, while the yellow-shaded region represents the simulation result. The peak positions, corresponding to the charge via the minimum ionization of muon, are in good agreement. The solid red lines represent the fit of these peaks with the Gaussian using the simulation result. The data for the KLG4 period IV is shown.

Part IV

Measurement of Atmospheric Neutrino Interactions at KamLAND

Chapter 9

KamLAND Data

This chapter describes the analysis of atmospheric neutrino data at KamLAND. This study uses the KamLAND data acquired between January 2003 and May 2018, corresponding to a total live time of 10.74 years. The data set of this analysis is summarized in Sec. 9.1. The detection method of the atmospheric neutrino signals at KamLAND is explained in Sec. 9.2. The selection criteria of atmospheric neutrino events are shown in Sec. 9.3 and 9.4. For precise determination of the strangeness axial coupling constant g_A^s, the neutron tagging efficiency is precisely estimated using cosmic muons as described in Sec. 9.5. The fiducial volume uncertainty for the neutron events is also checked in Sec. 9.6.

9.1 Data Set

The KamLAND data used in this study are based on a total live time of 10.74 years, acquired between January 2003 and May 2018. The data set is divided into four periods (period I−IV) by activities that change the detector response. These four periods correspond to the four periods of KLG4 described in Sec. 8.4. The atmospheric neutrino events observed in each period are compared with simulations using the corresponding KLG4. Thus, the analysis can consider the changes in various detector responses. Tab. 9.1 shows a summary of the data set. The data from 2016 Aug. to Nov. corresponding to the KamLAND-Zen failed 800 is excluded from the analysis.

Table 9.1: Sumamry of data set of this study. The data from 2016 Aug. to Nov. corresponding to the KamLAND-Zen failed 800 is excluded from period IV. These periods correspond to the periods of KLG4 shown Sec. 8.4.

Period	Date	Live time (years)	Detector status
I	2003 Jan. – 2007 May	3.77	Before the first purification
II	2009 Apr. – 2011 Aug.	1.79	After the second purification – before the KamLAND-Zen 400
III	2011 Oct. – 2015 Aug.	3.66	During the KamLAND-Zen 400
IV	2016 Apr. – 2018 May	1.52	After the OD refurbishment – before the KamLAND-Zen 800

9.2 Atmospheric Neutrino Signals in KamLAND

KamLAND detects neutrino interactions via scintillation light. Since there is no threshold for scintillation light, unlike Cherenkov light, scintillator detectors such as KamLAND can detect not only charged leptons and pions but also protons and neutrons with low energy thresholds. Protons directly produce scintillation light through ionization, while neutrons are detectable via proton recoils and later through capture on nuclei. Since the NCQE interactions mainly emit protons and neutrons, this feature of scintillator detectors makes it possible to measure the NCQE interactions.

Fig. 9.1 shows a schematic view of the detection of atmospheric neutrino interactions at KamLAND. A neutrino interaction in KamLAND produces a prompt event caused by the energy deposit of charged particles and proton recoils by neutrons. Neutrons are then captured by protons (^{12}C) with a lifetime of $207.5 \pm 2.8\,\mu$s [108] and emit gamma rays of 2.2 (4.9) MeV producing delayed events. From the thermal neutron capture cross section and elemental composition of KamLS, 99.5% of the neutrons are captured on proton (^{1}H), while the remainders are captured mostly on ^{12}C [108]. We can select the neutron capture events with high accuracy by performing delayed coincidence measurements using time and spatial correlations of prompt and delayed events.

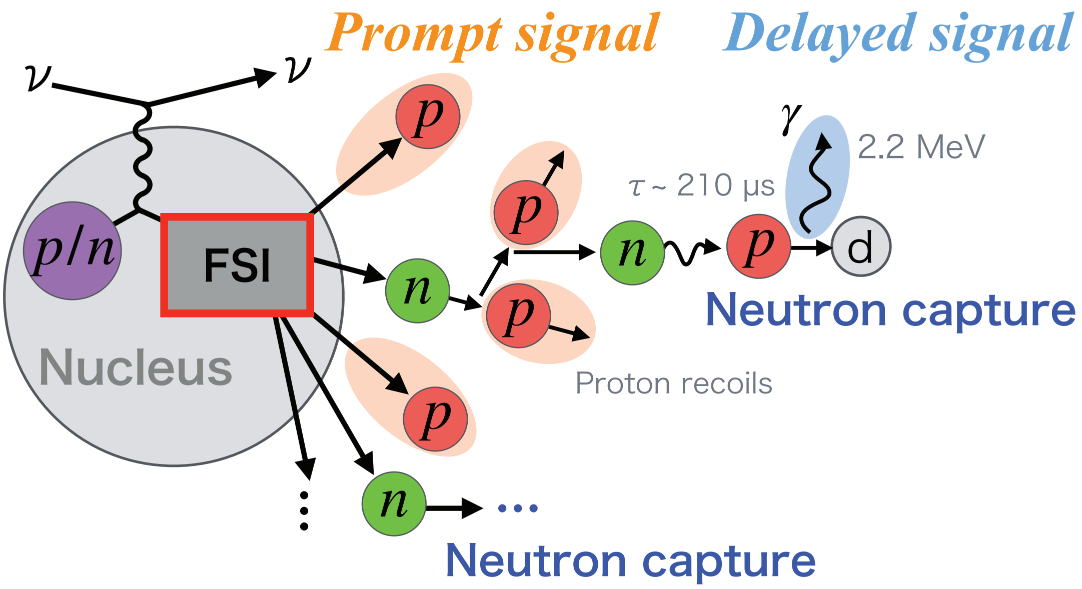

Figure 9.1: Detection of atmospheric neutrino interactions at KamLAND. A neutrino interaction in KamLAND produces a prompt signal by the energy deposit of charged particles. Neutrons are detectable as the prompt signal via proton recoils. A neutron thermalized in the detector is mostly captured by protons emitting a gamma ray. This gamma ray produces a delayed signal. By using time and spatial correlations between prompt and delayed signals, i.e., delayed coincidence measurements, we can select the neutron capture events with high purity.

Detectors used to measure neutrino interactions so far are optimized to measure charged leptons. Since protons tend to have a very short track length of only a few centimeters, protons and proton recoils by neutrons are very challenging to measure with current detectors. The neutron capture gamma rays are also tricky to measure because of the small energy deposit density. For these reasons, no experiment measured nucleon multiplicity by neutrino interactions with high efficiency. Recently, detectors sensitive to protons have been developed by significantly increasing the track resolution. However, even with these detectors, measuring neutrons will still be challenging. KamLAND can measure neutron multiplicity by the delayed coincidence method with a high neutron tagging efficiency of $\gtrsim 80\%$, while other experiments have reported detection efficiencies of about 20%.

KamLAND has two unique features. The first is the ability to measure various particles with a very low energy threshold of about 0.3 MeV. This low energy threshold makes measuring NC (especially NCQE) interaction possible. Second, it can measure neutron multiplicity associated with neutrino interactions with high efficiency. Using these KamLAND's unique features, which are quite challenging for other detectors, we can test and improve the neutrino-nucleon interaction models from a new viewpoint. This dissertation focuses on the neutron multiplicity associated with the NCQE interactions, but other exciting studies would be possible.

We give some notes on the energy and vertex used in this analysis. This analysis uses visible energy to evaluate atmospheric neutrino events. For CC events, the visible energy includes the energy deposit of the final-state lepton (electron or muon). On the other hand, in the case of NC events, the visible energy does not include that of the final-state lepton (neutrino), making it tend to have lower prompt visible energy than CC events. The vertex used here is almost equivalent to the centroid of the energy deposition. Since the KamLAND vertex fitters cannot distinguish the energy deposit of different particles produced by a neutrino interaction, they treat all the energy deposition at the same point source. A new fitter for reconstructing neutrino interaction points and end points of the charged particle is currently under development.

9.3 Prompt Event Selection

This section describes the selection of prompt events produced by charged particles and proton recoils by neutrons. The atmospheric neutrino flux (discussed in Sec. 10.1) is distributed over a wide energy range from MeV to TeV. The visible energy of NC interactions becomes small because the neutrino energy of the final state is not observable. As a result, the visible spectra of the prompt events in KamLAND have a wide energy range and a slow, monotonically decreasing trend.

9.3.1 Selection Criteria

Various criteria are applied to select prompt events as follows.

- Energy selection: $50 < E_{\text{prompt}} < 1000\,\text{MeV}$
- Radius selection:
  - $R_{\text{prompt}} < 450\,\text{cm}$ for $50 < E_{\text{prompt}} < 200\,\text{MeV}$ (low-E selection)
  - $R_{\text{prompt}} < 500\,\text{cm}$ for $200 < E_{\text{prompt}} < 1000\,\text{MeV}$ (high-E selection)
- OD cut:
  - $N_{200\text{OD}} < 5$ (period I–III)
  - $N_{200\text{OD}} < 9$ (period IV)

- Bad event cut: $VertexBadness < 30$
- Noise event cut: $N_{100} > Nhit_{\mathrm{ID}}/2 + 25$
- Muon veto: Exclude data for 2 ms immediately after cosmic muon events.
- Deadtime veto: Exclude for data 2 ms immediately after the dead time.
- J-PARC neutrino beam veto: Exclude data for 3 ms immediately after J-PARC neutrino beam launch timing.

Energy and Radius Selection

The energy selection criterion is as $50 < E_{\mathrm{prompt}} < 1000\,\mathrm{MeV}$ that can adequately select NCQE interactions, which dominate the low-energy region below 200 MeV. This analysis uses visible energy reconstructed by KatEnergy using only 17-inch PMTs (Energy17). The charge linearity in the region up to 1000 p.e./PMT is calibrated using the dye-laser calibration data. The charge roughly corresponds to 6 GeV in visible energy for events at the center of KamLAND. The upper energy cut is set to be 1 GeV, where the linearity is considered to be maintained. Since the background contribution of fast neutrons and radioactive isotopes becomes enormous below 50 MeV, the lower energy cut is set to be 50 MeV.

We apply two spherical fiducial volume selection criteria with different radii: A 450 cm radius for $50 < E_{\mathrm{prompt}} < 200\,\mathrm{MeV}$ (low-E selection), and a 500 cm radius for $200 < E_{\mathrm{prompt}} < 1000\,\mathrm{MeV}$ (high-E selection). A tighter radius cut is applied for the low-E selection because fast neutron backgrounds are present below 200 MeV. The detail of the fast neutron background is described in Sec. 10.3.

OD Cut

In order to cut cosmic muon backgrounds, the OD cut is also applied by using the number of hit OD PMTs within a 200-ns time window $N_{200\mathrm{OD}}$: $N_{200\mathrm{OD}} < 5$ for periods I–III and $N_{200\mathrm{OD}} < 9$ for period IV. Since the OD system was refurbished before the beginning of period IV, the threshold is adjusted, so that veto efficiencies are equal. The OD cut rejects atmospheric neutrino events where the final-state particles exit the ID. All the events selected in this analysis are fully contained in the ID.

Bad Event Cut

In extremely rare cases, cosmic muon events are tearfully separated into two events in the KamDAQ. Fig. 9.2 shows the typical event displays of the separated cosmic muon events. The following processes cause these events. First, a trigger issued by a low-energy or noise event just before the cosmic muon enters the KamLAND. Then, the event time window closes with a signal halfway through the cosmic muon, and the event is recorded as the first event (Fig. 9.2a). After that, the subsequent signals are then recorded as a separate event (Fig. 9.2b). Since the OD hit information tends to be recorded in the second event, the OD cut cannot veto the first event. Therefore, the first event of the separated cosmic muon events can contaminate atmospheric neutrino events.

These events can be characterized by a high-charge event immediately after and a very bad vertex reconstruction quality. We can easily identify the events by using a parameter $VertexBadness$, an indicator of vertex reconstruction quality in the V2 fitter. While the physics events tend to have $VertexBadness < 15$, the separated cosmic muon events have a huge value of over 30. Hence, this study establishes a cut condition of $VertexBadness < 30$. This cut condition successfully excludes six bad events, as shown in Fig. 9.3. For all of them, a high-charge event corresponding to the rest of the cosmic muon was recorded immediately after the event.

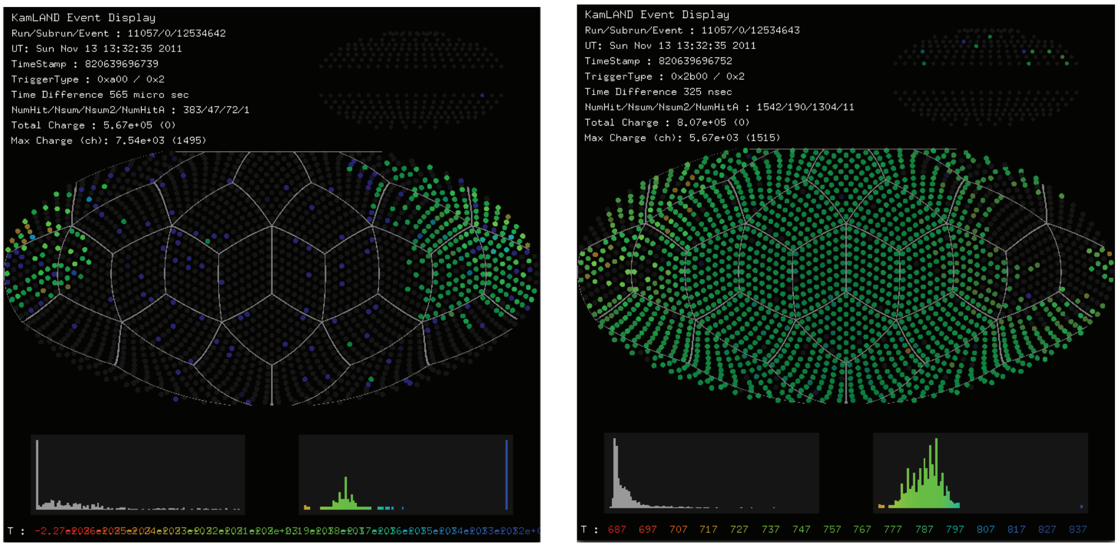

```
KamLAND Event Display
Run/Subrun/Event : 11057/0/12534642
UT: Sun Nov 13 13:32:35 2011
TimeStamp : 820639696739
TriggerType : 0xa00 / 0x2
Time Difference 565 micro sec
NumHit/Nsum/Nsum2/NumHitA : 383/47/72/1
Total Charge : 5.67e+05 (0)
Max Charge (ch): 7.54e+03 (1495)
```

```
KamLAND Event Display
Run/Subrun/Event : 11057/0/12534643
UT: Sun Nov 13 13:32:35 2011
TimeStamp : 820639696752
TriggerType : 0x2b00 / 0x2
Time Difference 325 nsec
NumHit/Nsum/Nsum2/NumHitA : 1542/190/1304/11
Total Charge : 8.07e+05 (0)
Max Charge (ch): 5.67e+03 (1515)
```

(a) First half event

(b) Second half event

Figure 9.2: Typical event displays of the tearfully separated muon events. The dots in the middle (small upper right) panel denote ID (OD) PMTs and the colors represent hit timing. The hit PMTs are separated between the first and second events. A parameter $VertexBadness$, which indicates the quality of the vertex reconstruction, tends to be larger than 30 for these events. (a) A muon entered from the top right of the figure. The PMT waveforms up to the halfway are recorded as the first event. Since OD hit information tends to be stored in the second event, the first event is not vetoed by OD cut. (b) The rest of the waveforms of ID PMTs and the entire information of OD PMTs are recorded as the second event. In this case, the time difference from the first event is 325 ns.

Other Cut and Veto Conditions

The noise event cut is also applied by using the number of hit ID PMTs ($Nhit_{\mathrm{ID}}$) and the number of hit 17-inch PMTs within 100 ns time window (N_{100}). The criteria is $N_{100} > Nhit_{\mathrm{ID}}/2 + 25$, using the tendency of noise events to have poor hit timing correlation giving small N_{100}. This cut is useful for low-energy regions [123], but almost means less in the high-energy region because noise events imitating high-energy events do not occur.

Immediately after cosmic muon events, the event reconstruction quality becomes poor due to PMT overshoots and after-pulses. In order to avoid these biases, data for 2 ms immediately after the cosmic muon events are vetoed and excluded from the analysis. Since the cosmic muon flux at KamLAND is about 0.34 Hz, the deadtime ratio caused by this veto is significantly small, about 0.07%.

KamDAQ has dead time due to various factors. For example, the HV device may trip, or the DAQ system may become temporarily busy, preventing the trigger from being

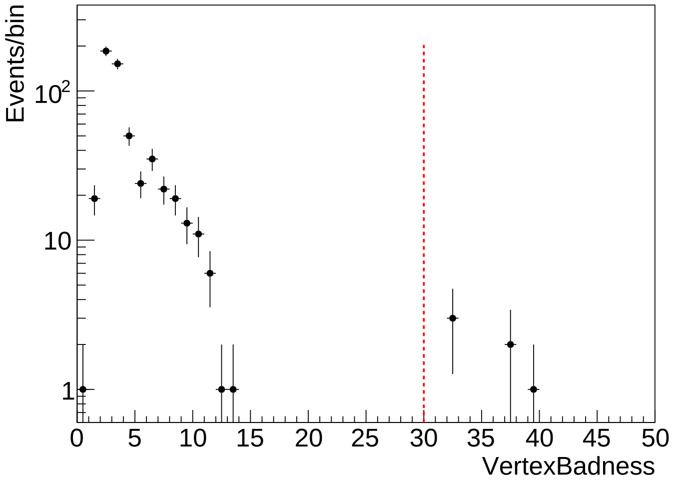

Figure 9.3: $VertexBadness$ distribution of atmospheric neutrino candidates. The red dashed line represents the cut condition of $VertexBadness < 30$. The bad events (tearfully separated cosmic muon events) have distinctly larger values than other physics events. All KamLAND atmospheric neutrino data sets are shown: both high-E and low-E selections during period I−IV.

issued. The time of these issues is accurately determined by monitoring hit rates and recording information about the hardware situation. The period during these issues is excluded from the physics analysis as deadtime. In this study, we additionally veto 2 ms to the dead time. This criterion is a conservative configuration widely applied in the KamLAND physics analysis.

Neutrino beam is launched from J-PARC in Ibaraki Prefecture to Super-Kamiokande, which is about 100 m away from KamLAND [142]. The beam is for T2K experiments to search the CP violation in the neutrino oscillation. Because of the very close distance between the KamLAND and the Super-Kamiokande, J-PARC neutrino beam events have also been observed at KamLAND. Events during the 3 ms from the beam launch time are vetoed to exclude these beam-induced events. The T2K Collaboration provides information on beam timing. We have developed a tool to synchronize with the KamLAND time [143]. The J-PARC neutrino beam is launched about once every three seconds, giving a sufficiently small deadtime ratio, about 0.1%.

9.3.2 Profile of Prompt Event Candidates

At first, the validity of the OD cut is checked in Fig. 9.4, which shows $N_{200\mathrm{OD}}$ distribution of atmospheric neutrino candidates. The threshold for $N_{200\mathrm{OD}}$ must be low enough to veto cosmic muons while high enough to select atmospheric neutrino events. The figure shows that the threshold satisfies these requirements. In addition, the data and simulation have a flat distribution and a small number of events around the threshold. Therefore, the uncertainty of $N_{200\mathrm{OD}}$ gives negligible impact on the atmospheric neutrino candidates.

The vertex distribution of neutrino events should be uniform within the detector. In contrast, background events such as the fast neutrons are non-uniform, having a larger contribution in the outer regions. Fig. 9.5 shows the vertex distribution of the atmospheric neutrino candidates. The clusters at the top and equator regions are due to OD untagged muons. Since the KamLAND OD has relatively low veto efficiency at the chimney and

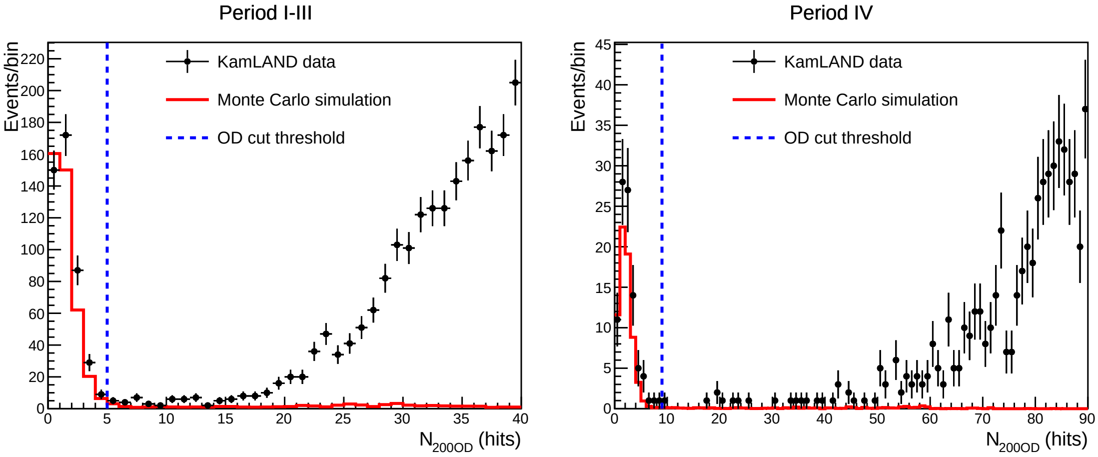

Figure 9.4: $N_{200\mathrm{OD}}$ distribution of atmospheric neutrino candidates for period I–III (left) and IV (right). The dots show KamLAND data, the red line represents the Monte Carlo simulation before the spectra fitting, and the blue dashed line shows the selection criteria: $N_{200\mathrm{OD}} < 5$ for periods I–III and $N_{200\mathrm{OD}} < 9$ for period IV. Period IV has increased hits due to the OD refurbishment. The simulation shows the sum of atmospheric neutrinos and fast neutron background events. The excess in the large $N_{200\mathrm{OD}}$ region corresponds to cosmic muon contributions, which are not included in the simulation. Both data and simulation have a flat distribution and a small number of events around the thresholds. Furthermore, the thresholds are sufficiently low to exclude the contribution of cosmic muons.

equator, cosmic muons incidents from these areas are sometimes not tagged by the OD cut. Cosmic muons tend to be reconstructed to a point near the start of the track, i.e., on the outside. Therefore, these OD untagged muons can be excluded by applying radius selection within 500 cm.

Fig. 9.6 shows the radius distribution. In the high-E selection (Fig. 9.6b), the distribution is uniform (flat) within the fiducial volume, indicating the radius cut significantly rejects the OD untagged muon. On the other hand, in the low-E selection (Fig. 9.6a), the distribution is non-uniform. The non-uniformity is evidence of contamination of the fast neutron background in the candidates. The contribution of the fast neutron background is estimated using the simulation described in Sec. 10.3.

Fig. 9.7 shows the energy spectra of the candidates. It has a wide energy range and a slow, monotonically decreasing trend within statistical errors. Above 200 MeV, the contribution of fast neutron events is negligible, but it is not below 200 MeV. It is also confirmed that the observed energy spectra are consistent with the simulation within the statistical errors.

Tab. 9.2 shows the number of atmospheric neutrino candidates in each period. As a result, we find 114 (425) events for low(high)-E selection. The event rate in each period is stable within statistical errors. Atmospheric neutrino flux has two kinds of time variation: seasonal variation and solar cycle variation. Both variations are small compared to the statistical errors. Details about the time variation are given in Sec. 10.1.

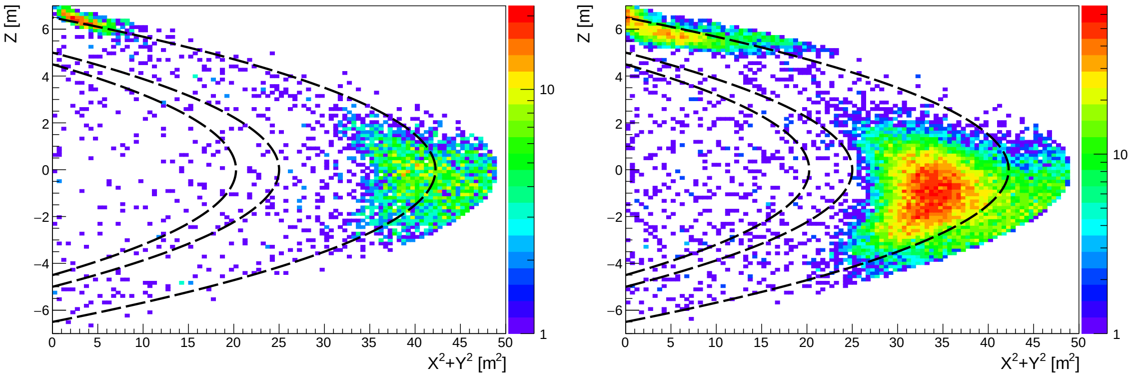

(a) Low-E selection (b) High-E selection

Figure 9.5: Vertex distribution of atmospheric neutrino candidates. The long dashed lines represent radii with $R = 450$, 500, and 650 cm. The KamLAND OD has relatively low veto efficiency at the chimney and equator. Therefore, two clusters around these regions are due to the OD untagged muons.

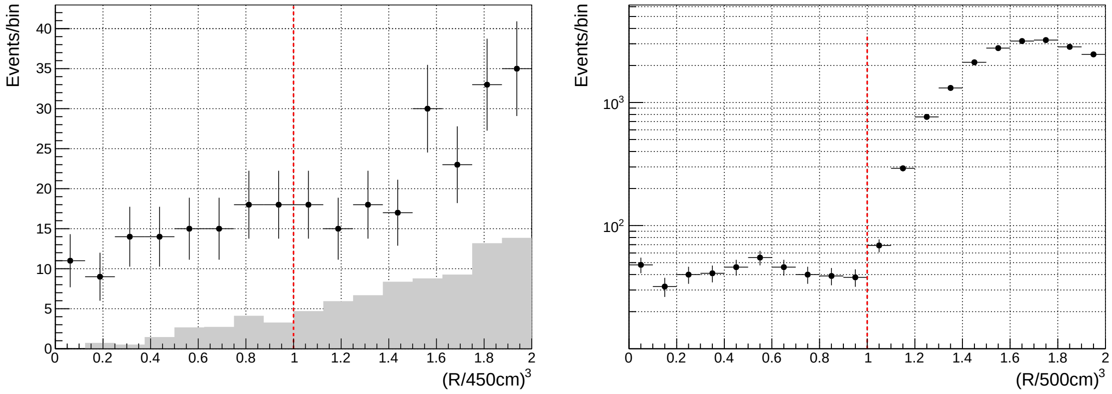

(a) Low-E selection (b) High-E selection

Figure 9.6: Radius distribution of atmospheric neutrino candidates. The gray-shaded region represents the fast neutron background contribution estimated by the simulation (see Sec. 10.3 for detail). The red line denotes the radius selection criteria. (a) The distribution within the fiducial volume is non-uniform because of the fast neutron background. (b) The distribution within the fiducial volume is uniform indicating that the fast neutron background contribution is negligible in the high-energy region. On the other hand, outside of the fiducial volume, there is seepage of the OD untagged muons, but these events are rejected by the 500 cm radius selection.

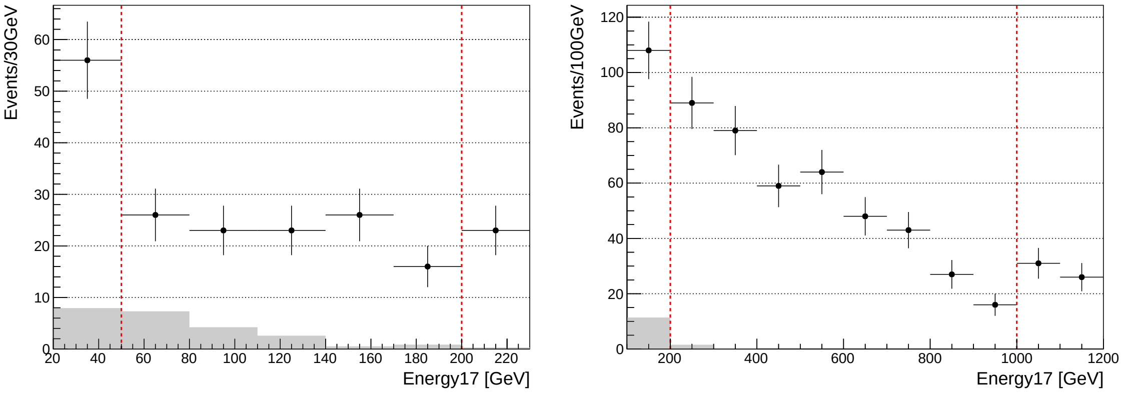

(a) Low-E selection

(b) High-E selection

Figure 9.7: Energy spectra of atmospheric neutrino candidates. The gray-shaded regions represent the fast neutron background contribution estimated by the simulation (see Sec. 10.3 for detail). The red lines denote the energy selection criteria.

Table 9.2: The number of atmospheric neutrino (prompt) candidates in each period. The statistical error is shown in the event rate. The event rate in each period is stable within the statistical error.

Period	Live time (years)	Events		Event rate (events/year)	
		Low-E	High-E	Low-E	High-E
I	3.77	33	148	8.8 ± 1.5	39.3 ± 3.2
II	1.79	18	76	10.4 ± 2.4	42.4 ± 4.9
III	3.66	39	133	10.7 ± 1.7	36.4 ± 3.2
IV	1.52	24	68	15.8 ± 3.2	44.8 ± 5.5
I–IV	10.74	114	425	10.6 ± 1.0	39.6 ± 1.9

9.4 Delayed Event Selection

This section contains the selection of delayed events produced by the neutron capture gamma rays. We select pure neutron capture events using the time correlation with the atmospheric neutrino candidates. Note that the presence or absence of delayed events is irrelevant to selecting prompt events.

9.4.1 Selection Criteria

Immediately after a high-charge event, such as atmospheric neutrino candidates, PMT after-pulses cause many noise events. The high event rate leads to channel-level electronics deadtime effects, and as a result, many PMT waveforms are not recorded, making accurate event reconstruction difficult. Several criteria are applied to select delayed (neutron capture) events, avoiding the deadtime effects. Since the neutrons emitted via the atmospheric neutrino interactions have high energy, a spatial correlation is not used in the selection.

- Time correlation selection: $10 < \Delta T < 1000\,\mu\mathrm{s}$
- Hit selection: $NsumMax > 275\,\mathrm{hits}$
- Radius selection: $R_{\mathrm{delayed}} < 600\,\mathrm{cm}$
- Noise event cut: $N_{100} > Nhit_{\mathrm{ID}}/2 + 25$

As for time correlation selection, we set $10 < \Delta T < 1000\,\mu\mathrm{s}$, excluding events with a time delay of less than $10\,\mu\mathrm{s}$. A parameter $NsumMax$, which is the number of hit 17-inch PMTs within a 125 ns time window, is used instead of the visible energy. This parameter is less affected by the electronics deadtime effects, especially missing waveforms. The expected number of hits for 17-inch PMTs with 2.2 (4.9) MeV gamma ray is almost 400 (1000) hits. Therefore, a sufficiently low threshold $NsumMax > 275$ hits are applied for the 2.2 MeV gamma rays

A spherical fiducial volume selection is applied: $R_{\mathrm{delayed}} < 600\,\mathrm{cm}$. In order to exclude the contribution of background events of PMT- and rock-derived gamma rays cannot be neglected in the outer region $R \gtrsim 650\,\mathrm{cm}$, a 600 cm radius is set. Since this selection is well inside the outer balloon ($R \simeq 650\,\mathrm{cm}$), neutron capture gamma rays have enough energy deposit in the KamLS. In addition, by selecting a wider region than the prompt events, the impact of fiducial volume uncertainty on the delayed events is significantly reduced (see Sec. 9.6).

Since the above selection criteria alone cannot completely reject noise events caused by PMT after-pulses, the noise event cut using N_{100} and $Nhit_{\mathrm{ID}}$ mentioned in Sec. 9.3.1, is also applied. This cut is helpful to reject the noise events caused by the after-pulses, which tend to have poor hit timing correlation.

9.4.2 Profile of Delayed Event Candidates

Fig. 9.8 shows the profile of delayed event candidates ($NsumMax$, R_{delayed}, ΔR, and ΔT). The ΔR represents the spatial difference between the prompt and delayed events. In the $NsumMax$ distribution of Fig. 9.8, there is a peak of around 400 hits due to the neutron capture gamma rays. There are also noise events with around 100 hits. The peak position changes as the number of bad channels increases, but the threshold of 275 hits clearly separates these noise events.

The radius distribution of delayed events (R_{delayed}) and the spatial separation between prompt and delayed events (ΔR) are shown with the results of the simulation. The number of observed events in the low-E selection (Fig. 9.8a) has slight excess. This excess will be explained by the negative g_A^s in the spectral fitting. Except for the excess, the simulation reproduces the KamLAND data well. This consistency indicates that the Geant4 neutron transport model used in the detector simulation reproduces the data very well. When looking at the radius distribution around the selection criteria, the distribution is close to flat, and the number of events is low. This distribution is due to the application of a wider radius selection criteria than that of prompt events. This distribution suppresses the impact of fiducial volume uncertainty on the number of delayed events. The simulation details are described in Sec. 10, and the estimation of the fiducial volume uncertainty is explained in Sec. 9.6.

The ΔT distributions in Fig.9.8 are fitted with a function,

$$f(\Delta T) = N_0 e^{-\Delta T/\tau_n} + N_{\text{const}}, \tag{9.1}$$

where $\tau_n = 207.5\,\mu$s. The constant term N_{const} corresponds to the background contamination in delayed events. It is consistent with zero within a large uncertainty:

$$N_{\text{const}} = \begin{cases} 0.22 \pm 0.37\,\text{events}/50\,\mu s & \text{(Low-E selection)} \\ 0.99 \pm 0.73\,\text{events}/50\,\mu s & \text{(High-E selection)} \end{cases} \tag{9.2}$$

The background event rate is also estimated using a long off-time window ($2 < \Delta T < 3000\,\text{ms}$):

$$(7.07 \pm 0.34) \times 10^{-3}\,\text{events}/50\,\mu s \quad \text{(Low-E selection)} \tag{9.3}$$

$$(2.90 \pm 0.07) \times 10^{-2}\,\text{events}/50\,\mu s \quad \text{(High-E selection)} \tag{9.4}$$

These low event rates show negligible contamination in the delayed events:

$$(0.154 \pm 0.007)\% \quad \text{(Low-E selection)} \tag{9.5}$$

$$(0.161 \pm 0.039)\% \quad \text{(High-E selection)} \tag{9.6}$$

The neutron tagging efficiency ϵ can be estimated from the actual number of observed events (N_{obs}) and the integral of the fit results,

$$\epsilon = \frac{N_{\text{obs}} - \int_{0\mu s}^{1000\mu s} N_{\text{const}} dt}{\int_{0\mu s}^{1000\mu s} N_0 e^{-t/\tau_n} dt}, \tag{9.7}$$

estimating the inefficiency caused by the channel-level electronics deadtime effects. The selection inefficiency caused by radius cut is taken into account in the detector simulation described in Chap. 10. The simulation also shows that the inefficiency associated with the gamma-ray escaping the LS is insignificant. Since events with a time delay of less than 10 μs are excluded by the selection, the maximum of neutron tagging efficiency is $\epsilon_{max} = 95.3\%$. We obtain the following results from the fit results shown in Fig. 9.8.

$$\epsilon = \begin{cases} 80.3^{+18.4}_{-13.8}\% & \text{(Low-E selection)} \\ 88.2^{+9.9}_{-8.5}\% & \text{(High-E selection)} \end{cases} \tag{9.8}$$

The uncertainties are calculated with the errors in the fitting, dominated by the statistical errors. Since the leading causes of this inefficiency are after-pulses and the overshoots that occur ∼ 100 ns after a high-charge event, the efficiency would depend on the charge intensity of the prompt event, i.e., the high-E selection is expected to have lower efficiency. However, no trend can be discerned clearly from the results due to the large uncertainties.

Furthermore, the efficiency would have time dependence caused by PMT aging, which appears in the increased number of bad channels. However, due to low statistics, the analysis performed here using neutrons associated with atmospheric neutrino events cannot evaluate the time dependence as well as the prompt energy dependence. We, therefore, prepare an alternative way to estimate the efficiency more precisely. The more precise analysis using cosmic muons is described in Sec. 9.5.

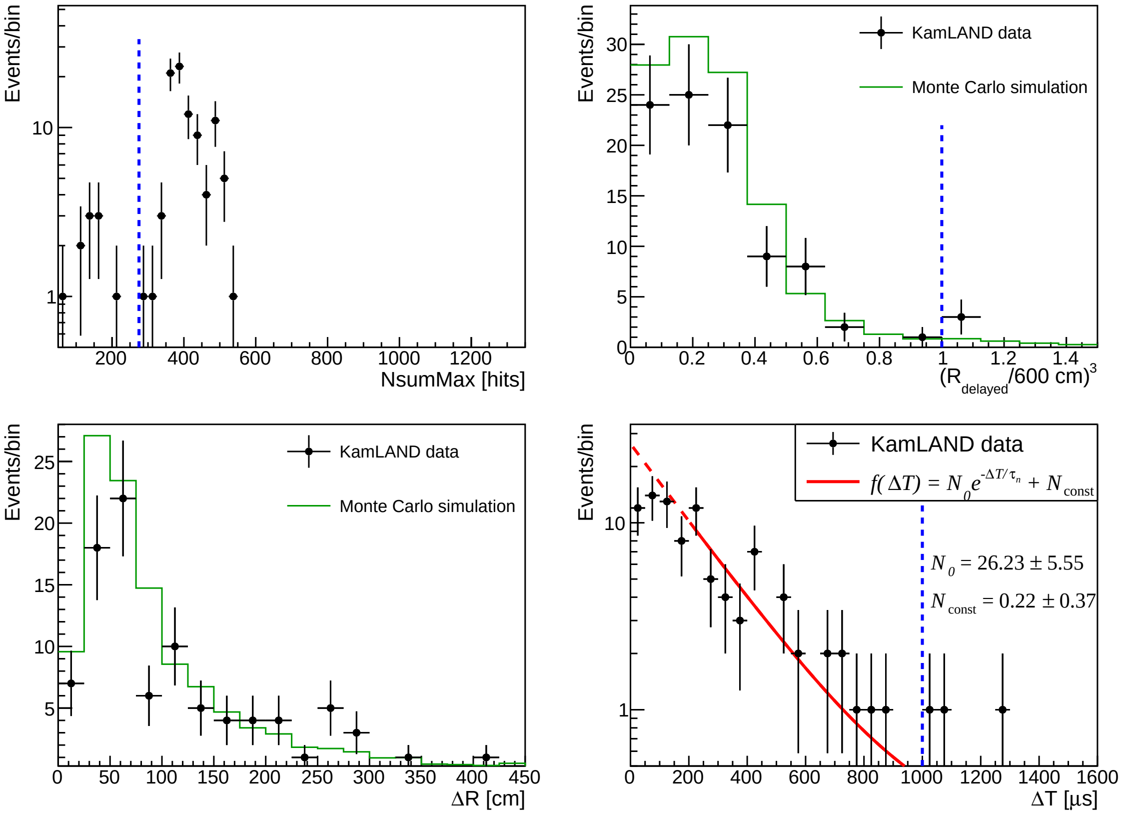

(a) Low-E selection. The excess of observed events in the distributions of R_{delayed} and ΔR will be explained by the negative g_A^s in the spectral fitting.

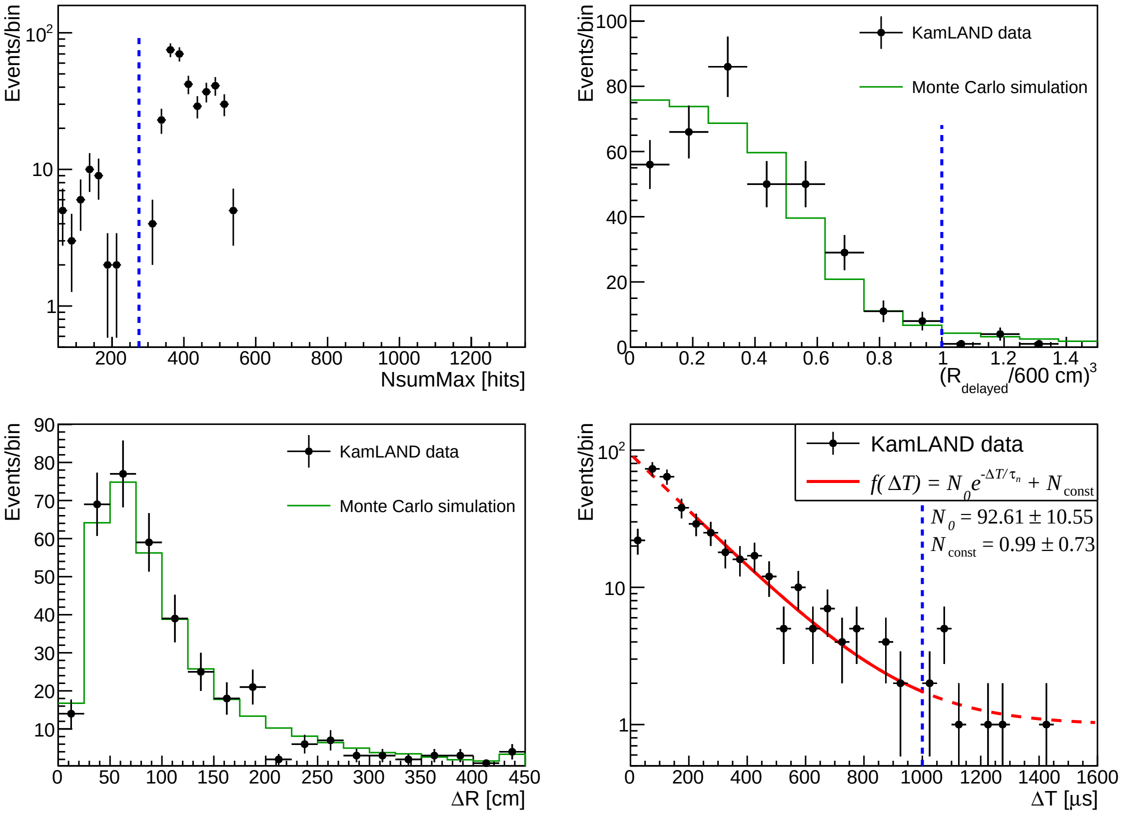

(b) High-E selection. A good consistency between the simulation and the data can be seen in the ΔR distribution, indicating the validity of the Geant4 neutron transport model.

Figure 9.8: Profile of delayed events candidates during periods I−IV for low-E (a) and high-E (b) selections. The blue dotted lines in $NsumMax$, R_{delayed}, and ΔT distributions represent the selection criteria. The solid green lines in R_{delayed} and ΔR distributions represent the result of the Monte Carlo simulation before spectral fitting; the simulation assumes $M_A = 1.2$ GeV and $g_A^s = 0$. The rightmost bin in ΔR distribution includes overflow. The red lines in ΔT distributions represent the fit result by Eq. 9.1 with the region of $200 < \Delta T < 1000\,\mu$s. The peak position of $NsumMax$ distribution changes as the number of bad channels increases, but the threshold of 275 hits is low enough to separate the noise events.

Tab. 9.3 shows a summary of neutron capture (delayed) event candidates in each period. As a result, we find 356 events in the high-E selection and 91 events in the low-E selection, with negligible background contamination. The event rate is unstable due to the time variation of the neutron tagging efficiency.

Fig. 9.9 shows the neutron multiplicity of the atmospheric neutrino candidates. Roughly half of the atmospheric neutrino candidates do not involve neutrons. The difference in dominant interaction channels causes the shape difference between these two selections. Normalization factors such as atmospheric neutrino flux and M_A do not change the shape of neutron multiplicity, while g_A^s changes it drastically. Thus, by fitting with consideration of neutron multiplicity, we can measure g_A^s with a suppressed dependence on the M_A.

Table 9.3: The number of neutron capture (delayed) event candidates in each period. The event rate is unstable due to the time variation of the neutron tagging efficiency.

Period	Events	
	Low-E	High-E
I	26	143
II	18	56
III	31	126
IV	16	31
I–IV	91	356

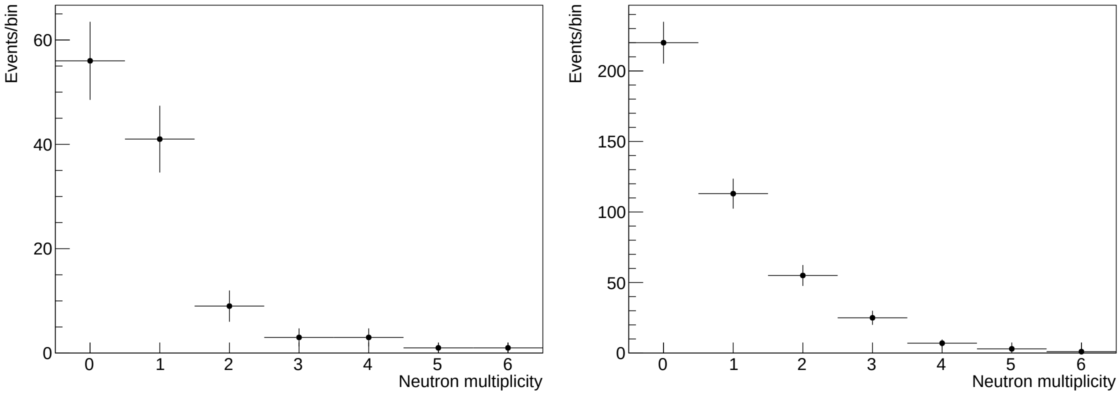

(a) Low-E selection

(b) High-E selection

Figure 9.9: Neutron multiplicity of atmospheric neutrino candidates for low-E (a) and high-E (b) selections. The difference in dominant interaction channels causes the shape difference between these two selections.

9.5 Estimation of Neutron Tagging Efficiency using Cosmic Muons

As mentioned above, the neutron tagging efficiency in KamLAND has prompt energy and time dependences, but difficult to evaluate these dependencies from the delayed event candidates due to low statistics. We prepare an alternative way to parameterize the efficiency as a function of prompt energy for each period as a more precise analysis. This analysis uses cosmic muons with high statistics as prompt events, uses the same data set as atmospheric neutrino analysis, and applies the same selection criteria for the delayed events described in Sec. 9.4.1.

The method of calculating the neutron tagging efficiency is the same as Sec. 9.4.1. The ΔT distributions are fitted with Eq. 9.1, and then the efficiencies are calculated according to Eq. 9.7.

9.5.1 Time Variation on a Run Basis

Before evaluating the energy dependence, the time variation of the efficiency is checked on a run basis. Since one run corresponds to about 24 hours, this evaluation is almost synonymous with analysis on a daily basis. In order to exclude muon events that have particularly high charge, we select muons with $E_{\mathrm{prompt}} < 3\,\mathrm{GeV}$, corresponding to $Q_{17} \lesssim$

6×10^5 p.e. This energy selection is larger than the typical through-going muon energy of 2 GeV and larger than the prompt events of atmospheric neutrinos.

Fig. 9.10 shows the time variation of the neutron tagging efficiency for each period on a run basis. Although the results have large uncertainty due to low statistics, they show a gradual decrease. The average efficiency (ϵ_{ave}) for each period is shown in the figure. While it is 87% for period I, it monotonically decreases to 61% for period IV. The efficiency decrease is mainly caused by PMT aging, as appeared in the increased number of bad channels. The time dependence can be adequately considered on a periodic basis rather than on a run basis because the change in the efficiency during each period is not large. Furthermore, the poor statistics make it difficult to evaluate the energy dependence on a run basis. Therefore, we estimate the energy dependence for each period instead of a run-basis analysis.

9.5.2 Energy and Period Dependence

In the investigation of the energy dependence, we divide the prompt energy in the range of $0 < E_{\text{prompt}} < 3000\,\text{MeV}$ with a bin width of 200 MeV. The ΔT distribution is fitted with Eq. 9.1 for each prompt energy bin. See Appendix E for more detailed information. Fig. 9.11 shows the result of the efficiency as a function of prompt energy E_{prompt} for each period up to 2000 MeV. The efficiency is monotonically decreasing in time and with prompt energy within statistical uncertainty, as expected. The uncertainty is smaller than that obtained in Sec. 9.4.2 due to higher statistics.

The energy dependence is parameterized with a second-order polynomial for each period,

$$\epsilon(E_{\text{prompt}}) = p_0 + p_1 E_{\text{prompt}} + p_2 E_{\text{prompt}}^2, \tag{9.9}$$

where E_{prompt} has units of GeV. The best-fit and 1σ uncertainty of the parameterization are shown in Fig. 9.11. The efficiency averaged over period I−IV is about 80% at $E_{\text{prompt}} = 1\,\text{GeV}$ and 88% at $E_{\text{prompt}} = 0.1\,\text{GeV}$. These values are consistent with the results obtained from the atmospheric neutrino candidates (Eq. 9.8). Fig. 9.12 shows the correlation matrix with the parameterization of Eq. 9.9. The parameters, p_0, p_1, and p_2, strongly correlated. To consider the prompt energy and time dependence in the spectral fitting, we use the values of p_0, p_1, p_2, and correlation matrices under the parameterization.

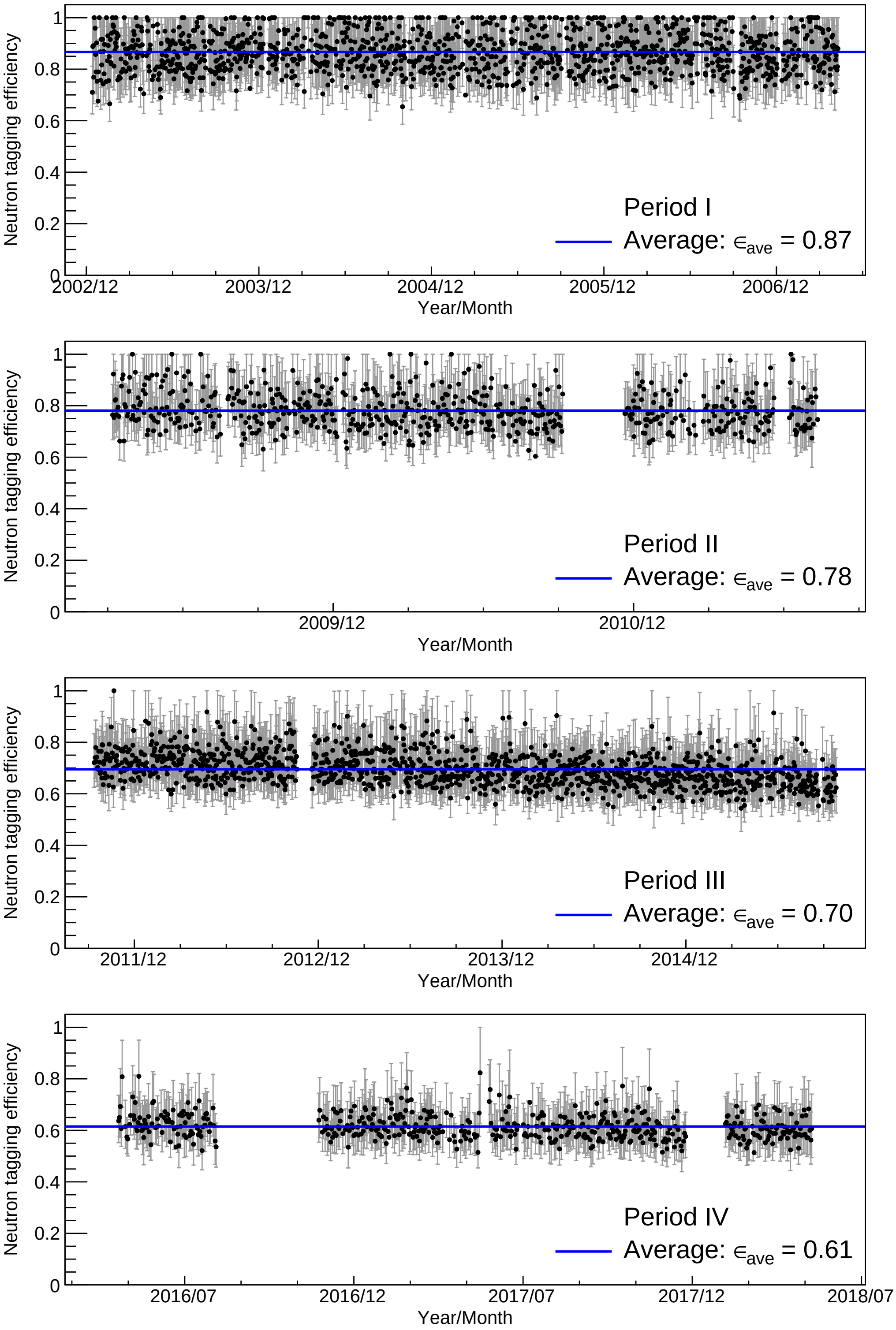

Figure 9.10: Time variation of the neutron tagging efficiency for each period on a run basis. The black dots represent the estimated efficiency run by run using cosmic muons with $E_{\mathrm{prompt}} < 3\,\mathrm{GeV}$. The horizontal blue lines represent the average efficiency, and the values are shown as the texts. The results show a monotonical and gradual decrease in efficiency.

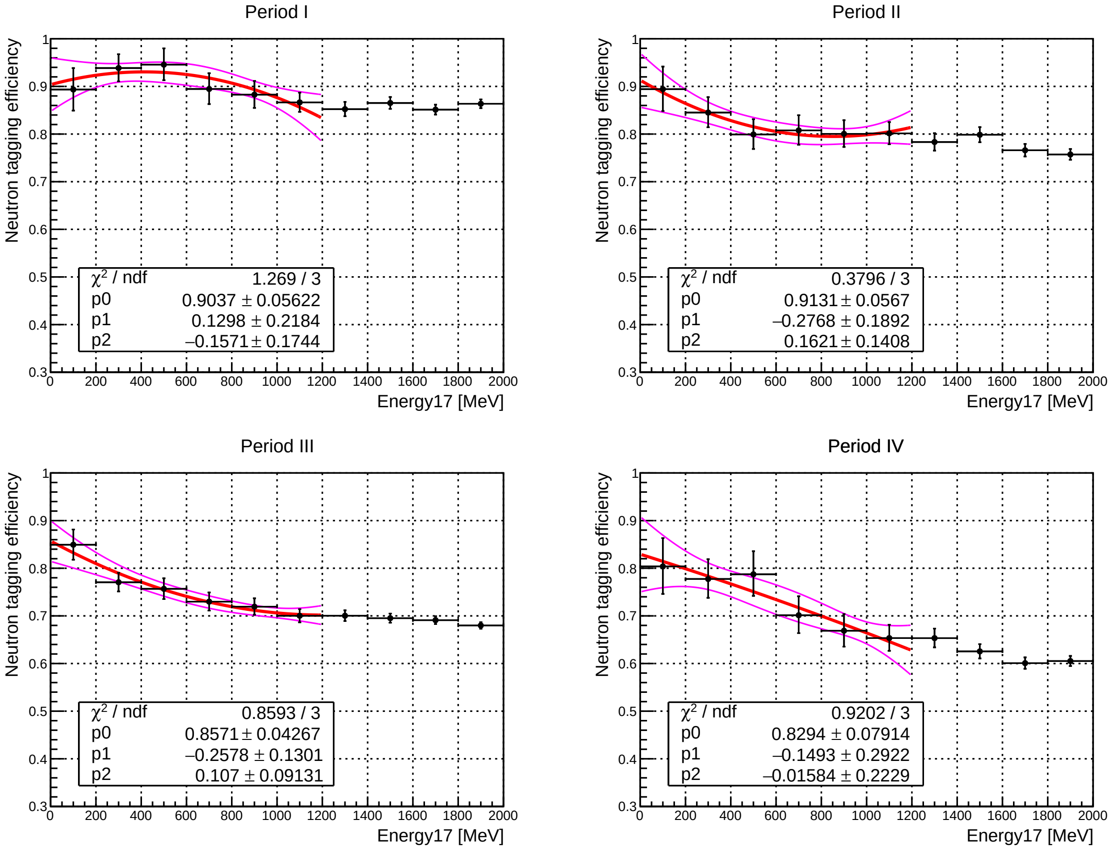

Figure 9.11: Neutron tagging efficiency as a function of prompt energy for each period. The red (magenta) lines represent the best-fit (1σ uncertainty) of the parameterization with the second-order polynomial of Eq. 9.9 in the region of $0 < E_{\mathrm{prompt}} < 1200\,\mathrm{MeV}$. The efficiency gradually and monotonically decreased within the uncertainty.

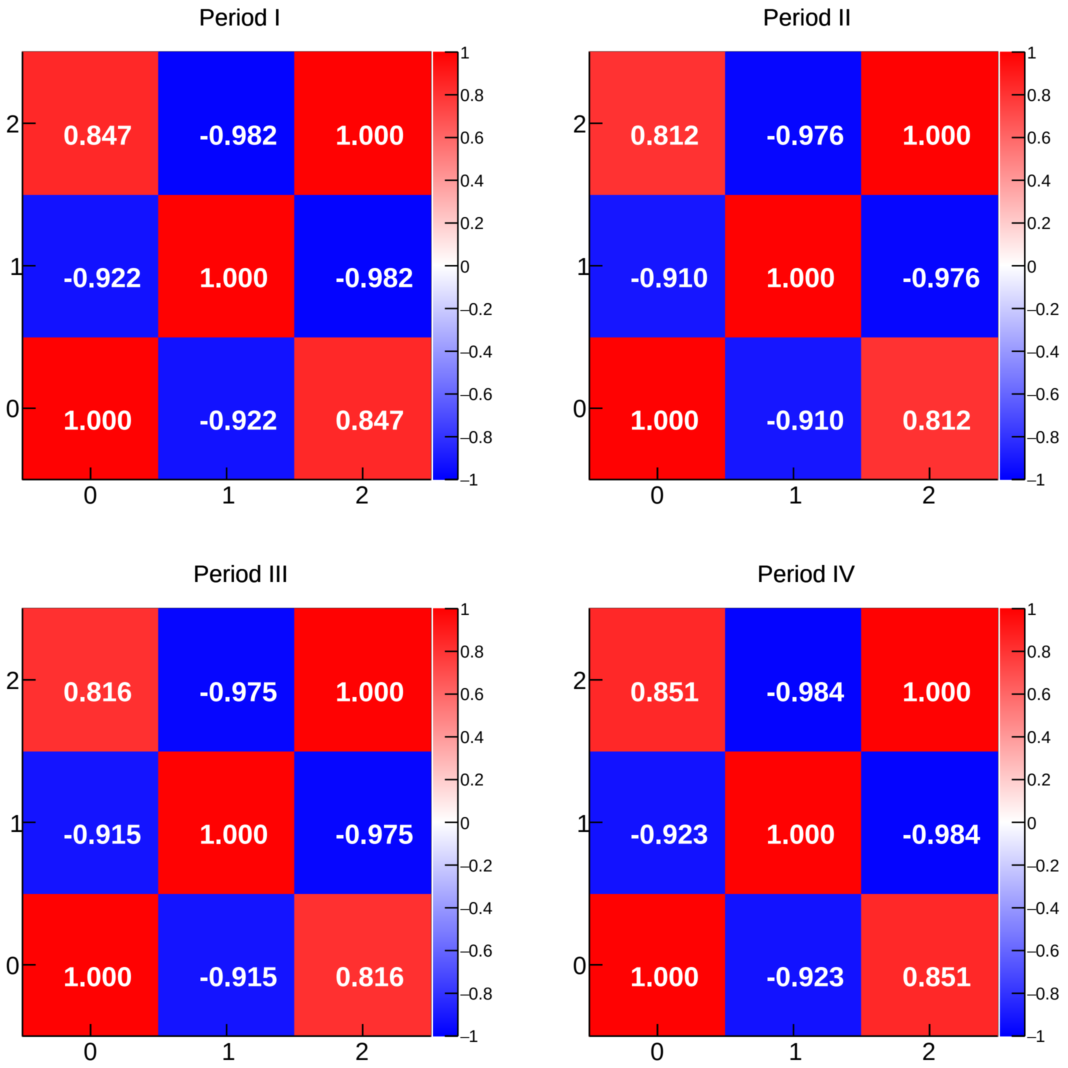

Figure 9.12: Correlation matrix in the parameterization of the neutron tagging efficiency. The bin number (0, 1, 2) corresponds to the parameter in Eq. 9.9 (p_0, p_1, p_2). The numbers in the two-dimensional panels represent the correlation coefficients. These three parameters have strong correlations with each other.

9.6 Fiducial Volume Uncertainty of Delayed Events

The fiducial volume uncertainty for the delayed (neutron capture) events is estimated using the same data set of cosmic muons in Sec. 9.5 except for prompt energy cut of muons. In Sec. 9.5, we applied prompt energy cut of $E_{\text{prompt}} < 3\,\text{GeV}$. In this study, we apply $E_{\text{prompt}} < 4\,\text{GeV}$ to avoid biasing of the cosmic muons pass.

From the number of neutron capture events within the fiducial volume of a 600 cm radius (N_{600}) and the total volume, namely no vertex cut (N_{total}), the event ratio R_{event} is defined as follows.

$$R_{\text{event}} \equiv \frac{N_{600}}{N_{\text{total}}} = \frac{805418}{1104566} = 0.7292 \pm 0.0011(\text{stat.}). \tag{9.10}$$

Here, N_{600} and N_{total} are the number of events subtracting the background contribution estimated by the long off-time window ($2 < \Delta T < 3000\,\text{ms}$). The volume ratio R_{volume} is defined using the volume within the 600 cm radius (V_{600}) and total volume (V_{total}) as follows:

$$R_{\text{volume}} \equiv \frac{V_{600}}{V_{\text{total}}} = \frac{4/3\pi \times 600^3\,(\text{cm}^3)}{1171 \pm 25\,(\text{m}^3)} = \frac{904.8\,(\text{m}^3)}{1171 \pm 25\,(\text{m}^3)} = 0.7727 \pm 0.0165(\text{syst}). \tag{9.11}$$

where $V_{\text{total}} = 1171 \pm 25\,\text{m}^3$ represents the total amount of KamLS filled in the outer balloon measured by flow meters. The fiducial volume uncertainty is obtained from the difference between the event and volume ratios.

$$\frac{|R_{\text{volume}} - R_{\text{event}}|}{R_{\text{volume}}} = 5.63 \pm 0.01(\text{stat}) \pm 0.12(\text{syst})\%. \tag{9.12}$$

Since the prompt energy selection is much higher than atmospheric neutrino events, this fiducial volume uncertainty is assumed to be much smeared by the after-pulses and overshoots of PMTs. We finally assign 5.7% uncertainty on the fiducial volume of delayed neutron events, corresponding to vertex bias of 11 cm at a 600 cm radius.

As shown in Fig. 9.8, the radius distribution of the delayed events R_{delayed} is flat, and the number of events is small around the selection criteria. This trend, caused by the wider radius cut of delayed events than prompt events, suppresses the relative change in the number of delayed events due to the fiducial volume uncertainty. The relative change is estimated using the simulation results (solid green line in Fig. 9.8), leading to 0.7% (0.4%) for high-E (low-E) selection, These results indicate a small impact on neutron selection and multiplicity. The impact of these relative changes by the fiducial volume uncertainty is much smaller than that of the neutron tagging efficiency with a few percent uncertainties.

Chapter 10

Monte Carlo Simulation

The detector responses of atmospheric neutrino events at KamLAND are estimated through various simulation processes. First, atmospheric neutrino interactions are simulated using NuWro. The model configuration of NuWro is shown in Sec. 4.1.1. The atmospheric neutrino flux used in the simulation is described in Sec. 10.1. In order to precisely consider the time variation of the flux, the effect of the solar cycle is parameterized using neutron monitor data (Sec. 10.1.2). We then simulate the nuclear de-excitation developed in Chap. 5 according to the outputs of NuWro. The effect of neutrino oscillations due to the passage through the Earth is considered (Sec. 10.2). After that, the detector responses are simulated by generating the samples of atmospheric neutrino events in the KLG4. The vertex and energy reconstructed by the KLG4 are used for comparisons with the KamLAND data.

Fast neutrons exist as background events in the atmospheric neutrino candidates. This contribution is also estimated using KLG4. Details are given in Sec. 10.3.

10.1 Atmospheric Neutrino Flux

The atmospheric neutrinos (ν_μ, $\bar{\nu}_\mu$, ν_e, $\bar{\nu}_e$) are generated via interactions of the cosmic rays with the nuclei in the atmosphere. The primary cosmic rays are dominated by protons ($\simeq 85\%$) and α ($\simeq 12\%$). These particles interact with the nuclei in the atmosphere, such as nitrogen and oxygen. These interactions produce many charged pions and decay to produce neutrinos as follows.

$$\begin{aligned} \pi^\pm \rightarrow\, & \mu^\pm + \nu_\mu(\bar{\nu}_\mu) && (10.1) \\ & \downarrow \\ & \mu^\pm \rightarrow\; e^\pm + \nu_e(\bar{\nu}_e) + \bar{\nu}_\mu(\nu_\mu). && (10.2) \end{aligned}$$

The neutrinos produced anywhere in the Earth's atmosphere propagate through the atmosphere and the Earth. Therefore, 3D calculations are necessary for both production and oscillation.

This study uses the flux at the Kamioka site predicted by Honda *et al.*, called HKKM 2014 [144, 145]. The prediction is based on 3D geometry, including a geomagnetic model and atmospheric density profile. The HKKM provides the flux data in a wide energy region of ($10^{-1}-10^{4}$) GeV at various sites, such as Kamioka, Gran Sasso, and South Pole. Various experiments, such as the Super-Kamiokande, have confirmed good agreements with the HKKM [146]. Fig. 10.1 shows the predicted all-direction averaged atmospheric neutrino flux at the Kamioka site, and Fig. 10.2 shows the relative uncertainty of the prediction. The atmospheric neutrino flux spreads in a wide energy region and monotonically decreases. The total relative uncertainty is less than 10% in the energy region 1−10 GeV, while it is more than 20% at ∼ 300 MeV. Above 10 GeV, the uncertainty linearly increases with $\log E_\nu$ from 7% (10 GeV) to 25% (1 TeV). Note that the contribution of $E_\nu \gtrsim 10\,\text{GeV}$ is negligible in this study, looking at the low-energy region of $E_{\text{visible}} < 1\,\text{GeV}$.

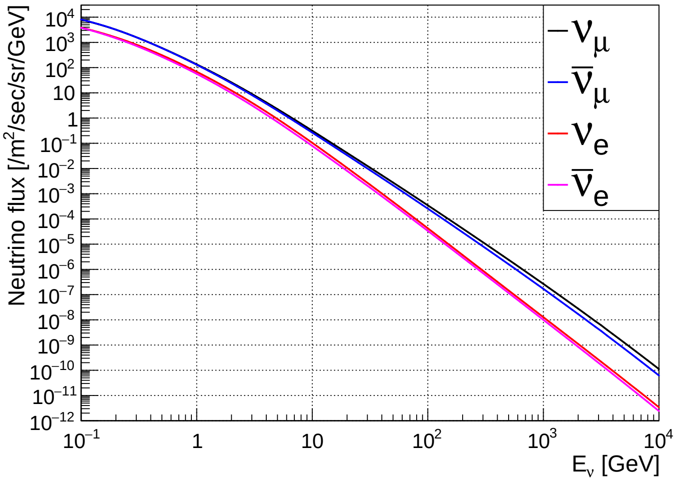

Figure 10.1: All-direction averaged atmospheric neutrino flux at the Kamioka site predicted by the HKKM 2014. The data is based on [144] with the solar minimum ignoring the neutrino oscillation. The flux is widely distributed in a region of $(10^{-1} - 10^{4})$ GeV and monotonically decreases as a function of neutrino energy.

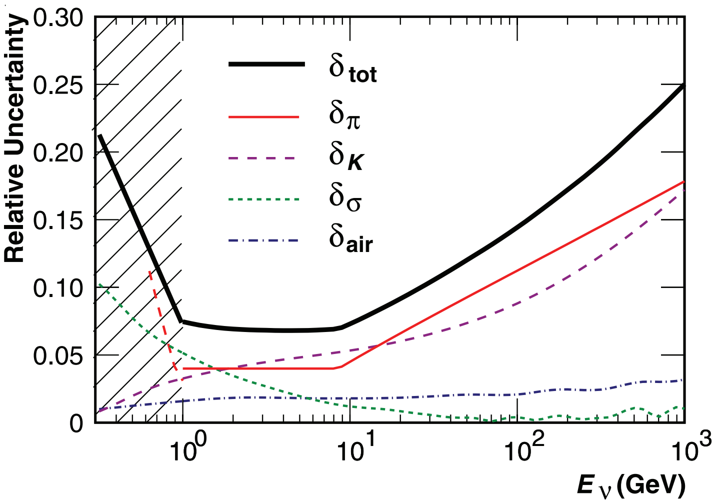

Figure 10.2: The uncertainty for atmospheric neutrino flux prediction. The red (violet dashed) line denotes the uncertainty of π (K) production, the green dotted line is for the hadronic interaction cross sections, the blue dashed-dotted line is for the atmospheric density profiles, and the solid black line represents the total error. The uncertainty in the shaded region below 1 GeV is estimated differently, and conservative error is assigned. The figure is from [147].

Fig. 10.3 shows the comparisons of neutrino ratios from those calculated in the different models to that of the modified DPMJET-III. The modified DPMJET-III is used in the calculation of HKKM. All models are modified to reproduce the atmospheric muon data. These results shown in the figure correspond to the model-dependent uncertainties. They find a large variation of the ratios above 100 GeV, where the kaon contribution becomes large, while it is relatively small below 100 GeV. Except for above 100 GeV, which gives negligible effect in this study, the neutrino ratios agree within ±5% for $\nu_e/\bar{\nu}_e$ and $\nu_\mu/\bar{\nu}_\mu$, and ±2% for $(\nu_\mu+\bar{\nu}_\mu)/(\nu_e+\bar{\nu}_e)$.

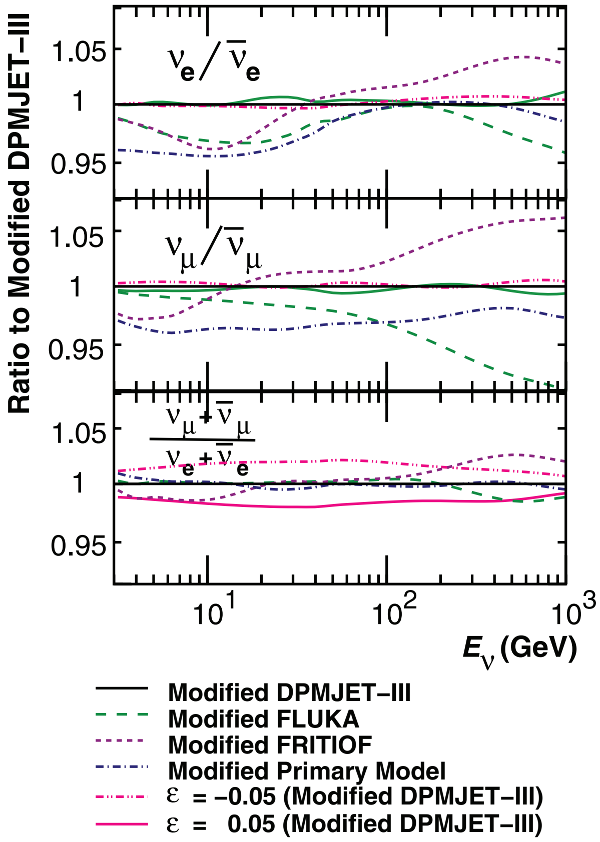

Figure 10.3: Comparisons of neutrino ratios calculated in the different models. The atmospheric neutrino fluxes are averaged over all directions. The ratios to that of the modified DPMJET-III, which is used in the calculation of HKKM, are shown. Except for above 100 GeV, which gives negligible effect in this study, the flavor ratios agree within ±5% for $\nu_e/\bar{\nu}_e$ and $\nu_\mu/\bar{\nu}_\mu$, and ±2% for $(\nu_\mu+\bar{\nu}_\mu)/(\nu_e+\bar{\nu}_e)$. The figure is from [147].

The changes in air density cause the seasonal variation of the flux. The effect is discussed in [144] and turned out to be negligible, much less than 1% in the region below 10 GeV at the Kamioka site. On the other hand, the effect of the solar cycle is non-negligible. The HKKM 2014 provides flux tables at solar maximum and minimum. The effect of the solar cycle is significant for low-energy upgoing neutrinos and changes the relative normalization by several percent. The detail is discussed in Sec. 10.1.2. In order to consider the neutrino oscillation effects in the Earth, this study uses the zenith-angle-dependent flux tables for the simulation.

10.1.1 Flux Below 100 MeV

HKKM 2014 does not provide the flux data for $E_\nu < 100\,\mathrm{MeV}$, where the contribution of μ and π decay in the mountain over the detector becomes non-negligible. It is challenging to predict the decay in the mountain in a realistic calculation time because the detector is tiny compared to the size of the Earth. Battistoni *et al.* predictted the flux below 100 MeV at the Kamioka site [148], and Honda *et al.* also reported preliminary results in [149]. They are consistent within the uncertainty, $\sim 30\%$, as shown in Fig. 10.4.

The local terrain structure, such as the mountain shape over the detector, is not considered in both predictions. Thus, the μ and π decay in the mountain, and the uncertainty would be underestimated. However, the contribution of the flux $E_\nu < 100\,\mathrm{MeV}$ is negligible in this study because of the small cross section. The flux predicted by Battistoni *et al.* [148] are used for $E_\nu < 100\,\mathrm{MeV}$ in this analysis, while the HKKM 2014 is adopted above 100 MeV.

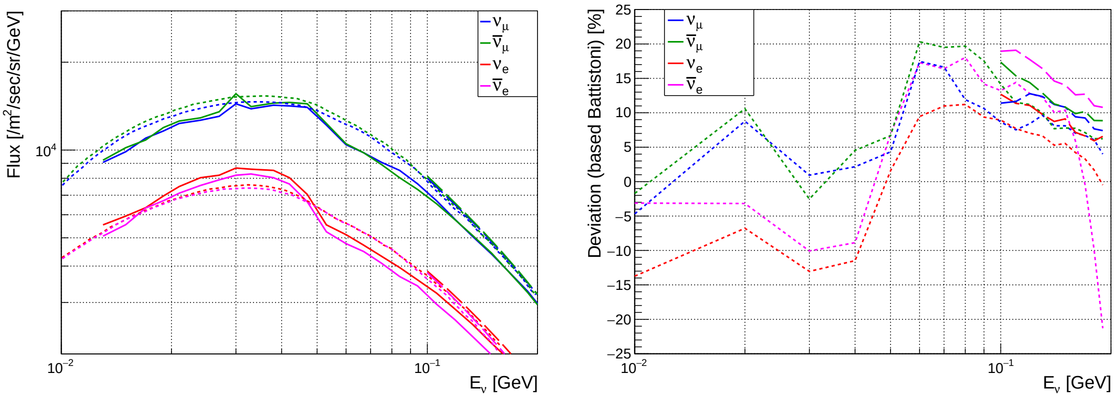

(a) Flux

(b) Deviation

Figure 10.4: Atmospheric neutrino flux below 100 MeV at the Kamioka site without neutrino oscillation. The solid line is from Battisoni *et al.* [148], the dotted line is from Honda *et al.* [149], and the long-dashed line only for $E_\nu \geq 100\,\mathrm{MeV}$ is from HKKM 2014 [144]. The dotted line and the long-dashed line are smoothly connected at 100 MeV. All of them agree within their uncertainty of $\sim 30\%$.

10.1.2 Effect of the Solar Cycle

The solar cycle is a cyclic change in solar activity with an approximately 11-year cycle, which has been commonly parameterized and observed as changes in the number of sunspots over several hundred years. In addition to the number of sunspots, the count rates observed by the neutron monitors (NM) are often used as an indicator of solar activity. The count rate of neutron monitors is known to have an inverse linear correlation with the number of sunspots, namely solar activity. We generally use the NM data when discussing solar activity in the cosmic rays and atmospheric neutrinos.

Solar activity has a negligible impact on the atmospheric neutrinos above about 5 GeV, but below that energy, they change the relative normalization by several percent. We need to consider the time variation of the solar activity in the KamLAND data set, which contains approximately 1.5 solar cycles.

How the Solar Cycle Affects Atmospheric Neutrino Flux

The effect of the solar cycle on the atmospheric neutrino is evident by looking at the low-energy upgoing neutrino fluxes, as shown in Fig. 10.5. Variations in the primary cosmic ray flux change the atmospheric neutrino flux. Fig. 10.6 shows the observed primary cosmic ray spectra with various levels of solar activity, indicating a strong correlation between the solar activity and suppression of flux below 10 GeV.

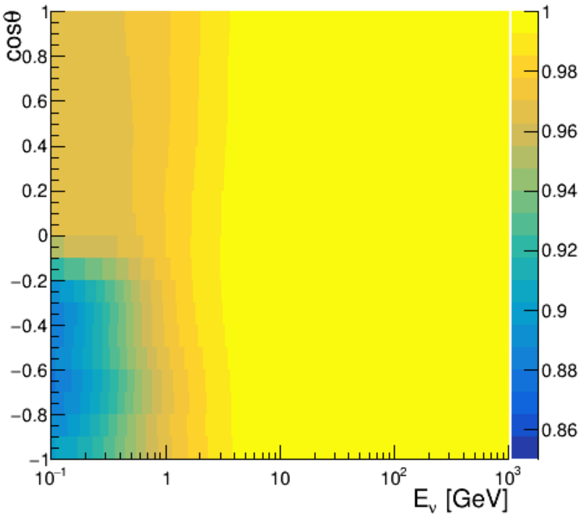

Figure 10.5: Predicted normalization change due to the solar cycle in HKKM 2014 at the Kamioka site. The zenith angle θ denotes the arrival direction of the neutrino. The z-axis (color map) shows the relative change in flux from the solar minimum to the solar maximum. The low-energy upgoing neutrino is largely affected. This figure shows the case of ν_μ, but all flavors have a similar trend. The data is based on [144].

During periods of high solar activity, called solar maximum, strong solar winds enhance the magnetic field around the Earth and block the main component of primary cosmic rays, the galactic cosmic rays. Then, the primary cosmic ray flux decreases. Contrarily, the flux increases during periods of low solar activity called solar minimum. This phenomenon mainly affects the primary cosmic rays below 10 GeV. Therefore, the atmospheric neutrinos show an apparent change in the low-energy region. For primary cosmic rays to enter the atmosphere, they must have energies higher than the cutoff value, called the rigidity cutoff. The rigidity cutoff is based on the fact that the primary cosmic rays with low energy are blocked due to geomagnetic effects. The value of the rigidity cutoff depends on the location, with the south and north poles having the lowest values. Therefore, the low-energy primary cosmic rays are mainly incident from the source and north poles. From the Kamioka site, the poles are below. Following these factors, the solar activity cycle affects the low-energy upgoing neutrinos.

Definition of Solar Minimum and Maximum in the HKKM

HKKM 2014 provides two flux tables at solar maximum and minimum, and they are defined using the count rate of the Climax NM [151] (c_{min} and c_{max}) as follows:

$$c_{\mathrm{min}} \equiv 4150\,\mathrm{counts/hour/100} \quad \text{(the solar minimum)} \tag{10.3}$$

$$c_{\mathrm{max}} \equiv 3500\,\mathrm{counts/hour/100} \quad \text{(the solar maximum)} \tag{10.4}$$

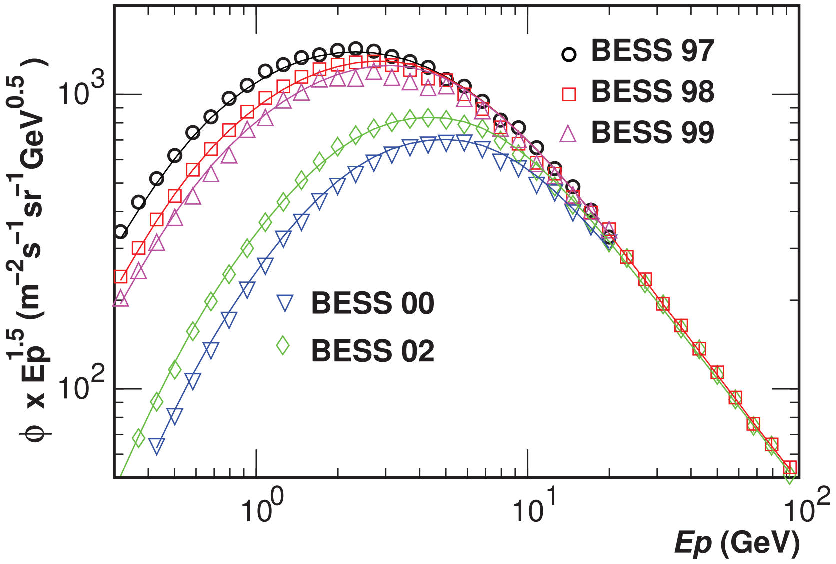

Figure 10.6: Primary cosmic ray spectra of proton observed by BESS experiment from 1997 to 2002. The Climax NM count rate (in units of counts/hour/100) was 4295 for BESS97, 4170 for BESS98, 4100 for BESS99, 3454 for BESS00, and 3600 for BESS02. For a small NM count rate corresponding to the solar maximum, the primary cosmic ray flux below 10 GeV is largely suppressed. The figure is from [150].

From the time variation of Climax NM count rates, the atmospheric neutrino flux changes due to solar activity can be accurately considered. However, the Climax NM was shut down in 2006, and no data are available for the period of this analysis.

Analysis of Neutron Monitor Data

We calculate parameters equivalent to the Climax NM count rate, denoted as the NM parameter, using other NM data. There are two requirements for other NM data. First, it must have been in operation for a long time because we need to obtain the correlation with Climax NM. Second, it must be in operation from 2003 to 2018, the period of this analysis. We select five NM data that satisfy these requirements: Newark, Thule, Moscow, Apatity, and Oulu [151–153]. Fig. 10.7 shows the time variation of these NM data. All NM data have similar trends and have a linear correlation with each other.

The correlation with the Climax NM data is fitted with a first-order polynomial using the period for both data available:

$$\begin{aligned}&(\text{Climax NM count rate [counts/hour/100]})\\&= p_0 + p_1 \times (\text{Another NM count rate [counts/hour/100]}),\end{aligned} \tag{10.5}$$

where the five NM data are used in the fit individually. Fig. 10.8 shows the correlations of the neutron monitor data and the fit results with the first-order polynomial. The best-fit values of p_0 and p_1 for each NM data are summarized in Tab. 10.1.

The count rate of each monitor is then converted to the NM parameter, which is directly comparable to the Climax NM count rate. Fig. 10.9 shows the trend of the NM parameter since 1996. Our data set indicates that solar cycle 24 had low solar activity. This result is quite consistent with that obtained by the Super-Kamiokande Collaboration [146]. The

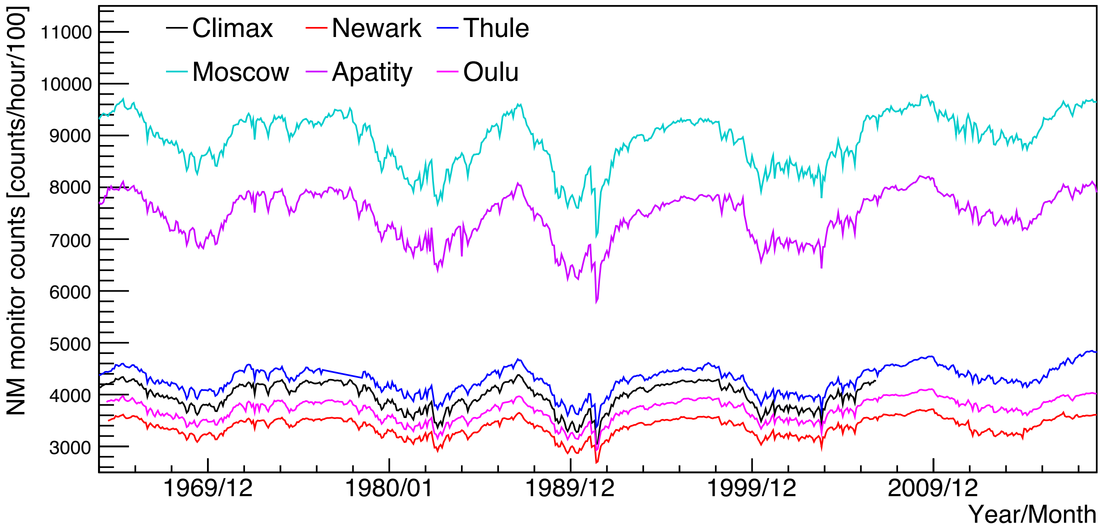

Figure 10.7: Time variation of neutron monitor data, Climax, Newark, Thule, Moscow, Apatity, and Oulu. The Climax NM was shut down in 2006, and no data have been available since then. All NM data have similar trends and have a linear correlation. The data is from [151–153].

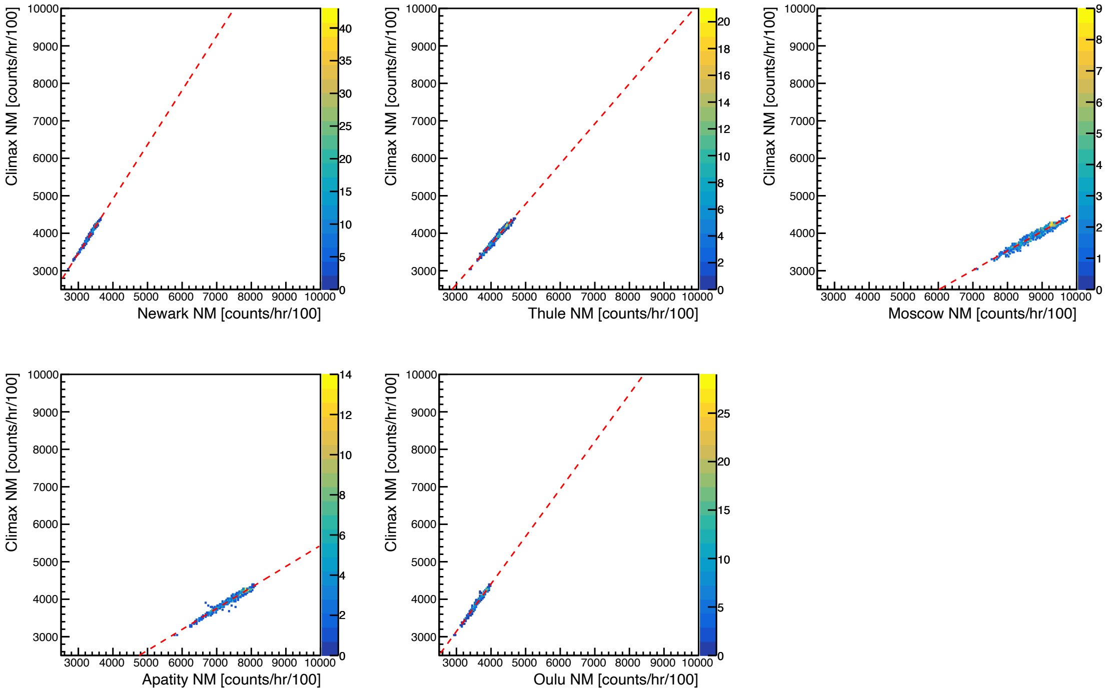

Figure 10.8: Correlation of the neutron monitor data with Climax neutron monitor data. The dashed red lines show the fit result with the first-order polynomial shown as Eq. 10.5.

Table 10.1: Fit results of the correlation of neutron monitor data. The correlation is fitted with a first-order polynomial written as Eq. 10.5.

Neutron monitor data	Parameter	
	p_0	p_1
Newark	-918.2	1.46
Thule	-576.6	1.07
Moscow	-642.6	0.521
Apatity	-168.8	0.560
Oulu	-665.4	1.27

livetime-averaged NM parameter for each period is shown in Tab. 10.2. The uncertainty of these count rates is 110 counts/hour/100 from the standard deviation of the five converted count rates. The relative normalization change due to the solar cycle is calculated with the following equation:

$$f_{\mathrm{exp}} = r f_{\mathrm{min}} + (1-r)\, f_{\mathrm{max}}, \tag{10.6}$$

$$r \equiv \frac{c_{\mathrm{max}} - c}{c_{\mathrm{max}} - c_{\mathrm{min}}}, \tag{10.7}$$

using the HKKM flux data with solar minimum and maximum (f_{min} and f_{max}) and livetime-averaged NM parameter (c). We calculate the atmospheric neutrino flux considering the solar cycle (f_{exp}), and its relative normalization change is tuned out to be about 3%.

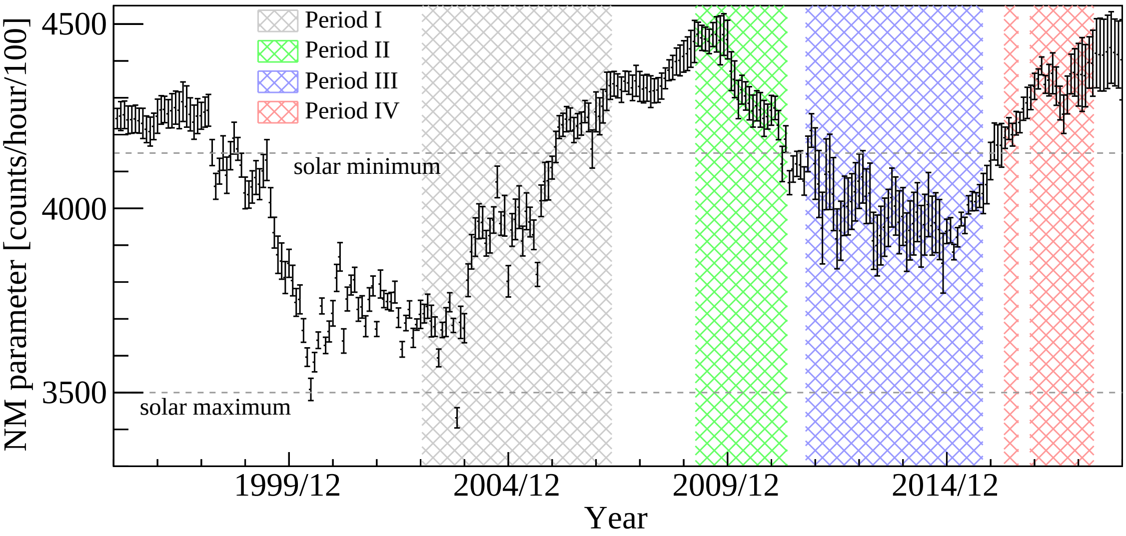

Figure 10.9: Trend of NM parameter. The shaded regions denote the analysis period in this analysis. The dashed lines represent the solar maximum and minimum defined in the HKKM 2014. The error bars are calculated from the standard deviation of the five converted count rates. The result reproduces one reported by Super-Kamiokande Collaboration.

Table 10.2: Livetime-averaged NM parameter. The HKKM defines 4150 counts/hour/100 as the solar minimum, and 3500 counts/hour/100 as the solar maximum.

Period	NM parameter (counts/hour/100)
Period I	3973
Period II	4327
Period III	3991
Period IV	4318

10.2 Oscillation in the Earth

The oscillation effect propagating through the atmosphere and the Earth is calculated with Prob3++, developed by members of the Super-Kamiokande Collaboration [154]. The theories of neutrino oscillation are in Sec. 1.2. The atmosphere is modeled as a vacuum. The Earth is modeled with a simplified version of the PREM (Preliminary Reference Earth Model) as shown in Tab. 10.3 [155]. The Earth has a sphere of radius 6371 km and has four layers. The full PREM with 82 layers provides no perceptive change in the Super-Kamiokande analysis [9]. Thus, the simplified profile with four layers is adopted in this analysis.

Table 10.3: A spherical density profile of the Earth, a simplified version of the Preliminary Reference Earth Model [155]. This profile is also adopted by Super-Kamiokande Collaboration [9].

Region	R_{min} [km]	R_{max} [km]	Density [g/cm^3]
Inner core	0	1220	13.0
Outer core	1220	3480	11.3
Mantle	3480	5701	5.0
Crust	5701	6371	3.3

Fig. 10.10 shows oscillation probabilities for neutrinos and antineutrinos assuming oscillation parameters of PDG 2018 (Tab. 1.1 [5]) with normal hierarchy. Matter effects in the Earth distort neutrino oscillation probabilities, which is absent in antineutrino. The boundaries of the outer core and the mantle region ($\cos\theta \sim 0.9$) and the mantle and the crust ($\cos\theta \sim 0.45$) are clearly seen. The uncertainties on the neutrino oscillation parameters give no perceptible change in the sensitivity of this analysis.

10.3 Fast Neutron Background Simulation

Fast neutrons produced by cosmic muon spallations in the surrounding rock and water are dominant backgrounds below 200 MeV. Fig. 10.14 shows the schematic view of the fast neutron backgrounds in KamLAND. If cosmic muons and produced charged particles do not pass through the OD, they are not vetoed by the OD cuts and become background events in the atmospheric neutrino candidates.

Fig. 10.12 shows the differential energy spectra of neutrons produced by muons in C_nH_{2n}. At the typical muon energy at KamLAND of 260 GeV, the dominant processes in the neutron production are the photonuclear interactions of gamma rays ($\gamma + N$), pion spallations ($\pi + N$), and inelastic scattering of neutrons ($n + N$) [141, 156]. The neu-

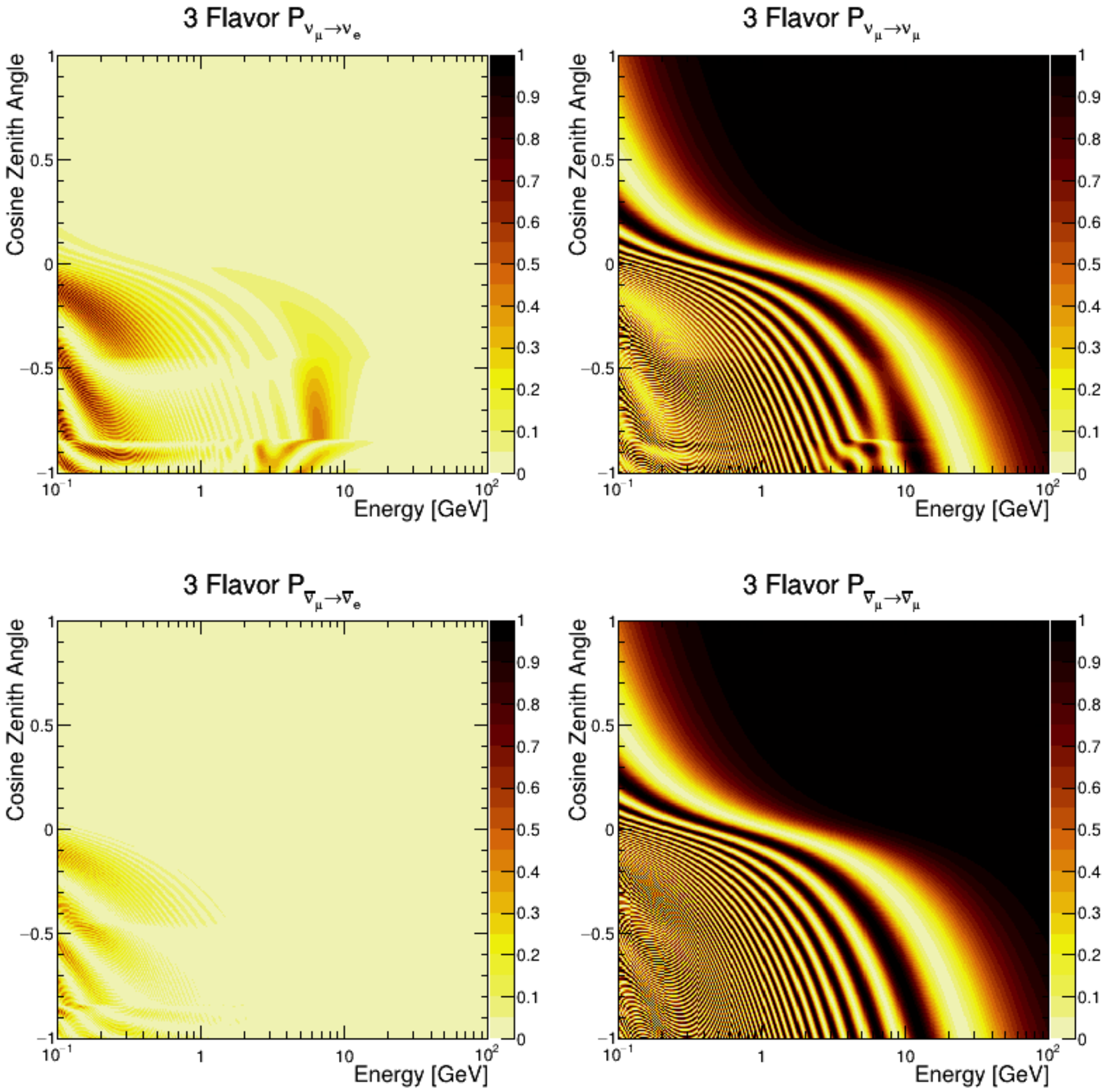

Figure 10.10: Oscillation probabilities for neutrinos (upper panels) and antineutrinos (lower panels) as a function of energy and zenith angle calculated with Prob3++ [154]. We assume oscillation parameters of PDG 2018 with normal hierarchy [5]. Matter effects in the Earth distort the probabilities of neutrinos depending on the zenith angle.

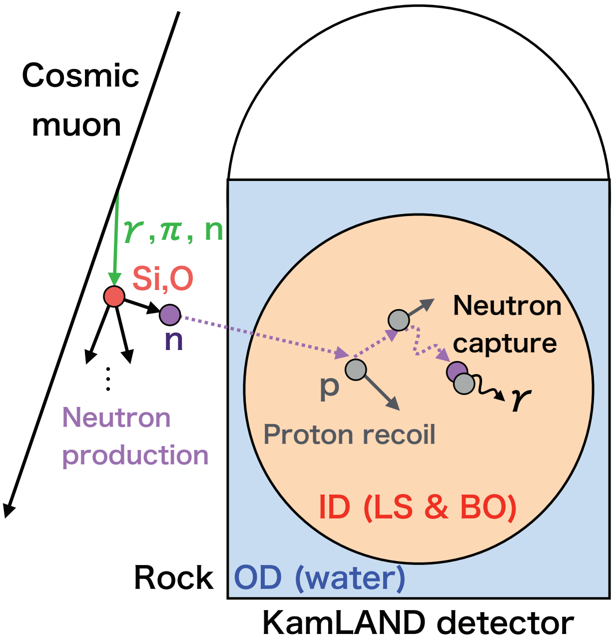

Figure 10.11: Schematic view of the fast neutron backgrounds in KamLAND. If cosmic muons and produced charged particles do not pass through the OD, these events cannot be tagged by the OD. The neutrons are generally captured by protons or carbons, producing delayed events. The photonuclear interactions of gamma rays, pion spallations, and inelastic scatterings of neutrons dominate the process contribution to neutron production.

trons produced via these reactions are rarely incident on the KamLAND ID producing prompt events by elastic and inelastic scattering in the KamLS. In most cases, they are finally captured by protons or carbons, producing delayed events. The neutron multiplicity can exceed one if multiple fast neutrons are incident simultaneously or neutrons are produced secondarily by inelastic scattering with carbon in ID. On the other hand, the neutron multiplicity can be zero mainly due to the inefficiency caused by selection criteria and detector response. In the case of low energy neutrons ($E \lesssim 30\,\mathrm{MeV}$), the channel contribution, where the neutrons are absorbed via the inelastic scattering with carbon in KamLS, becomes significant. For example, the following processes exist as such channels, which do not involve neutron emission:

$$n +^{12}\mathrm{C} \rightarrow^{8}\mathrm{Li} + \alpha + p \tag{10.8}$$

$$n +^{12}\mathrm{C} \rightarrow^{7}\mathrm{Li} + \alpha + d \tag{10.9}$$

In these processes, the incident neutrons are emitted as deuterons or α, which have lower separation energies than neutrons.

10.3.1 Simulation Method

The fast neutron background is simulated using KLG4. The simulation method is more or less the same as [20, 108], but these previous studies did not consider the events with zero neutron multiplicity to save computational time. These events are fully considered in this study. The thickness of the rock surrounding the OD for KLG4 is set to be 10 m, which is sufficiently large in the estimation of the fast neutrons. Simple chemical composition

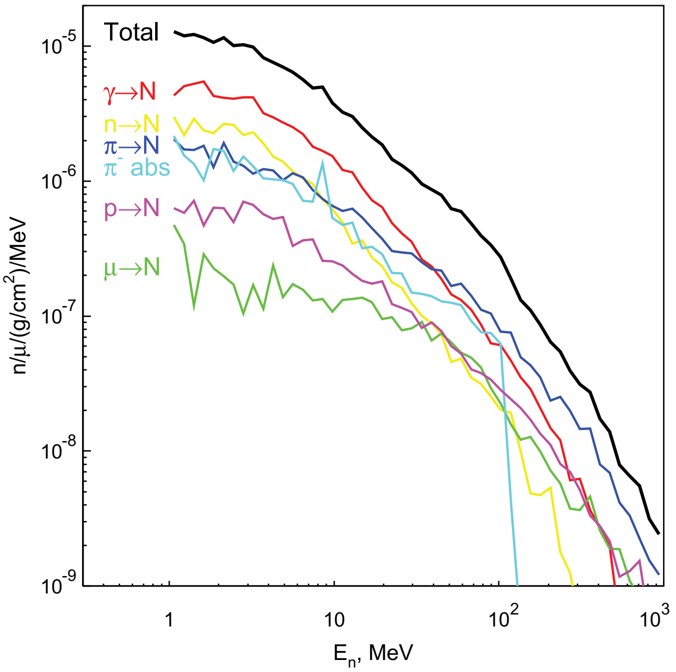

Figure 10.12: Differential energy spectra of neutrons produced in C_nH_{2n} by 280 GeV muons. The neutron productions are dominated by the photonuclear interactions (red), pion spallations (blue), and inelastic scatterings of neutrons (yellow). The results are obtained with Geang4 version 8.2. Other versions of Geant4 give similar trends. The figure is from [156].

and density of the rock are assumed: SiO_2 with $2.7\,\mathrm{g/cm^3}$. The details are discussed later. The cosmic muons are generated from outside of the rock according to the flux prediction of comic muons at the KamLAND site described in Sec. 6.1.1. Then, the KLG4 simulates the interactions of muons and detector responses.

In many cases, the charged particles, including cosmic muons, sufficiently produce Cherenkov and scintillation light in ID and OD. Since the Geant4 simulations spent most of the computational time tracking optical photons, this simulation is very time-consuming. In order to reduce the computation time, we determined the visible energy, vertex, and OD cut from the energy deposit in the simulation instead of tracking optical photons for both ID and OD in [108]. However, it is not ideal to set the OD cut as approximated by the energy deposit since OD has different veto efficiency at different positions. Therefore, we revised the simulation method to track the optical photon only for the OD in [20], while those in ID did not track. This configuration minimized the increase in computational time while more accurately accounting for the position dependence of the OD veto efficiency. In addition, two geometries are prepared to consider the changes in the veto efficiency before and after OD refurbishment (Appendix D.2). The visible energy and vertex are calculated from the energy deposit in the simulation, namely from the total energy deposit with the quenching effect and the centroid of them. This simulation adopts the same method as [20] in this study.

Muon Nuclear Capture and Muon Charge Ratio

Muon minus (μ^-) can occur muon nuclear capture in the matter by the following processes, which often emits a neutron. When μ^- stops in the matter, it is bound by the electric field of the nucleus forming a muonic atom. The muon minus in the muonic atom is then captured by the nucleus quickly as follows in a certain probability.

$$\mu^- + (Z, A) \rightarrow \nu_\mu + (Z-1, A). \tag{10.10}$$

The probability of this process, muon nuclear capture of the muonic atom, depends on the atomic number of the medium. The larger atomic number gives a higher probability, and it is about 8% in the case of carbon [157]. The muon mass-energy is transferred to the muon neutrino and neutron kinetic energies. The neutron is generally emitted from the nucleus, but its energy is less than 50 MeV kinetic energy. While the effect of muon nuclear capture is not significant for the energy range of this study, the fast neutron event rate with visible energy below 50 MeV is different between muon plus and minus. Therefore, the precise muon charge ratio measured by Kamiokande experiment [158] is adopted for application in other physics analyses in KamLAND.

$$R(\mu^+/\mu^-) = 1.37 \pm 0.06, \tag{10.11}$$

where $R(\mu^+/\mu^-)$ shows the ratio from muon minus to muon plus. This result corresponds to 0.422 for a fraction of muon minus and 0.578 for a fraction of muon plus. Since the KamLAND was built on the former site of the Kamiokande, the effect of local geometry is common.

Chemical Composition and Neutron Production Yield of Rock

The chemical composition of rock in Ikenoyama is unknown. There are discussions on several rock models in [108], such as the Inishi type, the standard rock, and the generic skarn. The paper also evaluated the impact of the specific gravity of the rock from 2.65 to 2.75 g/cm^3. The simulation results show that the difference caused by the rock types is not significant. Therefore, this simulation also assumes a simple chemical composition and density of the rock, SiO_2 with 2.7 g/cm^3. SiO_2 is the most dominant element in these rock types.

Although the neutron production yields in scintillators (C_nH_{2n}) predicted by Geant4 reproduce the experimental data well (Sec. 8.2.3), it is unknown for the rock (oxygen and silicon). Fig. 10.13 shows the neutron production yield as a function of average atomic weight for incident muons of 280 GeV predicted by several simulations. Since there is no experimental data, it is difficult to check the validity of the simulations. Furthermore, there are considerable differences around the atomic weight of 20, corresponding to silicon and oxygen. Thus, we are forced to assign large uncertainty to the simulation results.

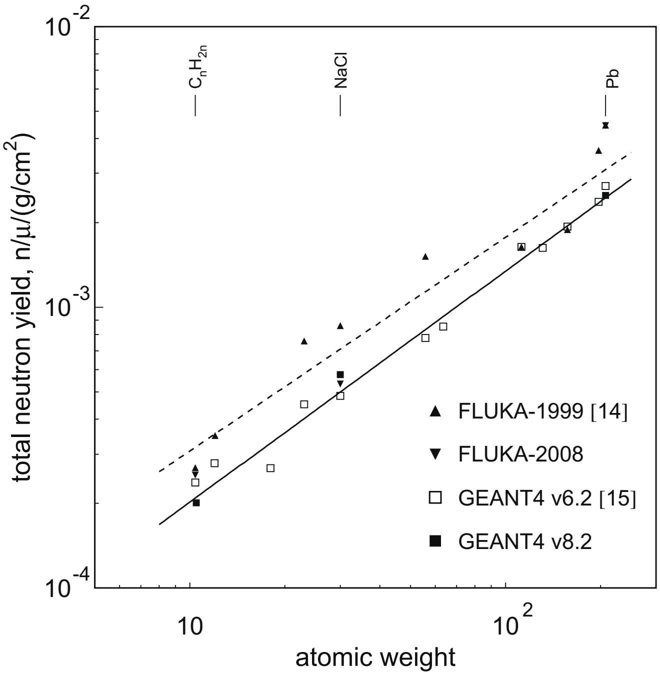

Figure 10.13: Neutron production yield as a function of average atomic weight for incident muons of 280 GeV. The dashed (solid) line represents a fit by a power-law dependence of FLUKA-1999 (Geant4 v6.2). The power-law dependence is parameterized by $R = bA^{\beta}$ where A represents the atomic weight. There are considerable differences around the atomic weight of 20, corresponding to silicon and oxygen. The figure is from [156].

10.3.2 Simulation Results

By preparing two geometries before and after OD refurbishment in the KLG4, this simulation is able to consider the change in OD veto efficiency. Since our results do not show any clear difference between these two geometries, the results shown here are averaged over the livetime of the two periods. Note that the livetime of the simulation corresponds roughly to 100 years [1].

---

[1] It took about (60 CPU) × (1 Month) to perform this simulation. We need more optimizations to reduce the computational time for more precise studies.

Fig. 10.14 shows the reproducibility confirmed in the events with one delayed (neutron capture) event. Since the OD cut is applied in the analysis, the OD untagged events (the green-shaded regions) can be the background. It can be seen that the small contribution of the OD untagged events above 200 MeV. This trend is caused by the fact that the neutrons produced by cosmic muons decrease monotonically and steeply as a function of neutron energy, as shown in Fig. 10.12. The shape of both radius and energy distributions roughly agree with the data, but there are deviations in normalization. There are various possible reasons for the discrepancy. First, the neutron production yield in the rock is uncertain. In addition, the visible energy and vertex are determined from the energy deposits instead of ID optical photon tracking to reduce the computation time. We therefore decided to assign large and conservative uncertainty: ±100% in the normalization [20].

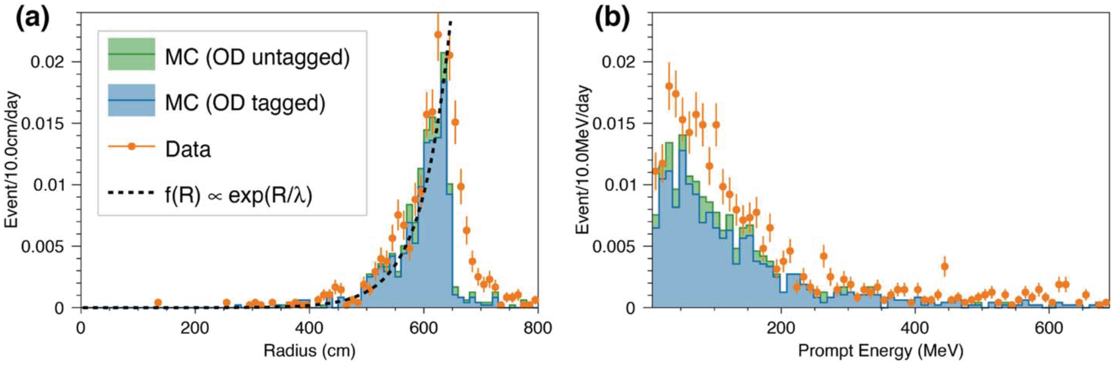

Figure 10.14: Radius distribution and energy spectra of the fast neutron events with one delayed (neutron capture) event. The events that have multiple delayed events are not included. The data correspond to 22.8 years in live time. (Left) Radius distribution in the energy range $7.5 < E_{\mathrm{prompt}} < 30$ MeV. (Right) Energy spectra within the 550 cm radius. The figure is from [20].

The expected fast neutron background event rate for the high-E selection is negligible: 0.15 events/year. On the other hand, it is 1.49 events/year for the low-E selection giving a non-negligible contribution. Fig. 10.15 shows the profile of expected fast neutron events for low-E selection. Fig. 10.15a shows the two-dimensional distribution for the visible energy and radius, Fig. 10.15b shows one-dimensional radius distribution. Above 200 MeV, the contribution is negligible, whereas, below the energy, there is a significant contribution, particularly in the outer region. In order to reduce this contribution, a tighter radius cut of 450 cm is set for the low-E selection in this study.

Fig. 10.15c shows the visible energy distribution for each neutron multiplicity. The result shows that events with one neutron multiplicity are the most dominant. At the same time, events with other neutron multiplicities exist to some extent. Inelastic scatterings can cause events with multiple neutrons in the detector or rock, while those of zero neutron multiplicity can be caused by selection inefficiency and neutron inelastic scatterings on carbon without neutron emission. We set a large and conservative uncertainty: ±100% in the normalization like [20].

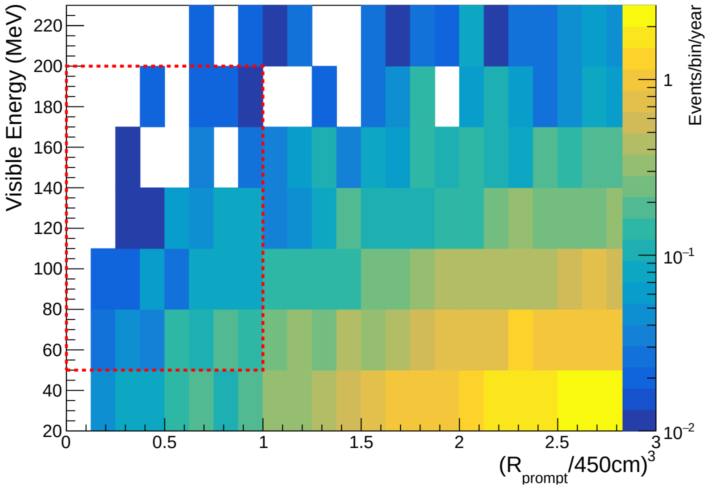

(a) Visible energy versus radius

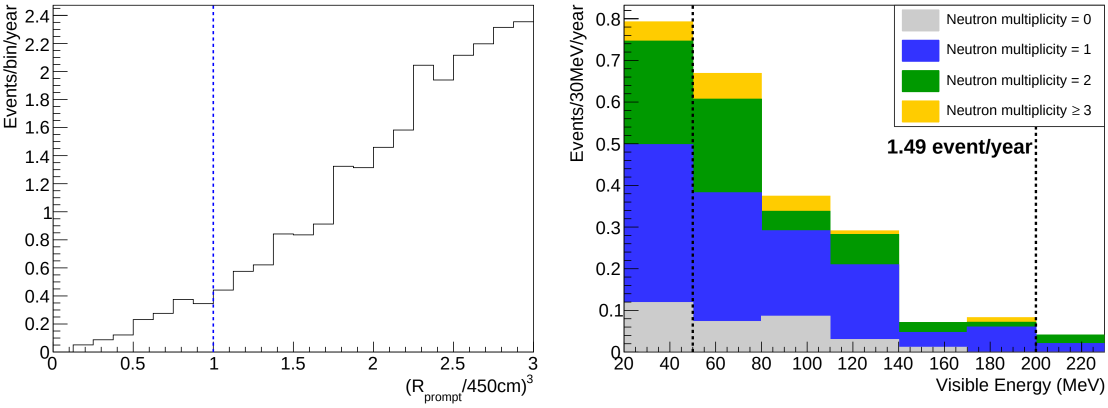

(b) Radius distribution

(c) Visible energy distribution

Figure 10.15: Expected fast neutron background. The dashed lines show the selection criteria of radius and energy for low-E selection. Neutron tagging efficiency due to the electronics dead time effects is not considered, namely assuming 100% efficiency. The fast neutron background for high-E selection is negligible.

Chapter 11

Analysis and Results

This chapter shows the analysis and results of simultaneous measurement of M_A and g_A^s by energy spectra fitting. A fit considering the neutron multiplicity associated with the atmospheric neutrino events makes it possible to measure g_A^s with a suppressed dependence on M_A.

Before discussing the fitting, Sec. 11.1 briefly introduces how g_A^s affects the KamLAND data. Then, the method of spectra fitting is explained in Sec. 11.2. The results obtained from the spectra fitting are shown in Sec. 11.3, and further discussion and investigations are in Sec. 11.4. Sec 11.5 introduces future prospects to improve the accuracy of g_A^s and the impact of this work on the next-generation detectors to search for new neutrino physics.

11.1 How g_A^s affects the KamLAND data

This section briefly introduces how g_A^s affects the KamLAND data. The effect of g_A^s appears as a change in the distribution of neutron multiplicities, while no clear change is seen in the visible energy distribution. Since the NCQE interaction is dominant below 200 MeV, the neutron multiplicity in the low-E selection is sensitive to g_A^s.

Fig. 11.1 shows the neutron multiplicity distribution of atmospheric neutrino events in the low-E selection ($50 < E_{\mathrm{prompt}} < 200\,\mathrm{MeV}$). Since negative g_A^s increases the NCQE cross section with protons, the total cross section with KamLAND LS with CH_2 composition increases. The NCQE interaction with free protons is not accompanied by neutron emission via FSI and nuclear de-excitation and typically leads to zero neutron multiplicity. Thus, negative g_A^s enhances the rate of NCQE events with zero neutron multiplicity (see Appendix F.1 for more detai). Fig. 11.2 shows the efficiency corrected mean neutron multiplicity as a function of visible energy. The observed data is compared with the simulation prior to the spectral fit with various values of g_A^s. The values of g_A^s significantly change the mean neutron multiplicity, particularly below 200 MeV, where the NCQE interactions dominate. These figures show that the observation of neutron multiplicity is quite effective for g_A^s measurements. The deficit of the mean neutron multiplicity around 300 MeV in Fig. 11.2 is hard to explain by small values of g_A^s. Since this region corresponds to the Δ region, we need careful investigation of the physics process related to pions, such as CC/NC RES, FSI, and SI. The discrepancy is partially explained by systematic uncertainties in the spectra fitting.

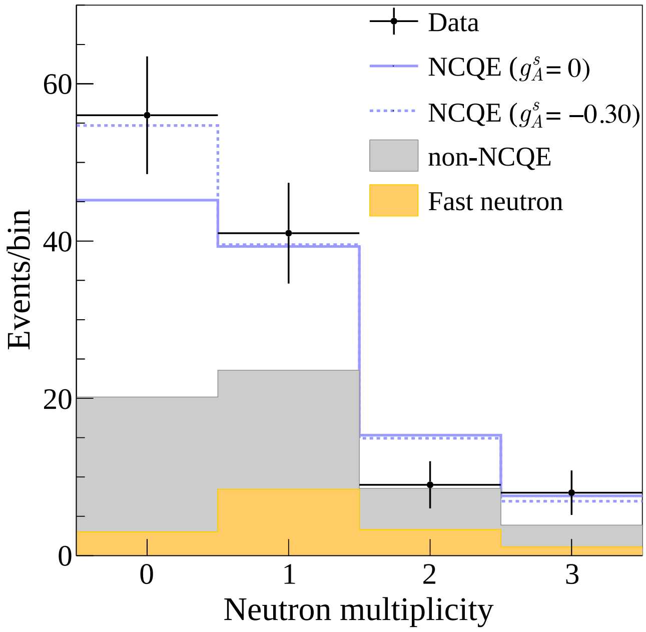

Figure 11.1: Neutron multiplicity of atmospheric neutrino events in the low-E selection ($50 < E_{\mathrm{prompt}} < 200\,\mathrm{MeV}$). The orange-shaded region represents the expected fast neutron background, the gray-shaded region shows the expected atmospheric neutrino events from interaction modes other than NCQE, and the blue solid (dashed) lines denote NCQE interactions with $g_A^s = 0$ (-0.30). The rightmost bin includes overflow. The simulation data are shown prior to the spectral fit, assuming $M_A = 1.2\,\mathrm{GeV}$.

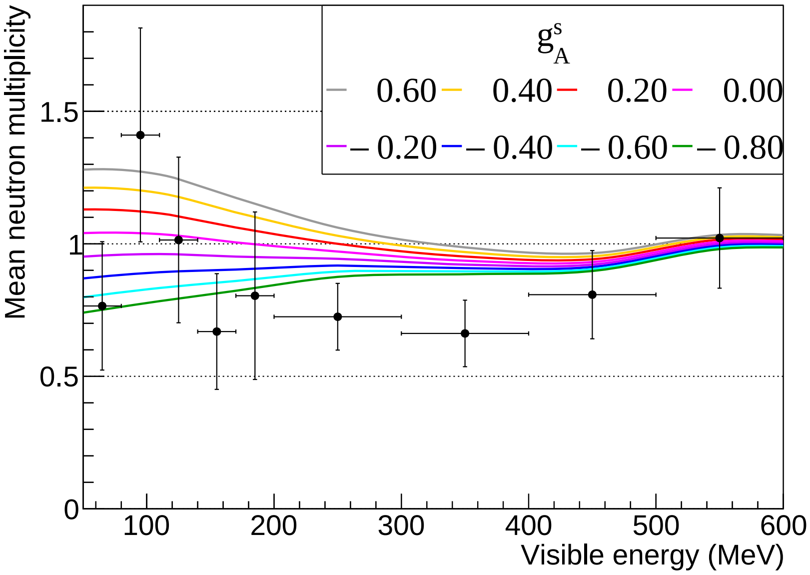

Figure 11.2: Efficiency corrected mean neutron multiplicity as a function of visible energy. The dots represent the KamLAND data, and colored lines denote simulation data prior to the spectral fit with various values of g_A^s, assuming $M_A = 1.2\,\mathrm{GeV}$. The simulation data are smoothed for readability with the values obtained for each visible energy bin. For lower values of g_A^s, the mean neutron multiplicity becomes smaller, particularly below 200 MeV, where the NCQE interactions dominate.

11.2 Spectra Fit

We simultaneously extract M_A and g_A^s from a fit of visible energy spectra. This fitting is based on a binned Chi-squared method incorporating the Poisson statistics and systematic uncertainties.

11.2.1 Definition of Chi-Squared

The χ^2 is composed of a Poisson term χ^2_{Poisson} and a penalty term χ^2_{penalty}:

$$\chi^2 = \chi^2_{\text{Poisson}} + \chi^2_{\text{penalty}}. \tag{11.1}$$

The Poisson term is defined using the number of observed events n_{ijk} and the number of expected events ν_{ijk}:

$$\chi^2_{\text{Poisson}} = \begin{cases} 2\sum_i \sum_j \sum_k [\nu_{ijk} - n_{ijk}] & (n_{ijk} = 0) \\ 2\sum_i \sum_j \sum_k [\nu_{ijk} - n_{ijk} + n_{ijk}\log(n_{ijk}/\nu_{ijk})] & (n_{ijk} > 0), \end{cases} \tag{11.2}$$

where the indices i, j, and k represent the i-th period, j-th visible energy, and k-th neutron multiplicity bins. There are four data collection period bins corresponding to periods I−IV. It also has thirteen visible energy bins, eight for the high-E selection, and five for the low-E selection. The data is divided into four neutron multiplicity bins, neutron multiplicity 0, 1, 2, and 3 or more. The analysis can consider neutron multiplicity by including the neutron multiplicity bins in the Poisson term. The Poisson term is based on the Poisson statistics as the name means and is valid for minority statistics like this study.

The penalty term is defined as:

$$\chi^2_{\text{penalty}} = \sum_l \left(\frac{E_l - O_l}{\sigma_l}\right)^2 + \sum_n \sum_m (E_n - O_n) M^{-1}_{nm} (E_m - O_m), \tag{11.3}$$

where l represents a systematic uncertainty parameter other than the neutron tagging efficiency, E_l is the expected value, O_l is the observed value in the fit, and σ_l is expected uncertainty of the parameter l. The indicides n and m denote parameters of the neutron tagging efficiency and M^{-1}_{nm} represents the error matrix described in Sec. 9.5. When minimizing the χ^2, the observed values in the fit (O_l and O_m) are moved in a wide range enough to consider the systematics properly.

11.2.2 Systematic Uncertainties

The systematic uncertainties considered in this analysis are summarized in Tab. 11.1, 11.2 and 11.3. These uncertainties can be divided into two categories: Those related to normalization and those related to neutron multiplicity. The latter ones affect the accuracy of g_A^s measurement.

In the normalization-related systematic uncertainties, the dominant contributions are from the atmospheric neutrino flux and the fiducial volume errors. The atmospheric neutrino flux particularly has a large normalization uncertainty (35%) in the low energy region. As a result, this analysis has almost no sensitivity to M_A, which changes the cross section normalization of QE.

The uncertainties related to neutron multiplicity can be divided into two categories: It originated from the KamLAND detector and originated from physics models. As detector-related systematic sources, there are neutron tagging efficiency and fast neutrons. As the physics model-related systematic sources, there are various sources: FSI, 2p2h interaction, nuclear de-excitation, and SI. The uncertainty of the FSI and SI depends on the accuracy of the nucleon-carbon and pion-carbon cross sections, which have certain deviations from the experimental data described in Sec. 4.1.1 and 8.2.2. Furthermore, for the FSI models, there are significant variations between the generators caused by the nuclear density and correction factors for nucleon-nucleon correlations (Sec. 4.2). The FSI model in NuWro uses a new optimized model for nucleons but a relatively old model for pions, which gives a larger inconsistency with the experimental data. This study assigns a large uncertainty of 50% to the pion FSI probability.

11.2.3 Minimization of Chi-Squared

To minimize χ^2, we use MINUIT in ROOT version 6.18.04, a data analysis environment and a set of related libraries being developed by CERN [159]. The MINUIT provides several minimizers, such as MIGRAD, MINIMIZE, and SIMPLEX. We use the MIGRAD, which is known to be the best one for nearly all functions. The MIGRAD is a sophisticated minimizer and generally converges in a single execution. [1]. More details about the MINUIT are in [161].

11.3 Results

Fig. 11.3 shows the best-fit energy spectra for all neutron multiplicities combined, and Fig. 11.4 shows the best-fit energy visible spectra with neutron multiplicity 0, 1, 2, and ≥ 3. Tab. 11.1, 11.2 and 11.3 show the systematic uncertainties and their best-fit values. The KamLAND data, which measures the neutron multiplicity with almost 80% efficiency, are well described by the simulations over a wide energy range, $50 - 1000\,\mathrm{MeV}$. The NCQE interaction dominates in the low-energy region, roughly below 200 MeV. The neutron multiplicity in this energy region determines the value of g_A^s.

Fig. 11.5 shows the two-dimensional allowed regions for M_A and g_A^s, and the one-dimensional $\Delta\chi^2$-profiles projected onto these parameters. We obtain the following results:

$$M_A = 0.86^{+0.31}_{-0.20}\,\mathrm{GeV}, \tag{11.4}$$
$$g_A^s = -0.14^{+0.25}_{-0.26}. \tag{11.5}$$

For reference, the MiniBooNE's result [64] compared in Fig. 11.5 is as follows:

$$M_A = 1.10^{+0.13}_{-0.15}\,\mathrm{GeV}, \tag{11.6}$$
$$g_A^s = -0.4^{+0.5}_{-0.3}. \tag{11.7}$$

When looking at M_A, this study does not have a good sensitivity due to the large normalization uncertainties such as flux and fiducial volume. Our result on M_A agrees with all

---

[1] In the analysis of KamLAND-Zen 800, a combination fit using the SIMPLEX and MIGRAD (once or twice) was performed [160].

[2] Scale factors corresponding to the FSI probability

[3] Scale factors corresponding to the SI probability

[4] Scale factors corresponding to the probabilities of neutron emission.

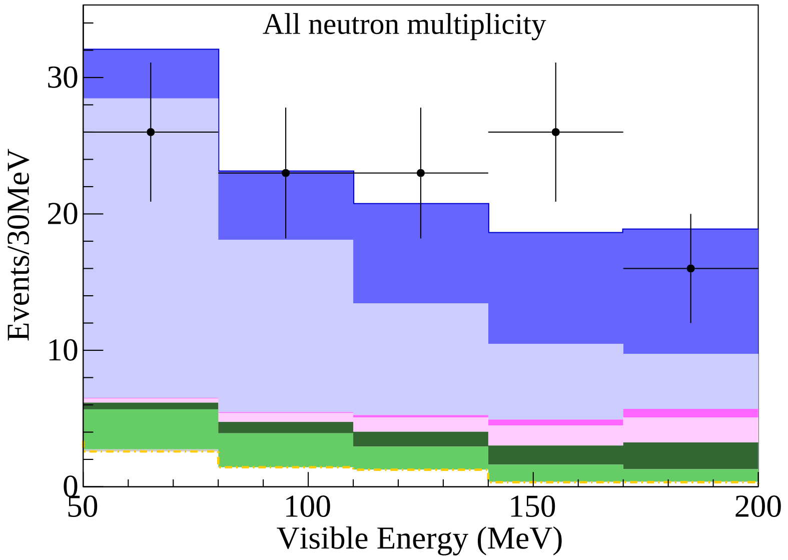

(a) Low-E selection ($50 < E_{\text{prompt}} < 200\,\text{MeV}$)

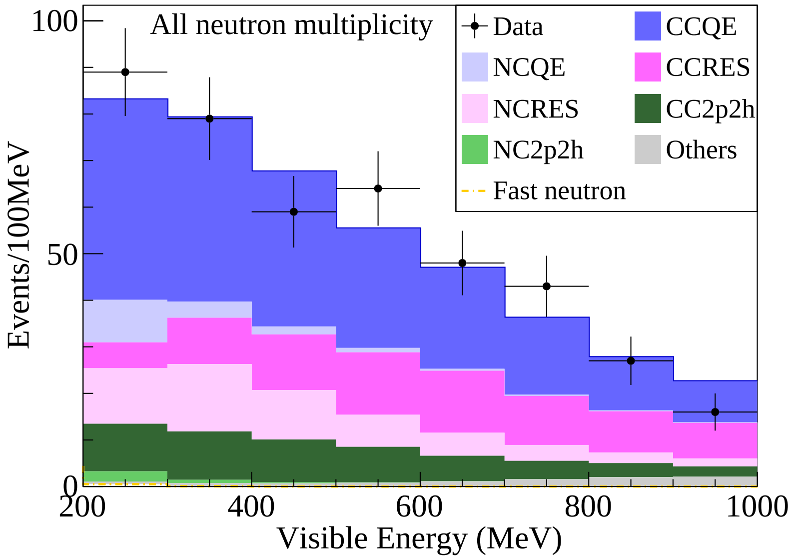

(b) High-E selection ($200 < E_{\text{prompt}} < 1000\,\text{MeV}$)

Figure 11.3: Best-fit visible energy spectra for all neutron multiplicity for low-E (a) and high-E (b). The “others” category in gray refers to deep-inelastic and coherent scattering.

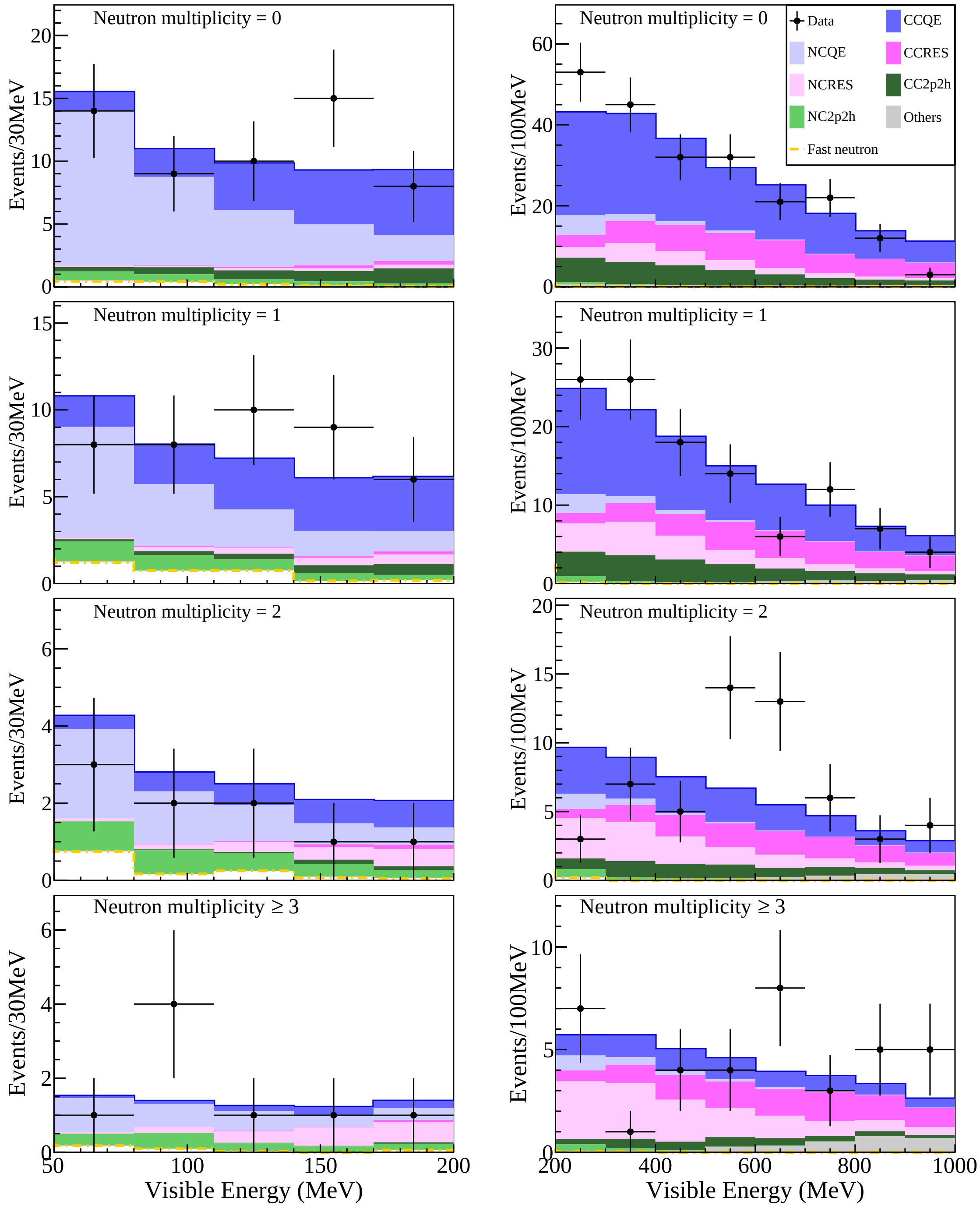

Figure 11.4: Best-fit visible energy spectra with neutron multiplicity 0, 1, 2, and ≥ 3. The left figures show the low-E selection, between 50 and 200 MeV. The right figures show the high-E selection, between 200 and 1000 MeV. The "others" category in gray refers to deep-inelastic and coherent scattering.

Table 11.1: Systematic uncertainties related to the flux, cross section, FSI and SI. They are common to all periods.

Parameter		Expected	Best-fit
Flux normalization	$E_\nu < 0.1\,\text{GeV}$	1.00 ± 0.35	0.98
	$0.1 < E_\nu < 1\,\text{GeV}$	1.00 ± 0.35	1.51
	$E_\nu > 1\,\text{GeV}$	1.00 ± 0.15	0.98
$\bar{\nu}_e/\nu_e$		0.00 ± 0.05	0.00
$\bar{\nu}_\mu/\nu_\mu$		0.00 ± 0.05	0.00
$(\nu_\mu + \bar{\nu}_\mu)/(\nu_e + \bar{\nu}_e)$		0.00 ± 0.02	0.00
Cross section normalization	CCRES	1.00 ± 0.10	1.01
	NCRES	1.00 ± 0.10	0.99
	CC 2p2h	1.00 ± 0.20	1.09
	NC 2p2h	1.00 ± 0.20	0.98
Ratio of *np* pair target in 2p2h		$0.85^{+0.15}_{-0.20}$	0.81
FSI [2]	nucleon	1.00 ± 0.28	0.91
	pion elastic	1.00 ± 0.50	1.09
	pion absorption	1.00 ± 0.50	1.08
SI [3]	nucleon	1.00 ± 0.07	1.00
	pion	1.00 ± 0.14	1.08

Table 11.2: Systematic uncertainties related to the branching ratios of nuclear de-excitation from $s_{1/2}$-hole state. They are common to all periods.

Parameter		Expected	Best-fit
Single-step de-excitation of $^{11}\text{B}^*$ (%)	Neutron	$18.7^{+6.1}_{-3.0}$	18.5
	Proton	$5.7^{+2.9}_{-1.1}$	5.7
	α	$3.3^{+4.4}_{-0.5}$	3.4
	Deuteron	$4.1^{+4.1}_{-0.6}$	4.1
	Triton	$1.5^{+14.9}_{-0.2}$	1.6
Multi-step de-excitation of $^{11}\text{B}^*$ (%)	Neutron	$25.3^{+9.0}_{-7.6}$	25.0
	Proton	$1.4^{+8.0}_{-0.2}$	1.7
	α	$0.08^{+12.04}_{-0.01}$	0.08
	Deuteron	$1.6^{+3.3}_{-0.4}$	1.6
	Triton	$0.6^{+1.7}_{-0.3}$	Fixed
Single-step de-excitation of $^{11}\text{C}^*$ (%)	Neutron	$4.2^{+1.7}_{-0.6}$	4.2
	Proton	31.0 ± 10.1	30.9
	α	$8.9^{+1.4}_{-1.3}$	9.0
Multi-step de-excitation of $^{11}\text{C}^*$ (%)	Neutron	$1.5^{+6.4}_{-0.2}$	1.5
	Proton	42.3 ± 6.7	42.3
	α	$1.7^{+10.0}_{-0.3}$	1.7
Neutron emission for multi-nucleon disappearance [4]	Two nucleon	$1.0^{+1.2}_{-1.0}$	−0.4
	Three or more	$1.0^{+1.8}_{-1.0}$	0.8

Table 11.3: Systematic uncertainties related to that are independent in period I, period II, period III, and period IV.

Parameter		Period I		Period II	
		Expected	Best-fit	Expected	Best-fit
Solar cycle		0.00 ± 1.00	-0.01	0.00 ± 1.00	0.03
Energy scale		1.00 ± 0.08	1.04	1.00 ± 0.08	0.92
Fiducail volume	Prompt	1.00 ± 0.10	0.99	1.00 ± 0.10	1.02
	Delayed	0.00 ± 1.00	0.02	0.00 ± 1.00	-0.02
Fast neutron normalization		1.00 ± 1.00	0.09	1.00 ± 1.00	0.31
Neutron tagging efficiency	p_0	0.90 ± 0.06	0.89	0.91 ± 0.06	0.91
	p_1	0.13 ± 0.22	0.18	-0.28 ± 0.19	-0.28
	p_2	-0.16 ± 0.17	-0.19	0.16 ± 0.14	0.16

Parameter		Period III		Period IV	
		Expected	Best-fit	Expected	Best-fit
Solar cycle [a]		0.00 ± 1.00	-0.05	0.00 ± 1.00	0.07
Energy scale		1.00 ± 0.08	0.95	1.00 ± 0.08	1.00
Fiducail volume	Prompt	1.00 ± 0.10	0.96	1.00 ± 0.10	1.08
	Delayed [b]	0.00 ± 1.00	0.13	0.00 ± 1.00	-0.11
Fast neutron normalization		1.00 ± 1.00	0.41	1.00 ± 1.00	0.99
Neutron tagging efficiency	p_0	0.86 ± 0.04	0.86	0.83 ± 0.08	0.81
	p_1	-0.26 ± 0.13	-0.25	-0.15 ± 0.29	-0.12
	p_2	0.11 ± 0.09	0.10	-0.02 ± 0.22	-0.02

---

[a] Error factor corresponding to 110 counts/hour/100 in NM parameter.

[b] Error factor corresponding to 0.7/0.4% changes on the number of tagged neutrons in high-E/low-E selection.

of the other measurements shown in Fig. 2.5 within the large error, giving almost no hint about the discrepancy between the conventional world average and recent experiments. When looking at the g_A^s, our result is consistent with the MiniBooNE's result giving little dependence on M_A. Our result is the most accurate measurement on g_A^s among NCQE measurements without M_A constraints. This feature, realized by measuring neutron multiplicity, is important in the current experimental situation where measured values of M_A vary from experiment to experiment.

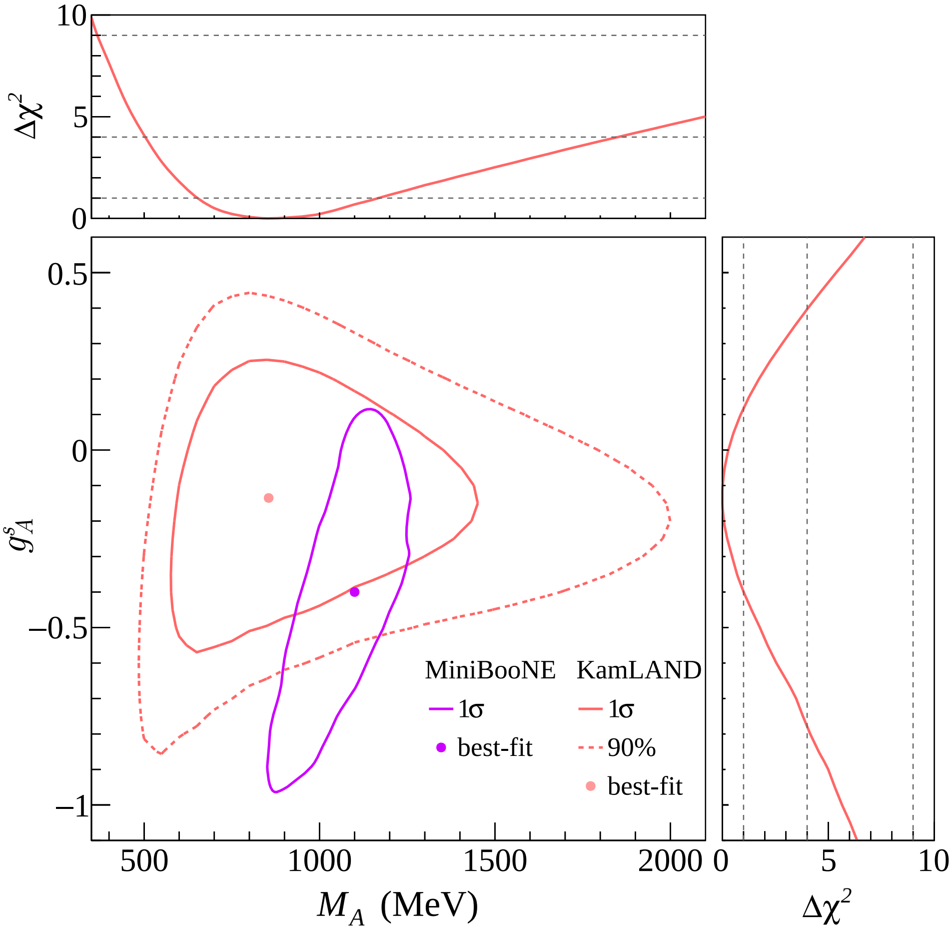

Figure 11.5: Two-dimensional allowed regions for M_A and g_A^s. The red contour and dot are the result of this work. The side panels show the one-dimensional $\Delta\chi^2$-profiles projected onto M_A and g_A^s. The violet contour and dot display the 1σ C.L. and best-fit value from MiniBooNE [64]. In both results, M_A is treated as a free parameter.

In our analysis, the systematic and statistical uncertainties on g_A^s are almost comparable:

$$g_A^s = -0.14 \pm 0.17(\mathrm{stat})^{+0.18}_{-0.20}(\mathrm{syst}). \tag{11.8}$$

Therefore, reducing both statistical and systematic errors is essential for further improvement of g_A^s measurement. This study successfully suppressed the M_A dependence, but it remains. The allowed region of g_A^s is relatively large in small M_A. If we rely entirely on the MiniBooNE CCQE cross section measurement and TEM for 2p2h interaction, the constraint on M_A can be obtained: $M_A = 1.14 \pm 0.07\,\mathrm{GeV}$ (see Appendix F.2). If we apply this constraint on M_A, the improved result can be obtained:

$$g_A^s = -0.12 \pm 0.17(\text{stat})^{+0.13}_{-0.14}(\text{syst}), \tag{11.9}$$

It means that M_A is still the main source of uncertainty in g_A^s measurement even in this study. As for others, the following sources related to the neutron multiplicity have almost equal contributions: the FSI (±0.06), 2p2h interaction (±0.06), nuclear de-excitation (±0.04), neutron tagging efficiency (±0.04). Among these sources, the 2p2h interaction is closely related to the determination of M_A, and the FSI accuracy is essential for directly measuring the 2p2h interaction. Therefore, it is crucial to understand the FSI and 2p2h interaction and to determine M_A through them.

11.4 Discussion

A summary of $g_A^s(\Delta s)$ measurements and the values adopted in neutrino Monte Carlo event generators is shown in Fig. 11.6. All the experimental results have consistent values and prefer a negative value of g_A^s. A negative g_A^s is reasonably explained by the current experimental measurements of hadronic matrix elements [82]. Our result gives the most accurate value on g_A^s among NCQE measurements without M_A constraints.

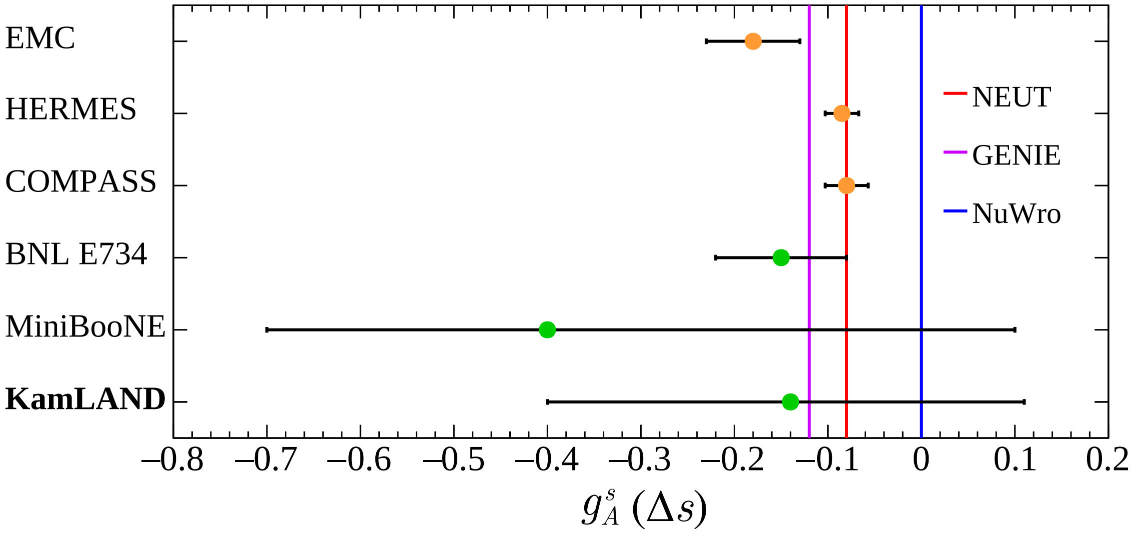

Figure 11.6: Summary of g_A^s (Δs) measurements. In addition to the result of this work, results from EMC [75, 80], HERMES [78], COMPASS [81], BNL E734 [65], and MiniBooNE [64] are also shown. Results with orange symbols are polarized lepton deep-inelastic scattering experiments, and ones with green symbols are NCQE scattering experiments. The red, violet, and blue vertical lines represent the values adopted in neutrino Monte Carlo generators in default. All of the results from NCQE measurements shown here are obtained with neglecting the strange vector form factors ($F_V^{1,s}(Q^2) = F_V^{2,s}(Q^2) = 0$).

We should note two points in the interpretation of Fig. 11.6. The first is that the impact of $SU(3)_f$ flavor symmetry breaking on polarized-lepton deep-inelastic scattering experiments is not included. The $SU(3)_f$ flavor symmetry breaking can shift these results by ±0.04, which is approximately equal to or larger than the errors. Therefore, it is important to measure g_A^s using the NCQE interactions, although the errors are currently large. The second point concerns the treatment of M_A and the 2p2h contribution. As described so far, it is difficult to determine a reasonable constraint on M_A in the current experimental situation. The MiniBooNE and KamLAND results were obtained without M_A constraints and included consideration of the 2p2h interaction. In contrast, the BNL E734 result did not consider any 2p2h interaction, and M_A was strongly constrained. The BNL E734 result could therefore be affected by the contribution of the 2p2h interaction and a larger M_A uncertainty.

The experimental NCQE data prefer smaller values than the results of polarized-lepton deep-inelastic scattering experiments and those adopted in neutrino Monte Carlo generators. However, they still have large uncertainties and must be more accurate to claim adequate theoretical inputs. Further improvements in both experimental accuracy and theoretical modeling will be necessary.

11.5 Future Prospects

The measurements of g_A^s using the NCQE interactions, including this study, still have significant errors. Further sensitivity is required to claim an appropriate value. In our analysis, the systematic and statistical uncertainties on g_A^s are almost comparable. Therefore, reducing both statistical and systematic errors is essential.

11.5.1 Reducing Statistical Uncertainties

In order to improve the statistics, lowering the visible energy threshold for the atmospheric neutrino event selection would be effective at first. As shown in Fig. 11.4, the NCQE interactions are dominant in the low-energy region, so a low energy threshold can increase the number of candidates. However, the contribution of fast neutron background, which has considerable uncertainty in the estimation, becomes significant in the energy region. The threshold can be lowered to about $20-30\,\mathrm{MeV}$, by further improving the simulation accuracy. It is challenging to see below $20\,\mathrm{MeV}$ because there are many decay events of radioactive isotopes due to the muon spallation. Furthermore, more quality of the de-excitation process is required.

Another promising contribution to statistics is using J-PARC neutrino events as an additional data set. The neutrino beam from J-PARC into Super-Kamiokande has a large enough spatial spread to be observable also at KamLAND [143]. The time width of the beam is very narrow, about $5\,\mu\mathrm{s}$. By strict timing selection using the beam launch time information, an approximately background-free threshold of about $5\,\mathrm{MeV}$ can be achieved. Although the statistics are much less than the data set of atmospheric neutrino events in this study, it will improve the result somewhat.

11.5.2 Reducing Systematic Uncertainties

As for the systematic uncertainties, the result has roughly equal contributions from various sources: the FSI, 2p2h interaction, nuclear de-excitation, and neutron tagging efficiency. Even though this result achieves less dependence on M_A, it still has room to improve the sensitivity on g_A^s by determining the value of M_A. As already discussed, g_A^s, M_A, 2p2h interaction, and FSI are closely related. We need to conduct a multifaceted verification by combined analysis using the results of other experiments to deepen our understanding of these components simultaneously.

FSI model

The FSI contributes slightly more significantly to systematic uncertainty in determining g_A^s than other sources. For the direct measurement of the 2p2h interaction and determining the value of M_A, the advanced prediction accuracy of the FSI is required. Electron scattering data can validate it, but it is challenging to model the dynamics of strong interactions in nuclei as introduced in Sec. 4.2. Careful investigations on the FSI models are desired to understand the significant differences among the generators and to optimize the models to give good consistency with experimental data.

2p2h inteaction

It is necessary to measure the 2p2h interaction directly and check the model's validity. It is vital to determine the value of M_A. Furthermore, since the contribution of 2p2h is estimated to be only $10-20\%$ of QE, an accurate high-statistics measurement is required. Direct measurement of the 2p2h interaction is quite challenging at KamLAND. However, a combined analysis with other experiments, which aim at the direct measurements of the 2p2h, such as NINJA experiment [57], will be effective in constraining g_A^s further.

Nieves *et al.* [51] and Martini *et al.* [52] have been developing microscopic models to describe the 2p2h interaction. However, since they mainly focus on the CC, only the TEM is currently available for NC 2p2h in the generators. We expect that NC 2p2h models other than the TEM will be developed and implemented into the generators to allow verification of various models.

Nuclear De-excitation

Simulation of nuclear de-excitation developed in Chap. 5 is another source of systematic error. Although this simulation was recently developed in this study, it agrees with experimental data and other predictions for neutron emission within 20%. In the case of the carbon target, the s-hole state, where neutrons can be emitted, occurs only about 1/3 probability. This low probability leads to a small contribution of the complicated de-excitation chain via the s-hole state. However, since there are discrepancies with the experimental data for triton and α emissions, additional experiments for validation and model improvement are the issue to be addressed.

We also expect to implement this de-excitation simulation as a standard in the neutrino Monte Carlo event generators. By providing the simulation in a way that can be used in other experiments and validated, multifaceted checks of the simulation can be achieved. While this study focused on carbon, developing a simulation for oxygen, which aims to contribute to more diverse experiments, particularly the water Cherenkov detector, is possible. Since oxygen has one more shell level than carbon, the excitation energy distribution and de-excitation process are more complicated.

Neutron Tagging Efficiency

This study only uses the data acquired by the KamFEE. The MoGURA has a higher neutron tagging efficiency than the KamFEE because it is more tolerant to high-rate afterpulses and overshoots after high-charge events. Therefore, by combining MoGURA data in this analysis, neutrons associated with the atmospheric neutrino events can be selected with higher efficiency. Since there is still room for improvement in the quality of

MoGURA event reconstruction, we need additional calibration and tool development to combine the data with the analysis.

11.5.3 Toward Next-Generation Experiments

In recent neutrino physics, the importance of accurately determining g_A^s and comprehensively predicting neutron multiplicity, including nuclear de-excitation, has increased dramatically. Detectors capable of measuring neutron multiplicity have been rare, but recent and next-generation detectors, such as Super-Kamiokande Gadolinium, Hyper-Kamiokande, and JUNO (see Sec. 1.3.4), will make it possible. These detectors will significantly improve the measurement statistics with a large volume (50 kton for Super-Kamiokande, 260 kton for Hyper-Kamiokande, and 20 kton for JUNO), so reducing these systematic uncertainties is essential. These experiments plan to use neutron tagging information to reduce the main background significantly, atmospheric neutrino events, in searches for supernova relic neutrinos (SRN. See Sec. 1.3.2) and proton decay (see Sec. 1.3.3). The dominant systematic uncertainty in these analyses comes from neutrino-nucleon interactions, especially the nuclear effects related to neutron emission. Therefore, the prediction accuracy of neutron emission in neutrino interactions will be the most crucial issue in these experiments.

This study provides significant knowledge to these next-generation experiments as the first study of measuring neutron multiplicity associated with neutrino interaction at about 80% efficiency. First, the nuclear de-excitation simulation developed in this study is in great demand in these next-generating experiments. The comparison of de-excitation prediction with the experiments shows the reliability of our simulation. Furthermore, this study is the first to compare the observed data and prediction, including de-excitation simulation for neutron multiplicity associated with neutrino interactions, setting it apart from other predictions. We expect to implement our simulation into the neutrino Monte Carlo generators so that all neutrino experiments can use and validate it. Second, the determination of g_A^s is significant for SRN searches since the NCQE interactions of atmospheric neutrinos are the main background. At present, uncertainties of neutrino-proton elastic scattering ($\nu p \to \nu p$) cross section due to g_A^s is about 30%. It will become a major uncertainty in supernova-burst neutrino flux measurement using the proton elastic scattering [162]. For further developments in neutrino astronomy, it is essential to improve the accuracy of g_A^s.

11.5.4 Settle the Open Question: Are the Strange Quarks in the Nucleon Polarized?

At last, let us emphasize that the value of g_A^s itself is an exciting topic in particle physics, besides the impact on the NCQE cross section. The strangeness axial coupling constant g_A^s corresponds to the contribution of the strange quarks existing as sea quarks to the nucleon spin. It provides us with fundamental information about nucleons that make up matter. We hope further discussion, including the impact of $SU(3)_f$ flavor symmetry breaking on the polarized l-N DIS results, will determine the value of g_A^s (Δs) and settle the open question, are the strange quarks in the nucleon polarized?

Part V

Summary

Chapter 12

Conclusion

This dissertation reported a new measurement of the strangeness axial coupling constant g_A^s using neutron multiplicity associated with the NCQE interaction of atmospheric neutrino at KamLAND. We established a systematic simulation method for nuclear de-excitation, which is required to predict the neutron multiplicity accurately. This analysis used KamLAND atmospheric neutrino data from January 2003 to May 2018, corresponding to 10.74 years of total live time. By fitting the visible energy spectrum for each neutron multiplicity, we obtain $g_A^s = -0.14^{+0.25}_{-0.26}$, which is the most accurate measurement obtained using NCQE interactions without M_A constraints. The experimental data on NCQE interactions, including this result, favor slightly smaller values than those used in the neutrino Monte Carlo generators. However, further improvements in accuracy are necessary to claim an appropriate value.

The main future tasks to be addressed are detailed investigations of the sources of the systematic uncertainty, which are closely related: the FSI models, 2p2h interaction, and the value of M_A. More careful investigations on the FSI models, including corrections, are desired to understand and improve agreements with experimental data. Although direct measurement of the 2p2h interaction is quite challenging at KamLAND, a combined analysis with other experiments, which aim at the direct measurements of the 2p2h, will be effective. Eventually, the discrepancy of M_A values, which has been a critical issue over the last 20 years, needs to be resolved.

This analysis is the first to measure neutron multiplicity with a detection efficiency of $\sim$80%. It is also the first to compare measured neutron multiplicity with simulations that consider nuclear de-excitation. This analysis will add significant knowledge to the many recent and next-generation experiments information. All of them must consider nuclear de-excitation processes when conducting studies that use neutron tagging information. We expect to integrate the nuclear de-excitation simulation developed here into neutrino event generators for use in other experiments.

The strangeness axial coupling constant allows us to investigate the fundamental nucleon structure: the contribution of the strange quarks existing as sea quarks to the nucleon spin. We hope the further discussion in the NCQE, polarized l-N DIS experiments, and $SU(3)_f$ flavor symmetry breaking will settle the open question, are the strange quarks in the nucleon polarized?

Appendix A

Supplements for the Nuclear De-excitation Simulation

A.1 Separation Energies

Tab. A.1 show the summary of separation energies of ^{12}C, ^{11}C, and ^{11}B.

Table A.1: Separation energies of ^{12}C, ^{11}C, and ^{11}B. The values are from TALYS [95] and written in the unit of MeV.

Particle	^{12}C	^{11}C	^{11}B
Neutron	18.72	13.13	11.45
Proton	15.96	8.69	11.23
Deuteron	25.19	14.90	15.82
Triton	27.37	27.22	11.22
^{3}He	26.28	9.22	27.21
Alpha	7.37	7.54	8.66

A.2 Energy Level Diagrams

Fig. A.1 and A.2 show the energy level diagrams of ^{11}B and ^{11}C, respectively.

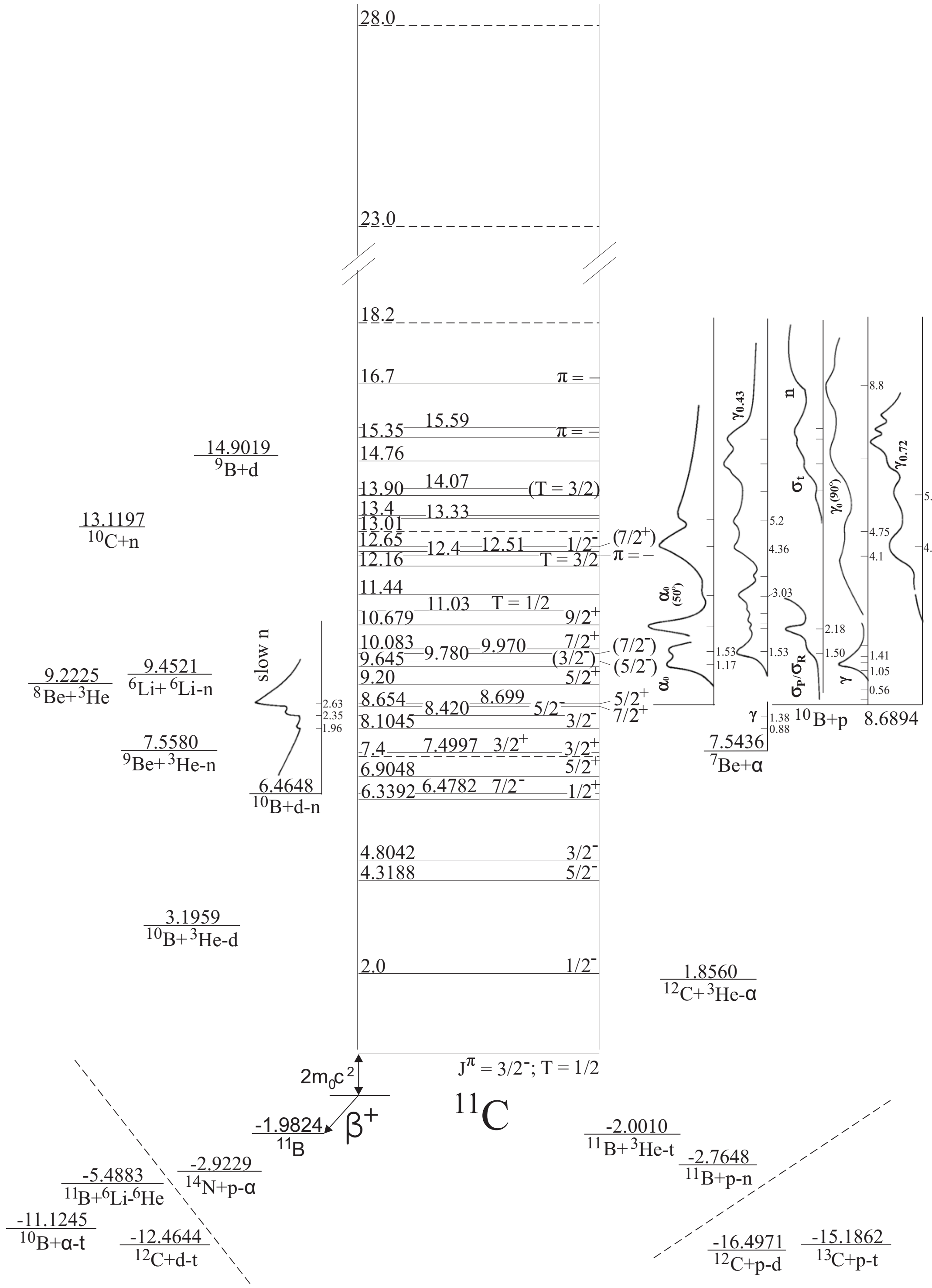

Figure A.1: Energy level diagram of ^{11}C. There is only one excited state with spin-parity $J^\pi = 1/2^-$ in the low-excitation-energy region of a few MeV: 2.0 MeV. The figure is from [163].

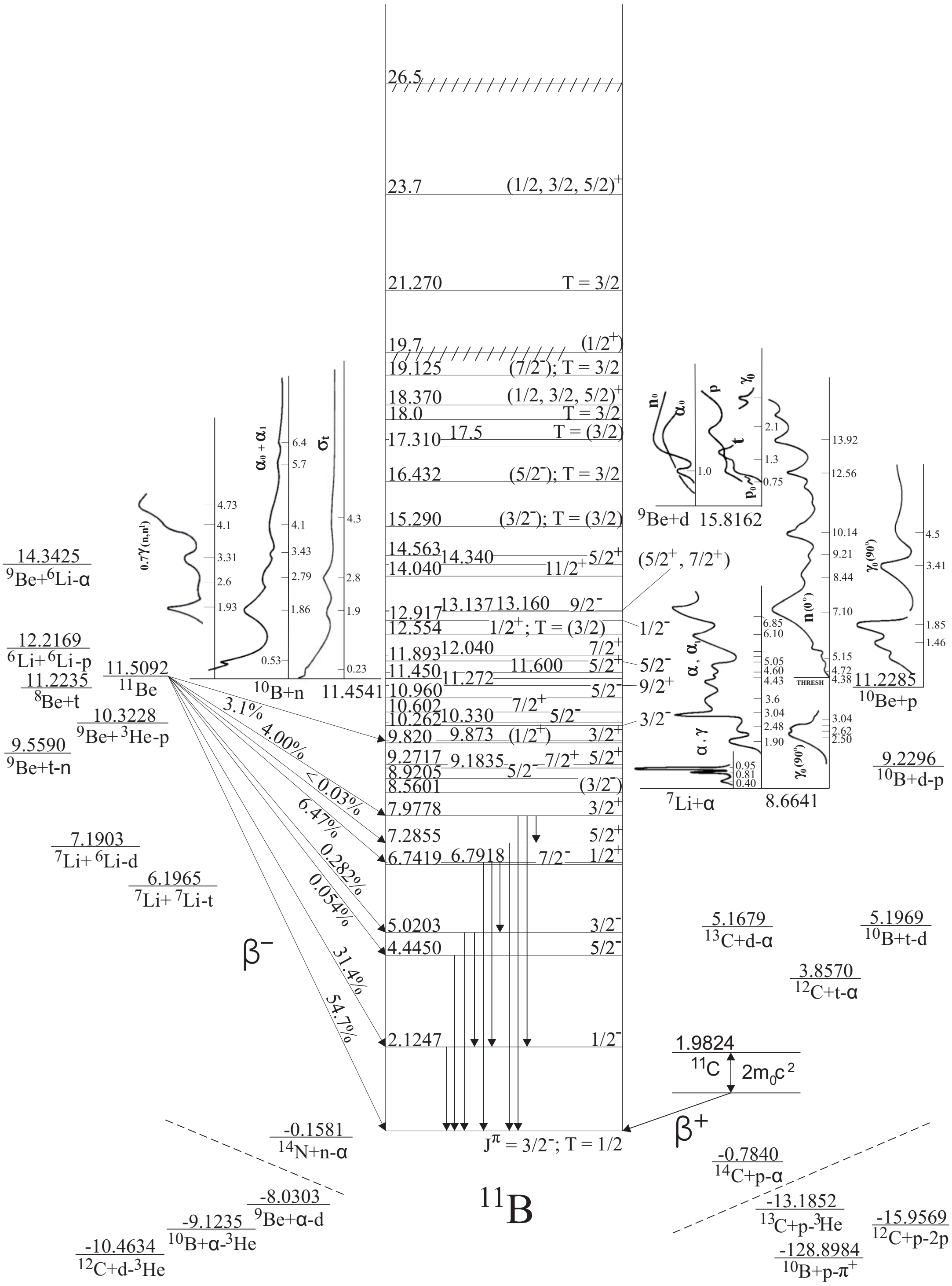

Figure A.2: Energy level diagram of ^{11}B. There is only one excited state with spin-parity $J^\pi = 1/2^-$ in the low-excitation-energy region of a few MeV: 2.1= MeV. The figure is from [163].

A.3 Prediction by Kamyshkov *et al.*

Fig. A.3 shows the branching ratios of ^{11}C* calculated by Kamyshkov *et al.* using SMOKER code [100]. They neglected decay modes of d, t, and ^{3}He. When focusing on the neutron branching ratio, the TALYS prediction (Fig. 5.3b) has a little smaller value than the SMOKER prediction. They did not discuss the de-excitation of ^{11}B* in this paper.

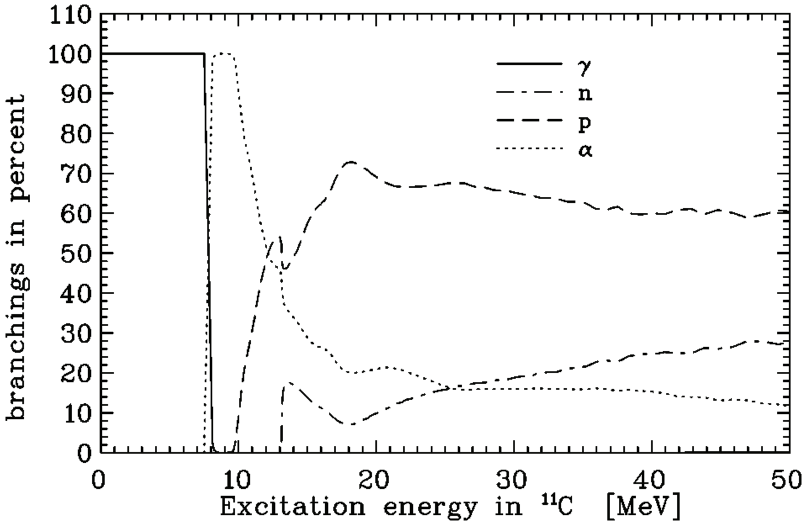

Figure A.3: Branching ratios of ^{11}C* with $J^\pi = 1/2^+$ as a function of excitation energy. The decay modes of triton, deuteron, and ^{3}He are neglected. The data are obtained using SMOKER code, and the figure is from [100].

A.4 Difference in the Branching Ratios of Daughter Nuclei

Fig. A.4 shows the branching ratios of ^{10}B* as a function of excitation energy. The left panel shows the one from $^{11}\mathrm{B}^* \to n + ^{10}\mathrm{B}^*$, and the right panel shows the one from $^{11}\mathrm{C}^* \to p + ^{10}\mathrm{B}^*$. While the branching ratios of the deuteron, α, and γ are the same, those of the proton, neutron, triton, ^{3}He are different. The difference is particularly clear for proton (the red lines) and neutron (the blue lines).

The difference is considered to be caused by the difference in spin-parity. The spin-parity of primary nucleus (^{11}C* and ^{11}B*) is common to be $J^\pi = 1/2^+$, but it would be differ in ^{10}B*. The results show that the difference only appears for the particles with different numbers of neutrons and protons, such as the proton, neutron, triton, and ^{3}He. Furthermore, it indicates the effect of a smaller contribution of modes that emit the same particle twice, as

$$^{11}\mathrm{B}^* \to n + ^{10}\mathrm{B}^* \to n + ^{9}\mathrm{B}^* \tag{A.1}$$

$$^{11}\mathrm{C}^* \to p + ^{10}\mathrm{B}^* \to p + ^{9}\mathrm{Be}^* \tag{A.2}$$

In this study, we comprehensively take this effect into account by preparing branching ratio tables of daughter nuclei for each parent nucleus, such as ^{11}B* and ^{11}C*.

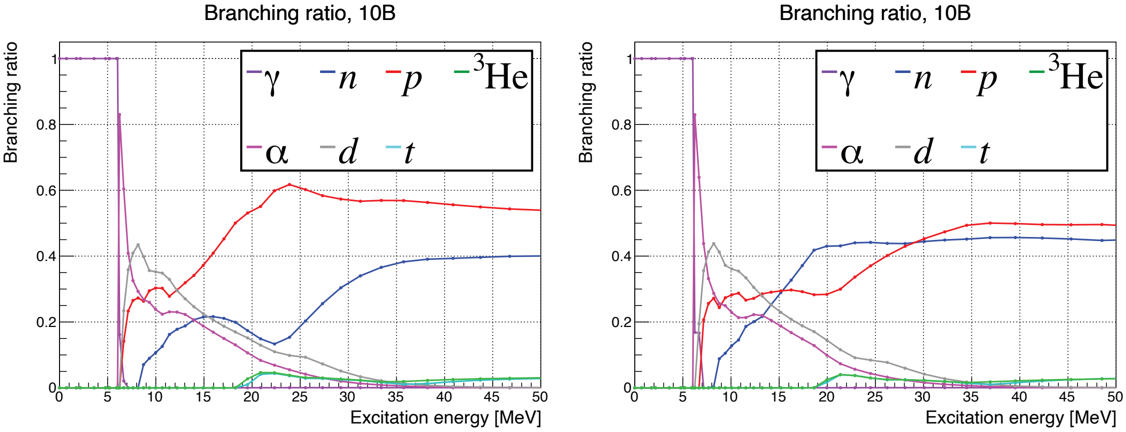

Figure A.4: Branching ratios of ${}^{10}\mathrm{B}^*$ as a function of excitation energy. The left figure shows ones from ${}^{11}\mathrm{B}^* \to n +{}^{10}\mathrm{B}^*$, and the right figure shows ones from ${}^{11}\mathrm{C}^* \to p +{}^{10}\mathrm{B}^*$. Although they are the same nucleus, ${}^{10}\mathrm{B}^*$, the branching ratios are different due to the difference in spin-parity. We assume spin-parity $J^\pi = 1/2^+$ both for ${}^{11}\mathrm{B}^*$ and ${}^{11}\mathrm{C}^*$.

Appendix B

KamFEE Trigger Types

The KamFEE trigger circuit sums the hit information ($Nsum$) sent from the KamFEE boards. If the $Nsum$ exceeds a certain threshold, a trigger is issued, and the ATWDs digitize the waveform. There are several trigger types, as follows.

B.1 ID Prompt and Delayed Trigger

ID prompt trigger is issued when the $Nsum$ of ID PMTs exceeds a certain value. ID delayed trigger is issued when the $Nsum$ of ID PMTs exceeds another certain value within 1 ms after the prompt trigger is issued. If these ID triggers are issued, it also issues an acquisition command to the OD, called ID to OD trigger. Fig. B.1 shows the time variation of $Nsum$ trigger threshold for the ID prompt and delayed trigger. The thresholds are adjusted to correspond to approximately 0.7 MeV (0.3 MeV) in visible energy for the prompt (delayed). We adopt a lower threshold for the delayed trigger to improve the detection efficiency of delayed events with low energy, such as ^{214}Bi-Po.

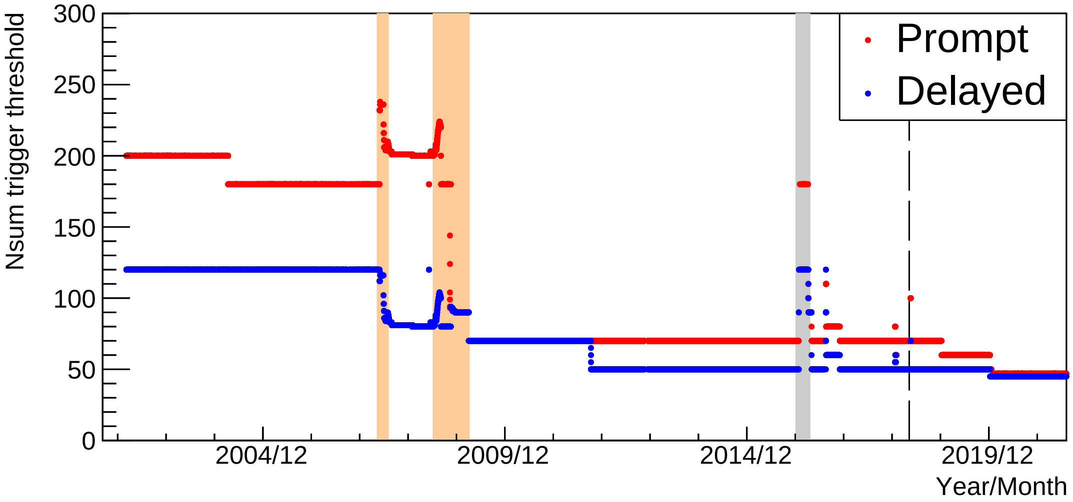

Figure B.1: Time variation of trigger threshold. The red (blue) dots represent the ID prompt (delayed) trigger threshold. The orange-shaded region represents the purification campaigns, and the gray-shaded region represents the OD refurbishment campaign. The data used in this analysis is up to May 2018, represented by the long dashed line.

These thresholds are low enough to detect atmospheric neutrino events. Since the atmospheric neutrino events are of low frequency, prompt events are generally acquired by the prompt triggers, and delayed events (neutron capture events) are acquired by the delayed events.

ID prescale triggers have also been implemented to achieve the lower threshold, but they are not relevant to high-energy events such as atmospheric neutrino events. Thus, we omit explanations.

B.2 OD Triggers

OD triggers are issued when the $Nsum$ of OD PMTs exceeds a certain value. If the OD triggers are issued, it also issues an acquisition command to the ID, called OD to ID trigger. These triggers are for fast neutron events with very low-energy deposition in the ID where the ID triggers would not be issued.

Fast neutron events that would be background events in this study have high energy deposits in the ID that the ID triggers are issued. Therefore, the OD triggers are not so relevant to this study.

Appendix C

Nuclear Level Diagrams

The level diagrams of radioactive source used in the KamLAND calibration are shown in this chapter. For these radioactive sources, only gamma-rays are actually visible in the calibration in KamLAND, as shown in Tab. 6.5. ^{60}Co, ^{137}Cs, and ^{203}Hg are accompanied by β^- decay to the excited state of the daughter nuclei. The low energy electrons emitted in this process are mostly absorbed by the source holder made with the stainless steel Thus, gamma-rays emitted via the de-excitation is observable. In the case of ^{68}Ge, it goes to ^{68}Ga by electron capture. ^{68}Ga mostly goes to the ground state of ^{68}Zn via β^+ decay. The positrons emitted in this process annihilate in the source holder, emitting two gamma-rays of 0.511 MeV.

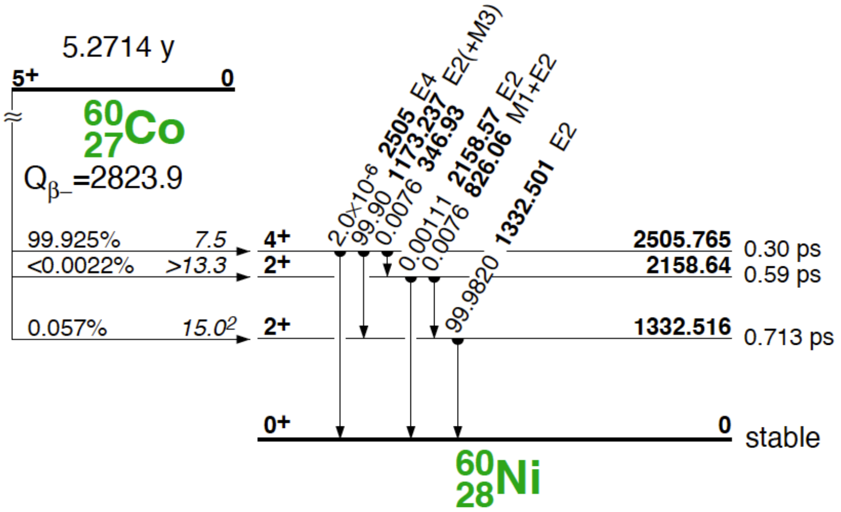

Figure C.1: Level diagram of ^{60}Co [164].

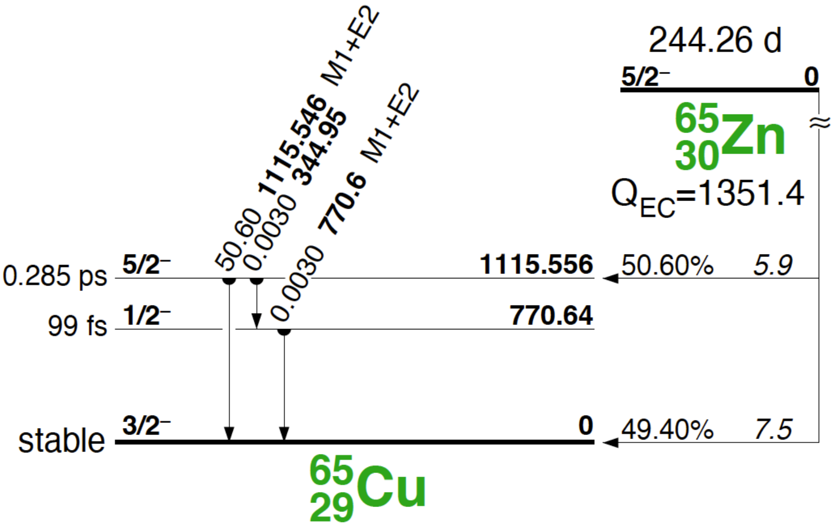

Figure C.2: Level diagram of ^{65}Zn [164].

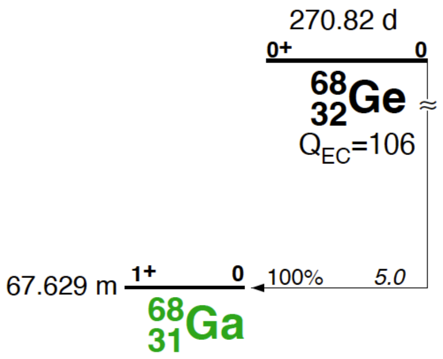

(a) Level diagram of ^{68}Ge [164].

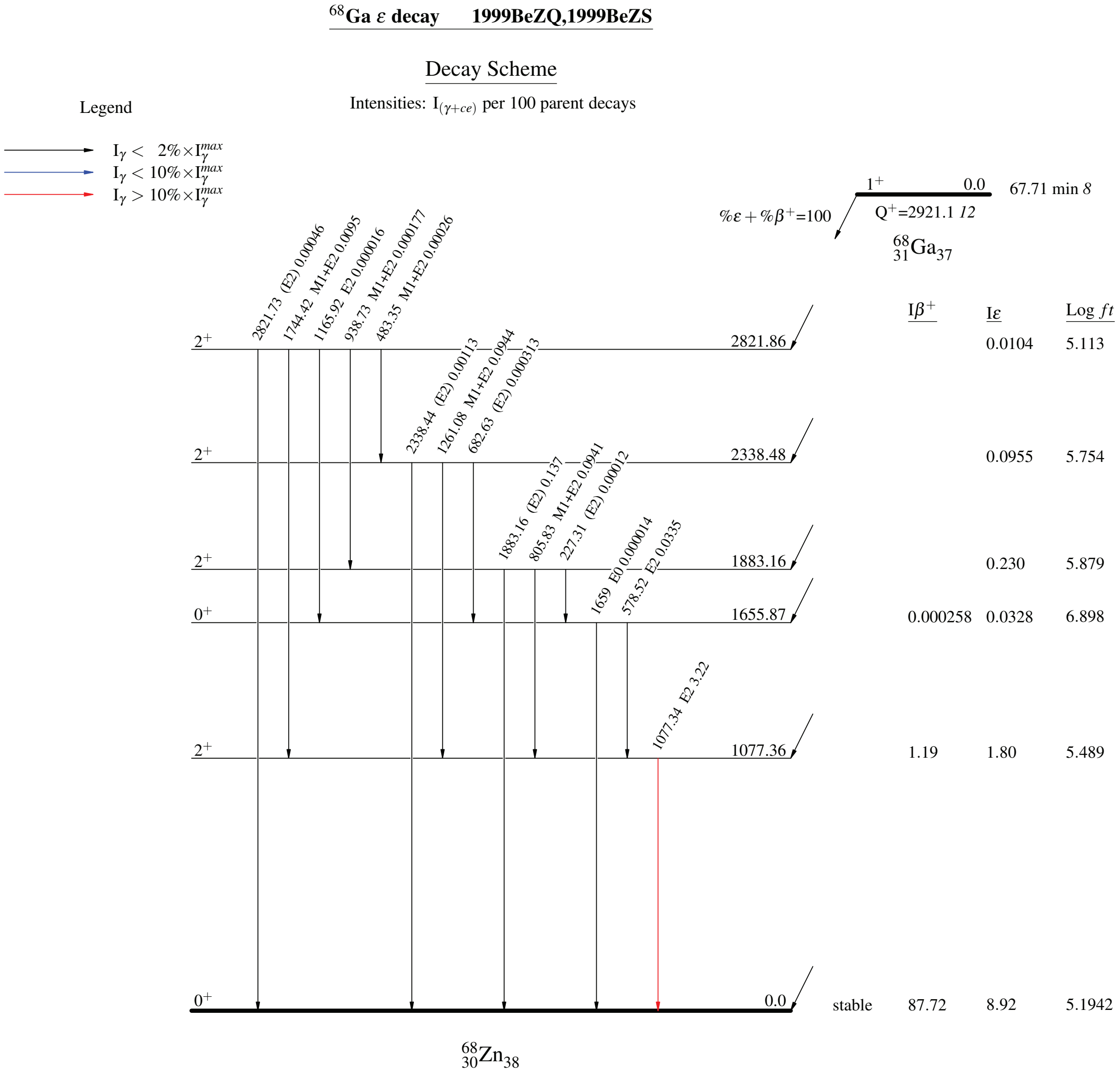

(b) Level diagram of ^{68}Ga [165].

Figure C.3: Level diagram related to ^{68}Ge

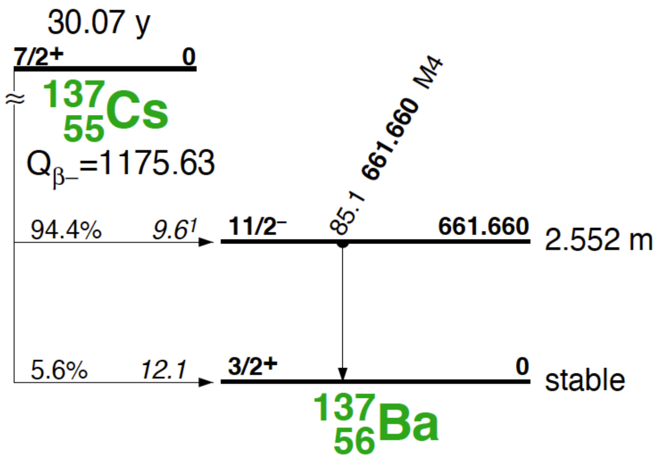

Figure C.4: Level diagram of ^{137}Cs [164].

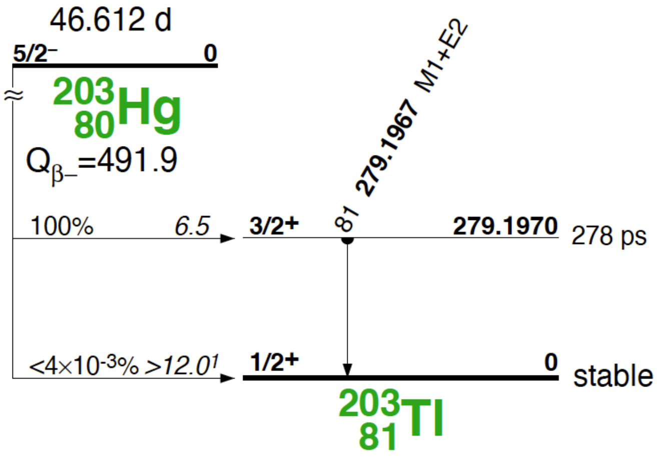

Figure C.5: Level diagram of ^{203}Hg [164].

Appendix D

Details of KamLAND Geant4

D.1 Modification of QGSP_BIC_HP

A code in the Geant4 “HadronPhysicsQGSP_BIC_HP” plays a role in registering the hadronic interaction model of the QGSP_BIC_HP. We found and fixed a bug in the model configuration in the source code.

In the proper configuration, the BIC model that gives a better description of the low-energy region should be registered below 1.2 GeV for mesons and 10 GeV for nucleons, as shown in the left side of Fig. D.1. This configuration is correctly implemented for nucleons, but the BIC is not registered for mesons, as shown in the right side of Fig. D.1. As a result, the LEP model complementing the QGS and BIC models was used instead. We modified this code to register the BIC model for pions below 1.2 GeV. We made no changes to kaon because the BIC model was not implemented. This modification changes π elastic scattering and slightly improves the consistency with KamLAND atmospheric neutrino data in the CC/NC RES region where secondary interaction of π produced by RES interaction plays an important role. [1]

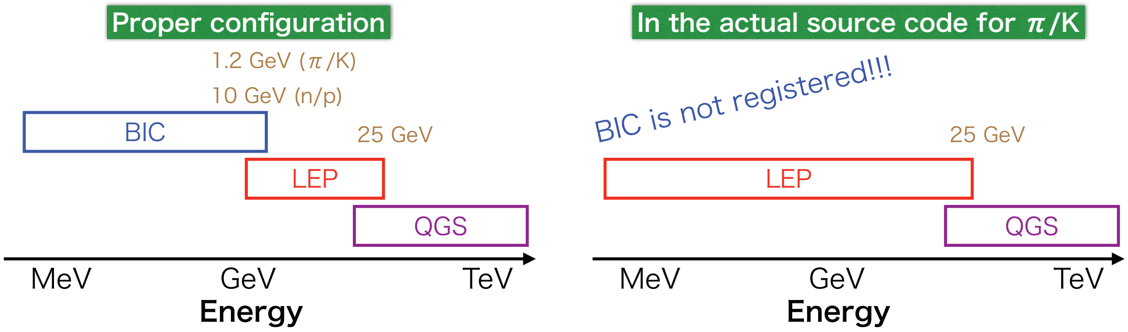

Figure D.1: Proper configuration (left) and the actual implementation (right) of hadronic models in the HadronPhysicsQGSP_BIC_HP. In the proper configuration, the BIC model should be registered below 1.2 GeV for mesons and 10 GeV for nucleons. However, the BIC is not registered for mesons in the actual implementation.

---

[1] In another package, “HadronPhysicsQGS_BIC”, the BIC was correctly adopted below 1.2 GeV for pions. The BIC is a relatively new model, while the LEP has been used for a long time. We assume that the update of HadronPhysicsQGSP_BIC_HP was forgotten when implementing the BIC model.

D.2 Geometry of KamLAND Geant4

For ID, there are several volumes with complex structures, especially on the outside, such as outer balloon supporting straps and acrylic plates. Fig. D.3 shows a side view of support frame of acrylic plate , and Fig. D.4 shows a side view of support straps of the outer balloon. These objects are important for reproducibility in the outer region. The support straps of the outer balloon are particularly important in energy reproducibility in the top and bottom regions because of the shadow effect (Sec. 7.6.1). Both complex volumes are faithfully reproduced.

Fig. D.5 and D.6 show the side and top views of OD geometry. Since the OD refurbishment changed the PMTs arrangement, we prepared two geometries before and after the OD refurbishment. Fig. D.7 shows the side view of 8-inch and 5-inch PMTs in the chimney. These PMTs are newly implemented on the KLG4 in this study.

Fig. D.8 shows the side view of the mini-balloon for KamLAND-Zen 400.

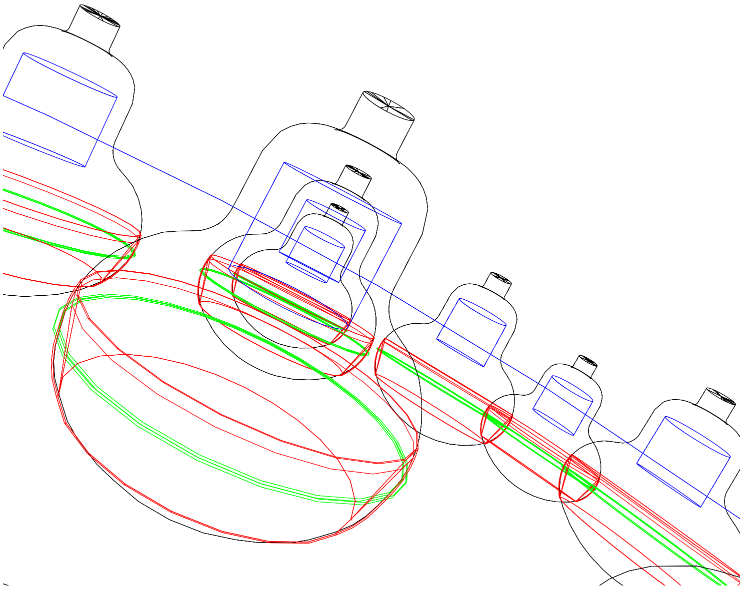

Figure D.2: Geometry of 17-inch PMTs in KamLAND Geant4. The black lines show the PMT glass surfaces, the red lines represent the masks that cover the outer region of 17-inch PMTs, and the green lines show belts to hold the masks.

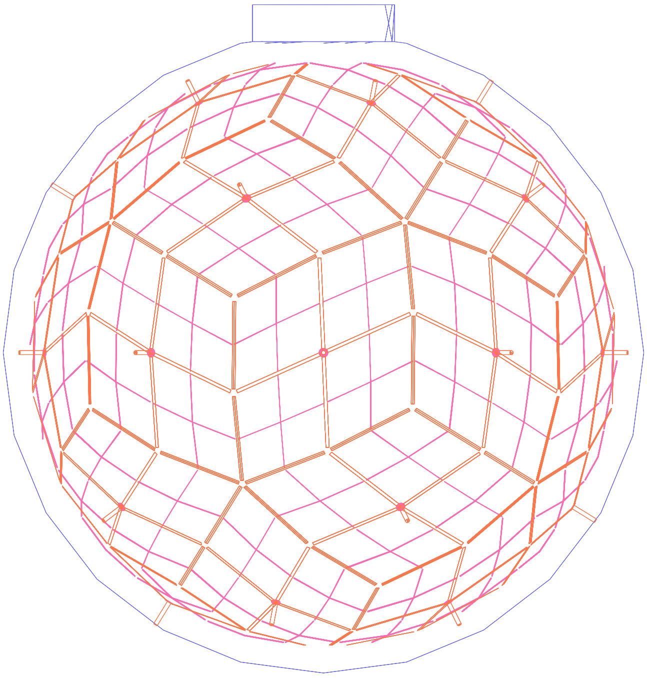

Figure D.3: Side view of the support frame of the acrylic plate. The blue line shows the stainless tank, and the red lines show the support frame of the acrylic plate. The frame divides the PMT surface space into diamond-shaped sections.

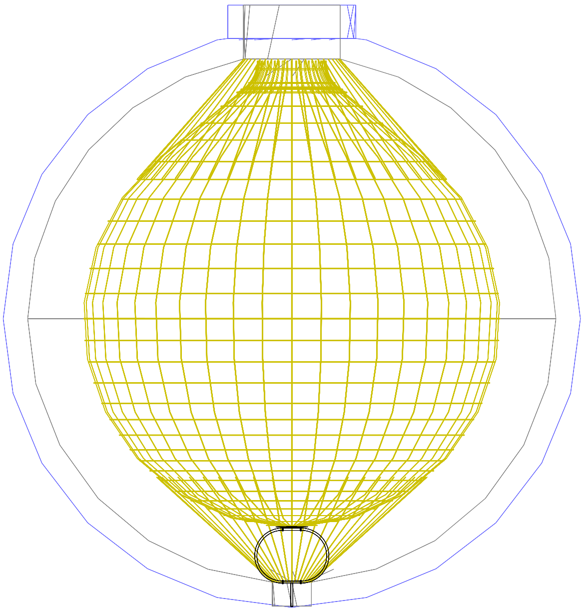

Figure D.4: Side view of support straps of the outer balloon. The blue line shows the stainless tank, and the gray line shows the acrylic plate. The yellow lines show the kevlar ropes that suspend the outer balloon.

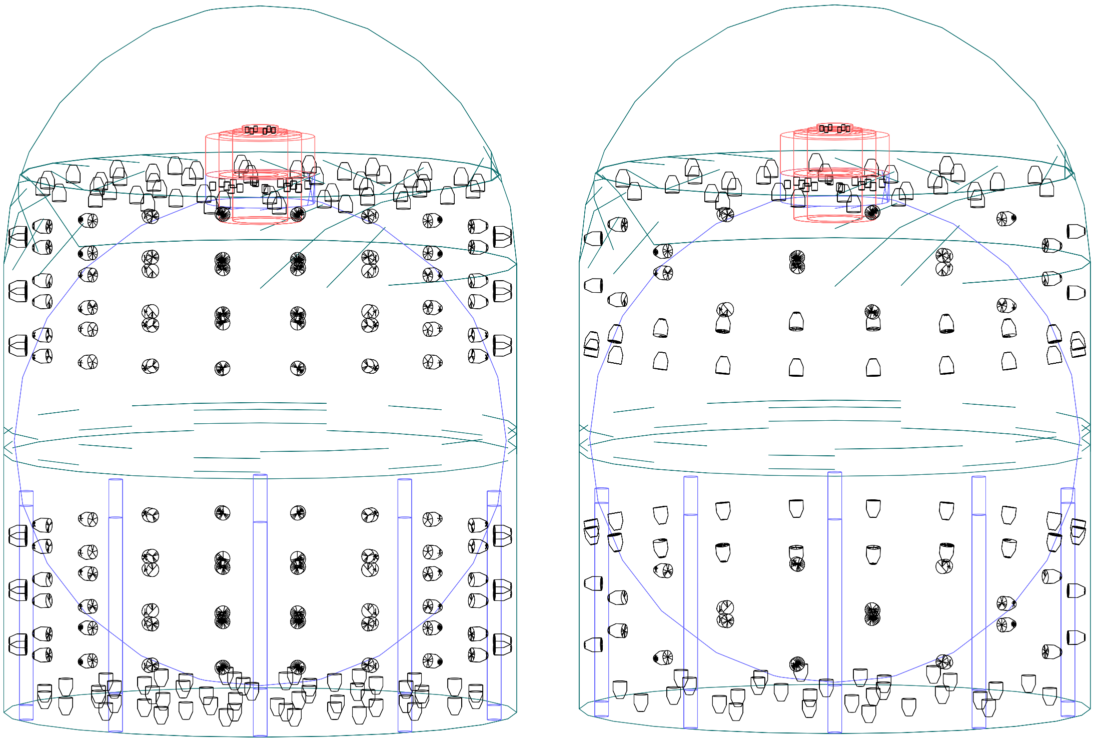

(a) Before OD refurbishment (b) After OD refurbishment

Figure D.5: Side view of OD geometry (a) before (b) after OD refurbishment. The black lines denote OD 20-inch, 8-inch, and 5-inch PMTs. The blue lines show the stainless tank and pillars. The red lines represent the chimney.

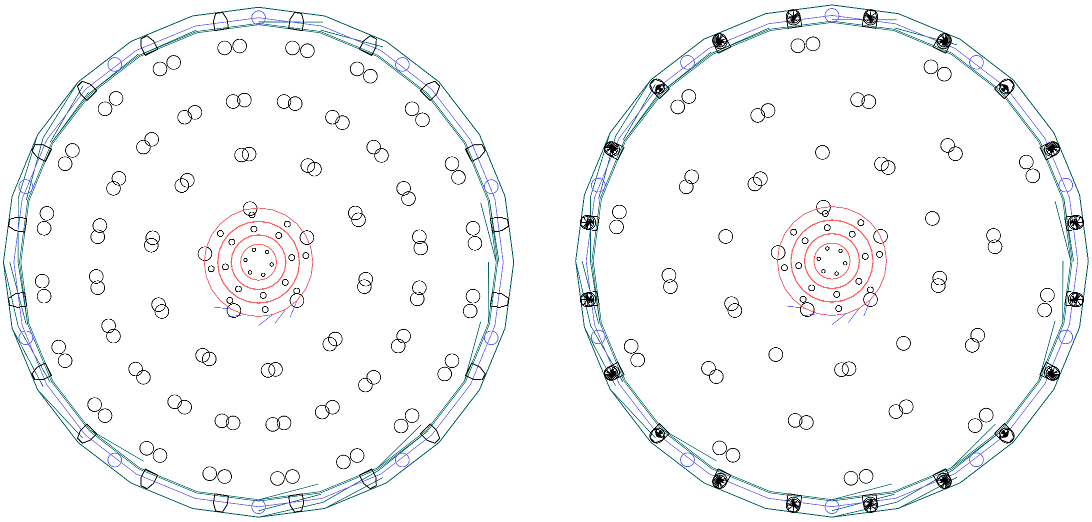

(a) Before OD refurbishment (b) After OD refurbishment

Figure D.6: Top view of OD geometry (a) before (b) after OD refurbishment. The black lines denote OD 20-inch, 8-inch, and 5-inch PMTs. The blue lines show the stainless tank and pillars. The red lines represent the chimney.

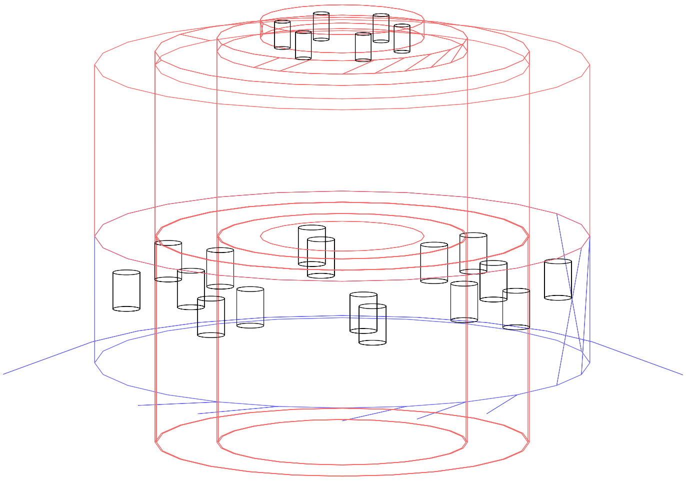

Figure D.7: Side view of 8-inch and 5-inch PMTs. The blue lines denote the stainless tank, and the orange lines represents complex geometry of the chimney. The black lines at the top show the six 5-inch PMTs facing down, and thoes of bottom show the sixteen 8-inch PMTs facing up.

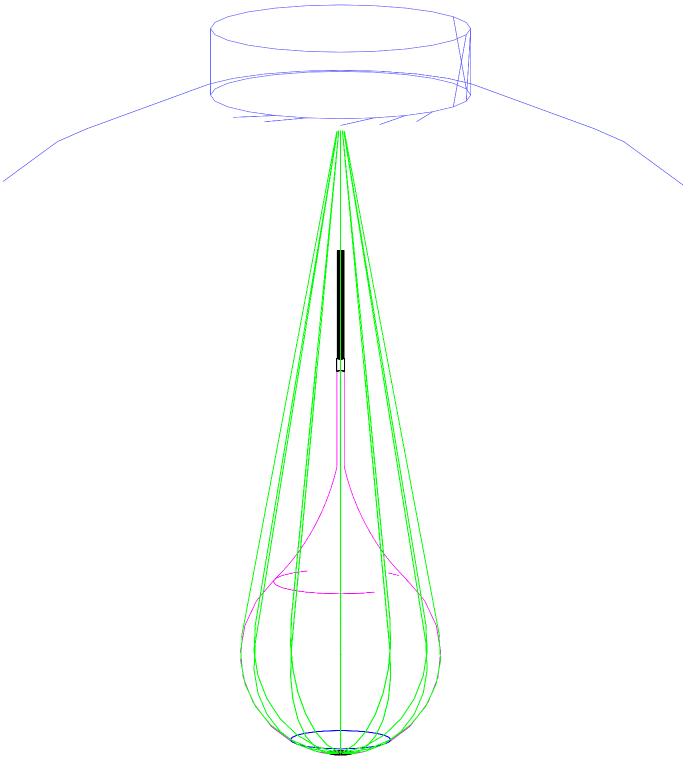

Figure D.8: Side view of the mini-balloon and straps for the KamLAND-Zen 400. The magent line denot the mini-balloon surface, the green lines represent the straps, the black shaded region represent the corrugated tube, and the blue line represents the sphere strainless tank.

D.3 Tuning of Optical Parameters and Detector Responses

The results of tuning for the KLG4 I−III are shown in the following sections. See Sec. 8.4 for the KLG4 period IV. The quality is almost equivalent for all periods. As for the radioactive source calibration, the peaks of hit, charge, aner energy agree within 3.5% (4.0%) for 17-inch PMTs only (with 20-inch PMTs), and the vertex deviation is less than 2.5 cm.

D.3.1 KLG4 Period I

The KLG4 period I corresponds to the period from the beggining of KamLAND to just before the start of the purification. We perform tuning using the radioactive source in 2006, which is obtained with ^{137}Cs and the composite source of ^{68}Ge and ^{60}Co. Fig. D.9 shows the vertex deviation. Fig. D.10 and D.11 show the hit, charge, and energy distributions of ^{137}Cs and the composite source of ^{68}Ge and ^{60}Co, respectively. Fig. D.12 shows the deviations of the peak positions.

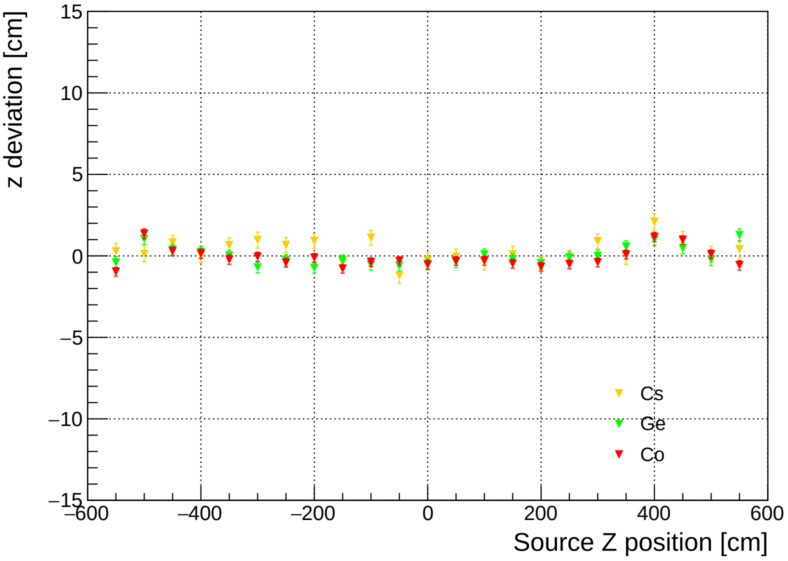

Figure D.9: Vertex deviation between reconstructed z and source z position in the KLG4 period I.

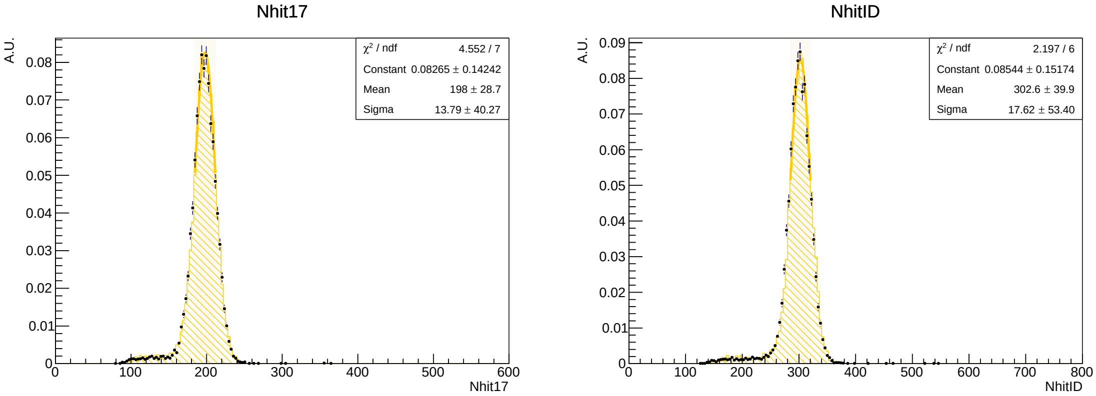

(a) The number of hit 17-inch PMTs (Nhit17)

(b) The number of hit ID PMTs (NhitID)

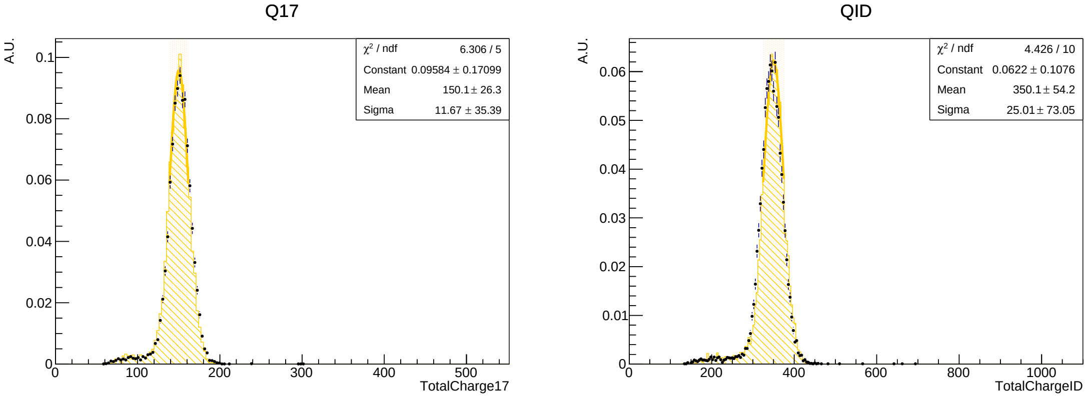

(c) Total charge of 17-inch PMTs (TotalCharge17)

(d) Total charge of ID PMTs (TotalChargeID)

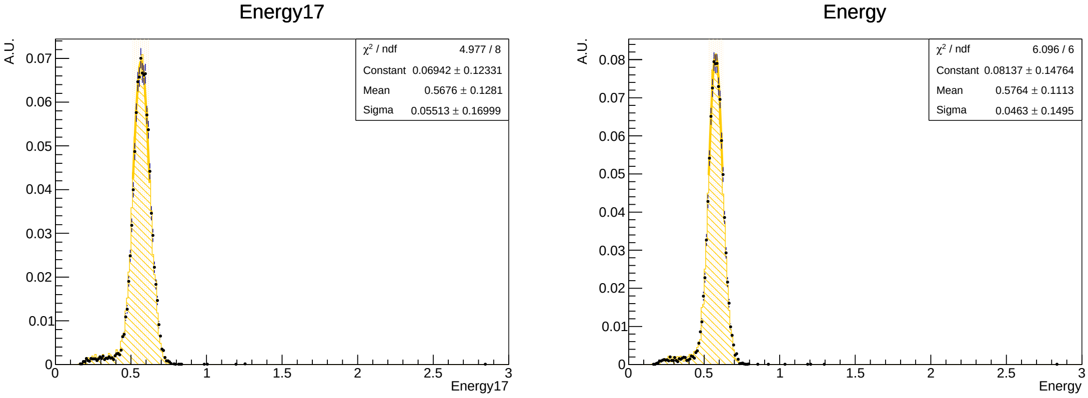

(e) Reconstructed Energy of 17-inch PMTs (Energy17)

(f) Reconstructed Energy of ID PMTs (Energy)

Figure D.10: Distributions of the number of hit PMTs, total charge, and reconstructed energy of ^{137}Cs source at the center of KamLAND. The data for the KLG4 period I is shown.

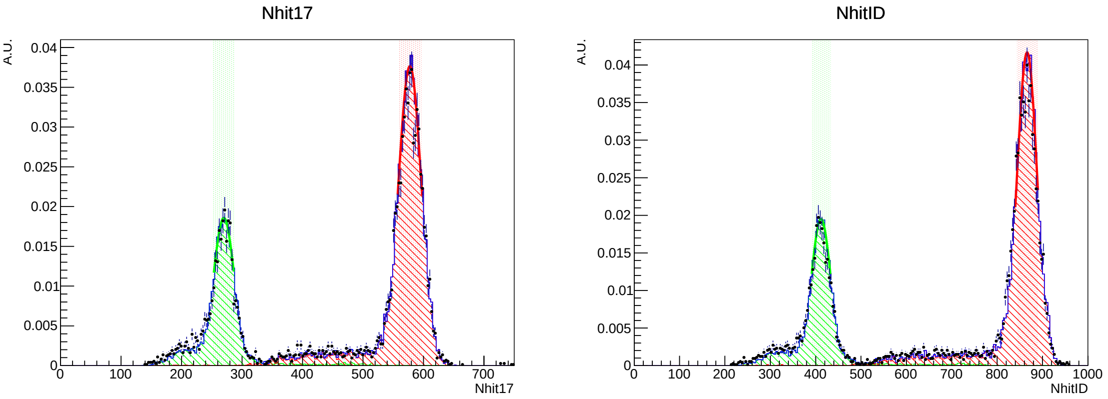

(a) The number of hit 17-inch PMTs (Nhit17)

(b) The number of hit ID PMTs (NhitID)

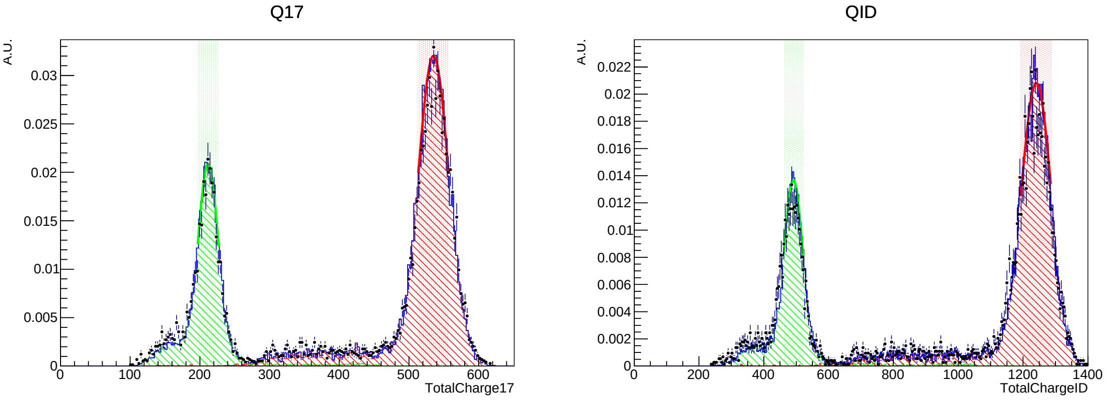

(c) Total charge of 17-inch PMTs (TotalCharge17)

(d) Total charge of ID PMTs (TotalChargeID)

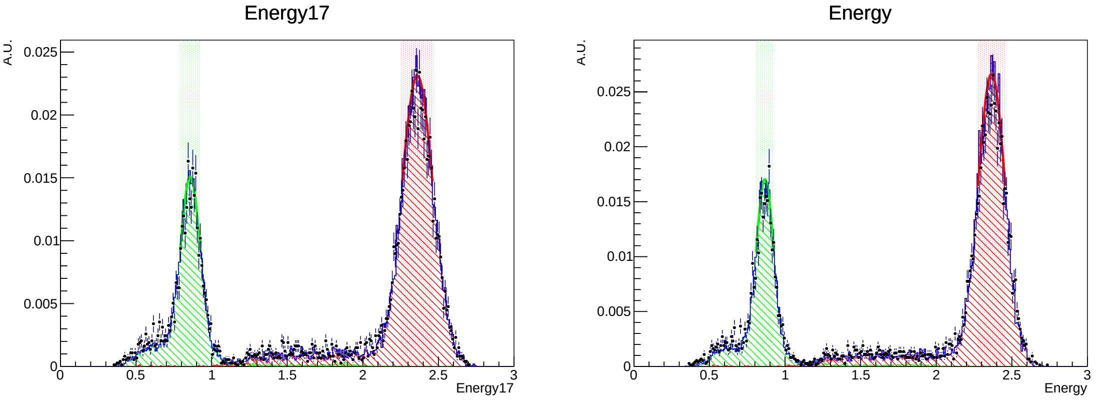

(e) Reconstructed Energy of 17-inch PMTs (Energy17)

(f) Reconstructed Energy of ID PMTs (Energy)

Figure D.11: Distributions of the number of hit PMTs, total charge, and reconstructed energy of the composite source (^{68}Ge and ^{60}Co) at the center of KamLAND. The data for the KLG4 period I is shown.

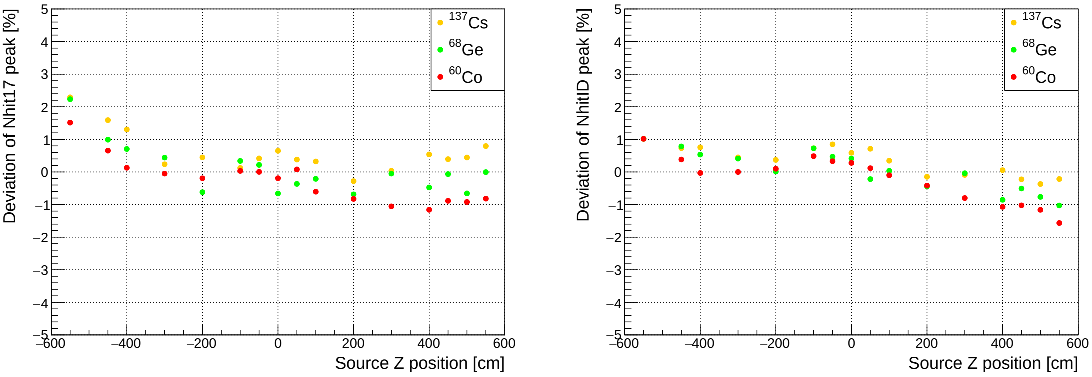

(a) The number of hit 17-inch PMTs (Nhit17) (b) The number of hit ID PMTs (NhitID)

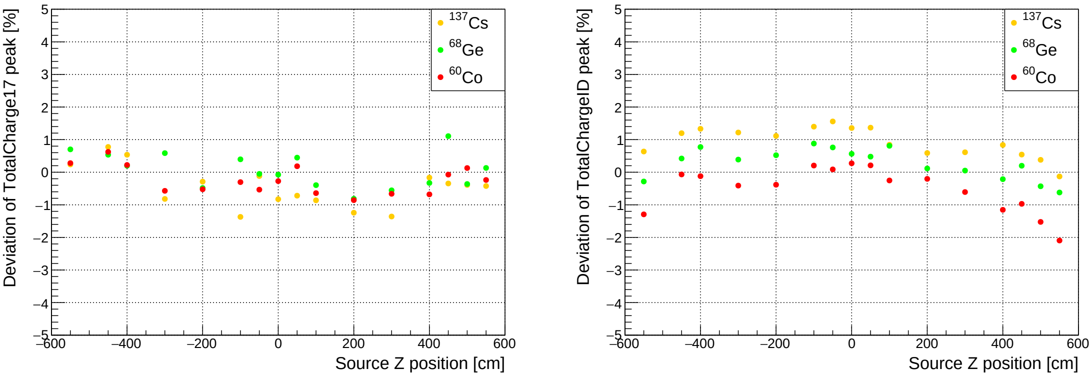

(c) Total charge of 17-inch PMTs (TotalCharge17)

(d) Total charge of ID PMTs (TotalChargeID)

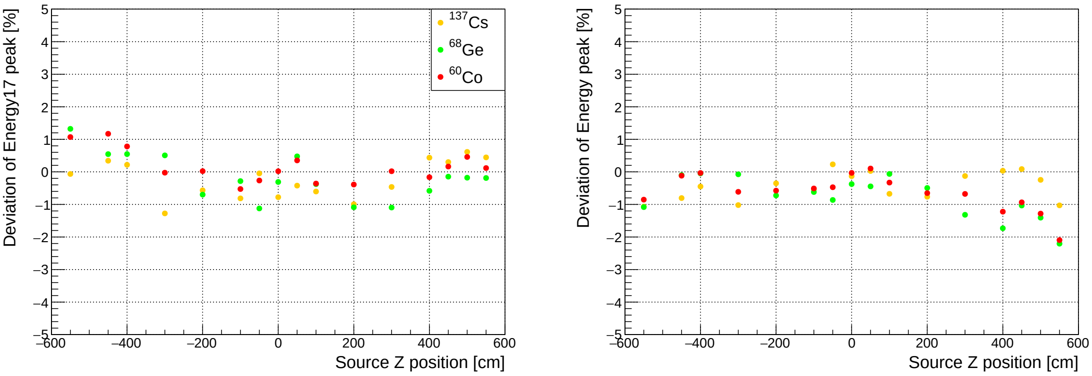

(e) Reconstructed Energy of 17-inch PMTs (Energy17)

(f) Reconstructed Energy of ID PMTs (Energy)

Figure D.12: Deviations of the peak positions in the hits, charge, and energy distributions at various z positions. The data for the KLG4 period I is shown.

D.3.2 KLG4 Period II

The KLG4 period II corresponds to the period from the end of purification to just before the start of KamLAND-Zen 400. We perform tuning using the radioactive source in 2011, which is obtained with ^{137}Cs and the composite source of ^{68}Ge and ^{60}Co. Fig. D.13 shows the vertex deviation. Since the intensity of ^{68}Ge was too weak in 2009, we do not use the calibration data acquired in 2009. Fig. D.14 and D.15 show the hit, charge, and energy distributions of ^{137}Cs and the composite source of ^{68}Ge and ^{60}Co, respectively. Fig. D.16 shows the deviations of the peak positions.

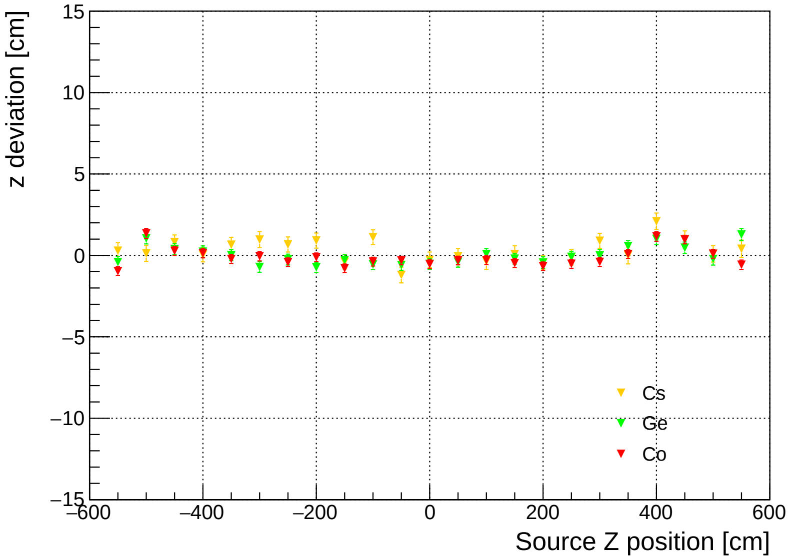

Figure D.13: Vertex deviation between reconstructed z and source z position in the KLG4 period II.

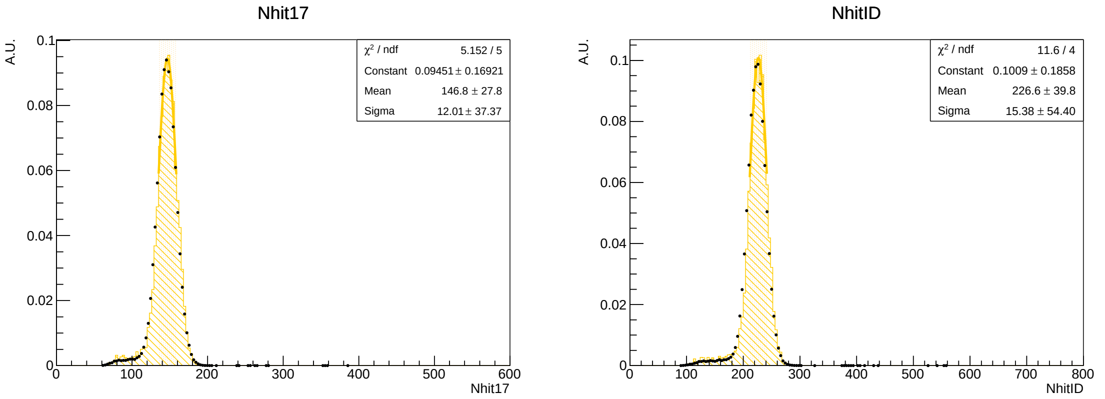

(a) The number of hit 17-inch PMTs (Nhit17)

(b) The number of hit ID PMTs (NhitID)

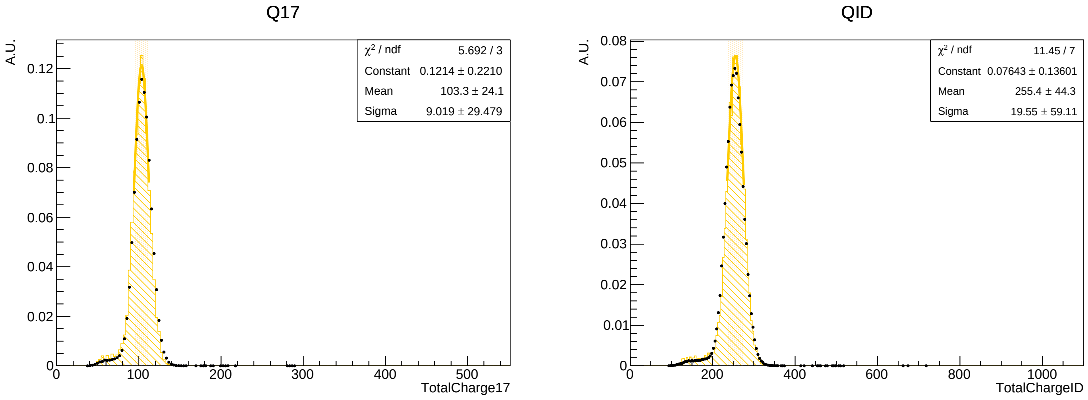

(c) Total charge of 17-inch PMTs (TotalCharge17)

(d) Total charge of ID PMTs (TotalChargeID)

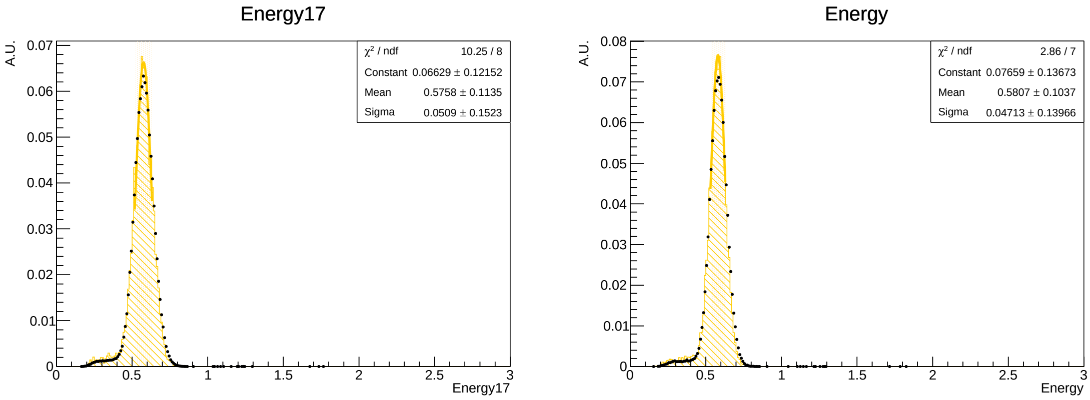

(e) Reconstructed Energy of 17-inch PMTs (Energy17)

(f) Reconstructed Energy of ID PMTs (Energy)

Figure D.14: Distributions of the number of hit PMTs, total charge, and reconstructed energy of ^{137}Cs source at the center of KamLAND. The data for the KLG4 period II is shown.

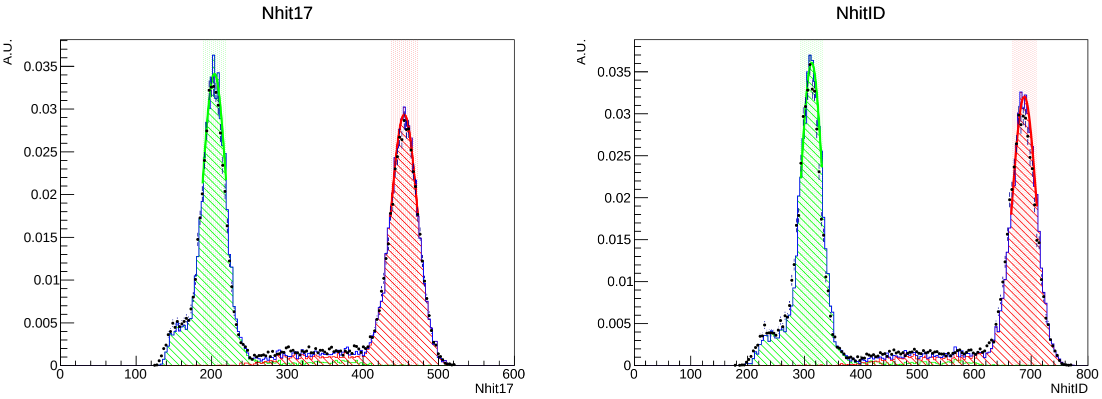

(a) The number of hit 17-inch PMTs (Nhit17)

(b) The number of hit ID PMTs (NhitID)

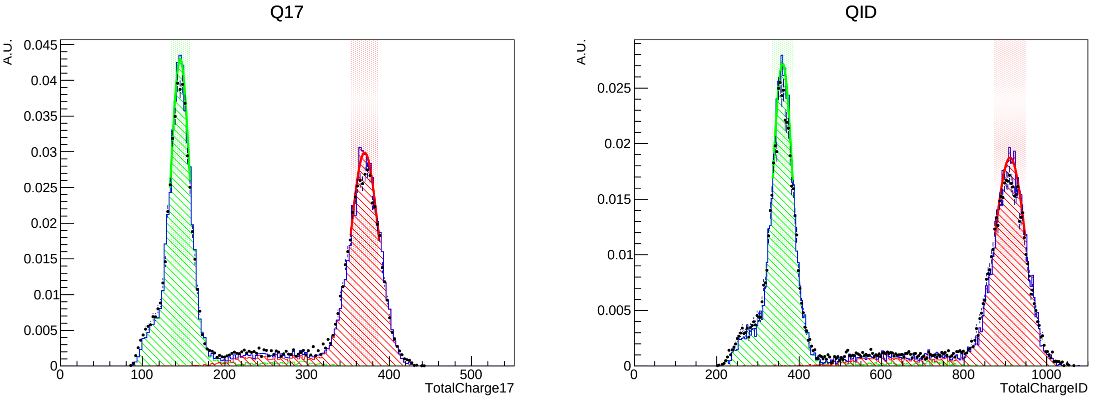

(c) Total charge of 17-inch PMTs (TotalCharge17)

(d) Total charge of ID PMTs (TotalChargeID)

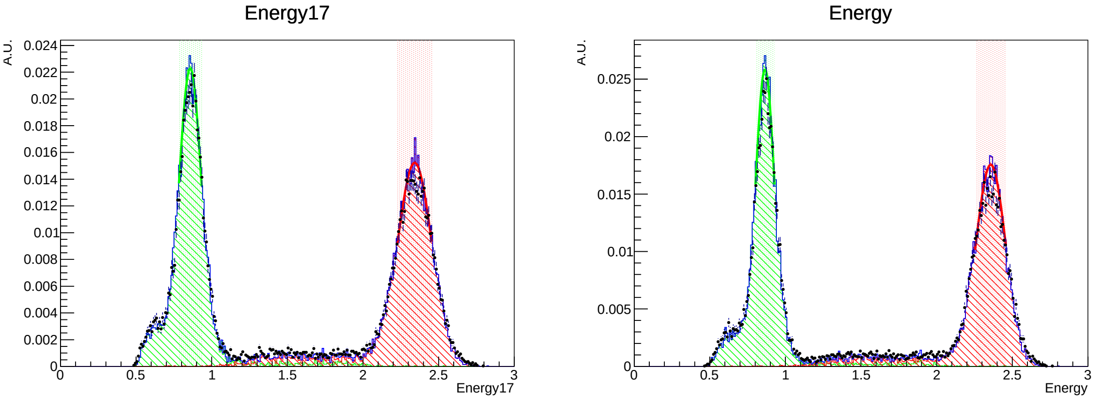

(e) Reconstructed Energy of 17-inch PMTs (Energy17)

(f) Reconstructed Energy of ID PMTs (Energy)

Figure D.15: Distributions of the number of hit PMTs, total charge, and reconstructed energy of the composite source (^{68}Ge and ^{60}Co) at the center of KamLAND. The data for the KLG4 period II is shown.

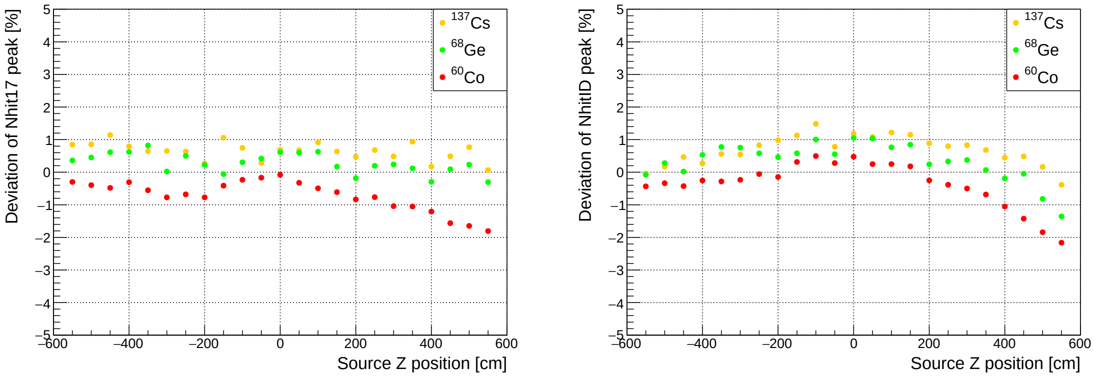

(a) The number of hit 17-inch PMTs (Nhit17) (b) The number of hit ID PMTs (NhitID)

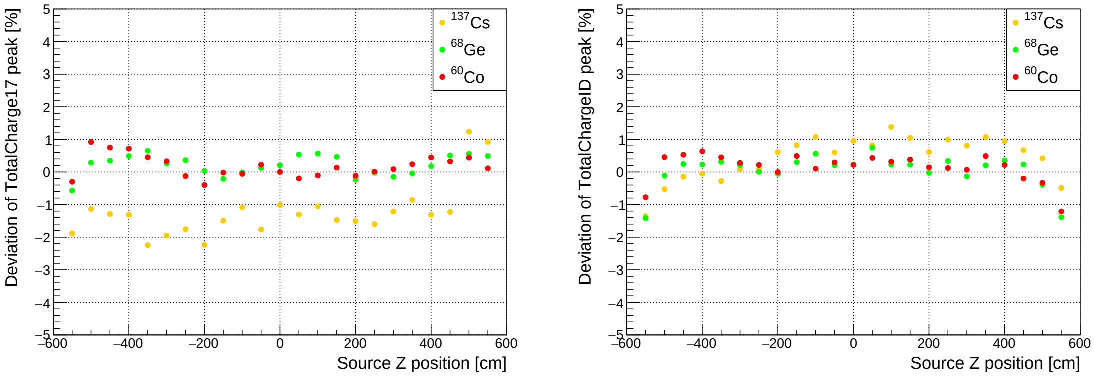

(c) Total charge of 17-inch PMTs (TotalCharge17)

(d) Total charge of ID PMTs (TotalChargeID)

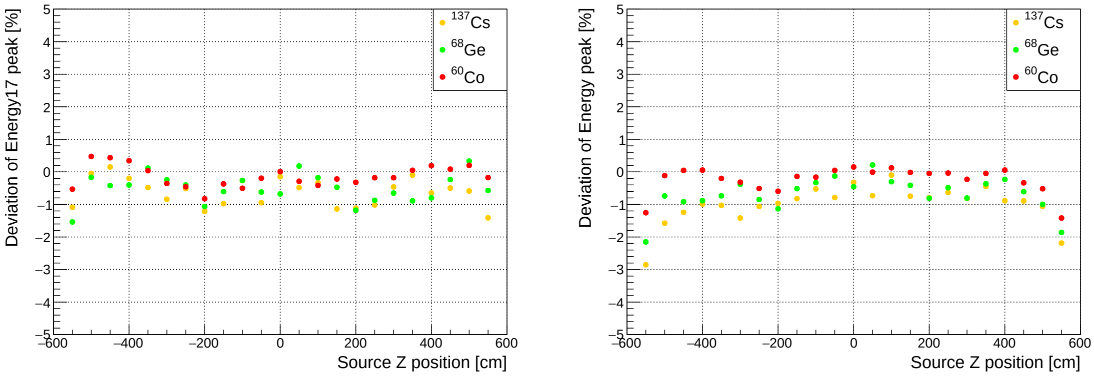

(e) Reconstructed Energy of 17-inch PMTs (Energy17)

(f) Reconstructed Energy of ID PMTs (Energy)

Figure D.16: Deviations of the peak positions in the hits, charge, and energy distributions at various z positions. The data for the KLG4 period II is shown.

D.3.3 KLG4 Period III

The KLG4 period III corresponds to the period from during the KamLAND-Zen400. We perform tuning using the radioactive source in 2015, which is obtained with the composite source of ^{136}Cs, ^{68}Ge, and ^{60}Co. In this calibration campaign, we installed the composite source into the inside of the MIB. We set exactly the smae ptical parameters of the KamLS and BO as those in KLG4 period II, and only the parameters related to XeLS and MIB are tuned here. Fig. D.17 shows the vertex deviation. Fig. D.18 shows the hit, charge, and energy distributions of the composite source of ^{137}Cs, ^{68}Ge, and ^{60}Co, respectively. Fig. D.19 shows the deviations of the peak positions.

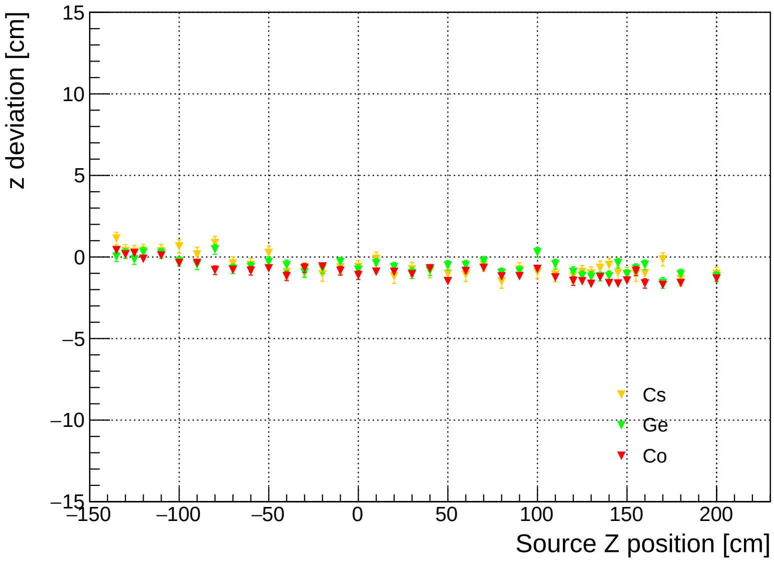

Figure D.17: Vertex deviation between reconstructed z and source z position in the KLG4 period III.

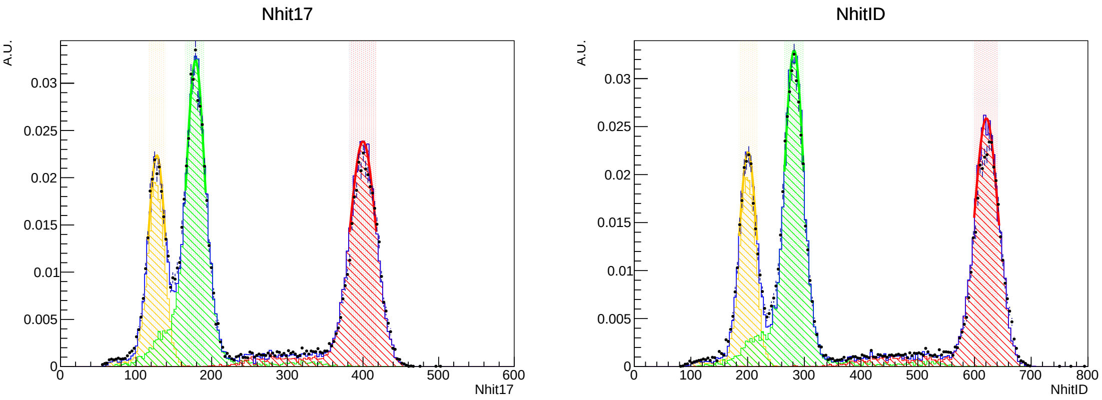

(a) The number of hit 17-inch PMTs (Nhit17)
(b) The number of hit ID PMTs (NhitID)

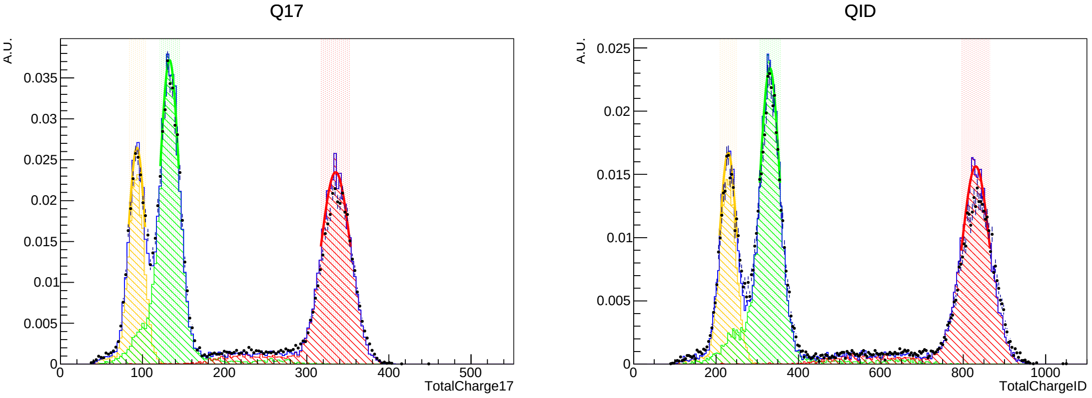

(c) Total charge of 17-inch PMTs (TotalCharge17)
(d) Total charge of ID PMTs (TotalChargeID)

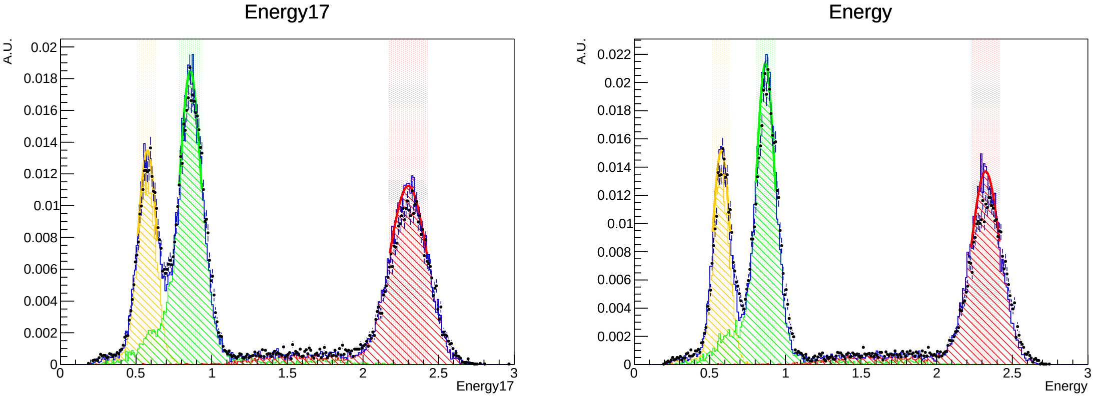

(e) Reconstructed Energy of 17-inch PMTs (Energy17)
(f) Reconstructed Energy of ID PMTs (Energy)

Figure D.18: Distributions of the number of hit PMTs, total charge, and reconstructed energy of the composite source (^{137}Cs/^{68}Ge/^{60}Co) at the center of KamLAND. The data for the KLG4 period III is shown.

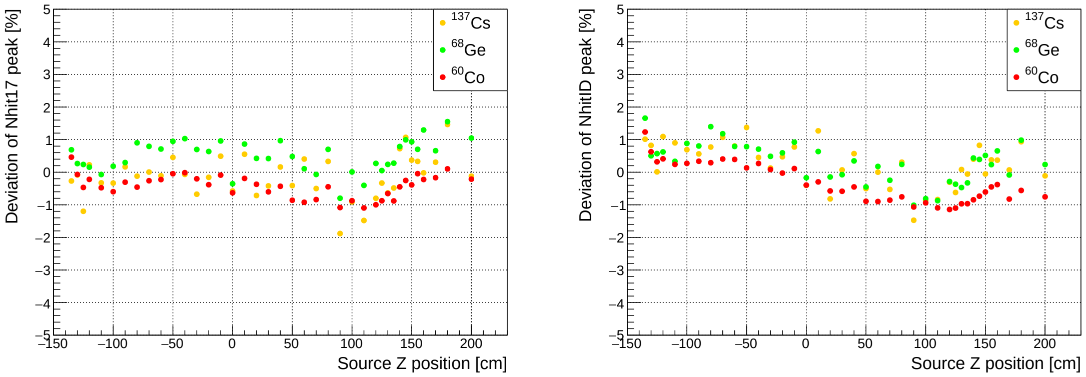

(a) The number of hit 17-inch PMTs (Nhit17) (b) The number of hit ID PMTs (NhitID)

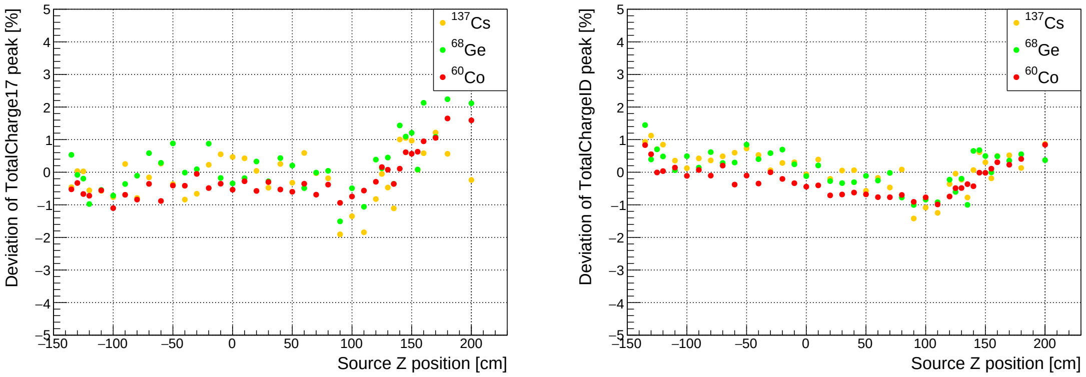

(c) Total charge of 17-inch PMTs (TotalCharge17)

(d) Total charge of ID PMTs (TotalChargeID)

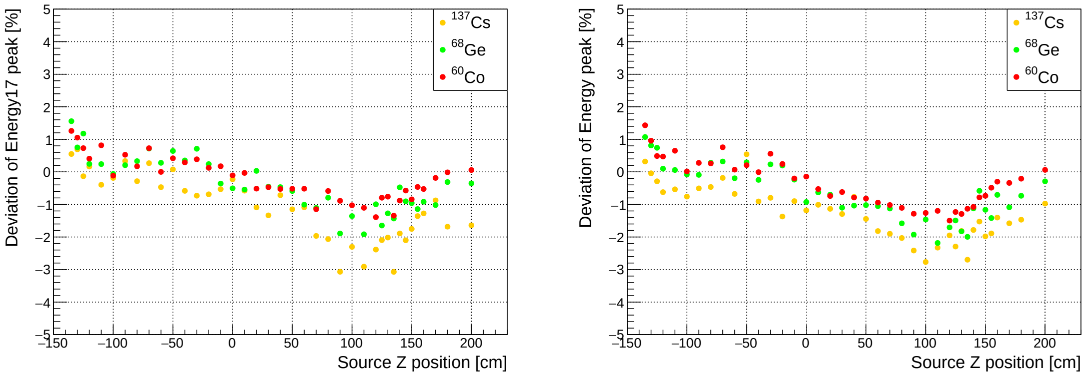

(e) Reconstructed Energy of 17-inch PMTs (Energy17)

(f) Reconstructed Energy of ID PMTs (Energy)

Figure D.19: Deviations of the peak positions in the hits, charge, and energy distributions at various z positions. The data for the KLG4 period III is shown.

Appendix E

Estimation of Neutron Tagging Efficiency using Cosmic Muons

Fig. E.1−E.4 shows the time difference between a cosmic muon event and a neutron capture event for each prompt energy of period I−IV. Fig. E.5 shows the neutron tagging efficiency as a function of prompt (muon) energy for each period up to 3000 MeV.

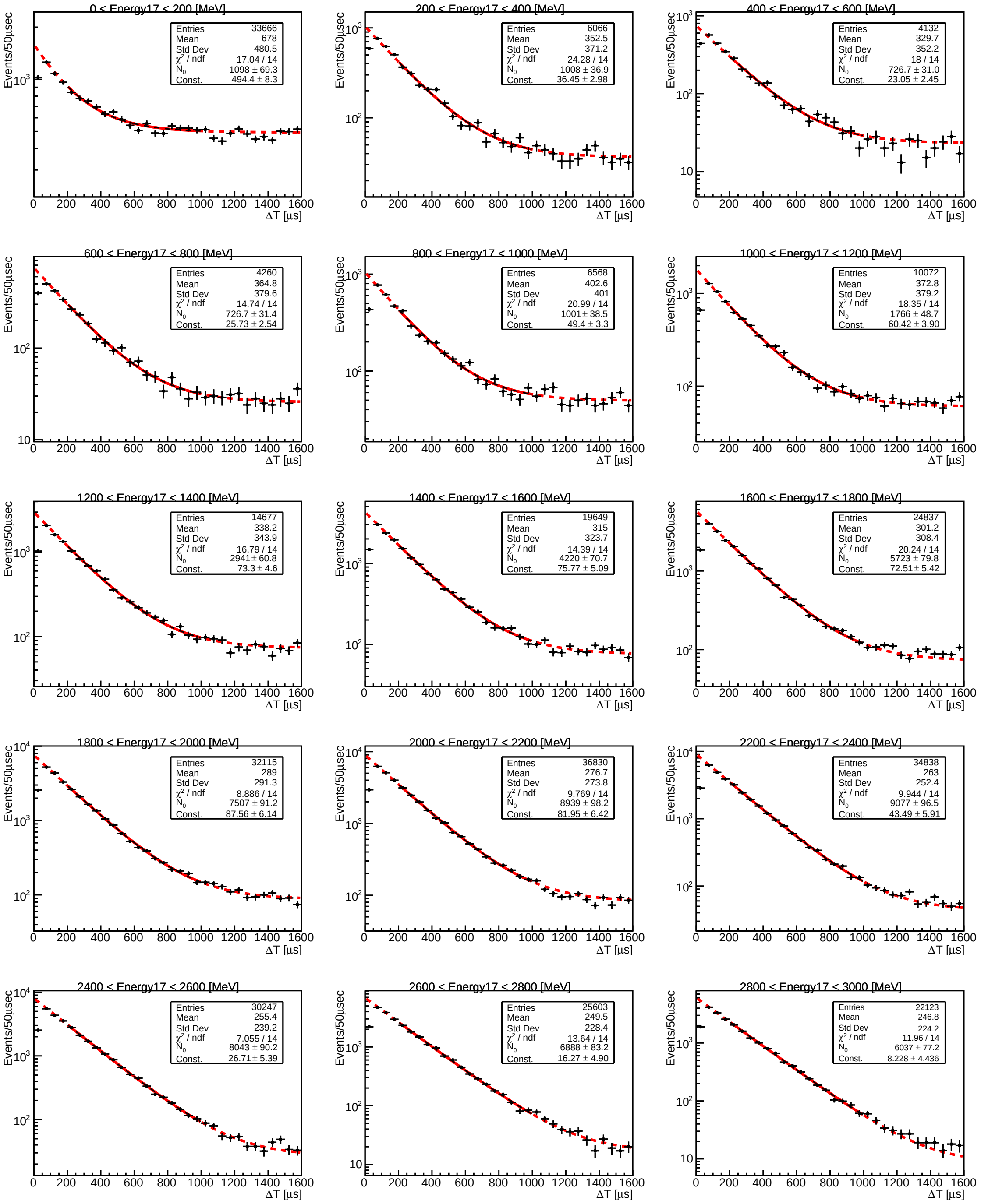

Figure E.1: Time difference between a cosmic muon event and a neutron capture event for each prompt energy bin of Period I

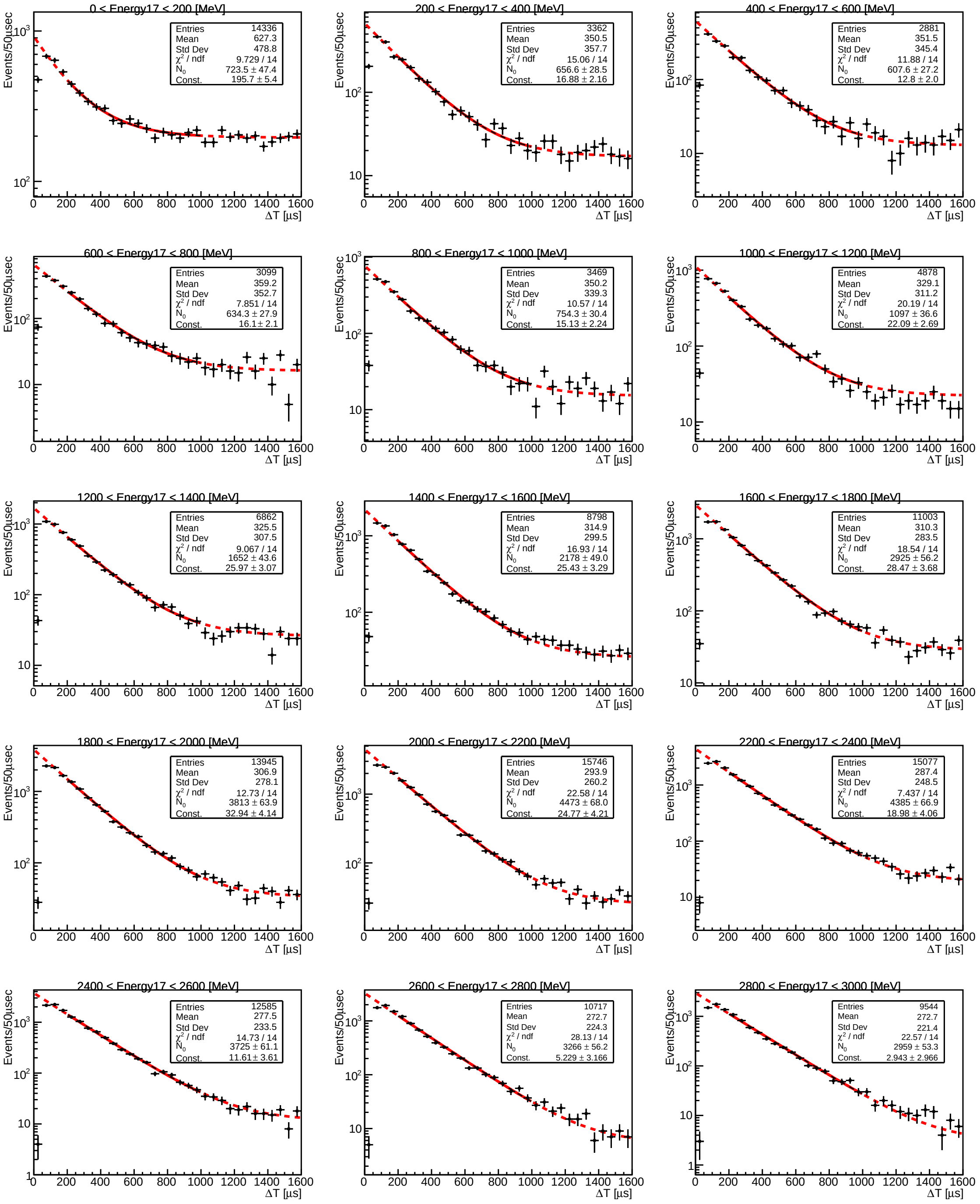

Figure E.2: Time difference between a cosmic muon event and a neutron capture event for each prompt energy bin of Period II

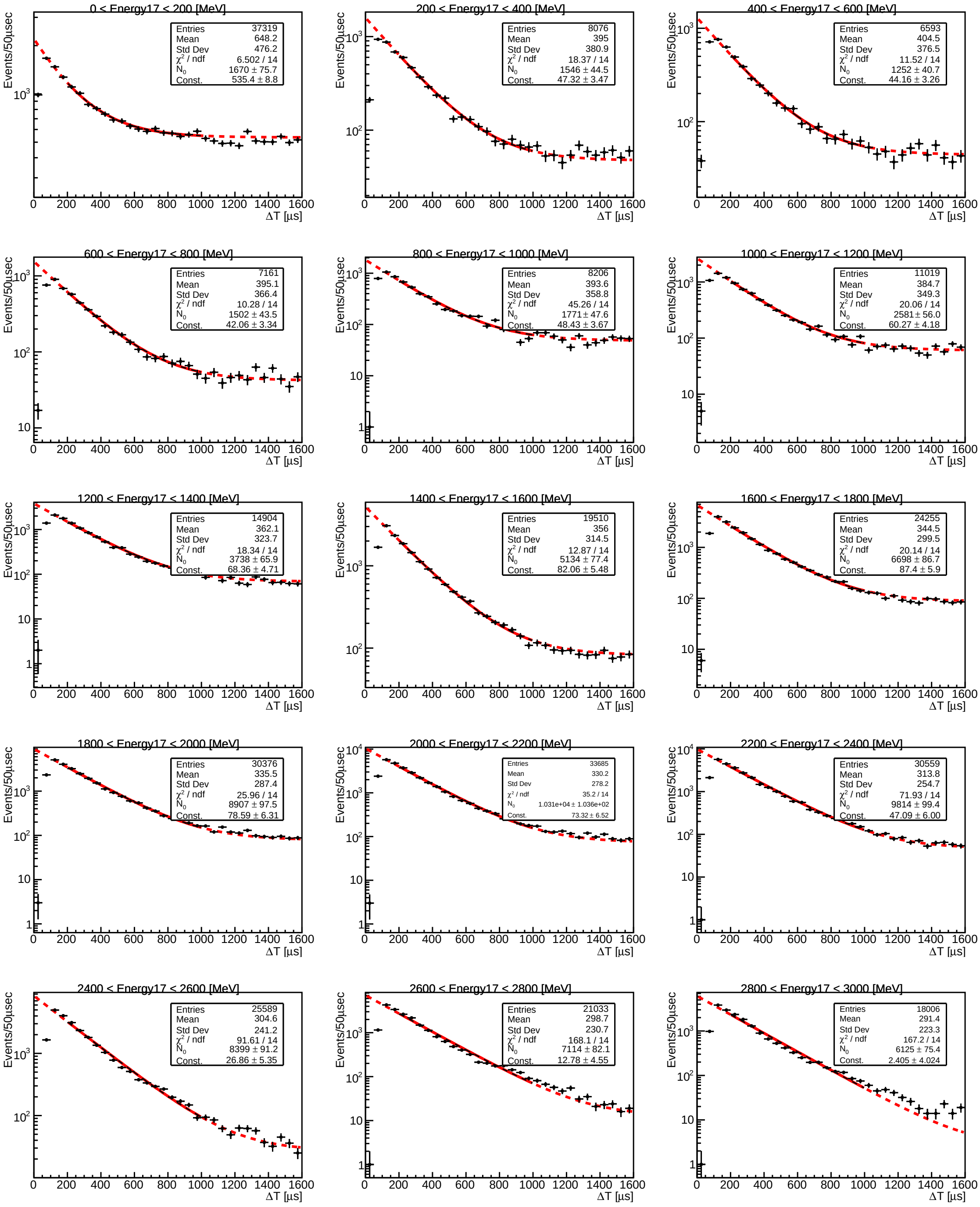

Figure E.3: Time difference between a cosmic muon event and a neutron capture event for each prompt energy bin of Period III

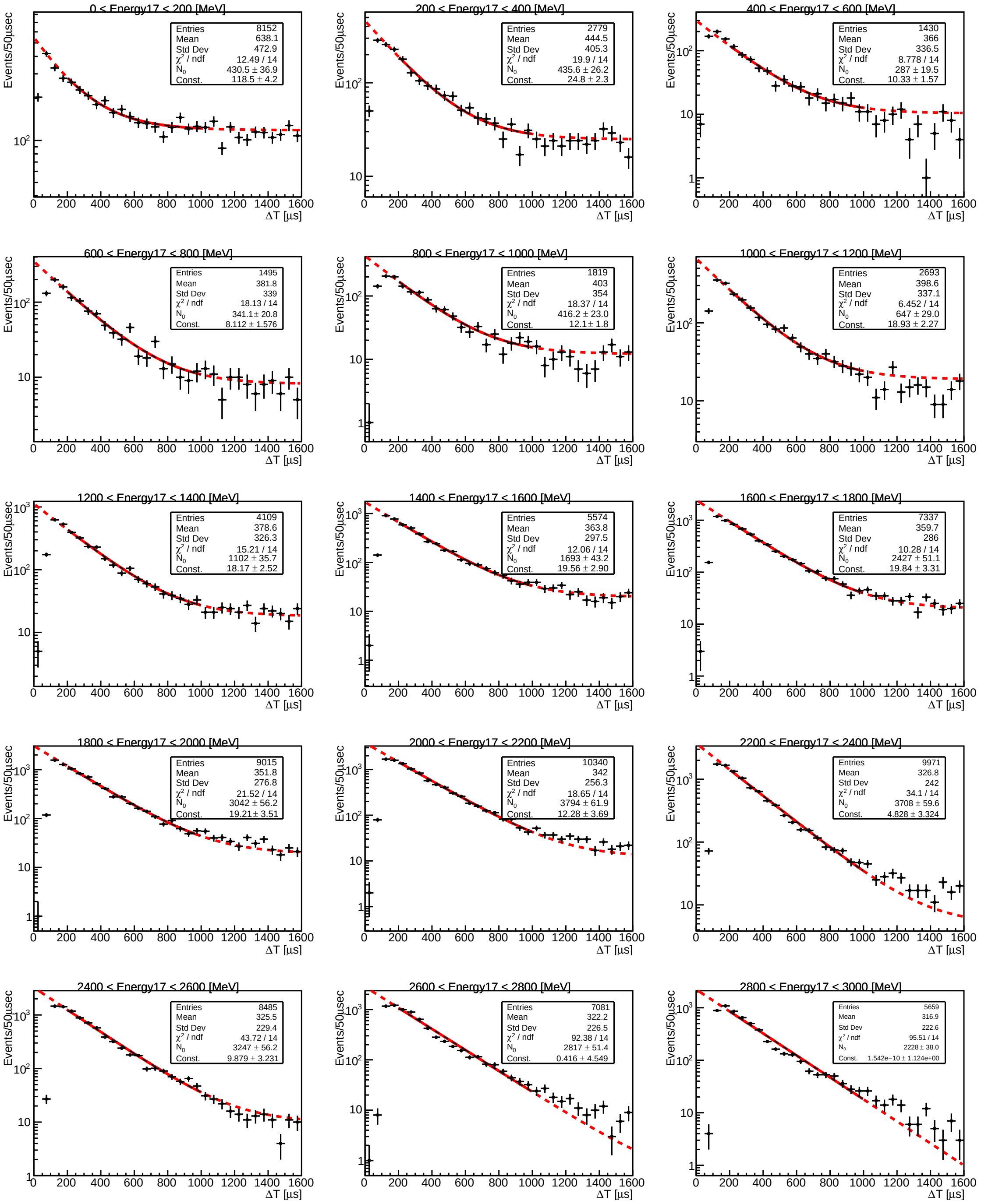

Figure E.4: Time difference between a cosmic muon event and a neutron capture event for each prompt energy bin of Period IV

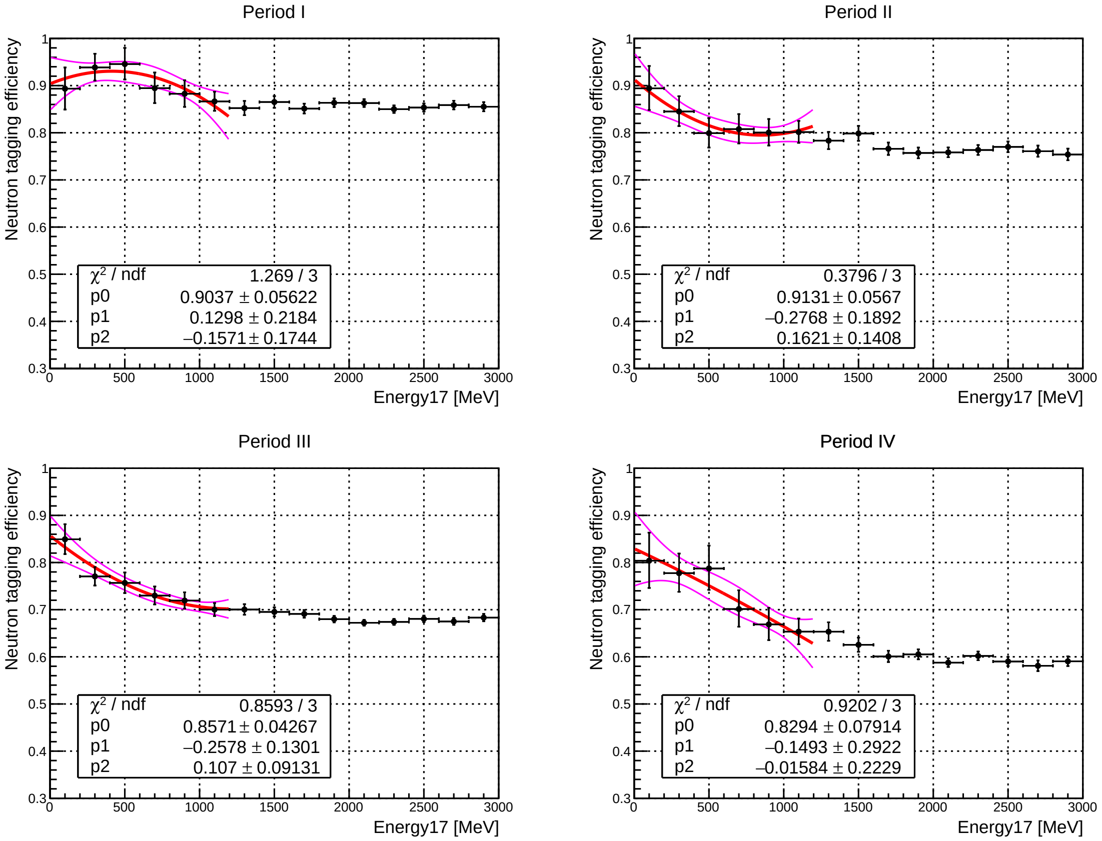

Figure E.5: Neutron tagging efficiency as a function of prompt energy for each period. The red (magenta) lines represent the best-fit (1σ uncertainty) of the parameterization with the second-order polynomial of Eq. 9.9 in the region $0 < E_{\mathrm{prompt}} < 1200\,\mathrm{MeV}$. These figure shows the same data as in Fig. 9.11, but over a wider region up to 3000 MeV.

Appendix F

Supplements for the Spectra Fit

F.1 Neutron multiplicity of NCQE in the low-E selection

Fig. F.1 shows the neutron multiplicity of atmospheric neutrino NCQE events in the low-E selection. The data is the same as Fig. 11.1, but this figure is for NCQE only, showing the distribution for each target. The NCQE cross sections for protons or neutrons are approximately proportional to the squared of the axial form factor (Eq. 2.28). It leads to

$$\text{(proton-target NCQE cross section)} \propto (g_A - g_A^s)^2, \tag{F.1}$$

$$\text{(neutron-target NCQE cross section)} \propto (-g_A - g_A^s)^2, \tag{F.2}$$

$$\tag{F.3}$$

neglecting the Q^2 dependence. If g_A^s is negative, the proton-target NCQE cross section increases, and the neutron-target NCQE cross section decreases. Moreover, the amount of change of the proton-target cross section is greater than that of the neutron-target. This trend leads to the fact that the decreases of the neutron-target NCQE events are almost canceled by the larger increase of the proton-target NCQE events, as shown in Fig. F.1.

F.2 Constrain the Axial Mass using the MiniBooNE Data

A constraint on the axial mass M_A is obtained using the CCQE cross section data published from the MiniBooNE [32]. The cross section data is fitted with the sum of CCQE and CC 2p2h cross sections using NuWro. Here, we assume the TEM for the CC 2p2h model. A normalization uncertainty of 20% for the TEM cross section is considered. Fig. F.2 shows the $\Delta\chi^2$ profile as a function of M_A, and Fig. F.3 shows the best-fit CCQE and CC 2p2h cross sections as a function of neutrino energy. The result $M_A = 1.14 \pm 0.07\,\text{GeV}$ is obtained. This constraint entirely relies on the MiniBooNE's data and TEM.

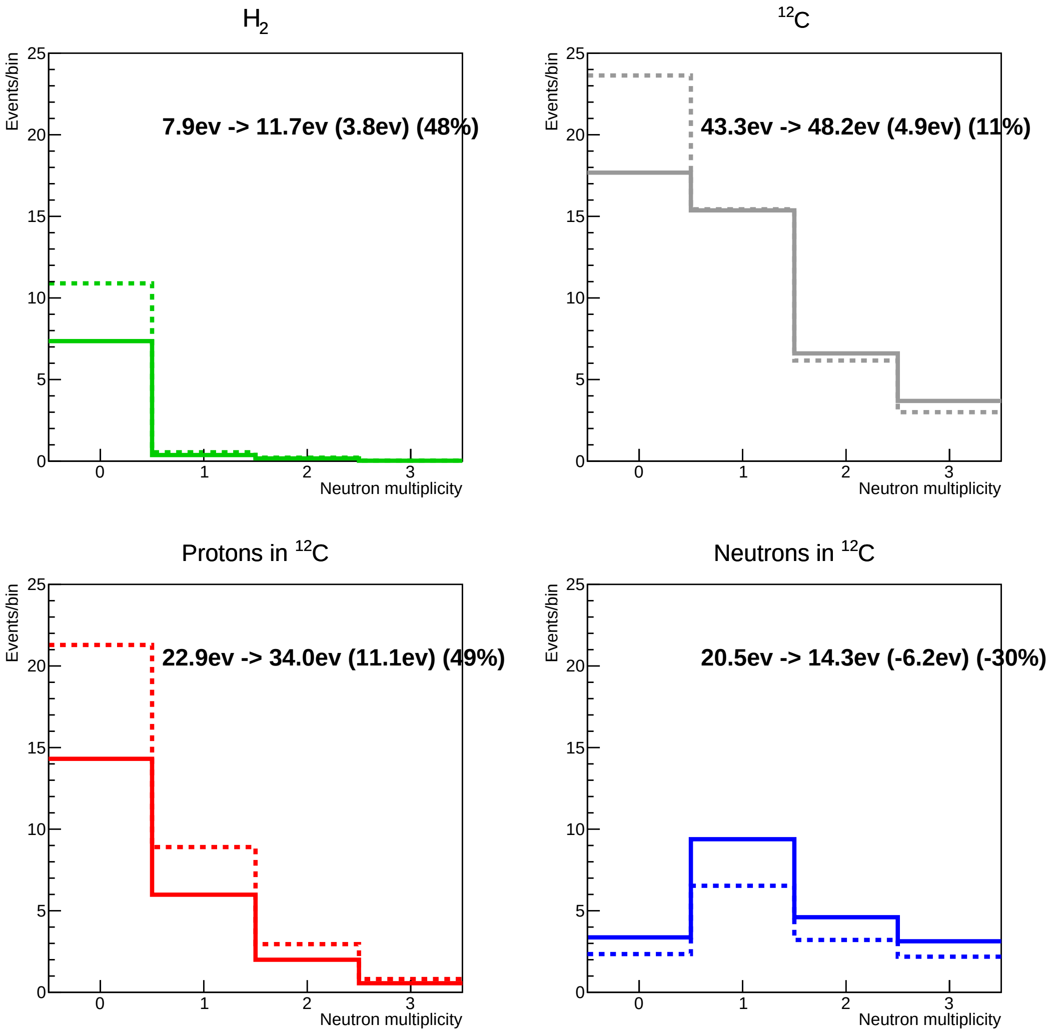

Figure F.1: Neutron multiplicity of atmospheric neutrino NCQE events in the low-E selection. The green (gray) histogram represents those of free proton (^{12}C) targets. The red (blue) histogram denotes those of proton (neutron) targets in ^{12}C. The solid (dashed) lines show the simulation results with $g_A^s = 0$ (-0.30), and the rightmost bin includes overflow. The simulation data are shown prior to the spectral fit, assuming $M_A = 1.2\,\mathrm{GeV}$. As can be seen in the ^{12}C target (gray histograms), the decreases of the neutron-target NCQE events are almost canceled by the larger increase of the proton-target NCQE events.

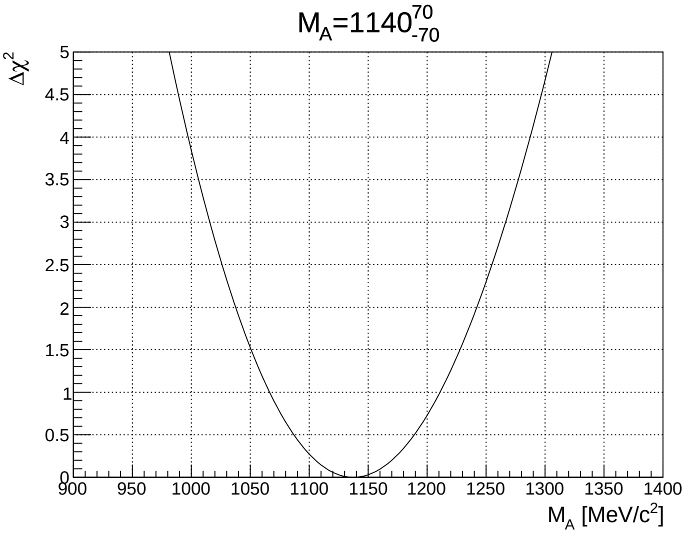

Figure F.2: $\Delta\chi^2$-profile as a function of M_A. A constraint of $M_A = 1.14 \pm 0.07\,\text{GeV}$ is obtained

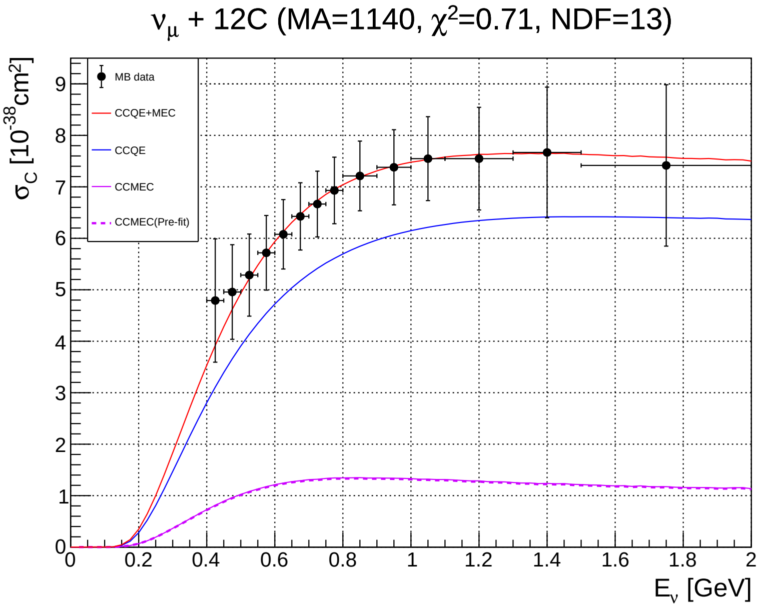

Figure F.3: Best-fit CCQE and CC 2p2h cross sections with the MiniBooNE data. The black dots represent the published data from the MiniBooNE [32]. The blue line denotes the CCQE cross section data. The violet dotted (solid) line represents the nominal (the best fit considering 20% normalization uncertainty) CC 2p2h cross section assuming TEM. The red line shows the sum of CCQE and CC 2p2h cross sections. We use NuWro to predict these cross section data.

Bibliography

[1] Y. Fukuda *et al.*, Evidence for oscillation of atmospheric neutrinos, Phys. Rev. Lett. 81 (1998) 1562–1567. `doi:10.1103/PhysRevLett.81.1562`.

[2] Z. Maki, M. Nakagawa, S. Sakata, Remarks on the Unified Model of Elementary Particles, Progress of Theoretical Physics 28 (5) (1962) 870–880. `arXiv:https://academic.oup.com/ptp/article-pdf/28/5/870/5258750/28-5-870.pdf`, `doi:10.1143/PTP.28.870`.

[3] V. Gribov, B. Pontecorvo, Neutrino astronomy and lepton charge, Physics Letters B 28 (7) (1969) 493–496. `doi:https://doi.org/10.1016/0370-2693(69)90525-5`.

[4] C. Lunardini, Diffuse supernova neutrinos at underground laboratories, Astroparticle Physics 79 (2016) 49–77. `doi:https://doi.org/10.1016/j.astropartphys.2016.02.005`.

[5] M. Tanabashi *et al.*, Review of particle physics, Phys. Rev. D 98 (2018) 030001. `doi:10.1103/PhysRevD.98.030001`.

[6] A. Gando *et al.*, Reactor on-off antineutrino measurement with kamland, Phys. Rev. D 88 (2013) 033001. `doi:10.1103/PhysRevD.88.033001`.

[7] S. Fukuda *et al.*, Determination of solar neutrino oscillation parameters using 1496 days of super-kamiokande-i data, Physics Letters B 539 (3) (2002) 179–187. `doi:https://doi.org/10.1016/S0370-2693(02)02090-7`.

[8] B. Aharmim *et al.*, Electron energy spectra, fluxes, and day-night asymmetries of ^{8}b solar neutrinos from measurements with nacl dissolved in the heavy-water detector at the sudbury neutrino observatory, Phys. Rev. C 72 (2005) 055502. `doi:10.1103/PhysRevC.72.055502`.

[9] K. Abe *et al.*, Atmospheric neutrino oscillation analysis with external constraints in super-kamiokande i-iv, Phys. Rev. D 97 (2018) 072001. `doi:10.1103/PhysRevD.97.072001`.

[10] K. Abe *et al.*, Constraint on the matter–antimatter symmetry-violating phase in neutrino oscillations, Nature 580 (7803) (2020) 339–344. `doi:10.1038/s41586-020-2177-0`.

[11] M. H. Ahn *et al.*, Measurement of neutrino oscillation by the k2k experiment, Phys. Rev. D 74 (2006) 072003. `doi:10.1103/PhysRevD.74.072003`.

[12] P. Adamson *et al.*, Combined analysis of ν_μ disappearance and $\nu_\mu \to \nu_e$ appearance in minos using accelerator and atmospheric neutrinos, Phys. Rev. Lett. 112 (2014) 191801. `doi:10.1103/PhysRevLett.112.191801`.

[13] M. A. Acero *et al.*, Improved measurement of neutrino oscillation parameters by the nova experiment, Phys. Rev. D 106 (2022) 032004. `doi:10.1103/PhysRevD.106.032004`.

[14] Y. Abe *et al.*, Indication of reactor $\overline{\nu}_e$ disappearance in the double chooz experiment, Phys. Rev. Lett. 108 (2012) 131801. `doi:10.1103/PhysRevLett.108.131801`.

[15] F. P. An *et al.*, Observation of electron-antineutrino disappearance at daya bay, Phys. Rev. Lett. 108 (2012) 171803. `doi:10.1103/PhysRevLett.108.171803`.

[16] J. K. Ahn *et al.*, Observation of reactor electron antineutrinos disappearance in the reno experiment, Phys. Rev. Lett. 108 (2012) 191802. `doi:10.1103/PhysRevLett.108.191802`.

[17] A. D. Sakharov, Violation of cp invariance, c asymmetry, and baryon asymmetry of the universe, Soviet Physics Uspekhi 34 (5) (1991) 392. `doi:10.1070/PU1991v034n05ABEH002497`.

[18] S. Pascoli, S. Petcov, A. Riotto, Leptogenesis and low energy cp-violation in neutrino physics, Nuclear Physics B 774 (1) (2007) 1–52. `doi:https://doi.org/10.1016/j.nuclphysb.2007.02.019`.

[19] K. Hirata *et al.*, Observation of a neutrino burst from the supernova sn1987a, Phys. Rev. Lett. 58 (1987) 1490–1493. `doi:10.1103/PhysRevLett.58.1490`.

[20] S. Abe *et al.*, Limits on astrophysical antineutrinos with the kamland experiment, The Astrophysical Journal 925 (1) (2022) 14. `doi:10.3847/1538-4357/ac32c1`.

[21] A. Takenaka *et al.*, Search for proton decay via $p \to e^+\pi^0$ and $p \to \mu^+\pi^0$ with an enlarged fiducial volume in super-kamiokande i-iv, Phys. Rev. D 102 (2020) 112011. `doi:10.1103/PhysRevD.102.112011`.

[22] K. Asakura *et al.*, Search for the proton decay mode $p \to \overline{\nu}K^+$ with kamland, Phys. Rev. D 92 (2015) 052006. `doi:10.1103/PhysRevD.92.052006`.

[23] Y. Hayato, Overview talk on proton decay searches, GLA2011.

[24] K. Abe *et al.*, First gadolinium loading to super-kamiokande, Nuclear Instruments and Methods in Physics Research Section A: Accelerators, Spectrometers, Detectors and Associated Equipment 1027 (2022) 166248. `doi:https://doi.org/10.1016/j.nima.2021.166248`.

[25] H.-K. Proto-Collaboration *et al.*, Hyper-kamiokande design report (2018). `doi:10.48550/ARXIV.1805.04163`.
URL `https://arxiv.org/abs/1805.04163`

[26] F. An *et al.*, Neutrino physics with JUNO, Journal of Physics G: Nuclear and Particle Physics 43 (3) (2016) 030401. `doi:10.1088/0954-3899/43/3/030401`.

[27] T. Golan, C. Juszczak, J. T. Sobczyk, Effects of final-state interactions in neutrino-nucleus interactions, Phys. Rev. C 86 (2012) 015505. `doi:10.1103/PhysRevC.86.015505`.

[28] C. Llewellyn Smith, Neutrino reactions at accelerator energies, Physics Reports 3 (5) (1972) 261–379. `doi:https://doi.org/10.1016/0370-1573(72)90010-5`.

[29] S. L. Adler, Tests of the conserved vector current and partially conserved axial-vector current hypotheses in high-energy neutrino reactions, Phys. Rev. 135 (1964) B963–B966. `doi:10.1103/PhysRev.135.B963`.

[30] R. Bradford *et al.*, A new parameterization of the nucleon elastic form factors, Nuclear Physics B - Proceedings Supplements 159 (2006) 127–132, proceedings of the 4th International Workshop on Neutrino-Nucleus Interactions in the Few-GeV Region. `doi:https://doi.org/10.1016/j.nuclphysbps.2006.08.028`.

[31] I. D. Kakorin, K. S. Kuzmin, V. A. Naumov, Running axial mass of the nucleon as a phenomenological tool for calculating quasielastic neutrino–nucleus cross sections, The European Physical Journal C 81 (12) (2021) 1142. `doi:10.1140/epjc/s10052-021-09945-5`.

[32] A. A. Aguilar-Arevalo *et al.*, First measurement of the muon neutrino charged current quasielastic double differential cross section, Phys. Rev. D 81 (2010) 092005. `doi:10.1103/PhysRevD.81.092005`.

[33] Fermilab today, `https://www.fnal.gov/pub/today/SpecialROWMiniBooNE121208.html`.

[34] V. Lyubushkin *et al.*, A study of quasi-elastic muon neutrino and antineutrino scattering in the nomad experiment, The European Physical Journal C 63 (3) (2009) 355–381. `doi:10.1140/epjc/s10052-009-1113-0`.

[35] S. F. Pate, D. W. McKee, V. Papavassiliou, Strange quark contribution to the vector and axial form factors of the nucleon: Combined analysis of data from the g0, happex, and brookhaven e734 experiments, Phys. Rev. C 78 (2008) 015207. `doi:10.1103/PhysRevC.78.015207`.

[36] Y. Hayato, L. Pickering, The neut neutrino interaction simulation program library, The European Physical Journal Special Topics 230 (24) (2021) 4469–4481. `doi:10.1140/epjs/s11734-021-00287-7`.

[37] A. M. Ankowski *et al.*, Analysis of γ-ray production in neutral-current neutrino-oxygen interactions at energies above 200 mev, Phys. Rev. Lett. 108 (2012) 052505. `doi:10.1103/PhysRevLett.108.052505`.

[38] C. Andreopoulos *et al.*, The genie neutrino monte carlo generator, Nuclear Instruments and Methods in Physics Research Section A: Accelerators, Spectrometers, Detectors and Associated Equipment 614 (1) (2010) 87–104. `doi:https://doi.org/10.1016/j.nima.2009.12.009`.

[39] D. Rein, L. M. Sehgal, Neutrino-excitation of baryon resonances and single pion production, Annals of Physics 133 (1) (1981) 79–153. `doi:https://doi.org/10.1016/0003-4916(81)90242-6`.

[40] S. L. Adler, Photo-, electro-, and weak single-pion production in the (3,3) resonance region, Annals of Physics 50 (2) (1968) 189–311. `doi:https://doi.org/10.1016/0003-4916(68)90278-9`.

[41] S. L. Adler, Application of current-algebra techniques to soft-pion production by the weak neutral current: v, a case, Phys. Rev. D 12 (1975) 2644–2665. `doi:10.1103/PhysRevD.12.2644`.

[42] K. M. Graczyk, J. T. Sobczyk, Form factors in the quark resonance model, Phys. Rev. D 77 (2008) 053001. `doi:10.1103/PhysRevD.77.053001`.

[43] K. M. Graczyk *et al.*, C_5^A axial form factor from bubble chamber experiments, Phys. Rev. D 80 (2009) 093001. `doi:10.1103/PhysRevD.80.093001`.

[44] M. Glück, E. Reya, A. Vogt, Dynamical parton distributions of the proton and small-x physics, Zeitschrift für Physik C Particles and Fields 67 (3) (1995) 433–447. `doi:10.1007/BF01624586`.

[45] A. Bodek, U. K. Yang, Modeling neutrino and electron scattering cross sections in the few gev region with effective lo pdfs, AIP Conference Proceedings 670 (1) (2003) 110–117. `arXiv:https://aip.scitation.org/doi/pdf/10.1063/1.1594324`, `doi:10.1063/1.1594324`.

[46] D. Rein, L. M. Sehgal, Coherent π 0 production in neutrino reactions, Nuclear Physics B 223 (1) (1983) 29–44. `doi:https://doi.org/10.1016/0550-3213(83)90090-1`.

[47] D. Rein, L. Sehgal, Pcac and the deficit of forward muons in π+ production by neutrinos, Physics Letters B 657 (4) (2007) 207–209. `doi:https://doi.org/10.1016/j.physletb.2007.10.025`.

[48] C. Berger, L. M. Sehgal, Partially conserved axial vector current and coherent pion production by low energy neutrinos, Phys. Rev. D 79 (2009) 053003. `doi:10.1103/PhysRevD.79.053003`.

[49] E. Piasetzky *et al.*, Evidence for strong dominance of proton-neutron correlations in nuclei, Phys. Rev. Lett. 97 (2006) 162504. `doi:10.1103/PhysRevLett.97.162504`.

[50] R. Subedi *et al.*, Probing cold dense nuclear matter, Science 320 (5882) (2008) 1476–1478. `doi:10.1126/science.1156675`.

[51] J. Nieves, I. R. Simo, M. J. V. Vacas, Inclusive charged-current neutrino-nucleus reactions, Phys. Rev. C 83 (2011) 045501. `doi:10.1103/PhysRevC.83.045501`.

[52] M. Martini *et al.*, Unified approach for nucleon knock-out and coherent and incoherent pion production in neutrino interactions with nuclei, Phys. Rev. C 80 (2009) 065501. `doi:10.1103/PhysRevC.80.065501`.

[53] K. Nakamura, Measurement of neutrino oscillation with a high intensity neutrino beam, Ph.D. thesis, Kyoto Univ. (2018).

[54] A. Bodek, H. S. Budd, M. E. Christy, Neutrino quasielastic scattering on nuclear targets, The European Physical Journal C 71 (9) (2011) 1726. `doi:10.1140/epjc/s10052-011-1726-y`.

[55] J. Arrington *et al.*, Hard probes of short-range nucleon–nucleon correlations, Progress in Particle and Nuclear Physics 67 (4) (2012) 898–938. `doi:https://doi.org/10.1016/j.ppnp.2012.04.002`.

[56] R. Gran *et al.*, Neutrino-nucleus quasi-elastic and 2p2h interactions up to 10 gev, Phys. Rev. D 88 (2013) 113007. `doi:10.1103/PhysRevD.88.113007`.

[57] A. Hiramoto *et al.*, First measurement of $\overline{\nu}_\mu$ and ν_μ charged-current inclusive interactions on water using a nuclear emulsion detector, Phys. Rev. D 102 (2020) 072006. `doi:10.1103/PhysRevD.102.072006`.

[58] R. Smith, E. Moniz, Neutrino reactions on nuclear targets, Nuclear Physics B 43 (1972) 605–622. `doi:https://doi.org/10.1016/0550-3213(72)90040-5`.

[59] O. Benhar *et al.*, Electron- and neutrino-nucleus scattering in the impulse approximation regime, Phys. Rev. D 72 (2005) 053005. `doi:10.1103/PhysRevD.72.053005`.

[60] J. Nieves, J. E. Amaro, M. Valverde, Inclusive quasielastic charged-current neutrino-nucleus reactions, Phys. Rev. C 70 (2004) 055503. `doi:10.1103/PhysRevC.70.055503`.

[61] Graczyk, K. M., Sobczyk, J. T., Algebraic solution of rpa equationsfor cc quasi-elastic neutrino-nucleus scattering, Eur. Phys. J. C 31 (2) (2003) 177–185. `doi:10.1140/epjc/s2003-01338-6`.

[62] S. Dytman *et al.*, Comparison of validation methods of simulations for final state interactions in hadron production experiments, Phys. Rev. D 104 (2021) 053006. `doi:10.1103/PhysRevD.104.053006`.

[63] L. A. Ahrens *et al.*, Measurement of neutrino-proton and antineutrino-proton elastic scattering, Phys. Rev. D 35 (1987) 785–809. `doi:10.1103/PhysRevD.35.785`.

[64] T. Golan *et al.*, Extraction of axial mass and strangeness values from the miniboone neutral current elastic cross section measurement, Phys. Rev. C 88 (2013) 024612. `doi:10.1103/PhysRevC.88.024612`.

[65] G. T. Garvey, W. C. Louis, D. H. White, Determination of proton strange form factors from νp elastic scattering, Phys. Rev. C 48 (1993) 761–765. `doi:10.1103/PhysRevC.48.761`.

[66] A. A. Aguilar-Arevalo *et al.*, Measurement of the neutrino neutral-current elastic differential cross section on mineral oil at $E_\nu \sim 1$ GeV, Phys. Rev. D 82 (2010) 092005. `doi:10.1103/PhysRevD.82.092005`.

[67] D. T. Spayde *et al.*, Parity violation in elastic electron-proton scattering and the proton's strange magnetic form factor, Phys. Rev. Lett. 84 (2000) 1106–1109. `doi:10.1103/PhysRevLett.84.1106`.

[68] D. Androić *et al.*, Strange quark contributions to parity-violating asymmetries in the backward angle g0 electron scattering experiment, Phys. Rev. Lett. 104 (2010) 012001. `doi:10.1103/PhysRevLett.104.012001`.

[69] Z. Ahmed *et al.*, New precision limit on the strange vector form factors of the proton, Phys. Rev. Lett. 108 (2012) 102001. `doi:10.1103/PhysRevLett.108.102001`.

[70] S. Baunack *et al.*, Measurement of strange quark contributions to the vector form factors of the proton at $Q^2 = 0.22\ (\mathrm{GeV}/c)^2$, Phys. Rev. Lett. 102 (2009) 151803. `doi:10.1103/PhysRevLett.102.151803`.

[71] J. Liu, R. D. McKeown, M. J. Ramsey-Musolf, Global analysis of nucleon strange form factors at low Q^2, Phys. Rev. C 76 (2007) 025202. `doi:10.1103/PhysRevC.76.025202`.

[72] Pate, Stephen, Trujillo, Dennis, Strangeness vector and axial-vector form factors of the nucleon, EPJ Web of Conferences 66 (2014) 06018. `doi:10.1051/epjconf/20146606018`.

[73] R. Acciarri *et al.*, Design and construction of the microboone detector, Journal of Instrumentation 12 (02) (2017) P02017. `doi:10.1088/1748-0221/12/02/P02017`.

[74] K. Woodruff, Neutral current elastic scattering and the strange spin structure of the proton`doi:10.2172/1484179`.

[75] W. Alberico, S. Bilenky, C. Maieron, Strangeness in the nucleon: neutrino–nucleon and polarized electron–nucleon scattering, Physics Reports 358 (4) (2002) 227–308. `doi:https://doi.org/10.1016/S0370-1573(01)00058-8`.

[76] M. Anselmino, A. Efremov, E. Leader, The theory and phenomenology of polarized deep inelastic scattering, Physics Reports 261 (1) (1995) 1–124. `doi:https://doi.org/10.1016/0370-1573(95)00011-5`.

[77] D. Groom *et al.*, Review of Particle Physics, The European Physical Journal, year = 2000, volume =.

[78] A. Airapetian *et al.*, Precise determination of the spin structure function g_1 of the proton, deuteron, and neutron, Phys. Rev. D 75 (2007) 012007. `doi:10.1103/PhysRevD.75.012007`.

[79] 柴. 利明, 陽子と中性子のスピン構造（解説）, 日本物理学会誌 67 (11) (2012) 738–745. `doi:10.11316/butsuri.67.11_738`.

[80] J. Ashman *et al.*, An investigation of the spin structure of the proton in deep inelastic scattering of polarised muons on polarised protons, Nuclear Physics B 328 (1) (1989) 1–35. `doi:https://doi.org/10.1016/0550-3213(89)90089-8`.

[81] V. Alexakhin *et al.*, The deuteron spin-dependent structure function g1d and its first moment, Physics Letters B 647 (1) (2007) 8–17. `doi:https://doi.org/10.1016/j.physletb.2006.12.076`.

[82] E. Leader, D. B. Stamenov, Can the polarization of the strange quarks in the proton be positive?, Phys. Rev. D 67 (2003) 037503. `doi:10.1103/PhysRevD.67.037503`.

[83] T. Golan, J. Sobczyk, J. Żmuda, Nuwro: the wrocław monte carlo generator of neutrino interactions, Nuclear Physics B - Proceedings Supplements 229-232 (2012) 499, neutrino 2010. `doi:https://doi.org/10.1016/j.nuclphysbps.2012.09.136`.

[84] D. Casper, The nuance neutrino physics simulation, and the future, Nuclear Physics B - Proceedings Supplements 112 (1) (2002) 161–170. `doi:https://doi.org/10.1016/S0920-5632(02)01756-5`.

[85] O. Buss *et al.*, Transport-theoretical description of nuclear reactions, Physics Reports 512 (1) (2012) 1–124, transport-theoretical Description of Nuclear Reactions. `doi:https://doi.org/10.1016/j.physrep.2011.12.001`.

[86] Nuwro user guide, `https://nuwro.github.io/user-guide/`.

[87] K. Niewczas, J. T. Sobczyk, Nuclear transparency in monte carlo neutrino event generators, Phys. Rev. C 100 (2019) 015505. `doi:10.1103/PhysRevC.100.015505`.

[88] L. Salcedo *et al.*, Computer simulation of inclusive pion nuclear reactions, Nuclear Physics A 484 (3) (1988) 557–592. `doi:https://doi.org/10.1016/0375-9474(88)90310-7`.

[89] E. S. P. Guerra *et al.*, Using world $\pi^{\pm}$-nucleus scattering data to constrain an intranuclear cascade model, Phys. Rev. D 99 (2019) 052007. `doi:10.1103/PhysRevD.99.052007`.

[90] A. M. Ankowski, Consistent analysis of neutral- and charged-current neutrino scattering off carbon, Phys. Rev. C 86 (2012) 024616. `doi:10.1103/PhysRevC.86.024616`.

[91] H. W. Bertini, Nonelastic interactions of nucleons and π mesons with complex nuclei at energies below 3 gev, Phys. Rev. C 6 (1972) 631–659. `doi:10.1103/PhysRevC.6.631`.

[92] M. Elkins *et al.*, Neutron measurements from antineutrino hydrocarbon reactions, Phys. Rev. D 100 (2019) 052002. `doi:10.1103/PhysRevD.100.052002`.

[93] genie-mc.org, `http://www.genie-mc.org/`.

[94] S. Abe, Nuclear de-excitation associated with neutrino-carbon interactions, Journal of Physics: Conference Series 2156 (1) (2021) 012189. `doi:10.1088/1742-6596/2156/1/012189`.

[95] A. Koning, D. Rochman, Modern nuclear data evaluation with the talys code system, Nuclear Data Sheets 113 (12) (2012) 2841–2934, special Issue on Nuclear Reaction Data. `doi:https://doi.org/10.1016/j.nds.2012.11.002`.

[96] S. Agostinelli *et al.*, Geant4—a simulation toolkit, Nuclear Instruments and Methods in Physics Research Section A: Accelerators, Spectrometers, Detectors and Associated Equipment 506 (3) (2003) 250–303. `doi:https://doi.org/10.1016/S0168-9002(03)01368-8`.

[97] Tendl-2021 nuclear data library, `https://tendl.web.psi.ch/tendl_2019/talys.html`.

[98] L. Lapikás *et al.*, Transparency of ^{12}C for protons, Phys. Rev. C 61 (2000) 064325. `doi:10.1103/PhysRevC.61.064325`.

[99] D. Dutta *et al.*, Quasielastic $(e, e^{'}p)$ reaction on ^{12}C,^{56} Fe, and ^{197}Au, Phys. Rev. C 68 (2003) 064603. `doi:10.1103/PhysRevC.68.064603`.

[100] Y. Kamyshkov, E. Kolbe, Signatures of nucleon disappearance in large underground detectors, Phys. Rev. D 67 (2003) 076007. `doi:10.1103/PhysRevD.67.076007`.

[101] K. Nakamura *et al.*, The reaction 12c(e, e′ p) at 700 mev and dwia analysis, Nuclear Physics A 268 (3) (1976) 381–407. `doi:https://doi.org/10.1016/0375-9474(76)90539-X`.

[102] J. Mougey *et al.*, Quasi-free (e, e'p) scattering on 12c, 28si, 40ca and 58ni, Nuclear Physics A 262 (3) (1976) 461–492. `doi:https://doi.org/10.1016/0375-9474(76)90510-8`.

[103] V. Panin *et al.*, Exclusive measurements of quasi-free proton scattering reactions in inverse and complete kinematics, Physics Letters B 753 (2016) 204–210. `doi:https://doi.org/10.1016/j.physletb.2015.11.082`.

[104] H. Hu *et al.*, Implementation of residual nucleus de-excitations associated with proton decays in 12c based on the genie generator and talys code, Physics Letters B 831 (2022) 137183. `doi:https://doi.org/10.1016/j.physletb.2022.137183`.

[105] M. Yosoi *et al.*, Structure and decay of the s-hole state in 11b studied via the 12c(p,2p)11b* reaction, Physics Letters B 551 (3) (2003) 255–261. `doi:https://doi.org/10.1016/S0370-2693(02)03062-9`.

[106] A. Suzuki, Antineutrino science in kamland, The European Physical Journal C 74 (10) (2014) 3094. `doi:10.1140/epjc/s10052-014-3094-x`.

[107] P. Antonioli *et al.*, A three-dimensional code for muon propagation through the rock: Music, Astroparticle Physics 7 (4) (1997) 357–368. `doi:https://doi.org/10.1016/S0927-6505(97)00035-2`.

[108] S. Abe *et al.*, Production of radioactive isotopes through cosmic muon spallation in kamland, Phys. Rev. C 81 (2010) 025807. `doi:10.1103/PhysRevC.81.025807`.

[109] 小関陽太郎, Kamland の液体シンチレーター、バッファーオイル、アクリル板の屈折率の測定結果レポート, KamLAND Collaboration Internal Note.

[110] 上澤康平, Kamland2-zen 実験で用いる新液体シンチレータの活性炭による純化, 東北大学大学院修士論文 (2018).

[111] 伊藤和嘉子, 液体シンチレーター中での光散乱及び再発光の分光、時間構造測定, 東北大学大学院修士論文 (2002).

[112] Y. Zhang *et al.*, A complete optical model for liquid-scintillator detectors, Nuclear Instruments and Methods in Physics Research Section A: Accelerators, Spectrometers, Detectors and Associated Equipment 967 (2020) 163860. `doi:https://doi.org/10.1016/j.nima.2020.163860`.

[113] 田頭健司, 高精度１７インチ光電子増倍管の性能計測研究, 東北大学大学院修士論文 (2000).

[114] S. Lorenz, Topological Track Reconstruction in Liquid Scintillator and LENA as a Far-Detector in an LBNO Experiment, Ph.D. thesis, Hamburg U., Hamburg (2016). `doi:10.3204/PUBDB-2016-06366`.

[115] H. Ozaki, J. Shirai, Refurbishment of KamLAND outer detector, PoS ICHEP2016 (2017) 1161. `doi:10.22323/1.282.1161`.

[116] A. Gando *et al.*, Measurement of the double-β decay half-life of ^{136}xe with the kamland-zen experiment, Phys. Rev. C 85 (2012) 045504. `doi:10.1103/PhysRevC.85.045504`.

[117] B. E. Berger *et al.*, The KamLAND full-volume calibration system, Journal of Instrumentation 4 (04) (2009) P04017–P04017. `doi:10.1088/1748-0221/4/04/p04017`.

[118] K. Ichimura, Precice measurement of neutrino oscillation parameters with kamland, Ph.D. thesis, Tohoku Univ. (2008).

[119] S. Obara, A search for supernova relic neutrinos with kamland during reactor-off period, Ph.D. thesis, Tohoku Univ. (2018).

[120] 三宅春彦, Kamland-zen 実験における低ゲイン pmt の光量応答性を考慮したエネルギー再構成による背景事象低減, 東北大学大学院修士論文 (2020).

[121] Top, `https://jp.optosigma.com/`.

[122] M. Sayuri, Search for neutrinoless double-beta decay in 136xe after intensive background reduction with kamland-zen, Ph.D. thesis, Tohoku Univ. (2016).

[123] H. Watanabe, Comprehensive study of anti-neutrino signals at kamland, Ph.D. thesis, Tohoku Univ. (2012).

[124] J. B. Birks, Scintillations from organic crystals: Specific fluorescence and relative response to different radiations, Proceedings of the Physical Society. Section A 64 (10) (1951) 874–877. `doi:10.1088/0370-1298/64/10/303`.

[125] K. Nakajima, First results from ^{7}be solar neutrino observation with kamland, Ph.D. thesis, Tohoku Univ. (2010).

[126] C. N. Chou, The nature of the saturation effect of fluorescent scintillators, Phys. Rev. 87 (1952) 904–905. `doi:10.1103/PhysRev.87.904`.

[127] S. Yoshida *et al.*, Light output response of kamland liquid scintillator for protons and 12c nuclei, Nuclear Instruments and Methods in Physics Research Section A: Accelerators, Spectrometers, Detectors and Associated Equipment 622 (3) (2010) 574–582. `doi:https://doi.org/10.1016/j.nima.2010.07.087`.

[128] F. Boreli, B. B. Kinsey, P. N. Shrivastava, Neutron cross-section measurements of ^{12}C between 14 and 25 mev, Phys. Rev. 174 (1968) 1147–1154. `doi:10.1103/PhysRev.174.1147`.

[129] E. L. Hjort *et al.*, Measurements and analysis of neutron elastic scattering at 65 mev, Phys. Rev. C 50 (1994) 275–281. `doi:10.1103/PhysRevC.50.275`.

[130] A. S. Meigooni, J. S. Petler, R. W. Finlay, Scattering cross-sections and partial kerma factors for neutron interactions with carbon at 20 less than en less than 65 MeV, Phys Med Biol 29 (6) (1984) 643–659.

[131] N. Olsson, B. Trostell, E. Ramstrom, Cross sections and partial kerma factors for elastic and inelastic neutron scattering from carbon in the energy range 16.5-22.0 MeV, Physics in Medicine and Biology 34 (7) (1989) 909–926. `doi:10.1088/0031-9155/34/7/011`.

[132] Y. Yamanouti *et al.*, Proc. int. Conf. on Nuclear Data for Science and Technology.

[133] R. G. P. Voss, R. Wilson, F. A. Lindemann, Neutron inelastic cross-sections between 55 and 140 mev, Proceedings of the Royal Society of London. Series A. Mathematical and Physical Sciences 236 (1204) (1956) 41–51. `arXiv:https://royalsocietypublishing.org/doi/pdf/10.1098/rspa.1956.0111`, `doi:10.1098/rspa.1956.0111`.

[134] M. H. MacGregor, W. P. Ball, R. Booth, Neutron nonelastic cross sections at 21.0, 25.5, and 29.2 mev, Phys. Rev. 111 (1958) 1155–1162. `doi:10.1103/PhysRev.111.1155`.

[135] D. A. Kellogg, Cross sections for products of 90-mev neutrons on carbon, Phys. Rev. 90 (1953) 224–232. `doi:10.1103/PhysRev.90.224`.

[136] C. I. Zanelli *et al.*, Total non-elastic cross sections of neutrons on c, o, ca, and fe at 40.3 and 50.4 mev, Phys. Rev. C 23 (1981) 1015–1022. `doi:10.1103/PhysRevC.23.1015`.

[137] J. DeJuren, N. Knable, Nuclear cross sections for 95-mev neutrons, Phys. Rev. 77 (1950) 606–614. `doi:10.1103/PhysRev.77.606`.

[138] M. Chadwick *et al.*, Evaluated cross-section libraries and kerma factors for neutrons up to 100 mev on sup 12c, UCRL-ID-120829.

[139] D. Ashery *et al.*, True absorption and scattering of pions on nuclei, Phys. Rev. C 23 (1981) 2173–2185. `doi:10.1103/PhysRevC.23.2173`.

[140] M. Aglietta et al., Measurement of the neutron flux produced by cosmic ray muons with LVD at Gran Sasso, in: 26th International Cosmic Ray Conference, 1999. `arXiv:hep-ex/9905047`.

[141] H. Araújo *et al.*, Muon-induced neutron production and detection with geant4 and fluka, Nuclear Instruments and Methods in Physics Research Section A: Accelerators, Spectrometers, Detectors and Associated Equipment 545 (1) (2005) 398–411. `doi:https://doi.org/10.1016/j.nima.2005.02.004`.

[142] K. Abe *et al.*, T2k neutrino flux prediction, Phys. Rev. D 87 (2013) 012001. `doi:10.1103/PhysRevD.87.012001`.

[143] 安部清尚, T2k ビームを用いた kamland でのニュートリノ反応研究, 東北大学大学院修士論文 (2020).

[144] M. Honda *et al.*, Atmospheric neutrino flux calculation using the nrlmsise-00 atmospheric model, Phys. Rev. D 92 (2015) 023004. `doi:10.1103/PhysRevD.92.023004`.

[145] Hkkm's atmospheric neutrino flux, `https://www.icrr.u-tokyo.ac.jp/~mhonda/`.

[146] E. Richard *et al.*, Measurements of the atmospheric neutrino flux by super-kamiokande: Energy spectra, geomagnetic effects, and solar modulation, Phys. Rev. D 94 (2016) 052001. `doi:10.1103/PhysRevD.94.052001`.

[147] M. Honda *et al.*, Calculation of atmospheric neutrino flux using the interaction model calibrated with atmospheric muon data, Phys. Rev. D 75 (2007) 043006. `doi:10.1103/PhysRevD.75.043006`.

[148] G. Battistoni *et al.*, The atmospheric neutrino flux below 100mev: The fluka results, Astroparticle Physics 23 (5) (2005) 526–534. `doi:https://doi.org/10.1016/j.astropartphys.2005.03.006`.

[149] M. Honda, , Atmospheric neutrino flux below 100 mev, Neutrino 2020 poster.

[150] M. Honda *et al.*, Reducing uncertainty in atmospheric neutrino flux prediction, in: 30th International Cosmic Ray Conference, Vol. 5, 2007, pp. 1491–1494.

[151] Climax neutron monitor, `http://cr0.izmiran.ru/clmx/main.htm`.

[152] Links to cosmic ray data, `http://cr0.izmiran.ru/common/links.htm`.

[153] Oulu cosmic ray station, `https://cosmicrays.oulu.fi/`.

[154] Github - rogerwendell/prob3plusplus: Software for calculating neutrino oscillation probabilities in matter or vacuum, `https://github.com/rogerwendell/Prob3plusplus`.

[155] A. M. Dziewonski, D. L. Anderson, Preliminary reference earth model, Physics of the Earth and Planetary Interiors 25 (4) (1981) 297–356. `doi:https://doi.org/10.1016/0031-9201(81)90046-7`.

[156] A. Lindote *et al.*, Simulation of neutrons produced by high-energy muons underground, Astroparticle Physics 31 (5) (2009) 366–375. `doi:https://doi.org/10.1016/j.astropartphys.2009.03.008`.

[157] D. Measday, The nuclear physics of muon capture, Physics Reports 354 (4) (2001) 243–409. `doi:https://doi.org/10.1016/S0370-1573(01)00012-6`.

[158] M. Yamada *et al.*, Measurements of the charge ratio and polarization of 1.2-tev/c cosmic-ray muons with the kamiokande ii detector, Phys. Rev. D 44 (1991) 617–621. `doi:10.1103/PhysRevD.44.617`.

[159] Root: analyzing petabytes of data, scientifically. - root, `https://root.cern/`.

[160] A. Takeuchi, First search for majorana neutrinos in the inverted mass hierarchy region with kamland-zen, Ph.D. thesis, Tohoku Univ. (2021).

[161] Minuit: Function minimization and error analysis, `https://cds.cern.ch/record/2296388/files/minuit.pdf`.

[162] J. F. Beacom, W. M. Farr, P. Vogel, Detection of supernova neutrinos by neutrino-proton elastic scattering, Phys. Rev. D 66 (2002) 033001. `doi:10.1103/PhysRevD.66.033001`.

[163] Energy level diagrams a=11, `https://nucldata.tunl.duke.edu/nucldata/figures/11figs/menu11.shtml#2012`.

[164] R. B. Firestone *et al.*, The 8th edition of the Table of Isotopes, Springer, Hungary, 1997.

[165] E. McCutchan, Nuclear data sheets for a = 68, Nuclear Data Sheets 113 (6) (2012) 1735–1870. `doi:https://doi.org/10.1016/j.nds.2012.06.002`.